Charles University in Prague
Faculty of Mathematics and Physics

DOCTORAL THESIS

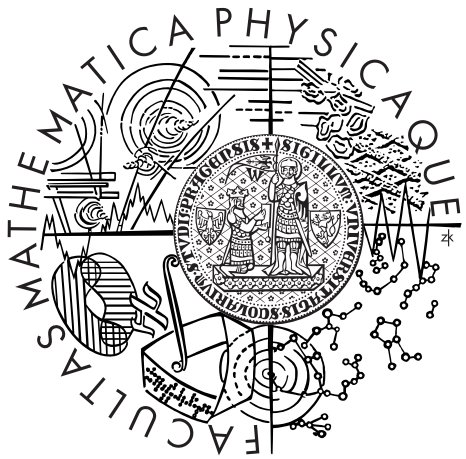

ŠTĚPÁN ROUČKA

LABORATORY ASTROCHEMISTRY AND APPLICATIONS OF COMPUTER SIMULATIONS

Department of Surface and Plasma Science
Supervisor of the doctoral thesis: Prof. RNDr. Rudolf Hrach, DrSc.
Advisor: Prof. RNDr. Juraj Glosík, DrSc.
Study programme: Physics
Study branch: Physics of Plasmas and Ionized Media

ACKNOWLEDGMENTS

During my PhD studies, I have enjoyed the collaboration with many people who deserve an acknowledgment for their contribution to this thesis. At the first place, I thank my supervisor Prof. RNDr. Rudolf Hrach, DrSc. for introducing me to the field of computer physics and my advisor Prof. RNDr. Juraj Glosík, DrSc. for giving me the opportunity to participate on the experimental research. I am grateful to both of them for the excellent supervision.

I also wish to thank Prof. Dieter Gerlich for his advisory on the ion trapping technology and for arranging the lending of the ion trapping equipment from the TU Chemnitz to Prague. I thank Prof. Roland Wester for offering me the opportunity to stay at the University of Innsbruck and to learn new experimental and computational techniques.

The work would not have been possible without the collaboration of my colleagues from the Laboratory of Elementary Processes in Plasma. I am especially grateful to Pavol Jusko for his work on the ion trapping experiments. I thank to other present and former group members, namely Radek Plašil, Petr Dohnal, Tomáš Kotrík, Illia Zymak, Dmytro Mulin, Peter Rubovič, Michal Hejduk, Jozef Varju, and Aleš Podolník.

My work was supported by grants GACR 202/08/H057, GAUK 25709, GAUK 659112, and COST CM0805.

V neposlední řadě děkuji všem svým přátelům a především své rodině za všestrannou podporu při studiu.

DECLARATION

I declare that I carried out this doctoral thesis independently, and only with the cited sources, literature and other professional sources.

I understand that my work relates to the rights and obligations under the Act No. 121/2000 Coll., the Copyright Act, as amended, in particular the fact that the Charles University in Prague has the right to conclude a license agreement on the use of this work as a school work pursuant to Section 60 paragraph 1 of the Copyright Act.

Prague, June 2012

Štěpán Roučka

BIBLIOGRAFICKÉ INFORMACE

NÁZEV PRÁCE: Laboratorní astrochemie a aplikace počítačových modelů
AUTOR: Štěpán Roučka
KATEDRA: Katedra fyziky povrchů a plazmatu
VEDOUCÍ DOKTORSKÉ PRÁCE: Prof. RNDr. Rudolf Hrach DrSc.

ABSTRAKT: Tato práce je zaměřena na laboratorní studium chemie iontů v podmínkách relevantních pro astrofyziku. Mezi tři hlavní výstupy práce patří: Za prvé: práce na experimentálním studiu rychlostního keficientu reakce asociativního odtržení $H^- + H \rightarrow H_2 + e^-$. V práci je popsáno měření rychlostního koeficientu v teplotním rozsahu 10–135 K. Za druhé: návrh nové aparatury pro detekci elektronů vzniklých v iontové pasti a pro měření jejich energie. Popsány jsou počítačové modely a předběžné experimentální výsledky. Za třetí: vývoj modelu chlazení elektronů v dohasínajícím plazmatu a jeho aplikace při analýze výsledků měření rekombinace H_3^+.

KLÍČOVÁ SLOVA: astrochemie, počítačové modelování, iontová past, dohasínající výboj

BIBLIOGRAPHIC INFORMATION

TITLE: Laboratory Astrochemistry and Applications of Computer Simulations
AUTHOR: Štěpán Roučka
DEPARTMENT: Department of Surface and Plasma Science
SUPERVISOR: Prof. RNDr. Rudolf Hrach DrSc.

ABSTRACT: This work is focused on laboratory studies of ion chemistry at conditions relevant for astrophysics. The three main outcomes of the thesis are: (1) The experimental study of the reaction rate coefficient of the associative detachment reaction $H^- + H \rightarrow H_2 + e^-$; measurement of the thermal rate coefficient at the temperatures in the range 10–135 K is described. (2) The design of a novel apparatus for detecting the electrons produced in the RF trap and measuring their energy; numerical simulations and preliminary experimental results are presented. (3) The development of a model of the electron cooling in the afterglow plasma and the application of the model in the analysis of the H_3^+ recombination measurements.

KEYWORDS: astrochemistry, computer modelling, ion trap, afterglow

LIST OF PUBLICATIONS

PUBLICATIONS IN IMPACTED JOURNALS

Dohnal, P., M. Hejduk, J. Varju, P. Rubovič, Š. Roučka, T. Kotrík, R. Plašil, J. Glosík, et al. (2012a). "Binary and ternary recombination of para- and ortho-H_3^+ with electrons; State selective study at 77–200 K." In: 136.24, 244304, p. 244304.
DOI: 10.1063/1.4730162.
URL: http://link.aip.org/link/?JCP/136/244304/1.

Dohnal, P., M. Hejduk, J. Varju, P. Rubovič, Š. Roučka, T. Kotrík, R. Plašil, R. Johnsen, et al. (2012b). "Binary recombination of para- and ortho-H_3^+ with electrons at low temperatures." In: *Philos. Trans. R. Soc. London, Ser. A*. in print.

Gerlich, D., P. Jusko, Š. Roučka, I. Zymak, R. Plašil, and J. Glosík (Apr. 2012). "Ion Trap Studies of $H^- + H \rightarrow H_2 + e^-$ between 10 and 135 K." In: *The Astrophysical Journal* 749, 22, p. 22.
DOI: 10.1088/0004-637X/749/1/22.

Glosík, J., I. Korolov, R. Plašil, T. Kotrík, P. Dohnal, O. Novotný, J. Varju, Š. Roučka, et al. (2009). "Binary and ternary recombination of D_3^+ ions with electrons in He-D_2 plasma." In: *Physical Review A: General Physics* 80.4, 042706, p. 042706.
DOI: 10.1103/PhysRevA.80.042706.

Glosík, J., R. Plašil, T. Kotrík, P. Dohnal, J. Varju, M. Hejduk, I. Korolov, Š. Roučka, et al. (2010). "Binary and ternary recombination of H_3^+ and D_3^+ ions with electrons in low temperature plasma." In: *Molecular Physics* 108.17, pp. 2253–2264.
DOI: 10.1080/00268976.2010.507555.

Hrach, R., Š. Roučka, V. Hrachová, and L. Schmiedt (2009). "Study of plasma-solid interaction in electronegative gas mixtures at higher pressures." In: *Vacuum* 84.1, pp. 94–96.
DOI: 10.1016/j.vacuum.2009.06.008.

Jusko, P., Š. Roučka, R. Plašil, D. Gerlich, and J. Glosík (2012a). "Electron Spectrometer – Multipole Trap: First Experimental Results." In: *Acta Universitatis Carolinae, Mathematica et Physica*. in preparation.

Kotrík, T., P. Dohnal, I. Korolov, R. Plašil, Š. Roučka, J. Glosík, C. Greene, and V. Kokoouline (2010). "Temperature dependence of binary and ternary recombination of D_3^+ ions with electrons." In: *Journal of Chemical Physics* 133.3, 034305, p. 034305.
DOI: 10.1063/1.3457940.

Kotrík, T., P. Dohnal, P. Rubovič, R. Plašil, Š. Roučka, S. Opanasiuk, and J. Glosík (2011c). "Cryo-FALP study of collisional-radiative

recombination of Ar^+ ions at 40–200 K." In: *The European Physical Journal - Applied Physics* 56.02, p. 24011.
DOI: 10.1051/epjap/2011110158.

Kotrík, T., P. Dohnal, Š. Roučka, P. Jusko, R. Plašil, J. Glosík, and R. Johnsen (Mar. 2011d). "Collisional-radiative recombination $Ar^+ + e + e$: Experimental study at 77–180 K." In: *Physical Review A: General Physics* 83 (3), p. 032720.
DOI: 10.1103/PhysRevA.83.032720.

Roučka, Š and R. Hrach (Nov. 2011). "Extending PIC Models to Higher Pressures - Enhanced Model of Collisions." In: *Plasma Science, IEEE Transactions on* 39.11, pp. 3244 –3250.
DOI: 10.1109/TPS.2011.2164789.

Zymak, I., P. Jusko, Š. Roučka, R. Plašil, P. Rubovič, D. Gerlich, and J. Glosík (2011b). "Ternary association of H^+ ion with H_2 at 11 K, experimental study." In: *The European Physical Journal Applied Physics* 56.2, 24010, p. 24010.
DOI: 10.1051/epjap/2011110172.

PUBLICATIONS IN WOS REGISTERED PROCEEDINGS

Only the proceedings registered by the Web of Science *are listed.*

Pekárek, Z., Š. Roučka, and R. Hrach (2008). "3D particle simulations of plasma-solid interaction: magnetized plasma and a cylindrical cavity." In: *Journal of Physics: Conference Series* 100.6, p. 062010.
URL: http://stacks.iop.org/1742-6596/100/i=6/a=062010.

Varju, J., Š. Roučka, T. Kotrík, R. Plašil, and J. Glosík (2010). "Application of NIR-CRDS for state selective study of recombination of para and ortho H_3^+ ions with electrons in low temperature plasma." In: *Journal of Physics: Conference Series* 227.1, p. 012026.
URL: http://stacks.iop.org/1742-6596/227/i=1/a=012026.

PUBLICATIONS IN CONFERENCE PROCEEDINGS

Jusko, P., Š. Roučka, D. Mulin, R. Plašil, and J. Glosík (2011a). "Atomic Beam Calibration for the $H^- + H$ Experiment." In: *WDS'11 Proceedings of Contributed Papers: Part II - Physics*. Prague, Czech Republic: Matfyzpress, pp. 165–168.

Jusko, P., I. Zymak, D. Mulin, Š. Roučka, R. Plašil, D. Gerlich, and J. Glosík (2012c). "Experimental determination of conditions in the trap: reaction temperature and reactant density." In: *XVIIIth Symposium on Atomic, Cluster and Surface Physics 2012 (SASP 2012) Contributions*. Ed. by M. Lewerenz and R. Dutuit O. Marquardt. Innsbruck University Press, pp. 200–203.

Jusko, P., Š. Roučka, I. Zymak, R. Plašil, D. Gerlich, and J. Glosík (2011b). "Combination of an Electron Spectrometer with an Ion

Trap: first results for $H^- + h\nu$ and $H^- + H$." In: *SAPP XVIII, Book of Contributed Papers*. Ed. by J. Országh, P. Papp, and Š. Matějčík. UK Bratislava, pp. 252–256.

Kotrík, T., P. Dohnal, S. Opanasiuk, P. Rubovič, Š. Roučka, R. Plašil, and J. Glosík (2011a). "New Cryo-FALP Experiment to Study Collisional Radiative Recombination of Ar^+ Ions at 40–200 K." In: *WDS'11 Proceedings of Contributed Papers: Part II - Physics*. Prague, Czech Republic: Matfyzpress, pp. 136–140.

Kotrík, T., P. Dohnal, R. Plašil, Š. Roučka, and J. Glosík (2011b). "Experimental Study of Collisional Radiative Recombination of Ar ions at low temperatures." In: *SAPP XVIII, Book of Contributed Papers*. Ed. by J. Országh, P. Papp, and Š. Matějčík. UK Bratislava, pp. 161–165.

Roučka, Š, A. Podolník, P. Jusko, T. Kotrík, R. Plašil, and J. Glosík (2009a). "Combination of a 22-pole Trap with an Electron Energy Filter – Study of Associative Detachment $H^- + H \rightarrow H_2 + e^-$." In: *WDS'09 Proceedings of Contributed Papers: Part II - Physics*. Prague, Czech Republic: Matfyzpress, pp. 121–128.

— (2010b). "Study of Capture and Cooling of H^- Ions in RF Octopole with superimposed Magnetic Field." In: *WDS'10 Proceedings of Contributed Papers: Part II - Physics*. Prague, Czech Republic: Matfyzpress, pp. 105–111.

Roučka, Š, P. Jusko, I. Zymak, D. Mulin, R. Plašil, and J. Glosík (2011b). "Influence of the 22-pole Trap Imperfections on the Interaction of Ions with a Neutral Beam." In: *WDS'11 Proceedings of Contributed Papers: Part II - Physics*. Prague, Czech Republic: Matfyzpress, pp. 158–164.

Roučka, Š, P. Jusko, I. Zymak, R. Plašil, D. Gerlich, and J. Glosík (2011e). "Study of Astrophysically Relevant Hydrogen Chemistry: combining an RF Ion Trap with a Cold Effusive Beam." In: *SAPP XVIII, Book of Contributed Papers*. Ed. by J. Országh, P. Papp, and Š. Matějčík. UK Bratislava, pp. 204–209.

Roučka, Š, P. Dohnal, M. Hejduk, J. Varju, P. Rubovič, S. Opanasiuk, R. Plašil, and J. Glosík (2012a). "Collisional Radiative Recombination of H_3^+ Ion in Low Temperature Plasma." In: *XVIIIth Symposium on Atomic, Cluster and Surface Physics 2012 (SASP 2012) Contributions*. Ed. by M. Lewerenz and R. Dutuit O. Marquardt. Innsbruck University Press, pp. 259–262.

Rubovič, P., T. Kotrík, P. Dohnal, Š. Roučka, M. Hejduk, S. Opanasiuk, R. Plašil, and J. Glosík (2011). "Swarm Experiments at 40-100 K, Cryo-FALP." In: *WDS'11 Proceedings of Contributed Papers: Part II - Physics*. Prague, Czech Republic: Matfyzpress, pp. 146–151.

Zymak, I., P. Jusko, Š. Roučka, D. Mulin, R. Plašil, and J. Glosík (2011a). "Association of H^+ with H_2 at low temperatures." In: *WDS'11 Proceedings of Contributed Papers: Part II - Physics*. Prague, Czech Republic: Matfyzpress, pp. 175–179.

Only the contributions presented by the author are listed.

Hrach, R., Š. Roučka, V. Hrachová, and L. Schmiedt (2008). "Study of plasma-solid interaction in electronegative gas mixtures at higher pressures." In: *12th Joint Vacuum Conference, 10th European Vacuum Conference*. (Sept. 22–26, 2008). poster presentation. Balatonalmadi, Hungary.

Roučka, Š, A. Podolník, P. Jusko, T. Kotrík, R. Plašil, and J. Glosík (2009b). "Combination of a 22-pole Trap with an Electron Energy Filter – Study of Associative Detachment $H^- + H \rightarrow H_2 + e^-$." In: *WE-Heraeus-Seminar "Anions - from the lab to the stars"*. (June 7–11, 2009). poster presentation. Bad Honnef, Germany.

— (2009c). "Combination of a 22-pole Trap with an Electron Energy Filter – Study of Associative Detachment $H^- + H \rightarrow H_2 + e^-$." In: *WDS'09*. (June 2–5, 2009). poster presentation. Prague, Czech Republic.

Roučka, Š and R. Hrach (2009). "Computational Study of Plasma-Solid Interaction at Increasing Pressures." In: *21st International Conference on Numerical Simulation of Plasmas*. (Oct. 6–10, 2009). poster presentation. Lisbon, Portugal.

Roučka, Š, P. Jusko, A. Podolník, T. Kotrík, R. Plašil, and J. Glosík (2010a). "Study of Associative Detachment Using RF Ion Trap With Electron Spectrometer." In: *3rd ITS LEIF Winter School: Complex Systems & Ion Optical Tools*. (Mar. 7–12, 2010). oral presentation. Pralognan, France.

Roučka, Š, A. Podolník, P. Jusko, T. Kotrík, R. Plašil, and J. Glosík (2010c). "Study of Capture and Cooling of H^- Ions in RF Octopole with superimposed Magnetic Field." In: *WDS'10,* (June 1–4, 2010). poster presentation. Prague, Czech Republic.

Roučka, Š, P. Jusko, I. Zymak, D. Mulin, R. Plašil, and J. Glosík (2011a). "Influence of the 22-pole Trap Imperfections on the Interaction of Ions with a Neutral Beam." In: *WDS'11*. (May 31–June 3, 2011). poster presentation. Prague, Czech Republic.

Roučka, Š, A. Podolník, P. Jusko, T. Kotrík, R. Plašil, and J. Glosík (2011c). "Interactions of H^- Anions with Atomic Hydrogen–Ion Trap study at 10–135 K." In: *XXVII International Conference on Photonic, Electronic and Atomic Collisions*. (July 27–Aug. 2, 2011). poster presentation. Belfast, Northern Ireland, UK.

Roučka, Š, P. Jusko, I. Zymak, R. Plašil, D. Gerlich, and J. Glosík (2011d). "Study of Astrophysically Relevant Hydrogen Chemistry: combining an RF Ion Trap with a Cold Effusive Beam." In: *SAPP XVIII, 18th Symposium on Application of Plasma Processes*. (Mar. 7–12, 2010). oral presentation. Vrátna, Slovakia.

Roučka, Š, P. Dohnal, M. Hejduk, J. Varju, P. Rubovič, S. Opanasiuk, R. Plašil, and J. Glosík (2012b). "Collisional Radiative Recombina-

tion of H_3^+ Ion in Low Temperature Plasma." In: *XVIIIth Symposium on Atomic, Cluster and Surface Physics*. (July 27–Aug. 2, 2011). poster presentation. Alpe d'Huez, France.

BACHELOR'S THESIS AND MASTER'S THESIS

Roučka, Š (2008a). "Počítačové modelování interakce nízkoteplotního plazmatu s pevnými látkami". BA thesis. Charles University in Prague, Faculty of Mathematics and Physics.

— (2008b). "Studium interakce plazma-pevná látka při středních tlacích." MA thesis. Charles University in Prague, Faculty of Mathematics and Physics.
URL: http://www.roucka.eu/diplomka.

CONTENTS

Scalar variables and constants are written in upright italics, as a, b, c, π. Vectors are written in boldface as $\mathbf{E}, \mathbf{B}, \boldsymbol{v}$ and their norms are denoted by the same letter in upright italics: E, B, v. Unit vectors, which usually coincide with the base vectors of the coordinate system, are indicated by the hat symbol: $\hat{\mathbf{x}}, \hat{\mathbf{y}}, \hat{\mathbf{z}}$. The exception is the reduced radius of the trap $\hat{r} = r/r_0$, which is normalized by the inscribed radius of the trap. Time derivatives are indicated by dots as $\mathbf{a} = \ddot{\mathbf{r}}$ and $\boldsymbol{v} = \dot{\mathbf{r}}$. Square brackets around a species name such as $[e^-]$ or $[H^-]$ indicate number densities of elements or numbers of particles depending on context. Angle brackets $\langle . \rangle$ denote averaging. The meaning of some common symbols used throughout the text is listed below. More specific quantities are explained directly in the text. Subscripts g, e, and i generally indicate the quantities associated with the neutral gas, electrons, and ions, respectively.

$\mathbf{r}$	radius vector
$\boldsymbol{v}$	velocity vector
$\mathbf{a}$	acceleration vector
$\mathcal{E}$	energy
$\mathbf{E}$	electric field
$\mathbf{D}$	electric displacement field
$\mathbf{B}$	magnetic field
$\mathbf{H}$	magnetizing field (H-field)
$\mathbf{J}$	electric current density
ρ	electric charge density
n	number density
q	electric charge
ϵ	electric permittivity
ϕ	electric potential
$\mathbf{A}$	magnetic vector potential
V_0	RF amplitude
Ω	RF angular frequency
r_g	gyroradius (Larmor radius)
ω_c	angular gyrofrequency (cyclotron frequency)
T	temperature
m	mass
$\mathcal{E}_\perp$	energy associated with perpendicular motion
$\mathcal{E}_\parallel$	energy associated with parallel motion

To understand hydrogen is to understand all of physics.

— unknown author

1 PREFACE

The work described in this thesis was done in the years 2008–2012 during my PhD studies in the Laboratory of Elementary Processes in Plasma at the Department of Surface and Plasma Science, Faculty of Mathematics and Physics, Charles University in Prague. The research of the Laboratory is focused on the ion chemistry relevant for the astrophysics. The major part of my work consists of numerical simulations and their application to the design of experiments and analysis of experimental results.

Our motivation and a brief overview of the current state of knowledge are presented in chapter 2. Chapters 3 and 4 present a review of the mathematical models of the electromagnetic fields and charged particles, which are used in this thesis. Some basic theory of the experimental techniques in use is in chapter 5. Chapter 6 describes the design, construction, and first experimental results of a unique apparatus capable of measuring the energy of electrons produced in the radio-frequency multipole ion trap. Our recent experimental study of the $H^- + H$ associative detachment is described in chapter 7. The results of this study were published in a paper (Gerlich et al., 2012) in The Astrophysical Journal. Chapter 8 is independent of the rest of the work—it presents a detailed model of electron cooling in the afterglow plasma and its application to the analysis of the experimental data. The results of the analysis are partly contained in the publications Kotrík et al., 2011b; Kotrík et al., 2011a; Dohnal et al., 2012a and Dohnal et al., 2012b.

You know, it would be sufficient to really understand the electron.

— Albert Einstein

2 INTRODUCTION

Understanding the interaction of ions with other particles is a fundamental problem in atomic physics. The field of ion collisions is very broad and includes interactions with photons, electrons, atoms, molecules, clusters, or other ions. Our experimental work focuses on some very simple interacting systems like $H^- + H$, $D^- + H$, $O^- + h\nu$, $H_3^+ + e^-$, and others. The choice of considered systems follows from our interest in reactions which are important in astrophysics. Moreover, it is advantageous to study the simple systems in order to obtain results directly comparable against ab initio quantum calculations.

There are basically two main motivations for our work. Our first aim is to provide experimental values of rate coefficients and cross sections which then serve as an input for kinetic models in astrophysics or even in industrial plasma processing. The other aim is a more fundamental quest for a detailed understanding of the underlying physics, where our results can serve as a benchmark for various theoretical models.

Despite the fact that a lot of experimental and theoretical effort is dedicated to investigating much more complex systems, leading mainly to organic chemistry and biomolecules, the are still many unsolved problems even for the simple diatomic collisions. We believe that studying simple systems in the end provides us with a better understanding in various fields from quantum mechanics to atomic and molecular physics, to plasma physics, and to astrophysics.

2.1 ION-MOLECULE REACTIONS IN ASTROPHYSICS

For decades, astronomers have been observing abundance of various molecules and cations ions in the interstellar space. Currently about 165 different molecular species have been detected in space, ranging in size from simple diatomics to aromatic hydrocarbons to fullerenes (Müller et al., 2001; Müller et al., 2005; *CDMS* 2012). The presence of anions in space had been only inferred from indirect observations until recently. The first directly detected anion in space was C_6H^-, observed by McCarthy et al., 2006. Since then, several other anionic species have been detected, in particular CN^-, C_3N^-, C_5N^-, C_4H^-, and C_8H^- (see, e. g., Agúndez et al., 2010 and references therein).

With the current advances in the spectroscopic astronomical instruments such as Planck (Planck Collaboration et al., 2011), Herschel

(Molinari et al., 2010), and especially ALMA (Semenov et al., 2008), there is a rapidly growing amount of data regarding the molecular composition and conditions in the interstellar medium. To understand the data, a large amount of laboratory work is needed. First, a laboratory spectroscopy of molecules and molecular ions is necessary to identify the observed species. Second, laboratory measurements of reaction rate coefficients and cross sections are essential for understanding the complicated chemical networks of interstellar space, which often include hundreds or even thousands of chemical reactions (see, e. g., Woodall et al., 2007).

The chemical composition of the interstellar matter is by itself a very interesting topic worth studying, because it lets us deduce information about the interstellar physical conditions and especially because it can help us to understand the conditions in the early Solar system. Those, which lead to the origin of life on the Earth and, possibly, elsewhere. Another motivation, which is relevant for this work, is the important role played by the chemical processes during the formation of galaxies, planets, and stars.

Although it may seem—at first sight—that the evolution of large scale celestial bodies is not greatly influenced by their chemical composition and by the chemical processes occurring in the surrounding medium, the astronomical observations and models suggest the exact opposite. All the solid bodies in the Universe ultimately originate from the condensation of gaseous and occasionally dusty clouds of matter. An important process in determining the behaviour of an astrophysical cloud is the conversion between different forms of energy, e. g., between macroscopic kinetic energy and thermal energy (friction) or between kinetic energy of particles and radiation (cooling).

For example, the presence of ions in the protoplanetary disks is essential to provide a coupling between the magnetic fields and matter, which leads to magnetohydrodynamical instabilities (Balbus and Hawley, 1991). These in consequence drive the accretion and determine the sizes and orbits of the newly forming planets (See, e. g., Wardle, 2007; Semenov et al., 2008 and references therein).

This work is motivated by another striking example of importance of chemistry in astrophysics. To explain our motivation we need to look into the early phase of universe evolution and into the formation of protogalaxies and protostars in particular. Before the first stars (population III) were formed, the elemental composition of the baryonic matter was determined by the Big Bang nucleosynthesis (BBN) process. The BBN, which occurred during the first 1000 s after the Big Bang (Walker et al., 1991), produced only small amounts of elements heavier than helium. The estimates of initial composition of the baryonic matter are summarized in the table 1.

Approximately 300 000 years after the Big Bang, the energy of the cosmic background radiation decreased enough to allow for the elec-

nucleus	relative number to ^{1}H
^{1}H	1
^{4}He	$8.3 \cdot 10^{-2}$
^{2}D	$2.8 \cdot 10^{-5}$
^{7}Li	$\approx \cdot 10^{-10}$

Table 1: Measured relative abundances of the elements after the Big Bang nucleosynthesis (Yao et al., 2006). The primordial density of ^{3}He has not been determined from observations, but the observations of more recent astronomical objects and models suggest a value of the order 10^{-5} (Balser et al., 1999). Other elements are expected to be present at relative concentrations below 10^{-10} (Vangioni-Flam et al., 2000).

tron-proton recombination and the formation of atoms. Only after the recombination epoch, first chemical processes could be initiated. Due to the elemental composition of the primordial gas, the chemistry was driven almost purely by hydrogen interactions.

The formation of the first stars was triggered, according to the ΛCDM cosmological model, by the presence of small spatial inhomogeneities in the initial dark matter distribution (see Abel et al., 2002; Glover, 2011). These inhomogeneities underwent a gravitational collapse and formed the so-called *dark matter halos*. The dark matter halos, of course, attract the surrounding baryonic matter—the primordial gas. However, a gravitationally compressed cloud of the primordial gas heats up and the thermal pressure can prevent the cloud from the further collapse and the formation of a protostar. Only if there is a sufficiently strong cooling process for a cloud of given mass, the collapse can lead to a protostar formation.

Astrophysical models of star formation indicate that a protostellar cloud consisting of purely atomic species would need to be very massive for the gravity to overcome the thermal pressure. This is because the radiative cooling by the electronic transitions in atomic species (i. e., Lyman-α cooling in atomic hydrogen) is inefficient at temperatures below 10^4 K. Only the presence of molecular hydrogen in the primordial gas can provide sufficient cooling by the rovibrational transitions and explain the formation of the low-mass stars in the early universe (Palla et al., 1983; Le Bourlot et al., 1999).

Since there are no significant amounts of elements heavier than helium in the primordial gas, the molecular hydrogen can be formed in the gas phase only, as opposed to the heterogeneous formation on dust surfaces in the more recent molecular clouds. There are basically three main pathways of the formation of the molecular hydrogen. At high redshifts, when the cosmic background radiation energy was high enough to destroy most of the H^- by photodetachment, the main

channel of H_2 formation was based on the charge transfer reaction (Glover et al., 2006):

$$H + H^+ \rightarrow H_2^+ + h\nu\,, \tag{1}$$
$$H + H_2^+ \rightarrow H_2 + H^+. \tag{2}$$

In the later phases, the H^- produced by the radiative attachment to H was able to survive long enough to form molecular hydrogen by the associative detachment reaction. Therefore, a sequence of reactions consisting of the radiative attachment followed by the associative detachment

$$e^- + H \rightarrow H^- + h\nu\,, \tag{3}$$
$$H^- + H \rightarrow H_2 + e^- \qquad \Delta H = -3.723 \text{ eV} \tag{4}$$

represents the major pathway to the formation of the molecular hydrogen in a wide range of conditions in the early universe (Glover et al., 2006). The symbol ΔH indicates the reaction enthalpy. Only in the late phases of the protostellar cloud collapse, when the number density of gas particles reaches $n > 10^8$ cm^{-3}, the three-body processes take over and rapidly convert the atomic hydrogen to H_2 in reactions (Palla et al., 1983; Turk et al., 2011)

$$H + H + H \rightarrow H_2 + H\,, \tag{5}$$
$$H + H + H_2 \rightarrow H_2 + H_2\,. \tag{6}$$

Influence of the different processes leading to the formation of H_2 has been studied using numerical models of the protostar formation. It has been shown for a range of initial conditions that the outcome of the models (i. e., the temperature and the density of the collapsing cloud at a certain time) strongly depends on the rate of the H_2 formation. In particular, Glover et al., 2006 shows that the uncertainty of the associative detachment (4) reaction coefficient leads to more than one order of magnitude uncertainties in the models of protostar formation from initially hot (10^4 K) clouds. Furthermore, also the ternary association reaction (6) was shown to have great influence during the late phases of the protostar formation (Turk et al., 2011). The uncertainty in the three body reaction coefficients is several orders of magnitude (Glover, 2008), which seriously complicates our understanding of the protostar formation process. The situation with the associative detachment uncertainties has, however, changed significantly since the publication by Glover et al., 2006. Details of the associative detachment properties will be discussed in the next section.

2.2 ASSOCIATIVE DETACHMENT REACTION

The associative detachment (AD) reaction is a general process, which can be symbolically described as

$$A + B^- \rightarrow AB^- \rightarrow AB(v, J) + e^-(E)\,. \tag{7}$$

The short-lived reaction complex AB^- plays a fundamental role in a number of important scattering processes besides the associative detachment. For example, in elastic and inelastic electron-molecule scattering, dissociative electron attachment, collisional detachment, or other types of reactive scattering (see, e. g., Smith and Leone, 1983; Čížek et al., 1998). Therefore, studying all of these phenomena can be considered as different views on the quantum-mechanical dynamics of the AB^- complex.

2.2.1 *The H_2^- Reaction Complex*

As was shown in the previous section, an important example of the AD is the reaction of $H^- + H$ described by equation (4)

$$H^- + H \rightarrow H_2 + e^- \qquad\qquad \Delta H = -3.723 \text{ eV}\,. \tag{4}$$

Its relevance for the chemistry of the astrophysical environments was first pointed out by Dalgarno (Pagel, 1959), proposing it as a mechanism for establishing the thermal equilibrium in the solar atmosphere.

The rate coefficient and cross section of the reaction were calculated by a number of theoretical studies. Among them, Bieniek and Dalgarno, 1979 emphasized the need for the state specific cross sections and presented such cross sections for two electron energies. Later, Sakimoto, 1989 calculated the energy dependence of the cross section down to very low energies 10^{-5} eV using the local complex potential. His calculations show that at low energies, the AD cross section is identical with the classical orbiting cross section up to a factor 2, which accounts for the fact that only the $^2\Sigma_g^+$ state of H_2^- contributes to the reactive scattering. The $^2\Sigma_u^+$ state is repulsive (Bieniek and Dalgarno, 1979) and the reaction via this state does not occur for collision energies below $\approx$ 0.75 eV (Miller et al., 2011). Results of Sakimoto, 1989 are significantly higher than the Langevin cross section, because the long-range interaction potential is more attractive than the polarization potential. Finally, Čížek et al., 1998 calculated the total cross section using the non-local resonance model with more accurate potential surfaces. His results are higher than other theoretical works at 300 K, but agree well with the results of Sakimoto, 1989 at low energies, as shown in figure 1. Čížek et al., 1998 also presents the rovibrational distribution of the produced molecule and kinetic energy distribution of the detached electron, which is shown in figure 2.

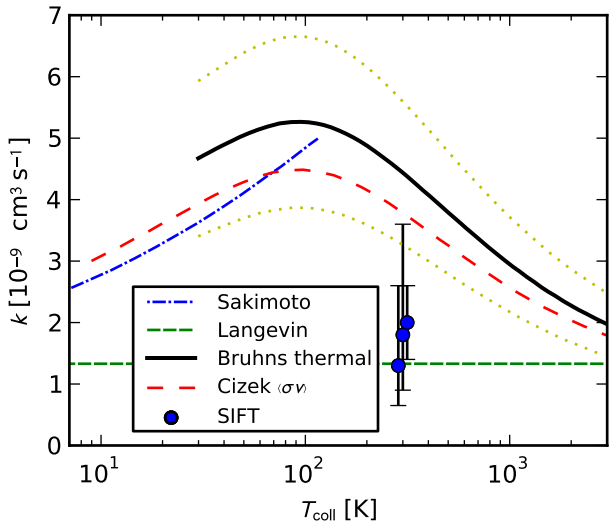

Figure 1: Overview of the calculated and measured temperature dependencies of the $H^- + H$ AD rate coefficient. Results of Sakimoto, 1989 and Čížek et al., 1998 are indicated by dash-dotted and long-dashed lines respectively. The Langevin rate is indicated by the short-dashed line. SIFT measurements at 300 K by Schmeltekopf et al., 1967; Fehsenfeld et al., 1973; Martinez et al., 2009 (from left to right) are indicated by circles with small offset in temperature for better readability. The thermal rate coefficient calculated by Bruhns et al., 2010 from the merged beam data of Kreckel et al., 2010 and multiplied by 1.086 to account for the presure corrections (Miller et al., 2011) is shown as the solid line with error margins indicated by the dotted lines.

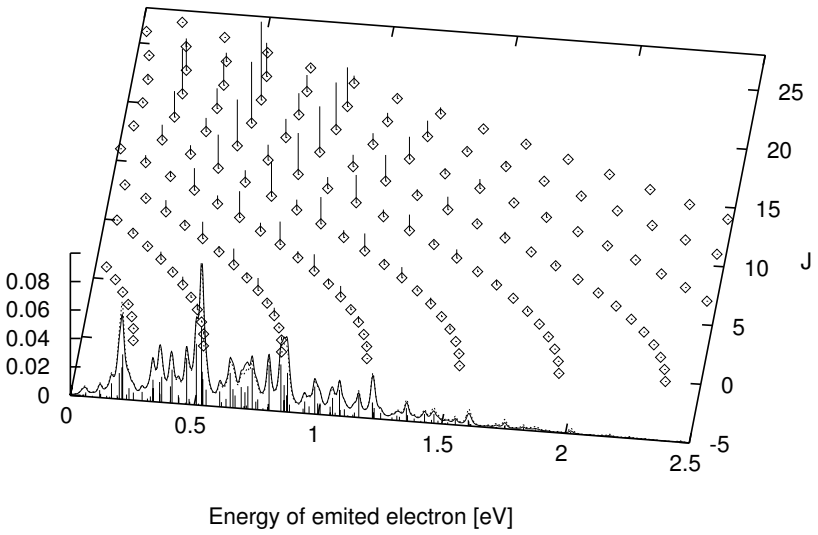

Figure 2: The distribution of products from the $H^- + H$ AD reaction at 0.01 eV collision energy. The electron kinetic energy and the H_2 rotational state J are shown. Reprinted from Čížek et al., 1998.

The experimental studies were limited until recently to flow-tube measurements at 300 K temperature. First experimental rate coefficient was obtained by Schmeltekopf et al., 1967. Their results were then reproduced by Fehsenfeld et al., 1973, and with improved accuracy by Martinez et al., 2009. The early experimental results had a relatively large error margin of a factor 2. As pointed out by Glover et al., 2006, the experimental results did not agree with the most recent theory by Čížek et al., 1998. It was shown that the overall uncertainty of the rate coefficient is a serious problem for the models of the star formation in the early universe, as discussed in the previous section. The question of the star formation motivated the research of Kreckel et al., 2010, who measured the total reaction cross section using a merged beam apparatus in a wide range of energies 0.003 eV to 1 eV. As shown in the figure 1, his results are in excellent agreement with the most recent theory of Čížek et al., 1998.

As mentioned before, the product energy distributions of $H^- + H$ AD have been calculated in the local complex potential approximation by Bieniek and Dalgarno, 1979 and in the non-local potential by Čížek et al., 1998, but no one has been able to measure them yet. The question of the product energy distributions of the $H^- + H$ associative detachment is the main motivation for building a new instrument in our laboratory, which will be capable of measuring energy distributions of electrons produced in a radiofrequency ion trap. The design and first results of said apparatus—called *electron spectrometer with a multipole trap* (ES-MPT)—are described in the chapter 6 in detail.

2.2.2 *The H_2O^- Reaction Complex*

Of course, the capabilities of the ES-MPT apparatus will not be limited to $H^- + H$ reactions. The first collision system which will be studied is $O^- + H_2$. At low energies, this reaction can proceed via two exothermic channels (Lee and Farrar, 1999)

$$O^- + H_2 \rightarrow H_2O + e^- \qquad \Delta H = -3.60 \text{ eV} \tag{8}$$

$$\rightarrow OH^- + H \qquad \Delta H = -0.28 \text{ eV}. \tag{9}$$

The main advantage of H_2O^- as a test system instead of H_2^- is that the reactant is not radical and can be simply leaked into a scattering cell, which surrounds the trap. In addition, the collisional cooling of a heavier O^- ion is more efficient than cooling of H^- due to the smaller radio-frequency (RF) heating (see section 6.4 for details). This system has been studied extensively, but our experimental techniques can provide new valuable information as will be explained in the following paragraph.

The rate coefficients of these reactions and their isotopic variants with D_2 have been measured at 300 K and higher temperatures by means of flow-drift tube and tandem mass spectrometry experiments

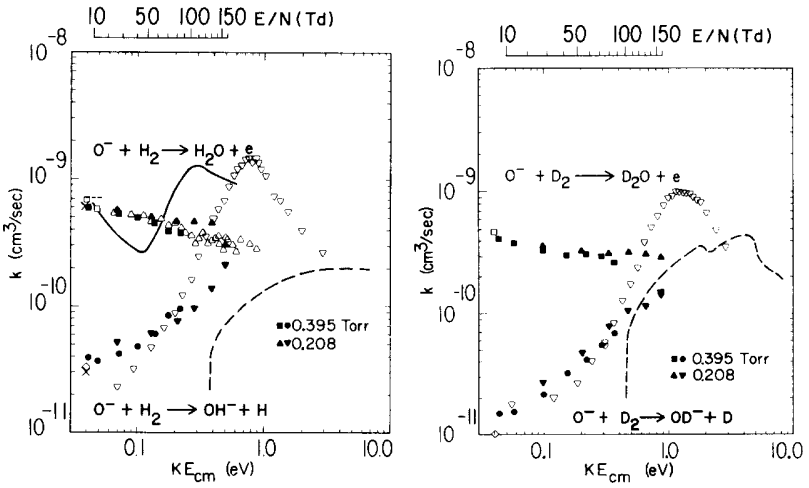

Figure 3: Overview of the measured $O^- + H_2$ reaction rates by McFarland et al., 1973. The reaction rates of the associative detachment reaction are indicated by the symbols ■, ▲, △ and by the solid line. The reaction rate for the production of $OH^- + H$ is indicated by the symbols •, ▼, ▽ and by the dashed line. The data of McFarland et al., 1973 are indicated by the solid symbols.

(see McFarland et al., 1973 and references therein). The measured rate coefficients are shown in figure 3.

The product energy distributions have been studied by several authors. Lee and Farrar, 1999 studied the vibrational distribution of the OH^- and OD^- products by measuring the product velocity distributions in a crossed beam apparatus. They have found strong unpredicted isotopic effects and claimed that these effects are possibly the strongest ever measured. Their measurements show that the fraction of the total energy stored in the vibrational excitation is much higher in the deuterated reaction. Especially at the lowest collision energy 0.5 eV. They suggest that the presence of the associative detachment channel can be related to these effects.

The energy distributions of the electrons from the associative detachment reaction have been studied in crossed beam experiments by Mauer and Schulz, 1973 and Esaulov et al., 1990 at collision energies down to 0.05 eV and 1 eV respectively. Their results are shown in the figure 4. Both experiments indicate small electron energy and high rovibrational excitation of the produced molecule.

The experiment of Mauer and Schulz, 1973 guides the electrons from the reaction cell into the retarding field analyzer using a constant magnetic field. In their experiment, the projection of the velocity distribution along the magnetic field is measured. They discuss that a collimation of electrons in their experiment is not needed, because the projection of the isotropic monoenergetic velocity distribution is peaked around the correct energy. This is not true as shown in section 5.2—the velocity distribution is actually uniform according to

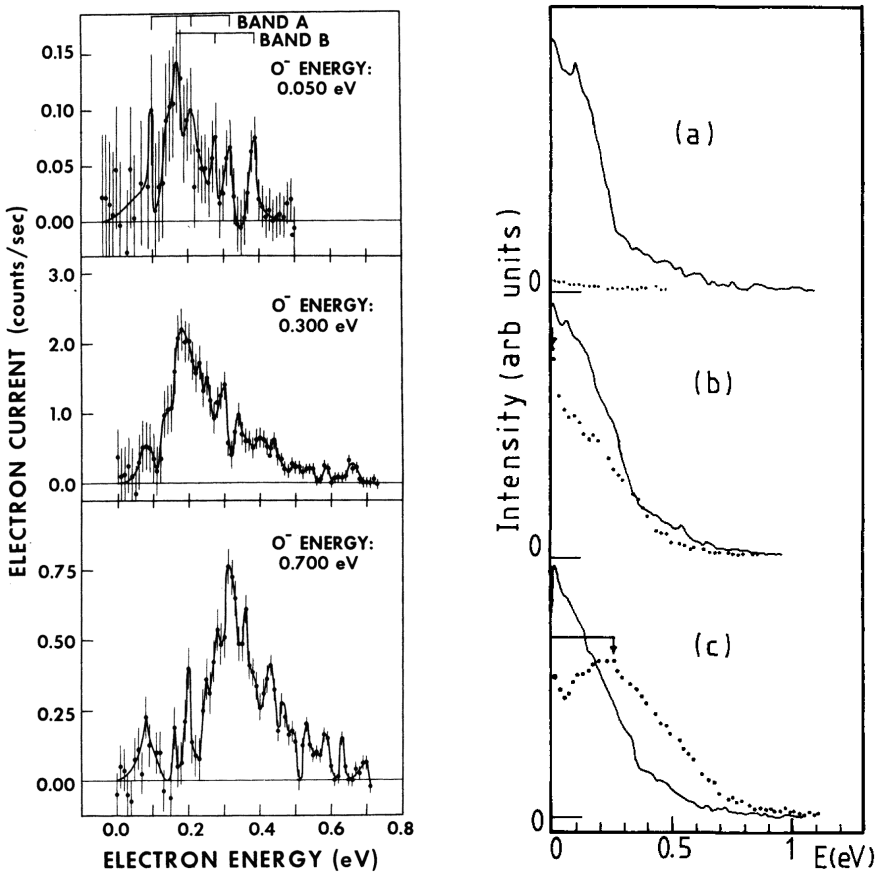

Figure 4: The energy distribution of electrons from reaction (8) measured by Mauer and Schulz, 1973 (left panel) and Esaulov et al., 1990 (right panel). The center of mass collision energies are written in the left plot. The collision energies in the right panel are (from top to bottom) 1 eV, 1.5 eV, and 2 eV. At collision energies above 1.46 eV, the electrons are produced also by collisional detachment.

equation (127). However, the electrons in their experiment are passing through a sequence of 0.5 mm holes, which can filter out some of the electrons with large gyroradii and large perpendicular velocities. Nevertheless, the data by Mauer and Schulz, 1973 do not seem to be very reliable, unless more information about their measurement procedure is obtained.

The data by Esaulov et al., 1990 agree with Mauer and Schulz, 1973 on the small energy of the electrons. However, in contrast to Mauer and Schulz, 1973, they do not observe any peaks corresponding to particular vibrational levels.

The isotopic effects on the energy distribution of electrons have not been studied so far. It was, however, suggested by Lee and Farrar, 1999 that the associative detachment channel may play a role in the strong isotopic effects observed in the reaction channel (9). Therefore, studying the isotopic effects on the associative detachment reaction is one of the aims of the newly built electron spectrometer with a multipole trap (ES-MPT) apparatus described in chapter 6. Study of the isotopic effects on the associative detachment of $F^- + H$ and $F^- + D$ by Smith and Leone, 1983 shows that these effects can provide valuable information about the underlying quantum mechanical processes.

3

MODELLING OF ELECTROMAGNETIC FIELDS

In principle, almost all processes occurring in the fields of molecular and atomic physics can be reduced to the electromagnetic interaction of elementary particles. However, for the purpose of this chapter, we limit our discussion only to the large scale electrostatic and magnetostatic fields. These are determined in the experiment by the potentials applied to the electrodes, currents in the electromagnets, and spatial distributions of charged particles in case of plasmatic experiments. Proper understanding of the large scale electromagnetic fields is essential for any experiment involving charged particles, because these fields consequently determine the spatial and energetic distributions of the studied particles. In this section, we explain our use of the numerical models to obtain the magnetic and electric fields as a solution to the Maxwell's equations

$$\nabla \cdot \mathbf{D} = \rho \qquad \text{Gauss's law,} \tag{10a}$$

$$\nabla \cdot \mathbf{B} = 0 \qquad \text{no monopoles,} \tag{10b}$$

$$\nabla \times \mathbf{E} = -\frac{\partial \mathbf{B}}{\partial t} \qquad \text{Faraday's law,} \tag{10c}$$

$$\nabla \times \mathbf{H} = \mathbf{J} + \frac{\partial \mathbf{D}}{\partial t} \qquad \text{Ampère's law,} \tag{10d}$$

in combination with the material relations

$$\mathbf{D} = \epsilon \mathbf{E}, \ \mathbf{H} = \mathbf{B}/\mu, \ \mathbf{J} = \sigma \mathbf{E}\,. \tag{11}$$

We are using a standard nomenclature described on the page xii. In the case of the static fields, the time derivatives can be neglected. In our experimental setups, the electrostatic field is completely determined by the electrode potentials and the space charge densities inside the vacuum vessel. Influence of the induced currents on the magnetic field is negligible in comparison with the external magnetic field generated by the electromagnets. Hence, the electrostatic and magnetostatic fields are not coupled in any way. The separate treatment of electric and magnetic fields will be presented in the following sections of this chapter.

Please note that we do not discuss complete mathematical foundations of the involved numerical methods. Only the principles and the information necessary to implement these methods with the help of the freely available libraries are presented. For detailed discussion refer to textbooks on computational physics or plasma modelling, e. g., Logg et al., 2012; Bossavit, 1998; Birdsall and Langdon, 1991; Hockney and Eastwood, 1988.

3.1 ELECTROSTATIC FIELDS

The governing equation for the electrostatic field is the Poisson equation. Since we are interested in the field in vacuum, we can substitute for $\mathbf{D}$ using the material equation (11). Then using the relation for the scalar potential $\mathbf{E} = -\nabla\phi$ we obtain

$$\Delta\phi = -\frac{\rho}{\epsilon_0}\,; \quad \mathbf{r} \in \Omega\,, \tag{12}$$

where $\mathbf{r}$ is the radius vector and Ω is the problem domain. Now in order to solve for the potential ϕ in the domain Ω, we need to specify the charge density ρ in this domain and the boundary conditions (Dirichlet, Neumann, or mixed) on the domain boundary $\partial\Omega$. In our calculations, we deal only with Dirichlet boundary conditions, i. e.,

$$\phi = \phi_0\,; \quad \mathbf{r} \in \partial\Omega\,. \tag{13}$$

3.1.1 *Finite Difference Method*

Probably the simplest approach to solving this kind of problem is the finite difference method (FDM). The aforementioned method replaces the continuous functions by functions defined on a discrete set of points and the differential operators are replaced by finite differences operating on these points. In particular, in Cartesian coordinates we use the central differences with second order accuracy ($O(\Delta x^2)$)

$$\frac{\partial f_i}{\partial x} \approx \frac{f_{i+1/2} - f_{i-1/2}}{\Delta x}\,, \qquad \frac{\partial^2 f_i}{\partial x^2} \approx \frac{f_{i-1} - 2f_i + f_{i+1}}{\Delta x^2}\,. \tag{14}$$

In the above equation, a standard nomenclature for expressing difference equations is used, i. e., $f_j \equiv f(x_j)$; $x_j \equiv j\Delta x$, where Δx is the spacing between grid points. We assume the simple case of homogeneous grid, i. e., $\Delta x = \text{const}$.

The Poisson equation on a homogeneous isotropic two dimensional (2D) Cartesian grid ($\Delta x = \Delta y = \text{const}$.) can thus be converted into a set of linear equations of the form

$$\frac{4\phi_{ij} - \phi_{i-1,j} - \phi_{i+1,j} - \phi_{i,j-1} - \phi_{i,j+1}}{\Delta x^2} = \frac{\rho_{ij}}{\epsilon_0}\,; \quad \mathbf{r}_{ij} \in \Omega \setminus \partial\Omega\,, \tag{15}$$

where we define the position vector as $\mathbf{r}_{ij} = (x_{ij}, y_{ij})$. In combination with Dirichlet boundary conditions

$$\phi_{ij} = \phi^0_{ij}\,; \quad \mathbf{r}_{ij} \in \partial\Omega\,, \tag{16}$$

these equations fully determine the desired solution.

The situation is more complicated in case of non-Cartesian grids. It is, however, useful to use curvilinear coordinate systems that can accommodate to the symmetry of the studied problem. In our experiments we often deal with cylindrically symmetric situation and

therefore we implement a solver of the Poisson equation in the 2D r-z cylindrical coordinates. The discretization of the Laplace operator in the cylindrical coordinates using the Gauss' law is described in the section 14-10 of Birdsall and Langdon, 1991. The radial part for the case of the homogeneous grid spacing in the radial direction can be written as

$$\Delta_r \phi \approx \begin{cases} \dfrac{(i-1/2)\phi_{i-1} - 2i\phi_i + (i+1/2)\phi_{i+1}}{i\Delta r^2} & r_i \in \Omega \setminus \partial\Omega; i \neq 0 \\ \dfrac{\phi_1 - \phi_0}{\Delta r^2} & i = 0\,. \end{cases} \tag{17}$$

The axial part of the Laplace operator is the same as in the Cartesian coordinates. By summing the axial and radial parts, we can obtain the discrete approximation for the Laplace operator in r-z coordinates and the Poisson equation then reads

$$\begin{aligned} \frac{\rho_{ij}}{\epsilon_0} = &-\frac{(i-1/2)\phi_{i-1,j} - 2i\phi_{ij} + (i+1/2)\phi_{i+1,j}}{i\Delta r^2} \\ &- \frac{\phi_{i,j-1} - 2\phi_{ij} + \phi_{i,j+1}}{\Delta z^2}\,; \qquad r_{ij} \in \Omega \setminus \partial\Omega; i \neq 0, \end{aligned} \tag{18a}$$

$$\frac{\rho_{ij}}{\epsilon_0} = -\frac{\phi_{1,j} - \phi_{0,j}}{\Delta r^2} - \frac{\phi_{i,j-1} - 2\phi_{ij} + \phi_{i,j+1}}{\Delta z^2}\,; \quad r_{ij} \in \Omega \setminus \partial\Omega; i = 0. \tag{18b}$$

One of the most powerful methods for solving the finite differenced Poisson equation is based on the *LU decomposition* (Pekárek et al., 2007). To explain the principle of this method, assume that the set of equations (15), (16) is written in the matrix form

$$\mathbf{A}\boldsymbol{\phi} = \boldsymbol{\rho}\,, \tag{19}$$

where the right-hand side vector $\boldsymbol{\rho}$ contains elements ρ_{ij}/ϵ_0 and ϕ^0_{ij}. The square matrix $\mathbf{A}$ has order n, where n is the number of grid points. It can be decomposed into an upper triangular matrix $\mathbf{U}$ and a lower triangular matrix $\mathbf{L}$, i. e., $\mathbf{A} = \mathbf{L}\mathbf{U}$. Using this LU decomposition, we can rewrite equation (19) into a system of equations

$$\mathbf{U}\boldsymbol{\phi} = \mathbf{x}\,, \tag{20a}$$

$$\mathbf{L}\mathbf{x} = \boldsymbol{\rho}\,, \tag{20b}$$

which can be solved easily using backsubstitution thanks to the triangular shape of $\mathbf{L}$ and $\mathbf{U}$. The most complicated step in this solution procedure is (as could be expected) the calculation of the LU decomposition, which has algorithmic complexity $O(n^3)$ for general and practically useful algorithms. Despite the complexity of the decomposition, this procedure is very useful for selfconsistent simulations of

plasmas, since the decomposition needs to be calculated only once for the given geometry. The solutions for various combinations of charge densities and boundary conditions can then be obtained very quickly by varying the right hand side vector $\boldsymbol{\rho}$ in equations (20).

In this work we use the freely available library unsymmetric multifrontal sparse LU factorization package (UMFPACK) (Davis, 2004b). The UMFPACK decomposition algorithms are optimized for dealing with sparse matrices. Therefore, they can take advantage of the sparse structure of matrix $\mathbf{A}$, which is essential for performing this calculation with large matrices on personal computers. Typical mesh sizes used in our calculations are of the order 200×200. Hence, the matrix $\mathbf{A}$ is typically of the order 40 000 and contains $1.6{\cdot}10^9$ elements, of which only about 200 000 elements are nonzero. Since only the nonzero elements need to be stored, this matrix is easily calculated and stored in the memory of a personal computer. The LU decomposition of a sparse matrix is not sparse in general. However, the UMFPACK library can ensure the optimal sparsity and accuracy of the LU decomposition by preordering of the matrix $\mathbf{A}$ For details of the UMFPACK algorithm see (Davis, 2004a; Davis and Duff, 1999).

The finite difference methods offer a relatively simple and efficient solution for dealing with partial differential equations on simple geometries. However, it becomes very difficult to accommodate the regular mesh and difference equations to the complicated geometries of many real experiments. Therefore, the complementary finite element method (FEM) is used in most cases with irregular geometry.

3.1.2 *Finite Element Method*

The finite element method approaches the solution by converting the partial differential equation (PDE) into a variational problem called the *weak formulation*. This procedure generally consists of multiplying the equation by a test function v and integrating over the domain Ω. For Poisson equation we thus obtain using the Green's identity (integration by parts)

$$\int_\Omega \nabla\phi \cdot \nabla v \, d\mathbf{r} = \int_\Omega \frac{\rho}{\epsilon_0} v \, d\mathbf{r} \,. \tag{21}$$

We drop the boundary integral, because we choose test functions equal zero on the Dirichlet boundary, where ϕ is known. Solving Poisson equation is now equivalent to finding $\phi \in V$ such that equation (21) is satisfied for all $v \in \hat{V}$. The test space $\hat{V}$ is defined as

$$\hat{V} = \{v \in H^1(\Omega) : v = 0 \text{ on } \partial\Omega\}, \tag{22}$$

and we are looking for ϕ in a trial space V, which automatically satisfies the Dirichlet boundary condition

$$V = \{v \in H^1(\Omega) : v = \phi_0 \text{ on } \partial\Omega\}. \tag{23}$$

Symbol $H^1(\Omega)$, denotes a Sobolev space of functions v defined as $H^1(\Omega) = \{v \in L^2(\Omega); |\nabla v|^2 \in L^2(\Omega)\}$.

In order to solve this infinitely dimensional problem numerically, we have to restrict the functions to some finitely dimensional subspaces $V_h \subset V$ and $\hat{V}_h \subset \hat{V}$ with dimension N. In particular, the finite element method uses a basis consisting of piecewise polynomial functions with "small support". The basis functions are defined in relation to a certain discrete mesh and are called *finite elements*, hence the name finite element method. For more information on various finite elements, see, e. g., (Logg et al., 2012). Assuming that the bases for our problem are defined by $\{v_k\}_{k=1}^N$ and $\{\hat{v}_k\}_{k=1}^N$, then the approximate solution $\phi_h \in V_h$ can be written as

$$\phi_h = \sum_{k=1}^{N} U_k v_k \,. \tag{24}$$

The values of coefficients are obtained by solving equation (21) for all the basis functions from the test space $\hat{V}_h$, i. e.,

$$\sum_{k=1}^{N} U_k \int_\Omega \nabla v_k \cdot \nabla \hat{v}_l \,\mathrm{d}\mathbf{r} = \int_\Omega \frac{\rho}{\epsilon_0} \hat{v}_l \,\mathrm{d}\mathbf{r}\,; \quad l = 1, 2, \ldots, N\,. \tag{25}$$

This set of linear equations has a sparse matrix in the matrix formulation and can be solved by the same methods as the finite difference equations.

3.2 MAGNETOSTATIC FIELDS

Similarly to the electrostatic field, also the Maxwell's equations for the magnetostatic field can be converted into a single second order equation using a potential formulation. From equation (10b) we see, using the Helmholtz decomposition, that $\mathbf{B}$ can be expressed as $\mathbf{B} = \nabla \times \mathbf{A}$. The Ampère's law (10d) then reads

$$\nabla \times \frac{1}{\mu} \nabla \times \mathbf{A} = \mathbf{J}. \tag{26}$$

In combination with known current density $\mathbf{J}$ and magnetic permittivity μ in domain Ω and with boundary conditions for $\mathbf{B}$ on $\partial\Omega$, the Ampère's law specifies the magnetic field $\mathbf{B}$. However, the vector potential is specified only up to a non-rotational component $\nabla\psi$. Therefore, we have to add an additional gauge equation to make the problem well posed. We use the Coulomb gauge

$$\nabla \cdot \mathbf{A} = 0\,, \tag{27}$$

to remove the ambiguity. Now, following the standard method for deriving the weak formulation, we multiply the equation by a test function $\boldsymbol{\nu}$ and perform integration by parts to obtain

$$\int_\Omega \frac{1}{\mu} \nabla \times \mathbf{A} \cdot \nabla \times \boldsymbol{\nu} \,\mathrm{d}\mathbf{r} = \int_\Omega \mathbf{J} \cdot \boldsymbol{\nu} \,\mathrm{d}\mathbf{r}\,. \tag{28}$$

In order to introduce the gauge condition, we reformulate the problem as: find such $\mathbf{A} \in V$ and $p \in Q$ that equations

$$\int_\Omega \frac{1}{\mu} \nabla \times \mathbf{A} \cdot \nabla \times \boldsymbol{\nu} \, d\mathbf{r} + \int_\Omega \nu \cdot \nabla p \, d\mathbf{r} = \int_\Omega \mathbf{J} \cdot \boldsymbol{\nu} \, d\mathbf{r}, \tag{29a}$$

$$\int_\Omega \mathbf{A} \cdot \nabla q \, d\mathbf{r} = 0, \tag{29b}$$

hold for all $\boldsymbol{\nu} \in \hat{V}$, $q \in \hat{Q}$. The trial and test spaces are defined as $V = \hat{V} = \{\boldsymbol{\nu} \in H(\mathrm{curl}, \Omega) : \boldsymbol{\nu} = (0,0,0) \text{ on } \partial\Omega\}$ and $Q = \hat{Q} = \{q \in H^1(\Omega) : q = 0 \text{ on } \partial\Omega\}$. The symbol $H(\mathrm{curl}, \Omega)$, denotes a Sobolev space of functions $\boldsymbol{\nu}$ defined as $H(\mathrm{curl}, \Omega) = \{\boldsymbol{\nu} \in L^2(\Omega); |\nabla \times \boldsymbol{\nu}|^2 \in L^2(\Omega)\}$. Equations (29) can be understood as a constrained optimization of the magnetic field energy functional using the method of Lagrange multipliers. However, for a proper discussion in relation to the finite element method, see, e. g., (Haase et al., 2001) or lecture notes by Schöberl, 2009.

3.3 IMPLEMENTATION OF THE FINITE ELEMENT METHOD

In this work, we deal with the finite element method from the end-user perspective. We are using free open source programs and libraries to solve the finite element problems. Typically, the solution of the finite element problem consists of two distinct steps, which are handled by different computer programs.

First, the geometry of the problem is defined and a computational mesh is generated on the given geometry. We are using the *NETGEN* (Schöberl, 1997) and *Gmsh* (Geuzaine and Remacle, 2009) mesh generators.

Second, the equations are solved on the mesh. We are mostly using the *FEniCS* software (Logg and Wells, 2010; Logg et al., 2012), which can solve arbitrary partial differential equations given in the weak formulation. For some problems we are using the *Elmer* software (see *Elmer* in the bibliography), which can solve a selection of predefined physical problems and can easily handle the boundary markers created by the mesh generator.

The implementation of the Poisson equation solver in FEniCS is fairly simple and well documented by Logg et al., 2012, for example. However, no implementation of the three dimensional (3D) magnetostatic solver in FEniCS was publicly available at the time of writing. Therefore, we have developed our own solver of equation (29) in FEniCS. A working example of our implementation is shown in the appendix A. Our implementation was benchmarked against the well established 2D magnetic field solver FEMM (Meeker, 2009). The model of the magnetic adiabatic collimator without the asymmetric deflecting coil (see section 6.2) was used as a benchmark problem.

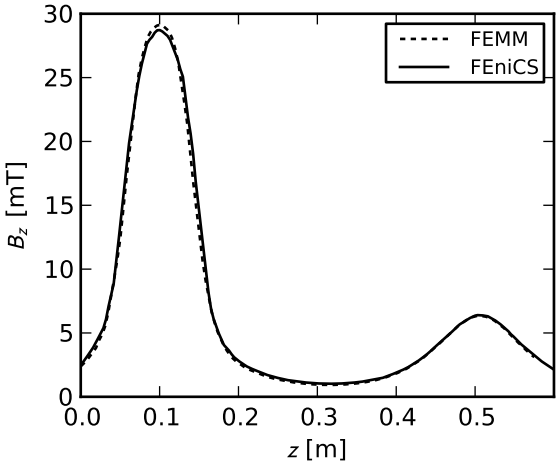

Figure 5: Benchmark of our implementation of the 3D axisymmetric magnetostatic problem in FEniCS against the 2D axisymmetric results of FEMM.

The comparison of the fields calculated by FEniCS and FEMM in figure 5 demonstrates a good agreement between both models.

4

MODELLING OF CHARGED PARTICLES

In this chapter we will explain some basic principles of the modelling of the charged particle motion under the influence of other particles and external electromagnetic fields. The analytical and numerical methods of solving the equations of motion are discussed in sections 4.1 and 4.2 respectively. The modelling of the particle collisions by the Monte Carlo method is explained in section 4.3.

4.1 ANALYTIC SOLUTIONS—DRIFTS

Under the influence of the electric field $\mathbf{E}$ and the magnetic field $\mathbf{B}$, the motion of a particle with mass m and charge q is governed by the Newton equation with the Lorentz force

$$m\frac{d\boldsymbol{v}}{dt} = q(\mathbf{E} + \boldsymbol{v} \times \mathbf{B})\,. \tag{30}$$

There are a few—either exact or approximate—analytic solutions to this equation in special configurations of electromagnetic fields. These special cases are very important for understanding the behavior of the charged particles in arbitrary electromagnetic fields. The solutions relevant for this work will now be introduced for further reference. More information on this topic can be found in plasma physics textbooks such as Chen, 1974 or Fitzpatrick, 2011.

4.1.1 *Constant Magnetic Field*

We shall start our discussion with the simplest non-trivial case, which is the case of the constant homogeneous magnetic field $\mathbf{B} = \mathbf{B}_0$ and zero electric field. We can easily see that the Lorentz force is perpendicular to the magnetic field, therefore the motion along the field lines is unrestricted by the magnetic field. It can be further observed that the magnetic field cannot do work on the particle, because the Lorentz force is perpendicular to the velocity direction. Therefore, the particle energy remains constant. Obviously, a motion with a constant force perpendicular to the direction of motion yields a circular trajectory in the plane perpendicular to the magnetic field, called *gyration*. The radius of gyration r_g, also known as the Larmor radius, can be determined by equating the magnitudes of the centripetal force and the Lorentz force in the equation

$$|q|v_\perp B = \frac{mv_\perp^2}{r_g}\,, \tag{31}$$

where $v_\perp$ is the component of initial velocity perpendicular to $\mathbf{B}$ and B is the magnitude of the magnetic field. The gyroradius is therefore given by the equation

$$r_g = \frac{m v_\perp}{|q|B}\,. \tag{32}$$

We immediately obtain the gyrofrequency, also known as the cyclotron frequency, in the form

$$\omega_c = \frac{v_\perp}{r_g} = \frac{|q|B}{m}\,. \tag{33}$$

To obtain an explicit formula for the trajectory, we can solve the equation of motion directly. We orient the z coordinate parallel to the magnetic field ($\mathbf{B} = B\hat{\boldsymbol{z}}$) and the x coordinate parallel to the initial velocity of the particle ($\boldsymbol{v}_0 = v_\perp \hat{\boldsymbol{x}}$). The origin of the coordinate system will be the gyration center. The equation of motion can be expressed in components as

$$\dot{v}_x = \frac{qB}{m} v_y\,, \qquad \dot{v}_y = -\frac{qB}{m} v_x\,, \qquad \dot{v}_z = 0\,. \tag{34}$$

By calculating the time derivative of the above equations, identifying the gyrofrequency, and substituting for $\dot{v}_x$ and $\dot{v}_y$ we obtain

$$\ddot{v}_x = -\omega_c^2 v_x\,, \qquad\qquad \ddot{v}_y = -\omega_c^2 v_y\,. \tag{35}$$

These harmonic oscillator equations have solutions which satisfy the initial conditions and motion equations in the form

$$v_x = v_\perp \cos(\omega_c t)\,, \qquad\qquad v_y = -v_\perp \operatorname{sign}(q) \sin(\omega_c t)\,, \tag{36}$$

where $v_\perp$ is the initial velocity component perpendicular to $\mathbf{B}$. Finally, integrating the solutions for velocity yields the equations of trajectories, where we can identify the previously defined gyroradius r_g

$$x = r_g \sin(\omega_c t)\,, \qquad\qquad y = r_g \operatorname{sign}(q) \cos(\omega_c t)\,. \tag{37}$$

4.1.2 *Constant Electric and Magnetic Fields*

If we superimpose constant uniform electric and magnetic fields $\mathbf{E}$ and $\mathbf{B}$, respectively, an analytic solution can still be obtained. According to the previous discussion, the unrestricted motion parallel to the magnetic field is described by a constant acceleration $|q|E_\parallel/m$, where $E_\parallel$ is the component of the electric field parallel to $\mathbf{B}$. Without loss of generality we now define $\mathbf{E}$ to be perpendicular to $\mathbf{B}$. A solution to this problem can be obtained without going into the details of the particle motion, just by considering the transformation formulas for

electromagnetic fields between two inertial frames moving with relative velocity $\mathbf{V}$. The transformation identities in the non-relativistic limit $V/c \ll 1$ read

$$\mathbf{E}' = \mathbf{E} + \mathbf{V} \times \mathbf{B}\,; \qquad \mathbf{B}' = \mathbf{B}\,. \tag{38}$$

In a frame moving at velocity $\mathbf{V} = \mathbf{E} \times \mathbf{B}/B^2$, the transformed field $\mathbf{E}'$ reduces to zero. Hence, the motion in the moving frame is the previously obtained gyration. In the non-moving frame, the particle gyrates with a superimposed drifting motion—called $\mathbf{E} \times \mathbf{B}$ drift—with a velocity

$$\boldsymbol{v}_E = \frac{\mathbf{E} \times \mathbf{B}}{B^2}\,. \tag{39}$$

Perhaps a more intuitive explanation to this drifting effect is obtained by realizing that the gyroradius is proportional to the velocity. Hence, it is smaller in regions with higher potential energy. During each gyration, the particle travels a slightly longer path on the low-potential side of its trajectory. This difference accounts for the overall drifting motion.

This solution can be generalized to any force field $\mathbf{F}$ by substituting $\mathbf{F}$ for $q\mathbf{E}$. The general drift velocity in the crossed fields is

$$\boldsymbol{v}_F = \frac{\mathbf{F} \times \mathbf{B}}{qB^2}\,. \tag{40}$$

This is the so called $\mathbf{F} \times \mathbf{B}$ (*F-cross-B*) drift.

4.1.3 *Inhomogeneous Magnetic Field*

Let us now move on to the case of an inhomogeneous magnetic field with a zero electric field. In this case, analytic solutions do not exist and we shall use the method of averaging.

Consider first a situation where the gradient of the magnetic field is perpendicular to the field, i. e., $\nabla B \perp \mathbf{B}$. Without loss of generality we orient the magnetic field along z and the gradient along y. For the method of averaging to be applicable, we assume that the magnetic field changes slowly on the scale of one gyroradius, i. e.,

$$r_g |\nabla B| \ll B\,. \tag{41}$$

The variation of $\mathbf{B}$ can now be treated as a perturbation. The lowest order correction to the unperturbed trajectory is obtained by averaging the Lorentz force $\mathbf{F}$ over one unperturbed orbit. It follows from the symmetry of the problem that the only nonzero average component can be in the z direction. Thanks to its slow variation, the magnetic field value can be replaced by its Taylor expansion from the gyration center

$$\mathbf{B}(\mathbf{r}) = \mathbf{B}_0 + (\mathbf{r} \cdot \nabla)\mathbf{B} + O(r^2)\,. \tag{42}$$

The y component of the Lorentz force can be evaluated using the Taylor expansion for B in combination with the equations of the gyration orbit (37)

$$F_y = -qv_x B_z(y) = -qv_\perp \cos(\omega_c t)\left(B_0 + r_g \operatorname{sign}(q)\cos(\omega_c t)\frac{\partial B}{\partial y}\right). \tag{43}$$

Averaging this equation over one gyration loop leads us to

$$\langle F_y\rangle = -qv_\perp r_g \operatorname{sign}(q)\frac{1}{2}\frac{\partial B}{\partial y}. \tag{44}$$

Or more generally

$$\langle \mathbf{F}\rangle = -qv_\perp r_g \operatorname{sign}(q)\nabla B/2. \tag{45}$$

This average force again leads to a drifting motion which can be expressed using equation (40)

$$\boldsymbol{v}_{\text{mag}} = v_\perp r_g \operatorname{sign}(q)\frac{1}{2}\frac{\mathbf{B}\times\nabla B}{B^2} \tag{46}$$

This drift is called *magnetic* or *grad-B* drift.

At last we will discuss the effects of a gradient in $\mathbf{B}$ parallel to the magnetic field, i. e., $\nabla B \| \mathbf{B}$. This situation is especially important for our experiment, which will be introduced in the next chapter. Due to its zero divergence, the magnetic field cannot be parallel to its gradient in a whole three dimensional volume. We will assume that the condition is satisfied only on the z axis in cylindrical coordinates, i. e., $\mathbf{B}(r=0)\|\nabla B(r=0)$ and $\mathbf{B}(r=0,z) = B(r=0,z)\hat{\mathbf{z}}$. We further assume that the field is rotationally symmetric around the z axis. The magnetic field must have a radial component, which can be estimated in the vicinity of the z axis using the zero-divergence relation of the Maxwell equations in the cylindrical coordinates

$$\frac{1}{r}\frac{\partial}{\partial r}(rB_r) + \frac{\partial B_z}{\partial z} = 0, \tag{47}$$

from which follows, assuming slowly varying field

$$B_r \approx -\frac{r}{2}\left.\frac{\partial B_z}{\partial z}\right|_{z=0}. \tag{48}$$

The azimuthal component of the field is zero thanks to the rotational symmetry and the absence of electric currents. Similarly to the previous case, we define an unperturbed trajectory with the gyration center on the z axis. Due to the field symmetry, the only net force acting on the test particle must be in the z direction. The z component of the Lorentz force in the cylindrical coordinates is $F_z = -qv_\theta B_r$. Plugging into this expression B_r from (48) yields

$$F_z = \frac{1}{2}qv_\theta r\frac{\partial B_z}{\partial z}. \tag{49}$$

It can be seen from the Lorentz force in our configuration that $qv_\theta = -|q|v_\perp$. Averaging of this constant expression is trivial and inserting $r = r_g$ from expression (32) leads to

$$\langle F_z \rangle = -\frac{1}{2}\frac{mv_\perp^2}{B}\frac{\partial B_z}{\partial z}\,. \tag{50}$$

We now define the magnetic moment μ as

$$\mu = \frac{1}{2}\frac{mv_\perp^2}{B}\,. \tag{51}$$

This force can be generalized in the form

$$\mathbf{F}_\parallel = -\mu(\hat{\mathbf{B}}\cdot\nabla)\mathbf{B}\,, \tag{52}$$

where $\hat{\mathbf{B}}$ is a unit in the direction of $\mathbf{B}$. Defining a vector magnetic dipole $\boldsymbol{\mu} = \mu\hat{\mathbf{B}}$, we see that this is actually the well-known force exerted on a magnetic dipole

$$\mathbf{F}_\parallel = -(\boldsymbol{\mu}\cdot\nabla)\mathbf{B}\,. \tag{53}$$

It may seem that the magnetic field can do work through this force—by accelerating particles along the field lines. We will show the essence of this apparent work by looking at the behavior of the magnetic moment during this acceleration.

We start from the motion equation for the gyration center. The equation can be projected along $\mathbf{B}$ by scalar multiplication with $\hat{\mathbf{B}}$. Like in the previous discussion, we assume that the curvature of $\mathbf{B}$ is negligible along the path. Therefore, the order of the projection and the differentiating can be exchanged leading to

$$m\frac{d\hat{\mathbf{B}}\cdot\boldsymbol{v}}{dt} = -\mu(\hat{\mathbf{B}}\cdot\nabla)B\,. \tag{54}$$

We identify the parallel velocity $v_\parallel = \hat{\mathbf{B}}\cdot\boldsymbol{v}$ and multiply the equation by $v_\parallel$ to obtain

$$mv_\parallel\frac{dv_\parallel}{dt} = -\mu(v_\parallel\hat{\mathbf{B}}\cdot\nabla)B\,. \tag{55}$$

The left hand side can be rewritten as a derivative of energy. The right-hand side can be interpreted as a convective derivative along the trajectory

$$\frac{d}{dt}\left(\frac{1}{2}mv_\parallel^2\right) = -\mu\frac{dB}{dt}\,. \tag{56}$$

Using the law of energy conservation, we can substitute $v_\parallel$ for $v_\perp$ by changing the sign of the derivative

$$\frac{d}{dt}\left(\frac{1}{2}mv_\perp^2\right) = \mu\frac{dB}{dt}\,. \tag{57}$$

Finally, substituting the magnetic moment from the equation (51) yields

$$\frac{d}{dt}(\mu B) = \mu \frac{dB}{dt}. \tag{58}$$

Therefore,

$$\frac{d\mu}{dt} = 0, \tag{59}$$

the magnetic moment is conserved. It is often called *the first adiabatic invariant* in plasma physics. Using the definition of the magnetic moment, it means that the kinetic energy associated with the motion perpendicular to the magnetic field is proportional to the magnitude of the field. For brevity, this energy is denoted $\mathcal{E}_\perp$ and the part associated with the parallel motion is denoted as $\mathcal{E}_\parallel$. The velocities $v_\parallel$ and $v_\perp$ are obtained by projection onto orthogonal subspaces. Therefore, the total energy is

$$\mathcal{E} = \mathcal{E}_\perp + \mathcal{E}_\parallel \tag{60}$$

This has some important consequences. First, when a particle is flying into an increasing magnetic field, the $\mathcal{E}_\perp$ is increasing to keep the magnetic moment constant. It can continue only until all the energy is transformed into $\mathcal{E}_\perp$, at which point the particle motion along the magnetic field stops. The resulting reflection from the high-field regions is called the *magnetic mirror* effect.

On the other hand, when the particle is moving to the low field, the energy is transformed into $\mathcal{E}_\parallel$. Hence, the particles are being collimated. This process is called the *magnetic adiabatic collimation*.

4.2 NUMERICAL INTEGRATION OF EQUATIONS OF MOTION

Numerical modelling of the particle trajectories is considered a basic tool for understanding the behavior of particles in electromagnetic fields. A simple and widely used method of numerical integration of the motion equations is the *leap-frog method*. It is obtained by time-centered differencing of the motion equation with a time step Δt

$$\boldsymbol{v}_{t+\Delta t/2} = \boldsymbol{v}_{t-\Delta t/2} + \frac{\Delta t}{m}\mathbf{F}_t, \tag{61}$$

$$\boldsymbol{x}_{t+\Delta t} = \boldsymbol{x}_t + \boldsymbol{v}_{t+\Delta t/2}\Delta t, \tag{62}$$

where $\boldsymbol{x}$, $\boldsymbol{v}$, and $\mathbf{F}$ are the position, velocity, and force vectors, respectively. This scheme is a second-order method. Its implementation is straightforward in case of electrostatic field. Since the velocities are known at half-integer multiples of time step, the initial velocities $\boldsymbol{v}_0$ should be first advanced by $\Delta t/2$ backwards. However, in case of our Monte Carlo simulations, no influence of this offset of initial

conditions was observed. This is because the initial conditions are random and the evolution is further randomized by collisions. Nevertheless, in highly collisional simulations, different integrators are recommended (Roučka and Hrach, 2011) to avoid the need of velocity and position synchronization at each collision.

In case of a superimposed magnetic field, the centered formula for the Lorentz force is obtained by averaging the corresponding velocities

$$\mathbf{F}_t = q\left(\mathbf{E}_t + \frac{\boldsymbol{v}_{t-\Delta t/2} + \boldsymbol{v}_{t+\Delta t/2}}{2} \times \mathbf{B}_t\right). \tag{63}$$

As we already know from section 4.1 in this chapter, the magnetic field causes rotation of the velocity vector around $\mathbf{B}$ with frequency ω_c. The time centered approach to incorporating this rotation consists of accelerating the particle by half step $q\mathbf{E}\Delta t/2m$, then rotating the $\boldsymbol{v}$ by approximately $\omega_c\Delta t$, then accelerating by the rest of the half step. This method is commonly called HARHA, which stands for *half acceleration, rotation, half acceleration*. The actual implementation of the solution of the equation (62) in the vector form is given by Birdsall and Langdon, 1991. Using a substitution

$$\boldsymbol{v}_{t-\Delta t/2} = \boldsymbol{v}^- - \frac{q\mathbf{E}}{m}\frac{\Delta t}{2}; \qquad \boldsymbol{v}_{t+\Delta t/2} = \boldsymbol{v}^+ + \frac{q\mathbf{E}}{m}\frac{\Delta t}{2}, \tag{64}$$

the half acceleration steps are incorporated into $\boldsymbol{v}^-$ and $\boldsymbol{v}^+$. This substitution eliminates the electric field from the equation (62), reducing it to

$$\frac{\boldsymbol{v}^+ - \boldsymbol{v}^-}{\Delta t} = \frac{q}{2m}(\boldsymbol{v}^+ + \boldsymbol{v}^-) \times \mathbf{B}. \tag{65}$$

It can be seen by scalar multiplying the equation with $(\boldsymbol{v}^+ + \boldsymbol{v}^-)$ that $v^+ = v^-$. Hence it represents pure rotation. The half-angle of rotation $\theta/2$ is equal to the angle between $\boldsymbol{v}^+$ and the *average vector* $(\boldsymbol{v}_\perp^+ + \boldsymbol{v}_\perp^-)/2$ when projected onto the plane of rotation. It can be determined by considering the angles in the right angle triangle with sides $v_\perp^+$, $|\boldsymbol{v}_\perp^+ + \boldsymbol{v}_\perp^-|/2$, and $|\boldsymbol{v}_\perp^+ - \boldsymbol{v}_\perp^-|/2$

$$\left|\tan\frac{\theta}{2}\right| = \frac{|\boldsymbol{v}_\perp^+ - \boldsymbol{v}_\perp^-|}{|\boldsymbol{v}_\perp^+ + \boldsymbol{v}_\perp^-|}, \tag{66}$$

where the $\perp$ symbol denotes the component perpendicular to $\mathbf{B}$, i. e., the projection onto the plane of rotation. Applying the equation (65) to these perpendicular components yields

$$\left|\tan\frac{\theta}{2}\right| = \frac{qB}{m}\frac{\Delta t}{2} = \frac{\omega_c\Delta t}{2}. \tag{67}$$

Therefore, for small values of $\omega_c\Delta t$, the angle of rotation is close to the expected value $\theta = \omega_c\Delta t$.

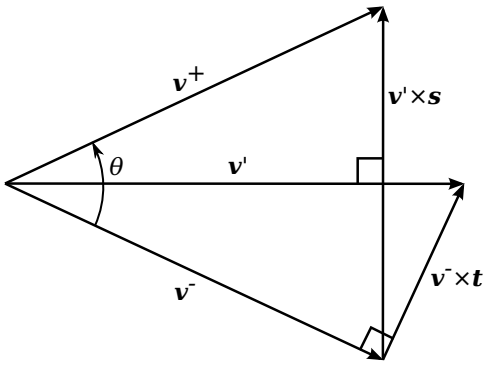

Figure 6: Illustration of the vector transformations used in the Boris' algorithm. Projection of vectors on the plane perpendicular to $\mathbf{B}$ is shown. Figure based on Birdsall and Langdon, 1991.

The Boris' algorithm for calculating the rotation (Birdsall and Langdon, 1991) starts with defining vectors $\boldsymbol{v}'$ and $\mathbf{t}$ as

$$\boldsymbol{v}' = \boldsymbol{v}^- + \boldsymbol{v}^- \times \mathbf{t}\,; \qquad \mathbf{t} = \hat{\mathbf{B}} \tan\frac{\theta}{2} = \frac{q\mathbf{B}}{m}\frac{\Delta t}{2} \tag{68}$$

The vector $\mathbf{t}$ is chosen so that $\boldsymbol{v}'$ is perpendicular to the *difference vector* $(\boldsymbol{v}_\perp^+ - \boldsymbol{v}_\perp^-)$. That means that it bisects the angle between $\boldsymbol{v}^-$ and $\boldsymbol{v}^+$, as illustrated in figure 6.

The direction of the difference vector is now given by $\boldsymbol{v}' \times \mathbf{B}$. The rotated velocity can therefore be determined from equation of the type

$$\boldsymbol{v}^+ = \boldsymbol{v}^- + \boldsymbol{v}' \times \mathbf{s}\,, \tag{69}$$

where the vector $\mathbf{s}$ is collinear with $\mathbf{B}$ and its magnitude is determined from from the requirement $v^+ = v^-$. In particular

$$\mathbf{s} = \frac{2\mathbf{t}}{1+\mathbf{t}^2}\,. \tag{70}$$

For more details of this calculation, see Birdsall and Langdon, 1991.

4.3 MONTE CARLO COLLISIONS

The influence of collisions is incorporated into our model by means of the Monte Carlo method. In order to simulate a collision, we first have to randomly decide *when* the collision occurs and then randomly calculate *what* are the consequences of the collision.

Let us first deal with the question of when the collision occurs. A common approach to modelling the occurrence of collisions starts with the assumption that the observed particle is moving in a static medium with randomly distributed scattering centers—background gas. The expected number of collisions on a path element dx is given by

$$N_x\, dx = n\sigma\, dx\,, \tag{71}$$

where n is the number density of the scattering centers and σ is the scattering cross section. The probability that the position of the first collision x_c exceeds $x + dx$ is

$$\text{Prob}\{x_c > x + dx\} = \text{Prob}\{x_c > x\}(1 - n\sigma\, dx)\,. \tag{72}$$

Rewriting this expression formally as

$$\frac{\text{Prob}\{x_c > x + dx\} - \text{Prob}\{x_c > x\}}{dx} = -n\sigma\,\text{Prob}\{x_c > x\} \tag{73}$$

yields a simple differential equation with a solution

$$\text{Prob}\{x_c > x\} = \exp(-n\sigma x)\,, \tag{74}$$

where we assumed that the particle starts at $x = 0$. The probability distribution of collision positions is obtained by differentiating the cumulative distribution function above and reversing the sign, which is caused by changing the inequality from $x_c > x$ to $x_c < x$. The result is

$$f(x)\, dx = n\sigma \exp(-n\sigma x)\, dx\,. \tag{75}$$

The collision events are then typically simulated by sampling a random free path x_c from distribution (75) and then letting the particle collide as soon as it reaches the distance x_c. It has to be emphasised, that the basic assumption of this method is the stationarity of the scattering centers. Therefore, it is not applicable to collisions where the thermal velocities of the scattering gas are comparable to the ion velocities. There are some ways how to correct for the temperature of the gas using a variable mean free path, but such models require also specific corrections to the random sampling of the interacting particles, which can become very complicated. Furthermore, as far as we know, a generalization of these correction to non-maxwellian distributions has never been implemented, although it is possible.

Nevertheless, this slightly incorrect model with variable mean free path and without the corrections in the scattering code is implemented in the widely used ion simulation code SIMION (Manura, 2007).

The proper way to describe the collisions of nearly thermal particles is based on rewriting the relation (71) in terms of collisions per element of time

$$N_t\, dt = n\sigma v\, dt\,, \tag{76}$$

where v is the relative velocity of the particle and the scattering centers. Now it becomes easy to incorporate a general distribution function of the gas particles $f(\boldsymbol{x}, \boldsymbol{v}, t)n(\boldsymbol{x}, t)\, d\boldsymbol{x}\, d\boldsymbol{v}$. The distribution function is separated into a normalized velocity distribution

$$\int_{\boldsymbol{v}} f(\boldsymbol{x}, \boldsymbol{v}, t)\, d\boldsymbol{v} = 1 \tag{77}$$

and a spatial distribution part $n(\mathbf{x}, t)$. The time dependence is neglected in the further discussion without loss of generality. The collision frequency of a particle with velocity $\boldsymbol{v}$ and position $\mathbf{x}$ with gas particles from a phase space element $d\boldsymbol{v}'$ is given as

$$N_{\boldsymbol{v}'t}(\mathbf{x}, \boldsymbol{v}, \boldsymbol{v}')\, d\boldsymbol{v}' = f(\mathbf{x}, \boldsymbol{v}')n(\mathbf{x})\sigma(g)g\, d\boldsymbol{v}'\,, \tag{78}$$

where the relative velocity of particles is $g = |\boldsymbol{v} - \boldsymbol{v}'|$. The above expression is very important for the modelling of collisions since it represents the velocity distribution of the incident gas particles. Returning to our previous comments about the problems associated with the mean-free-path generating model: this is the correct three dimensional velocity-dependent distribution, from which the interacting gas particles should be sampled. However, due to its complicated nature, it is often replaced with the less accurate Maxwell or Maxwell-flux distribution as in the SIMION (Manura, 2007). We will now show that a simple and efficient model of collisions can be developed without any of these approximations.

The total collision frequency, which is needed to decide about the occurrence of the collision is obtained by integrating expression (78)

$$\nu(\mathbf{x}, \boldsymbol{v}) = \int_{\boldsymbol{v}'} f(\mathbf{x}, \boldsymbol{v}')n(\mathbf{x})\sigma(g)g\, d\boldsymbol{v}'\,. \tag{79}$$

As we can see, the collisions are a non-homogeneous Poisson process, with a complicated position and velocity dependent rate given by the equation (79). Fortunately, the evaluation of (79) can be simplified using the *null collision method* (Skullerud, 1968; Vahedi and Surendra, 1995). The null collision method can be formally described as a mathematical transformation, which turns a non-homogeneous Poisson process into a homogeneous Poisson process. It is equivalent to adding a fictive interaction—the *null collision*—which does not influence the particle in any way. The cross section $\sigma_0(g, \mathbf{x})$ for the null collision is chosen according to the equation

$$(\sigma(g) + \sigma_0(g, \mathbf{x}))n(\mathbf{x}) = \nu_{max}\,, \tag{80}$$

which makes the integral of the total cross section in (79) independent on velocity and position. Thanks to the distribution function normalization the total collision frequency is

$$\nu(\mathbf{x}, \boldsymbol{v}) = \nu_{max}\,. \tag{81}$$

The ν_{max} is typically calculated as

$$\nu_{max} = \max_{g}\{\sigma(g)g\} \max_{\mathbf{x}}\{\mathbf{x}\}, \tag{82}$$

where the maximum is evaluated only for velocities and positions relevant for a given problem. With the known constant collision frequency, we can easily simulate the collisions either by sampling the

random time t_c between the collisions from the exponential distribution

$$f(t)\,dt = \nu_{max}\exp(-\nu_{max}t)\,dt\,, \tag{83}$$

or by calculating a collision in each time step Δt with probability

$$\text{Prob}\{t_c < \Delta t\} = 1 - \exp(-\nu_{max}\Delta t)\,. \tag{84}$$

The second approach, which is more suitable for simulations with a fixed discretization of the time axis, is used in this work. Once a collision is decided to happen according to these probabilities, a random interacting particle is sampled from the gas distribution $f(\mathbf{x}, \boldsymbol{v}')$. The type of collision is chosen between null or non-null with probabilities $\sigma_0(g, \mathbf{x})g n(\mathbf{x})/\nu_{max}$ and $\sigma(g)g n(\mathbf{x})/\nu_{max}$, respectively. Of course, only the probability of the real collision needs to be evaluated. The null collision cross section was just a mathematical aid and is not needed in the actual simulation. Extension of this procedure to multiple collision processes with multiple species is straightforward by calculating the total collision probability and applying the null collision method for each interacting species separately.

4.3.1 *Langevin Scattering*

If not otherwise stated, the Langevin scattering cross section is used for ion-neutral scattering. The Langevin theory assumes that the particles interact by the induced electric dipole $\mathbf{p}$ of the neutral particle $\mathbf{p} = \alpha\mathbf{E}$, where α is the polarizability of the neutral. The polarizability of particles is usually given in *polarizability volume* units Å^3, which are related to SI units and atomic units by

$$\frac{\alpha}{\text{Å}^3} = \frac{b_0^3}{\text{Å}^3}\frac{\alpha}{\text{a.u.}} = 10^{24}\frac{\alpha}{\text{cm}^3} = \frac{10^{30}}{4\pi\epsilon_0}\frac{\alpha}{\text{C}\cdot\text{m}^2\cdot\text{V}^{-1}}\,, \tag{85}$$

where $b_0 \approx 0.529\,177$ Å is the Bohr radius. Evaluating these expressions numerically gives

$$\frac{\alpha}{\text{Å}^3} = 0.148185\frac{\alpha}{\text{a.u.}} = 10^{24}\frac{\alpha}{\text{cm}^3} = 8.9875\cdot 10^{39}\frac{\alpha}{\text{C}\cdot\text{m}^2\cdot\text{V}^{-1}}\,. \tag{86}$$

In SI units the magnitude of the electric field of the ion with charge q at the position of the neutral separated by vector $\mathbf{r}$ is $\mathbf{E} = q\hat{\mathbf{r}}/4\pi\epsilon_0 r^2$. The induced dipole moment is

$$\mathbf{p} = \alpha\mathbf{E} = \frac{\alpha q\hat{\mathbf{r}}}{4\pi\epsilon_0 r^2}\,. \tag{87}$$

To calculate the potential energy of the interacting particles, one can not simply use the formula for the electric dipole potential, because

it is valid for a fixed dipole moment only. The formula for the electric field has to be used instead. On the axis of symmetry, it is given by

$$E_r = \frac{1}{4\pi\epsilon_0}\left(\frac{3(\mathbf{p}\cdot\hat{\mathbf{r}})\hat{\mathbf{r}}-\mathbf{p}}{r^3}\right)\cdot\hat{\mathbf{r}} = \frac{2p\,\mathrm{sign}(q)}{4\pi\epsilon_0 r^3} = \frac{2\alpha q}{(4\pi\epsilon_0)^2 r^5}\,. \quad (88)$$

The interaction potential is calculated from

$$V(r) = \int_r^\infty qE\,dr = -\frac{1}{2}\frac{\alpha q^2}{(4\pi\epsilon_0)^2 r^4} \quad (89)$$

The effective potential of the collision system can be written as

$$V_{\mathrm{eff}}(r) = V(r) + \frac{J^2}{2\mu r^2} = -\frac{1}{2}\frac{\alpha q^2}{(4\pi\epsilon_0)^2 r^4} + \mathcal{E}_k\frac{b^2}{r^2}\,, \quad (90)$$

where $J = \mu b v_0$ is the angular momentum, $\mathcal{E}_k$ is the reduced kinetic energy, v_0 is the impact velocity, and b is the impact parameter. The induced potential is steeper than the repulsive centrifugal potential near the origin. We define b_t as the impact parameter for which the particle is just able to reach the maximum of the centrifugal barrier. This is called the orbiting impact parameter. The position of the maximum $r_{\max}$ can be calculated by solving $dV_{\mathrm{eff}}/dr = 0$ for r. And the appropriate impact parameter b_t for a given reduced energy $\mathcal{E}_k$ is obtained by solving $\mathcal{E}_k = V_{\mathrm{eff}}(r_{\max})$ for b, which yields

$$b_t = \sqrt[4]{\frac{2\alpha q^2}{\mathcal{E}_k(4\pi\epsilon_0)^2}}\,. \quad (91)$$

For $b < b_t$, a large angle elastic or reactive scattering occurs, which cannot be described in detail with this simple theory. We define the Langevin scattering cross section

$$\sigma_L = \pi b_t^2 = \frac{q}{2\epsilon_0 v}\sqrt{\frac{\alpha}{\mu}}\,. \quad (92)$$

and the Langevin reaction rate

$$k_L = \langle\sigma_L v\rangle = \frac{q}{2\epsilon_0}\sqrt{\frac{\alpha}{\mu}} \quad (93)$$

The large angle elastic scattering at $b < b_t$ is simulated as isotropic scattering in the center of mass frame. This is known to be a good approximation of these collisions (Nanbu and Kitatani, 1995). The collision partner is picked for each collision as a random sample from the Maxwell distribution.

The small angle Langevin collisions at $b > b_t$ with appropriate differential cross section and adjustable cutoff for b are implemented in our model according to the algorithm of Nanbu and Kitatani, 1995. However, no influence of these collisions on the ion energy distributions was observed. Therefore, these collisions are generally not included in our models.

4.3.2 *Electron Collisions*

The collisions of electrons with neutrals are also simulated as isotropic scattering in the center of mass frame. Inelastic or superelastic collisions are incorporated by subtracting or adding the energy difference in the center of mass frame, before the isotropic scattering step.

The Coulombic collisions of electrons with charged particles are included in our models in a rather approximate way by treating them as isotropic scattering with cross section σ_c in the center of mass system. This corresponds to the large scattering limit of the model by Takizuka and Abe, 1977. The cross section is given by

$$\sigma_c(v) = \pi\Lambda^2 \ln\frac{\lambda_D}{\Lambda}\,, \tag{94}$$

where Λ is the impact parameter for $\pi/2$ scattering angle. It is defined as (see, e. g., Chen, 1974; Callen, 2006)

$$\Lambda = \frac{Z_i q^2}{4\pi\epsilon_0 \mu v^2}\,, \tag{95}$$

where Z_i is the secondary particle charge state, μ is the reduced mass, and v is the relative velocity. The logarithm $\ln\lambda_D/\Lambda$ is known as the Coulomb logarithm with a cutoff parameter λ_D. The cutoff parameter is taken as identical to the Debye length

$$\lambda_D = \sqrt{\frac{\epsilon_0 k_B T_e}{n_e q_e^2}}\,, \tag{96}$$

where n_e is the electron number density and T_e is the electron temperature. There are discrepancies in the literature regarding the exact definition of the scattering cross section and Coulomb logarithm (Petschek and Byron, 1957; Dougal and Goldstein, 1958; Martín et al., 2008), but for the qualitative evaluation of the influence of the Coulombic collisions, these differences do not matter.

The Coulombic collisions differ from the collisions with neutrals in the fact that the scattering medium is not necessarily evenly distributed with maxwellian velocity distribution. The actual distribution of the interacting ions or electrons has to be taken into account. Therefore, when a collision occurs, the interacting partner is generated as a randomly selected particle from the simulation instead of sampling from the Maxwell distribution. The collision effects are calculated for both particles simultaneously, which ensures the conservation of momentum and energy inside the particle ensemble.

5

EXPERIMENTAL TECHNIQUES

5.1 RF ION TRAPPING

One of the basic tools for studying the properties of ions is the ion trapping technique. As the name implies, this technique allows the experimenter to store an ensemble of ions under a well defined conditions. In principle, almost all experiments with ions involve some kind of ion confinement. It could be diffusion limited motion in high density plasmatic experiments (discharges), magnetic confinement in high temperature plasmatic experiments (tokamaks), or for example radial confinement by electrostatic lenses and magnetic lenses in ion beam and storage ring experiments. However, the term ion trap is used only for devices which can confine the ions in all three dimension for potentially unlimited time. The two most widespread types of ion traps are the Penning trap and the Paul Trap.

The Penning trap (pioneered by Dehmelt, see, e. g., Dehmelt and Walls, 1968) uses a homogeneous magnetic field to restrict the motion of the charged particle in the direction perpendicular to the magnetic field. A quadrupolar electrostatic field is then used for confinement in the parallel direction (Penning trap with non-quadrupolar electrostatic field is called the Penning-Malmberg trap).

This section will now further discuss the Paul trap, developed by Paul (see Paul, 1990), and its generalization called the *multipole rf trap*.

Since the RF trapping technique is involved in the majority of experiments related to this work, we will explain it in more detail. To understand the principle of RF trapping we need to investigate the motion of a charged particle in an oscillatory electric field. This problem has been investigated thoroughly by Gerlich, 1992 and the following introduction follows closely his work (Gerlich, 1992).

5.1.1 *The Effective Potential*

We assume that a particle of charge q and mass m is moving in an oscillatory electric field $\mathbf{E}(\mathbf{r}, t) = \mathbf{E}_0(\mathbf{r}) \cos(\Omega t)$, where Ω denotes the angular frequency of oscillations. The motion of the studied particle is then described as

$$m \frac{d^2\mathbf{r}}{dt^2} = q\mathbf{E}_0(\mathbf{r}) \cos \Omega t \,. \tag{97}$$

To solve this equation, we use an ansatz in the form

$$\mathbf{r}(t) = \mathbf{R}_0(t) + \mathbf{R}_1(t)\,; \qquad \mathbf{R}_1(t) = -\mathbf{A}(t) \cos \Omega t \,, \tag{98}$$

where $\mathbf{A}(t)$ is an amplitude vector. In the simple case of homogeneous $\mathbf{E}_0$, the solution is easily obtained in the form of a uniform motion—so called *secular motion*—combined with harmonic oscillations of amplitude

$$\mathbf{A} = \frac{q\mathbf{E}_0}{m\Omega^2}\,. \tag{99}$$

Assuming that the electric field $\mathbf{E}_0$ varies only slowly on the length scale of oscillations $|2\mathbf{A}|$

$$|2(\mathbf{A}\nabla)\mathbf{E}_0| \ll E_0\,, \tag{100}$$

we can use the first two terms of the Taylor expansion to obtain

$$\mathbf{E}_0(\mathbf{R}_0 - \mathbf{A}\cos\Omega t) = \mathbf{E}_0(\mathbf{R}_0) - (\mathbf{A}\cdot\nabla)\mathbf{E}_0(\mathbf{R}_0)\cos\Omega t\,. \tag{101}$$

By plugging this expansion together with the ansatz (98) into the equation of motion (97) we get

$$m\frac{d^2\mathbf{R}_0}{dt^2} = (q\mathbf{E}_0(\mathbf{R}_0) - m\Omega^2\mathbf{A}(t))\cos\Omega t - q(\mathbf{A}(t)\cdot\nabla)\mathbf{E}_0(\mathbf{R}_0)\cos^2\Omega t\,. \tag{102}$$

Now, again using the assumption of slow variation of $\mathbf{E}_0$, the amplitude vector can be replaced by the special solution (99) corresponding to the local field, i. e., $\mathbf{A}(t) \approx q\mathbf{E}_0(\mathbf{R}_0(t))/m\Omega^2$.

$$m\frac{d^2\mathbf{R}_0}{dt^2} = -\frac{q^2}{m\Omega^2}(\mathbf{E}_0\cdot\nabla)\mathbf{E}_0(\mathbf{R}_0)\cos^2\Omega t\,. \tag{103}$$

At last, rewriting the vector derivative using the identity

$$(\mathbf{E}_0\cdot\nabla)\mathbf{E}_0 = \frac{1}{2}\nabla\mathbf{E}_0^2 - \mathbf{E}_0\times(\nabla\times\mathbf{E}_0) \tag{104}$$

and averaging over one oscillation period we arrive at the equation of motion for the non-oscillatory secular motion

$$m\frac{d^2\mathbf{R}_0}{dt^2} = -\frac{q^2}{4m\Omega^2}\nabla\mathbf{E}_0^2\,. \tag{105}$$

The effective force on the right hand side of this equation is sometimes called the *ponderomotive force*. We can identify a term formally equivalent to a potential, which we shall call the *effective potential* from now on. This potential is defined as $V^* = q^2\mathbf{E}_0^2/4m\Omega^2$, or more generally in case of a superimposed electrostatic potential ϕ_s:

$$V^* = \frac{q^2\mathbf{E}_0^2}{4m\Omega^2} + q\phi_s\,. \tag{106}$$

The equation of motion (105) essentially means that under given assumptions, the total average energy of the particle is conserved. We

say that the average energy is an adiabatic constant of motion. It follows from the definition of the oscillatory motion $\mathbf{R}_1$ in equations (98), (99) that the time averaged energy of the oscillatory motion is equal to the effective potential

$$\left\langle \frac{1}{2} m \dot{\mathbf{R}}_1^2 \right\rangle = \frac{q^2 E_0^2}{4m\Omega^2}\,, \tag{107}$$

i. e., the effective potential energy is stored in the form of the kinetic energy of the oscillatory motion.

5.1.2 *Adiabaticity*

The approximate solution in the form of the effective potential is called the *adiabatic approximation*. To obtain a convenient description of the range of validity of this approximation, we rewrite the condition (100) using the equation (99) for $\mathbf{A}$ and identity (104) as

$$\frac{q|\nabla E_0^2|}{m\Omega^2} \ll E_0\,. \tag{108}$$

This equation suggests to define the adiabaticity parameter as

$$\eta = 2q|\nabla E_0|/m\Omega^2 \tag{109}$$

which reduces the equation (108) to $\eta \ll 1$. It was shown by numerical simulations and also experimentaly confirmed (Gerlich, 1992) that the adiabaticity of motion is valid with good accuracy for

$$\eta < 0.3\,. \tag{110}$$

5.1.3 *Linear Multipole Traps*

A special—but widely used—subset of the RF multipole traps are the linear multipole traps. These traps have cylindrically symmetric effective potential and the trapping along the axis of symmetry is achieved using static potentials The potential of an ideal linear $2n$-pole is a solution to the Poisson equation in vacuum with boundary condition $\phi(r = r_0, \Phi) = \phi_0 \cos n\Phi$. It is described in cylindrical coordinates by equation

$$\phi(r, \Phi) = \phi_0 \hat{r}^n \cos n\Phi\,, \tag{111}$$

where $\hat{r} = r/r_0$ denotes the reduced radius. We denote the azimuth coordinate by Φ to avoid ambiguity with the potential ϕ. This field can be approximated by placing $2n$ parallel conducting rods with diameter d in a circular configuration with inscribed radius r_0. Potential $\pm\phi_0$ is assigned to the rods in alternating manner. In first approximation, the rod diameter is related to r_0 by equation

$$r_0 = (n-1)\frac{d}{2}\,. \tag{112}$$

The effective potential of the linear multipole is obtained by plugging the equation (111) into the expression for the effective potential (106), which yields

$$V^* = \frac{1}{8}\frac{(qV_0)^2}{\varepsilon}\hat{r}^{2n-2} + qU_0\hat{r}^n \cos n\Phi\,, \tag{113}$$

where V_0 is the amplitude of the alternating potential applied to the rods and U_0 is the static part of the potential. Unless otherwise stated, the static potential is assumed to be zero. The characteristic energy ε is given by equation

$$\varepsilon = \frac{1}{2n^2} m\Omega^2 r_0^2. \tag{114}$$

Similarly, the adiabaticity parameter η can be expressed from equations (109) and (111) as

$$\eta = \frac{n-1}{n}\frac{qV_0}{\varepsilon}\hat{r}^{n-2}\,. \tag{115}$$

Detailed derivation of these equations is given by Gerlich, 1992.

5.1.4 *Optimal Operating Conditions*

If the trapping should be effective, the particle trajectory must be contained within the radius r_0 and the adiabaticity condition $\eta < 0.3$ must be satisfied on the trajectory. We define the reduced turning radius $\hat{r}_m$ as the maximal reduced radius reached by the particle. The conditions for safe operation of the trap are (Gerlich, 1992)

$$\hat{r}_m < 0.8\,, \tag{116}$$

$$\eta(\hat{r}_m) < 0.3\,, \tag{117}$$

where the safety factor 0.8 allows for the oscillatory motion near the rods.

For a particle with energy $\mathcal{E}_m$, the maximal possible turning radius is obtained by setting $\mathcal{E}_m = V^*$

$$\mathcal{E}_m = \frac{1}{8}\frac{(qV_0)^2}{\varepsilon}\hat{r}_m^{2n-2}\,. \tag{118}$$

Combining this equation and the expression (115) for ε we can obtain the minimal amplitude V_0 required to confine the particle with energy $\mathcal{E}_0$ within the radius $\hat{r}_m$ and maximal adiabaticity η_m

$$qV_0 = 8\frac{n-1}{n}\frac{\mathcal{E}_m}{\eta_m \hat{r}_m^n}\,. \tag{119}$$

The minimal value of ε, which is practically adjusted by changing the frequency Ω, is obtained by reinserting the above equation into (115)

$$\varepsilon = 8\frac{(n-1)^2}{(n\eta_m\hat{r}_m)^2}\mathcal{E}_m\,. \tag{120}$$

5.2 MAC-E FILTER

The name *MAC-E filter* stands for the Magnetic Adiabatic Collimator with Electrostatic filter. The MAC-E filter is an energy spectrometer developed in the field of particle physics (Beamson et al., 1980) for measuring energies of charged particles with high efficiency and precision. The largest device of this type is the KATRIN experiment in Karlsruhe (KATRIN collaboration, 2005; Weinheimer, 2002). The KATRIN experiment for measuring the mass of electron neutrinos from the tritium β decay has the designed relative energy resolution of the order 10^{-4} and should commence operation in 2012.

As the name implies, an energy spectrometer with electrostatic filter operates by imposing an electrostatic potential barrier on the path of the analyzed particles. This type of spectrometer is also known as a *retarding field analyzer* in some research fields. Measuring the transmission of the spectrometer as a function of the barrier height leads to the integral spectrum (also called retarding spectrum). The spectrometer actually measures the distribution of the kinetic energy associated with the motion antiparallel to the retarding force. For such a spectrometer to operate with a reasonable resolution, the particles must be collimated before hitting the retarding barrier, i. e., the velocity vectors must be close to parallel. This is most simply achieved using a small entrance aperture for the spectrometer, which rejects all the uncollimated particles. Unfortunately, this approach rejects most of the particles and reduces the signal by orders of magnitude. Another approach consists of making the retarding barrier in the shape of a spherical cap centered around the particle source. This approach allows for high detection efficiency, but unfortunately cannot be used for all types of particle sources.

The principle of the MAC-E filter lays in the adiabatic transformation of a random initial velocity into a collimated velocity in a decreasing magnetic field. This process was described in detail in section 4.1. The particles—typically electrons—are produced in a region of a high magnetic field. In theory, a 4π acceptance angle can be achieved, since all the electrons are captured and guided to the detection system. The magnetic field is configured in such way that the intensity decreases along the electron trajectory.

To illustrate the capability of the MAC-E filter, assume that a particle is produced at a point (1) with energy $\mathcal{E}_0$ and a random velocity direction. Let it travel from field $\mathbf{B}(1)$ at point (1) to field $\mathbf{B}(2)$ at point (2). The retarding potential barrier is placed at (2). The conservation of magnetic moment implies

$$\frac{\mathcal{E}_\perp(1)}{B(1)} = \frac{\mathcal{E}_\perp(2)}{B(2)}\,. \tag{121}$$

Since the retarding barrier actually measures only the value of $\mathcal{E}_\parallel(2)$, we rewrite the above equation using the law of energy conservation (60) into

$$\frac{\mathcal{E}_0 - \mathcal{E}_\parallel(1)}{B(1)} = \frac{\mathcal{E}_0 - \mathcal{E}_\parallel(2)}{B(2)}\,. \tag{122}$$

To overcome the barrier of height $\mathcal{E}_B$ at point (2), the particle must satisfy $\mathcal{E}_\parallel(2) > \mathcal{E}_B$. Inserting $\mathcal{E}_\parallel(2)$ from equation (122) into this inequality gives a condition for the initial energy

$$\mathcal{E}_\parallel(1) > \mathcal{E}_0 - (\mathcal{E}_0 - \mathcal{E}_B)\frac{B(1)}{B(2)}\,. \tag{123}$$

To get a picture of the transmission properties of the MAC-E filter, we assume that the particles are produced with an isotropic monoenergetic velocity distribution. The initial velocity is $v_0 = \sqrt{2\mathcal{E}/m}$. The condition for the initial value of velocity component v_z follows from (123)

$$\frac{v_z}{v_0} > \sqrt{1 - \left(1 - \frac{\mathcal{E}_B}{\mathcal{E}_0}\right)\frac{B_1}{B_2}} \tag{124}$$

The distribution of $\boldsymbol{v}_0/v_0$ is uniform on the surface of a unit sphere

$$f_{\theta\phi}\,d\theta\,d\phi = \frac{1}{4\pi}\sin\theta\,d\theta\,d\phi \tag{125}$$

The distribution in the z coordinate is obtained by substituting $dz = \sin\theta\,d\theta$

$$f_{z\phi}\,dz\,d\phi = \frac{1}{4\pi}\,dz\,d\phi\,, \tag{126}$$

and integrating

$$f_z\,dz = \frac{1}{4\pi}\int_0^{2\pi} d\phi f_{z\phi}\,dz = \frac{1}{2}\,dz\,. \tag{127}$$

The distribution is uniform in z. Therefore, the fraction of particles satisfying (124) is simply calculated as

$$N = \frac{1}{2}\left(1 - \sqrt{1 - \left(1 - \frac{\mathcal{E}_B}{\mathcal{E}_0}\right)\frac{B_1}{B_2}}\right)\,. \tag{128}$$

The factor $1/2$ accounts for the particles initially receding from the spectrometer. We neglect it in the further discussion, since these particles can be reflected back to the spectrometer by placing a high electrostatic barrier on their escape path. Evaluating also the extreme cases finally leads us to the transmission function of the spectrometer

$$T(\mathcal{E}, \mathcal{E}_B) = \begin{cases} 1 & \mathcal{E}_B \leqslant \mathcal{E}_0\left(1 - \frac{B_2}{B_1}\right) \\ 1 - \sqrt{1 - \left(1 - \frac{\mathcal{E}_B}{\mathcal{E}_0}\right)\frac{B_1}{B_2}} & \mathcal{E}_0 > \mathcal{E}_B > \mathcal{E}_0\left(1 - \frac{B_2}{B_1}\right) \\ 0 & \mathcal{E}_B \geqslant \mathcal{E}_0\,. \end{cases} \tag{129}$$

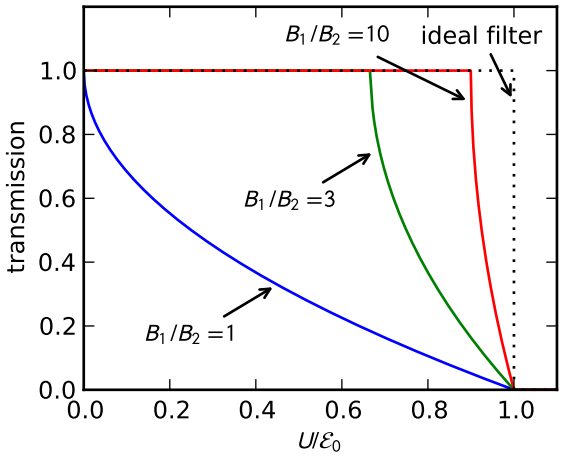

Figure 7: Transmission of the MAC-E filter calculated from the equation (129).

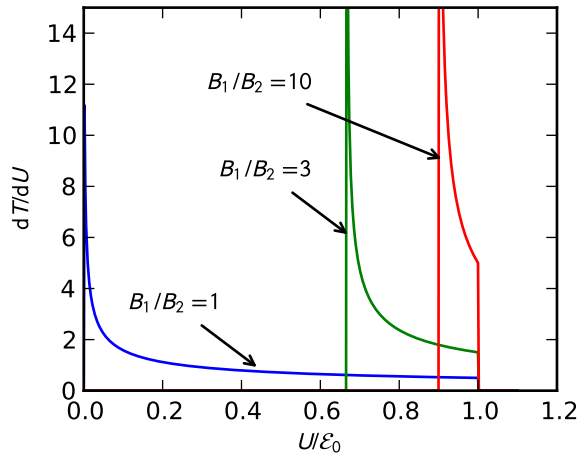

Figure 8: Theoretical spectrum obtained by the MAC-E filter calculated from the equation (130).

Illustration of the transmission function for various magnetic field ratios is shown in figure 7.

The measured spectrum, which is obtained by differentiating the retarding curve is theoretically given by

$$\frac{dT}{d\mathcal{E}_B} = \begin{cases} \frac{B_1}{\mathcal{E}_0 B_2}\left[1-\left(1-\frac{\mathcal{E}_B}{\mathcal{E}_0}\right)\frac{B_1}{B_2}\right]^{-1/2} & \mathcal{E}_0 > \mathcal{E}_B > \mathcal{E}_0\left(1-\frac{B_2}{B_1}\right) \\ 0 & \text{otherwise}\,. \end{cases} \tag{130}$$

Spectra corresponding to the transmission curves in figure 7 are plotted in figure 8. We define the resolution $\Delta\mathcal{E}$ of the MAC-E filter as the

theoretical peak width. It follows from equation (130) that the relative resolution is

$$\frac{\Delta E}{E} = \frac{B_2}{B_1} \,. \tag{131}$$

6

THE ES-MPT APPARATUS

It has been explained in the section 2.2 that the associative detachment reaction of a given collision complex can proceed via many reaction pathways. Different pathways lead to the production of neutral molecules in different rovibrational excited states. Consequently, the kinetic energy of the products is related to the internal energy by the law of energy conservation. Direct experimental observation of this energy redistribution provides a valuable information, which is often directly comparable to the quantum mechanical models. This product energy distribution also determines, whether the heat of association in a collapsing protogalactic cloud is thermalized inside the cloud via electrons or radiated away by rovibrational transitions. Therefore, it should be considered as input data to the astrophysical models of the protostar formation, similarly to the heating by the three-body association (Glover, 2011).

In the past, there have been several experiments devoted to the measurement of the product energy distribution from the associative detachment. These experiments were either based on observing the chemiluminiscence of the produced molecules in a flowing afterglow apparatus (Smith and Leone, 1983; Zwier et al., 1980) or on measuring the product electron energy distributions in ion beam experiments (Mauer and Schulz, 1973; Zivanov et al., 2003).

The flowing afterglow technique is capable of producing good results in thermal (300 K) conditions. Unfortunately the homonuclear molecules such as H_2 are excluded from this method due to their low emission probabilities.

The ability of ion beam experiments to study the thermal distributions is somewhat limited. Nevertheless, measurements at ion energies down to 0.05 eV and 0.2 eV are claimed by Mauer and Schulz, 1973 and Zivanov et al., 2003, respectively. To investigate the product energy distributions under the thermal conditions at temperatures of 300 K and below, we have started a development of a novel experimental technique. Our experiment is based on the combination of an ion trap with an electron spectrometer. Hence the name *electron spectrometer with a multipole trap* (ES-MPT). This approach—in principle—retains all the advantages of the ion trapping technique, i. e., the possibility to independently vary temperature of ions and interacting neutrals in a broad range of conditions. The initial implementation, however, uses a room temperature trap with a possibility to connect a source of neutrals with variable temperature. The following sections are dedicated to the description of this apparatus.

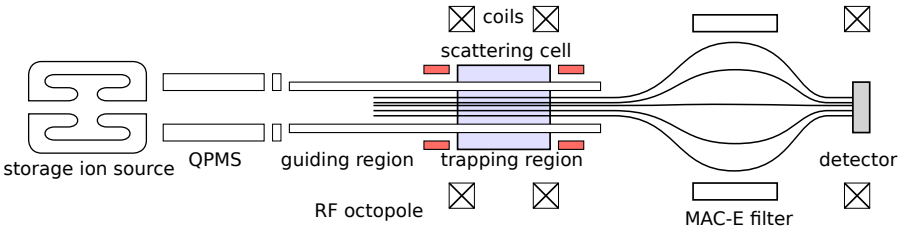

Figure 9: Schematic drawing of the main components of the ES-MPT apparatus.

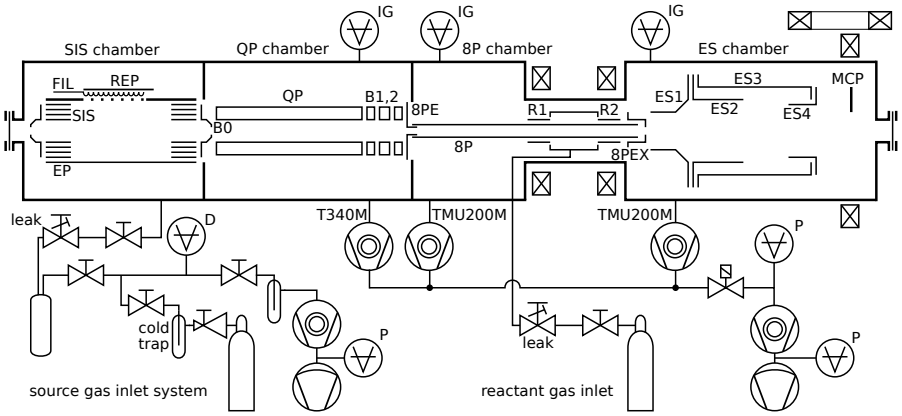

Figure 10: Piping and instrumentation diagram of the ES-MPT apparatus showing the vacuum system, gas inlet system, and electric potentials inside the vacuum vessel. Abbreviated naming of the components is shown. The high vacuum pumps are magnetically suspended turbomolecular pumps and fore pumps are diaphragm pumps (symbols according to DIN28401). Gauge abbreviations IG, P, and D denote the ionization gauge, Pirani gauge, and diaphragm manometer respectively. The coils are indicated by the crossed squares.

6.1 DESIGN OF THE ES-MPT APPARATUS

The configuration of the experimental setup is schematically shown in figure 9 and a more detailed piping and instrumentation diagram is presented in figure 10. The abbreviated names of electrodes from figure 10 will be used in the following text.

The ions are produced by the electron bombardment of a suitable precursor gas in the RF *storage ion source* (SIS). The precursor gas is filled through a cold trap into a reservoir and then leaked into the storage ion source (SIS) vacuum chamber. Electrons emitted from a heated filament (FIL) are accelerated by a repeller (REP) to hit the precursor particles and produce ions. The RF field applied to the stack of electrodes (SIS) and static field applied to the endplate electrodes (EP) confines the produced ions inside the SIS.

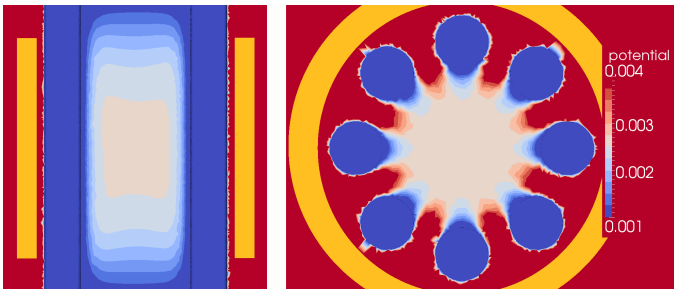

Figure 11: Calculated penetration of a finite ring electrode potential into the trap. The potential is shown in units of fraction of the ring electrode potential. The left plot shows a cut along the axis, going through the octopole rods. The right panel shows a cut perpendicular to the axis.

After extraction from the ion source by pulsing the B0 electrode, the ions are mass selected in a *quadrupole mass spectrometer* (QPMS) and injected into an RF octopole ion guide (8P). The ions are then trapped inside the RF octopole. The axial trapping potential barrier is produced by applying voltages to two ring electrodes R1 and R2 surrounding the octopole. The height of the barrier on axis is approximately 0.003 times the ring electrode potential as shown in our calculation in figure 11. The trapping area is enclosed in a scattering cell, which is connected to a gas inlet system.

Both ring electrodes are placed near the tip of the octopole, so that the trapping volume coincides with the extraction region of the electron spectrometer. Therefore, the trapping area is only approximately 3 cm long. The magnetic field of the electron spectrometer (MAC-E filter) guides the electrons produced in the trap into the weak field region, where a retarding potential barrier is applied by the electrodes ES2 and ES3 (filtering region). The magnetic field then increases again to focus the electrons into the detector.

The microchannel plate (MCP) detector (model F4655-12 by HAMAMATSU) is used to detect the ions and electrons. The MCP front plate is biased to 200 V for detection of both electrons and anions. A 2000 V voltage is applied across the MCP plates. The pulses from the MCP are discriminated and counted with a 100 MHz counter or with a multichannel analyzer (model MCD-2 by FAST ComTec).

The apparatus is optically transparent on axis. This allows us to calibrate the spectrometer using monoenergetic electrons from photodetachment. In the future experiments, the transparency on axis will be essential for delivering an effusive atomic beam into the trap.

The RF devices in the apparatus, i. e., the storage ion source, the quadrupole mass spectrometer and the octopole ion guide were originally designed and manufactured in the laboratory of Prof. Gerlich (Gerlich, 1992). The inscribed radius of the octopole is $r_0 = 3$ mm

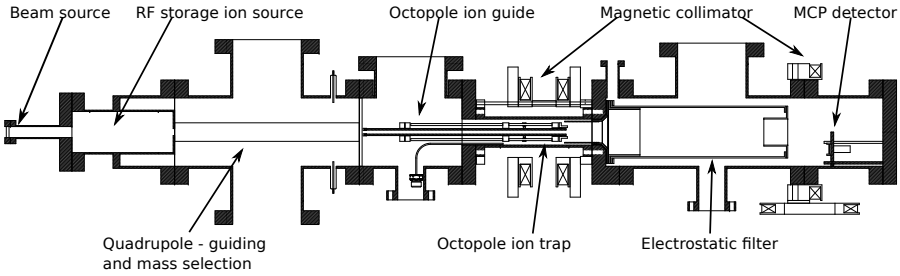

Figure 12: CAD drawing of the ES-MPT apparatus.

and the rod diameter d is in accordance with formula (112) equal $d = 2$ mm. The total length of the octopole rods is $l = 294.5$ mm.

The complete current setup is shown in correct scale in figure 12.

6.2 DESIGN OF THE MAC-E FILTER

The electromagnetic fields of the MAC-E filter are designed to achieve the relative resolution

$$\frac{\Delta\mathcal{E}}{\mathcal{E}} = \frac{B_{min}}{B_{max}} = \frac{1}{30}\,. \tag{132}$$

The possibility of combining the electron spectrometer with the more advanced variable-temperature 22-pole trap was also initially considered (see the preliminary design consideration by Roučka et al., 2009). However, the 22-pole trap requires a much larger housing, with many feed-throughs and a connection to the cold head. Combining the spectrometer with the 22-pole trap would require manufacturing a new chamber, mounting flange, and several ferromagnetic shields to shape the field properly. Therefore, it was decided to use the 22-pole trap for measuring the temperature dependencies of the rate coefficients only (for which it is best suited) and to build the spectrometer around a more compact octopole trap. The octopole trap fits into a standard CF40 flange. This allowed us to make the construction much simpler by placing the electromagnets outside of the vacuum chamber as shown in figure 12.

To minimize the manufacturing costs and to retain the compatibility with our current equipment, we have designed the spectrometer to fit into our standard vacuum chambers with two CF100 flanges separated by 270 mm distance. The field in the trap is produced by two coils configured approximately as Helmholtz coils as indicated in figure 13. In order to achieve the required field ratio 1 : 30 on a short distance of approximately 20 cm, the Helmholtz coils are surrounded by two ferromagnetic rings made of construction steel. These rings enhance the field between them and shield the field outside, thus increasing the field ratio. The configuration of coils was developed with the help of computer simulations with the FEMM software (Meeker,

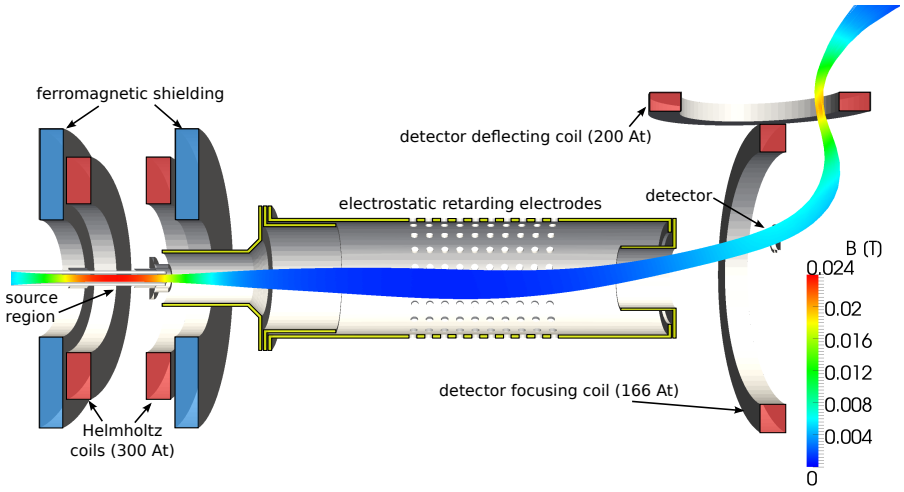

Figure 13: Electromagnetic design of the MAC-E filter - cross section. Coils, ferromagnetic shields, and electrostatic retarding electrodes are indicated by red, blue, and yellow color respectively. Calculated magnetic flux tube emanating from the ion trapping region is shown in color corresponding to the magnetic field intensity.

2009) and FEniCS software (Logg and Wells, 2010; Logg et al., 2012) in combination with Netgen (Schöberl, 1997) for 3D unstructured mesh generation from a constructive solid geometry. The initial design was done with the FEMM software. Unfortunately, FEMM can only solve 2D problems. Therefore, to model the final design including the deflecting coil, we have used the more general FEniCS software capable of solving 3D problems. The results of both models were shown to agree on axisymmetric problems (see figure 5).

To maintain relatively low current densities in the copper coils, we have decided to use approximately 30 mT field in the trap region and approximately 1 mT field in the filtering region. These constraints lead us to design the Helmholtz coils for 1350 ampere-turns each. The currents in the focusing and deflecting coil are 900 ampere-turns and 750 ampere-turns respectively, so that the whole trapping area is projected by magnetic field lines into the detector. This projection is illustrated in figure 13, where the calculated magnetic flux tube emanating from the trapping region is shown. The magnetic field intensity is color coded on the surface of the tube.

The coils are wound from 1.18 mm diameter enameled wire. The Helmholtz coils, focusing coil, and deflecting coil have 300, 200, and 166 turns respectively. This means that the required current is 4.5 A.

The accuracy of our calculations was verified by comparing the calculations with a measured magnetic field using a Hall probe (Roučka et al., 2010). For simplicity, we have measured only the z-component (axial component) of the field on the axis of the spectrometer. The deflecting coil was not used in this measurement. The results shown

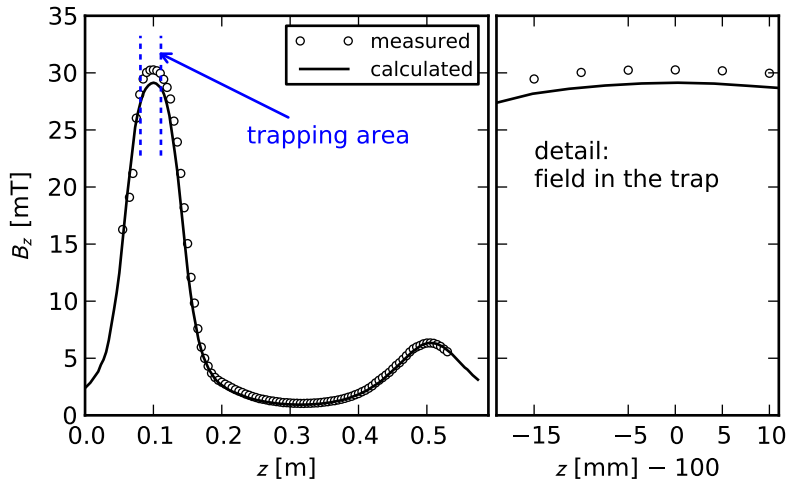

Figure 14: Measured magnetic field generated by the Helmholtz coils and the focusing coil with 4.5 A current. The z axis is calibrated so that the center of symmetry of the Helmholtz coils is located at $z = 0.1$ m. The area between the end electrodes is indicated in the left panel and it is shown in detail in the right panel.

in figure 14 demonstrate a good agreement between the model and the measurement. The higher measured field in the trapping region can be explained by a slightly higher magnetic permittivity of the ferromagnetic rings, since the magnetic properties of the construction steel were not precisely known in advance. This small discrepancy is acceptable for our experiment, because it actually improves the ratio of the magnetic fields.

Regarding the electric retarding field, we have two basic requirements. First, the barrier height should be approximately the same for all possible particle trajectories. Second, the filtering should occur only in the low B-field region.

The electric field is produced by four concentric cylindrical electrodes, which are indicated in figure 13. The electrodes are named ES1, ES2, ES3, and ES4 in the order of increasing distance from the trap. The entrance and exit electrodes ES1 and ES2 are kept at a constant voltage equal to the trap direct current (DC) potential. The retarding voltage U_B is applied to the longest electrode ES3 and a smaller fraction ($0.3 \cdot U_B$) is applied to ES2. The main electrode ES3 contains holes to speed up the pumping of the spectrometer volume.

For simulating the relatively complex geometry of the spectrometer, the NETGEN software was used for mesh generation from STEP files containing the geometry. Elmer solver (*Elmer*) was chosen instead of FEniCS for its better ability to deal with boundary markers for assigning the boundary conditions to electrodes. The calculated detailed view of the potential barrier for $U_B = 1$ V is shown in figure 15. Two rows of venting holes were included in the simulation to investigate their possible influence on the symmetry of the barrier.

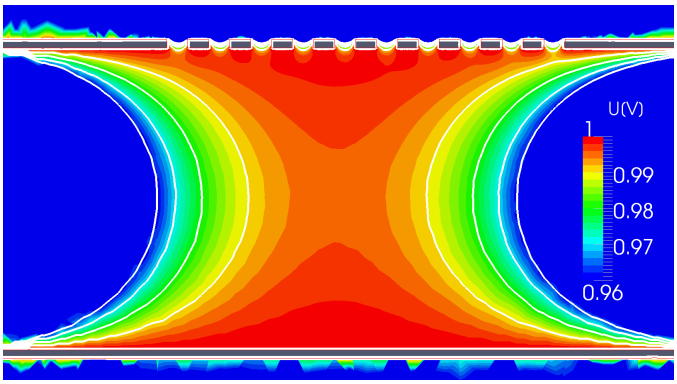

Figure 15: Simulated electrostatic retarding barrier for $U_B = 1$ V. White equipotentials are located at 0.96 V, 0.97 V, 0.98 V, 0.99 V, and 1.00 V.

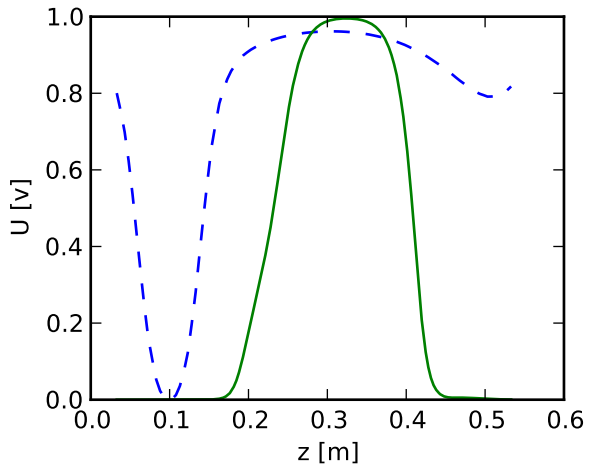

Figure 16: Electrostatic retarding potential on the axis of the spectrometer for $U_B = 1$ V is shown in solid line. The dashed line indicates the condition (134) for $\mathcal{E}_0 = qU_B$.

This simulation shows that the barrier is constant for all particles with accuracy better than 0.5 %. The influence of the holes is negligible.

The second condition for the electrostatic field is more precisely formulated as: Filtering of particles with energy $\mathcal{E}_0$ by a potential barrier $U_B = q\mathcal{E}_0$ occurs only in the low B-field region. Otherwise, the resolution of the MAC-E filter would drop to the value $\Delta\mathcal{E}/\mathcal{E} = B'/B(1)$ determined by the field B' in the place where the filtering occurs. To determine the conditions needed to satisfy this constraint, we need to look again at the adiabatic transformation of velocity in the collimator. It follows from the equation (122) that the minimal energy $\mathcal{E}_{\parallel}(2)$ associated with the parallel motion of a particle at point (2) is related to the initial energy $\mathcal{E}_0$ by

$$\mathcal{E}_{\parallel}(2) \geqslant \mathcal{E}_0 \left(1 - \frac{B(2)}{B(1)}\right) . \tag{133}$$

The condition for no filtering potential then relates the local electrostatic barrier to the shape of the magnetic field by equation

$$U(2) < \frac{\mathcal{E}_0}{q}\left(1 - \frac{B(2)}{B(1)}\right). \tag{134}$$

For a given particle energy $\mathcal{E}_0$, when increasing the barrier height, this condition should be first violated in the region of the lowest magnetic field. It is illustrated graphically in figure 16 that this condition is satisfied in our design of electromagnetic fields.

6.3 MOTION IN SUPERIMPOSED RF AND MAGNETIC FIELDS

The following section discusses the general issues of the particle motion in superimposed RF and magnetic fields. Realistic simulations and experimental results are presented in the next section.

The problem of the particle motion in a RF field is by itself relatively complicated. In the ES-MPT we superimpose the ion-trapping RF field with an inhomogeneous magnetic field for electron guiding, which further increases the complexity of the particle behavior. In order to assess the feasibility of running the linear multipole RF trap in a weak magnetic field, we investigate briefly the problem of ion motion in a superposition of RF and magnetic field. This problem can be viewed from many different perspectives, each of which is suitable for a certain range of physical conditions. Since we do not aim for a general rigorous treatment, our discussion is based on a study of a specific simple geometry. We will see though that most of our observations could be generalized.

For a theoretical generalization of the effective potential and possible applications see Dodin and Fisch, 2006; Dodin and Fisch, 2005 and references therein. An important special case of particle behavior in combined RF and magnetic fields is the cyclotron resonance, which has numerous applications, e. g., mass spectrometry, precision measurements, or particle acceleration. However, in the cyclotron resonance applications, a strong magnetic field is used for particle trapping and a small RF field is used for exciting the particles, as opposed to our experiments, where particles trapped in RF field interact with small magnetic field.

Possibly the simplest device featuring inhomogeneous RF electric field is the cylindrical capacitor—a hypothetical device consisting of two infinitely long coaxial cylindrical electrodes. The electric field between the electrodes follows from the Gauss' law and is easily expressed in the cylindrical coordinates as

$$\mathbf{E} = C_E \frac{\hat{\mathbf{r}}}{r}, \tag{135}$$

where $\hat{\mathbf{r}}$ denotes a unit vector in the direction of the r coordinate. The integration constant C_E is determined by the electrode dimensions

and potentials. We assume that the magnetic field $\mathbf{B}$ is homogeneous, constant and parallel to the z axis.

To simplify our discussion, we demonstrate the behavior by calculating the trajectories of H^- ions under particular boundary conditions for electric field and initial conditions for particle motion. We vary only the magnetic field intensity. The following RF field parameters were used: $C_E = 0.005$ V; $\Omega/2\pi = 10$ MHz. The simulation always starts in the maximal phase of the RF field, so that the initial velocity corresponds to the velocity of the secular motion. For an H^- particle starting at a distance of $r_0 = 50$ µm from the axis, the adiabaticity parameter given by equation (109) takes the value $\eta \approx 0.024$, which is safely below the critical threshold 0.3 (Gerlich, 1992).

An important parameter for describing the interplay of magnetic and electric fields in determining the particle trajectory is the ratio of the cyclotron frequency ω_c to the RF frequency Ω. We denote it as Ξ,

$$\Xi = \omega_c/\Omega\,. \tag{136}$$

Let us first deal with the conceptually simplest yet the most useful case, where $\Xi \ll 1$. In this regime, which corresponds to the conditions in our experiment, the magnetic gyration has much larger period than the RF micromotion. In the worst case of H^- trapping, the cyclotron frequency at $B = 30$ mT is $\omega_c/2\pi = 457$ kHz. The coupling between the RF and gyration is therefore negligible. Since the magnetic field is small, the assumptions used for the derivation of the effective potential in section 5.1 are still valid. Especially the assumption of micromotion amplitude depending only on the particle position. By repeating the procedure for obtaining the effective potential with added Lorentz force term $q\,d\mathbf{r}/dt \times \mathbf{B}$ and using the same ansatz as in the section 5.1, we arrive at a solution in the form

$$m\frac{d^2\mathbf{R}_0}{dt^2} = \frac{q^2}{4m\Omega^2}\nabla E_0^2 + q\frac{d\mathbf{R}_0}{dt} \times \mathbf{B}\,. \tag{137}$$

Here we again obtain an equation completely in terms of the drift motion, because the contributions of the oscillatory motion to the Lorentz force vanish by averaging over 1 RF period.

In the special case of the cylindrical magnetron, equation (137) can be further solved by observing that the ponderomotive force is perpendicular to $\mathbf{B}$. The motion is therefore described by the well know drifting motion in crossed fields, so called $\mathbf{F} \times \mathbf{B}$ drift (see section 4.1.2). The RF guiding center $\mathbf{R}_0$ will perform a cyclotron rotation around a magnetic guiding center at $\mathbf{R}_B$, which is in turn orbiting the center of the magnetron. Here we introduce the terms *RF guiding center* and *magnetic guiding center* which denote the guiding center obtained by averaging over one RF period or over one gyration period respectively. The superposition of the small scale RF micromotion, the

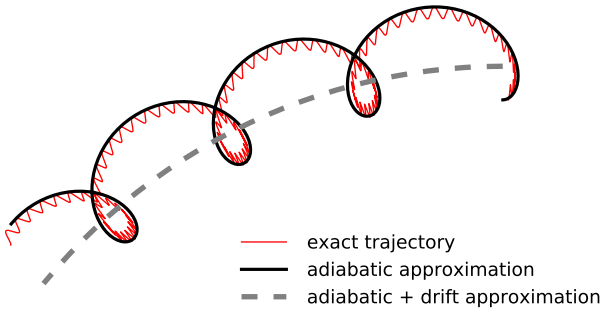

Figure 17: Particle trajectory in a cylindrical RF magnetron for $\Xi = 0.038$. The exact trajectory is shown as a thin solid red line. The adiabatic approximation resulting from averaging over one RF period is shown in a thick solid black line. The gyration center approximation obtained by further averaging the adiabatic approximation over one cyclotron rotation is shown as a dashed grey line.

intermediate scale cyclotron rotation, and the large scale drift motion (also called magnetron motion) is demonstrated in figure 17.

Inserting the expression for the effective potential into the general equation of the $\mathbf{F} \times \mathbf{B}$ drift velocity in a non-uniform effective force field (see, e. g., Baumjohann and Treumann, 2012 or Chen, 1974) yields an equation for gyration center motion

$$\frac{d\mathbf{R}_B}{dt} = \frac{q}{4m\Omega^2}\left(1 + \frac{1}{4}r_g^2\Delta\right)\frac{\nabla E_0^2 \times \mathbf{B}}{\mathbf{B}^2}, \tag{138}$$

where r_g denotes the gyroradius. Evaluating this equation for the magnetron field (135) leads to an analytic expression for the drift velocity

$$\frac{d\mathbf{R}_B}{dt} = \frac{q}{2m\Omega^2}\left(1 + \frac{3}{4}\frac{r_g^2}{r^2}\right)\frac{C_E^2}{r^3\mathbf{B}^2}. \tag{139}$$

The second order term in r_g/r accounting for the electric field inhomogeneity is usually neglected. In our model problem, it would change the drift velocity by approximately 1 %. A good agreement with this formula was observed for the experimentally relevant range of parameters $\Xi \lesssim 0.1$.

We have observed that the conclusions of the adiabatic theory (section 5.1) are still mostly valid in the case $\Xi \ll 1$. Just simple modifications are needed to account for the influence of the magnetic field. Despite the fact that only small magnetic field is used in our experimental setup, we will take at least a qualitative look at the particle behavior at higher intensities of the magnetic field. Our simulations show that a resonant coupling between the RF driving force and gyration becomes significant already at $\Xi \approx 0.1$. This coupling is visible as a slight increase in the particle kinetic energy. Nevertheless, the particle trajectories still follow the adiabatic approximation within few percent for $\Xi < 0.3$.

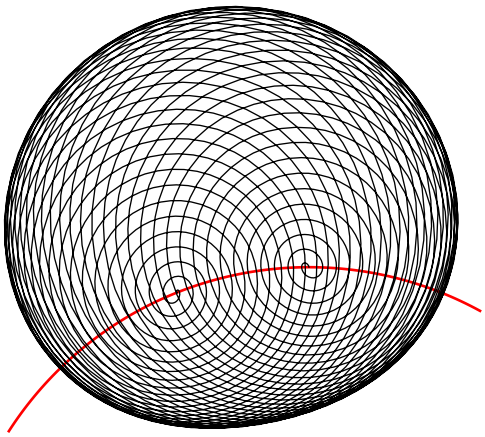

Figure 18: Particle trajectory near resonance, $\Xi = 0.983$. Particle starts with zero initial velocity at maximal amplitude of RF field in the center of the spiral to the right. One beat period, which consists of resonant acceleration followed by resonant deceleration, is shown. The gyration center follows the magnetron orbit indicated by the solid red line.

As the cyclotron frequency becomes comparable to the excitation frequency, the adiabatic approximation is not applicable any more. The presence of *beats*–typical for mechanical systems near resonance– is observed, as illustrated by figure 18. The figure shows a part of the trajectory for $\Xi = 0.983$. The particle, starting in the center of the right spiral, is first spiraling outward due to resonant acceleration. As soon as the phase difference between the exciting force and the cyclotron rotation grows to π, the particle continues spiraling inward due to resonant deceleration.

The figure 18 also demonstrates an important observation of our simulations that no matter how much energy the particle gains by resonant heating, the gyration center always follows a circular orbit around the magnetron center. The angular velocity of this orbiting motion strongly depends on the resonant heating and even changes direction when crossing the $\Xi = 1$ resonance, but the gyration center never leaves this circle, regardless of the initial velocity and magnetic field intensity in our simulations.

To conclude our analysis, we have numerically calculated the maximum energy reached by a test particle as a function of the superimposed magnetic field. The result of our calculation for particle starting with a zero velocity at a radius $r_0 = 50$ μm is shown in the figure 19. Calculations were also performed for several higher starting radii up to 250 μm and for starting azimuthal velocities in the range ± 20 m/s. The initial conditions influence the line shapes slightly, but the qualitative picture remains the same. The maximum in energy was determined over 6000 RF oscillations, which correspond to 300 μs time.

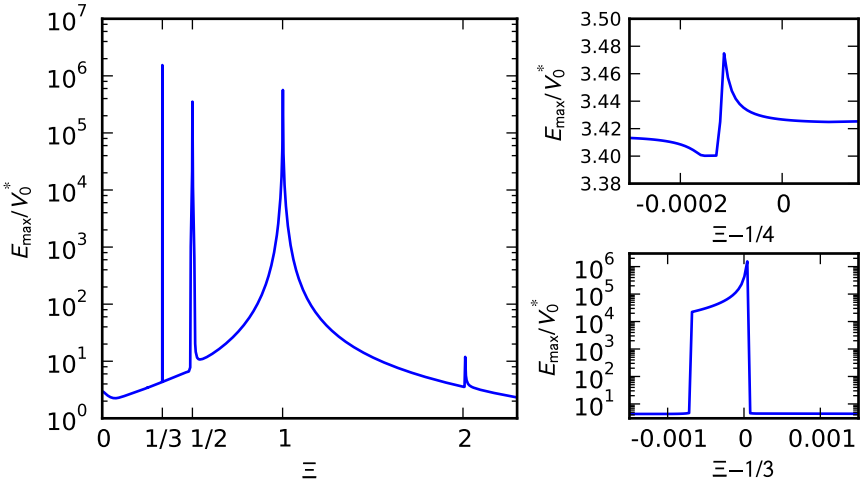

Figure 19: Resonant increase of the particle's kinetic energy as a function of $\Xi = \omega_c/\Omega$.

The plotted energy is normalized by the local effective potential energy at the starting point, $V_0^* = V^*(r_0)$. We can see in the graph that for the smallest magnetic fields, where $\Xi \lesssim 0.1$, the energy is decreasing, which is caused by decreasing gyroradius. However, already at $\Xi \approx 0.1$ the tail of the cyclotron resonance peak starts influencing the energy. Additional resonances are observed at integer fractions $1/2$, $1/3$, and $1/4$ and also at double of the cyclotron frequency. The smallest resonant feature, which was found at $\Xi \approx 1/4$, is enlarged in the top right subplot. Resonances at lower Ξ were not found, although some narrow peaks cannot be excluded. The very narrow and sharp resonance at $\Xi = 1/3$ is enlarged in the bottom right subplot.

6.4 RF OCTOPOLE TRAP IN MAGNETIC FIELD

The previous section showed that there should be no issues with the resonant heating in the magnetic field in our experiment and that the particle motion is described by the adiabatic approximation in equation (137). This section presents mainly the results of numerical simulations regarding the ion trapping and cooling in the octopole trap. We use a two dimensional model of an infinitely long octopole, therefore, neglecting the effects of end electrodes. The realistic multipole potential is calculated on a rectangular grid using the finite difference method described in the section 3. The trajectories in all our simulations are calculated accurately without use of the adiabatic approximation. All simulations deal with the octopole with dimensions $r_0 = 3$ mm, $d = 2$ mm.

An example of the effects of magnetic fields on a H^- particle trajectory in the RF octopole is shown in figure 20. As expected, the

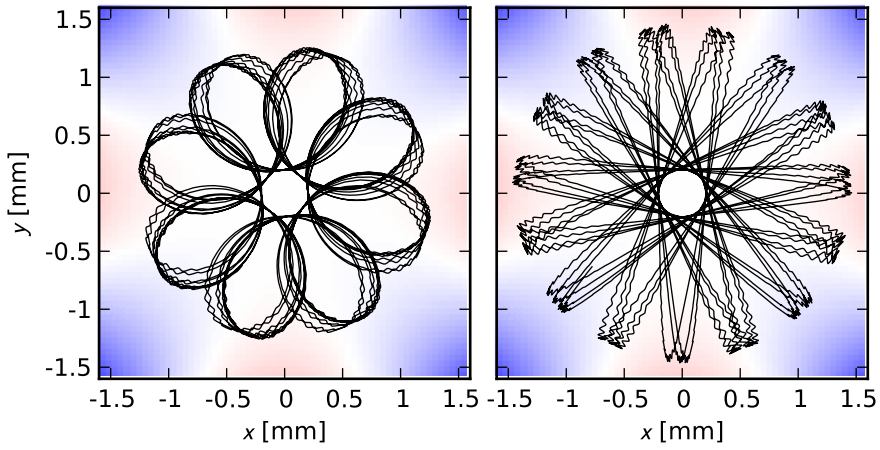

Figure 20: Trajectories of the H^- ion in a RF octopole trap with superimposed magnetic field $B_z = 30$ mT (left panel) and without magnetic field (right panel). The initial conditions are the same otherwise. The operating conditions are $\Omega/2\pi = 20$ MHz, $V_0 = 20$ V. The colored background illustrates the calculated octopole potential.

particle in the magnetic field is drifting around the trap center by the crossed-fields drift (cf. equation (138)).

An important issue in the studies of ion chemistry in the RF traps is the temperature of the ions. The ions in our experiments are cooled by the buffer gas cooling. In the buffer gas cooling process, an inert gas in thermal equilibrium with the trap containment is leaked into the trap. The ions are typically thermalized in just a few collisions, depending on the mass ratio. However, if the ion collides with the buffer gas particle in the effective potential field, the collision can lead to transformation of the effective potential energy into the kinetic energy of the secular motion. This type of collision leads to the so called *RF heating*.

To illustrate this effect, assume for simplicity that all the energy is stored in the form of the effective potential energy. The instantaneous velocity is given by time derivative of $\mathbf{R}_1$ from equation (98)

$$\dot{\mathbf{R}}(t) = \dot{\mathbf{R}}_1(t) = \frac{qE_0}{m\Omega} \sin \Omega t \,. \tag{140}$$

A collision with a much heavier cold buffer gas particle at time t_c can lead to a complete reversal of the velocity direction in the worst case

$$\dot{\mathbf{R}}'(t_c) = -\dot{\mathbf{R}}(t_c) \,, \tag{141}$$

where primes indicate the values after the collision. Since the effective potential energy is unaffected by the collision, the resulting velocity after collision becomes a superposition of the original oscillatory motion and a secular motion

$$\dot{\mathbf{R}}'(t_c) = \dot{\mathbf{R}}'_0(t_c) + \dot{\mathbf{R}}_1(t_c) \,. \tag{142}$$

Solving this equation for $\dot{\mathbf{R}}_0'$ by inserting from (140) and (141) gives us the secular velocity gained in the collision

$$\dot{\mathbf{R}}_0'(t_c) = -\frac{2qE_0}{m\Omega}\sin\Omega t_c\,. \tag{143}$$

And calculating the gain in the kinetic energy results

$$\frac{1}{2}m\dot{\mathbf{R}}_0'^2(t_c) = -\frac{q^2E_0^2}{m\Omega^2}\sin^2\Omega t_c = 4V^*\sin^2\Omega t_c\,, \tag{144}$$

where a zero static component of the effective potential is assumed. Therefore, a velocity-reversing collision with a heavy particle in a region of high RF field and in the zero phase of the field can lead to a gain of 4 times the initial total energy. These are the most unfavorable conditions and in general the balance between the RF heating and buffer gas cooling strongly depends on the type of the trap, operating conditions of the trap and the mass ratio of the buffer gas vs. the ions. Obviously, it is desirable to use higher-order multipoles, where the potential is steeper and the ions spend less time in the high-field regions. Also, the atomic mass of the buffer gas should be smaller than the ion mass to prevent such strong energy exchange in the RF field. Systematic studies of these effects can be found in Asvany and Schlemmer, 2009.

In this section we present the simulated particle energy distributions in the octopole trap under the conditions relevant for our experiment. The results were obtained by injecting an ensemble of typically 1000 ions into the trap. After a certain time of equilibration, typically several milliseconds, the particle positions and energies were averaged into a histogram for several milliseconds. Rather high buffer gas pressures about 10^{-3} mbar were used to speed up the simulation. Decreasing the pressure did not have effect on the distributions. Unless stated otherwise, the collisions are simulated as isotropic scattering in the center of mass frame with the Langevin-type cross section.

Parameters which we found suitable for our calculations are $\Delta t = 2\cdot10^{-9}$ s and $\Delta x = 5\cdot10^{-5}$ m. Using finer discretization of time and space did not cause any significant difference in the results.

The calculated energy distributions of O^- ions cooled by helium buffer gas at 300 K are shown in figure 21. The octopole operating conditions are $\Omega/2\pi = 6$ MHz, $V_0 = 10$ V. Influence of a superimposed magnetic field 25 mT was investigated, but no effect was observed. The mean ion energy corresponds to approximately 370 K in both cases due to the RF heating. The O^- spatial distribution (or more precisely a cut of the 2D spatial distribution) under the same conditions is shown in figure 22. Again, no influence of magnetic field on the density distribution is observed. For comparison, the theoretical Boltzmann distribution given by

$$f(\mathbf{x})\,d\mathbf{x} = K\exp\left(-\frac{V^*}{k_B T}\right)d\mathbf{x} \tag{145}$$

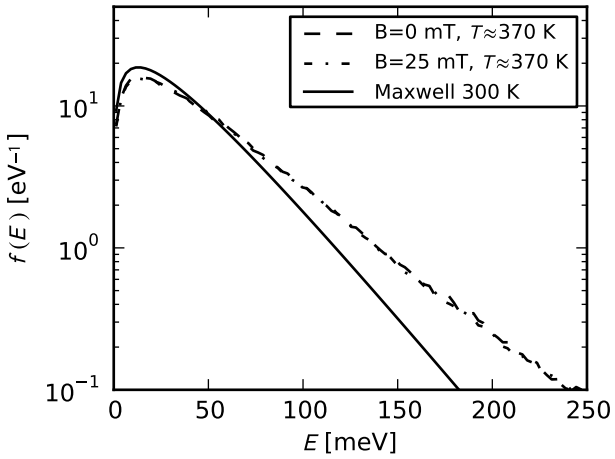

Figure 21: Cooling of O^- by collisions with He in the RF octopole at $\Omega/2\pi = 6$ MHz, $V_0 = 10$ V. The figure demonstrates the negligible influence of the magnetic field on the energy distribution.

is shown for the ideal multipole potential (113) and temperature 300 K. Thanks to the relatively small RF heating and the steep effective potential, the theoretical distribution is in a good agreement with the calculated results.

Similar calculations were also carried for the H^- ions under operating conditions $\Omega/2\pi = 20$ MHz, $V_0 = 20$ V. Due to their low mass, cooling by the relatively heavy helium atoms is problematic as shown in figure 23. The resulting H^- temperature is approximately 800 K, which is much higher than the helium buffer gas temperature. A more suitable buffer gas for H^- is molecular hydrogen, thanks to its low mass and no reactive collisions with H^-. Using the H_2 as a buffer leads to a significantly lower temperature of about 500 K. It was also speculated that the small angle Langevin scattering can contribute positively to the cooling, since these collisions have relatively smaller heating effect. The effect of including these collisions with impact parameter up to 9 times the Langevin impact parameter b_t (see sec 4.3.1) is shown in figure 23. No influence of these collisions on the overall energy distribution was observed.

The influence of magnetic field on the energy distribution was also calculated, but no difference was observed, just like in the case of O^-. However, a slight difference in the density distribution due to the magnetic field was found, as shown in figure 24. We assume that this difference is caused by slight perturbations to the adiabatic theory due to the low mass of the H^- ions.

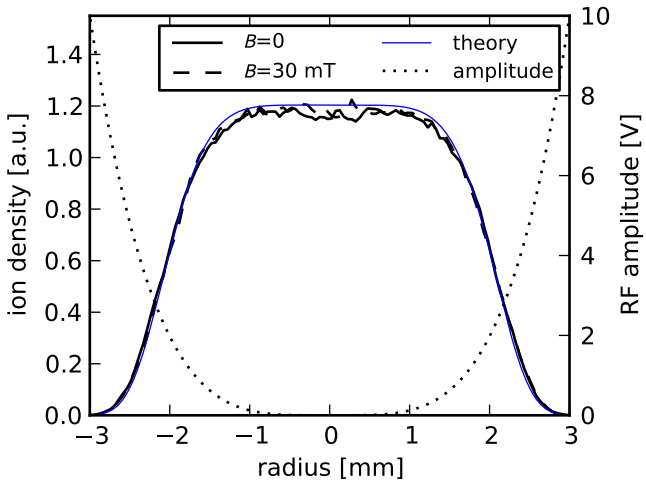

Figure 22: Density distributions of O^- corresponding the simulation in figure 21. The RF field amplitude on the plane going through the rod axes is illustrated by the dotted line.

6.5 ENERGY RESOLUTION OF THE ES-MPT

The resolution limit imposed by the ratio of the magnetic fields in the spectrometer is approximately 3 %. It has already been discussed that the imperfections of the electrostatic retarding barrier should not introduce errors bigger than approximately 1 %. The real potential of the spectrometer electrodes will be disturbed by patch fields, which are caused by the polycrystalline surface of the stainless steel electrodes and by adsorbates on the surfaces. The patch fields can reach values up to 100 mV on the surface, but should fall off rapidly to the order of millivolts close to the axis, as discussed by Rossi and Opat, 1992 and Darling et al., 1992. The biggest error—in accordance with our first estimates (Roučka et al., 2010)—is caused by the influence of the RF field on the electron energy.

A simple idealized model to estimate this influence was developed by Roučka et al., 2010. If we assume that the electron leaves the trap before the RF potential changes significantly, the electron energy will just be shifted by the potential where the electron was formed. In the experiments with a gaseous reactant leaked into the trap or with broad interacting beams, the electron production rate is proportional to the local ion density. Therefore, the measured energy distribution of initially monoenergetic electrons, i. e., the *instrument function*, is equal to the distribution of ions as a function of the local electric potential. To estimate the worst case, we calculate the influence on the electrons produced in the maximal phase of the RF field.

Transformation of the O^- and H^- ion distributions calculated in the previous section (figures 22 and 24) into the amplitude distributions is shown in figure 25. We can see from the figure that the expected

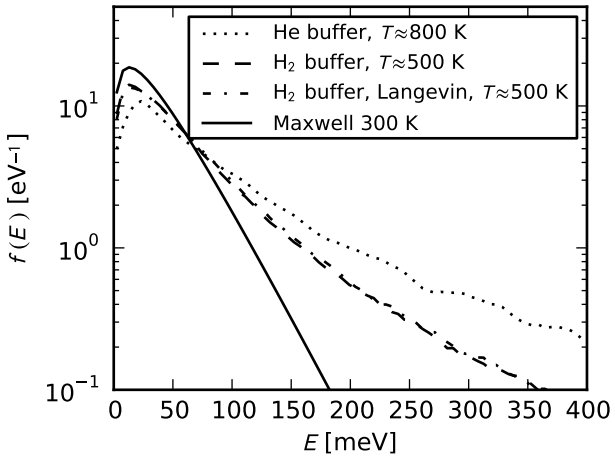

Figure 23: Cooling of H^- in the RF octopole. The influence of different buffer gasses and small angle Langevin scattering is illustrated.

instrument function has a long tails, but a sharp peak at the correct energy should be retained.

Unfortunately, at the typical electron energy 1 eV, it takes about 100 ns for the electron to fly straight out of the trap (approximately 5 cm). This is comparable to the period of the RF field. Therefore, this model can be used as a qualitative estimate only.

A more accurate three dimensional particle simulation was developed to study the spectrometer resolution in detail. Electrodes included in the simulation are: 8 octopole rods, 2 trapping ring electrodes, octopole exit electrode, 4 spectrometer electrodes, MCP front surface, MCP mount, and the vacuum chamber. The configuration of coils and electrodes accurately represents our experimental setup and is shown in figure 13.

In this simulation, the models of electrostatic field, magnetic field and particle trajectories are combined to give a comprehensive picture of the MAC-E filter operation. The flow of the simulation is shown in figure 26. First, the fields are pre-calculated. The solutions of the Poisson equation for the static fields, RF fields, and retarding barrier field are calculated separately. The resulting field is calculated as a superposition of these fields during the particle simulation, employing the linearity of the Poisson equation. The fields are stored in the VTK unstructured grid format (*VTK: The Visualization Toolkit*), which allows easy interchange of field data on arbitrary geometries between programs, although for the price of relatively slow interpolation from the unstructured grid.

The initial positions of the electrons are randomly distributed in a 20 mm long cylinder which is located in the trap and approximates the ion distribution. The cylinder diameter was varied between 2 and 4 mm in the simulation, to investigate the possible consequences of

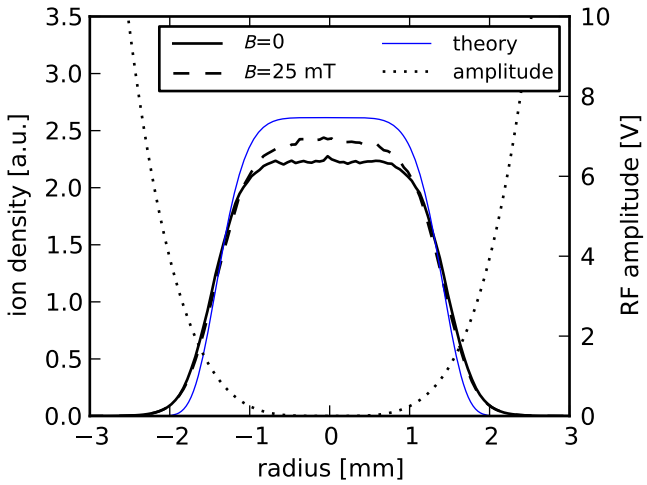

Figure 24: Density distribution of H^- in the RF octopole with the H_2 buffer gas at different magnetic field intensities. The deviation from the Boltzmann distribution at 300 K is caused mainly by the elevated temperature of the ions.

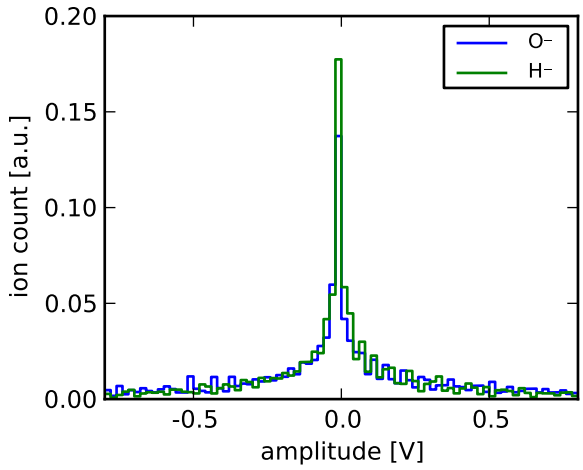

Figure 25: The amplitude-distribution of H^- and O^- ions—a simple estimate of the RF influence on the measured electron energy.

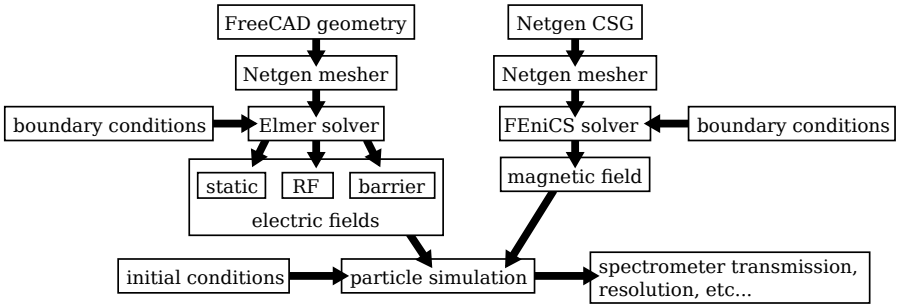

Figure 26: Flow diagram of the simulation of the MAC-E filter.

color	λ [nm]	$\hbar\omega$ [eV]	$\mathcal{E}_{\text{electron}}$ [eV]
red	660	1.879	0.418
green	532	2.331	0.870
blue	405	3.062	1.601

Table 2: Overview of the laser wavelengths used in the photodetachment experiments. The right column shows energy of electrons produced by photodetachment of O^- with electron affinity 1.4610 eV (Bartmess, 2012).

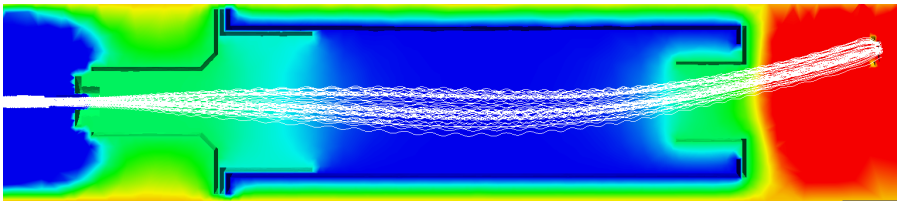

Figure 27: Electron trajectories in the MAC-E filter without the RF field. Electrons with initial energy 1.1 eV are passing a 1 V potential barrier. The color-coded electrostatic potential is shown in the background. See figure 15 for a quantitative picture of the potential.

focusing the interacting beam of selecting the electrons using an aperture.

In order to make the calculations comparable to the experimental data, we simulate electrons with energies which can be produced by the lasers available in our laboratory. The overview of used wavelengths is shown in table 2. The initial velocities are randomly isotropically distributed.

First we simulated the measured spectra of electrons from the photodetachment without the influence of the RF field. For a given initial distribution of electrons, the number of electrons reaching the detector was recorded as a function of retarding voltage. An example of electron trajectories in this simulation is shown in figure 27, where most of the electrons reach the detector.

The retarding spectra normalized by the electron count at the zero potential barrier are shown in figure 28. The differential spectra in figure 28 are obtained by numerical differentiation with a Savitzky-Golay smoothing filter. Identical filter parameters were used for all data in the graph to make the plots comparable. The full width at half maximum (FWHM) of the peaks indicates that the resolution of the spectrometer is better than 10 %.

The next set of simulations already includes the RF octopole field with parameters $\Omega/2\pi = 6$ MHz, $V_0 = 10$ V. The electrons were injected in a random phase of the RF field. A strong dependence of the RF influence on the initial radial position was expected, therefore two different diameters of the electron source were used: d = 2 mm

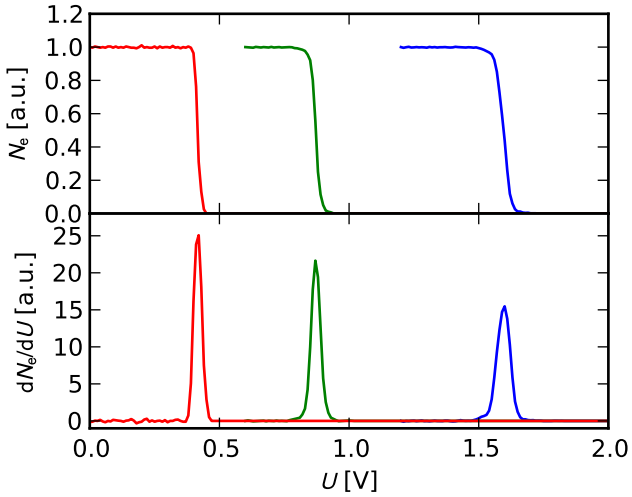

Figure 28: Simulated spectra of electrons produced by the photodetachment of O^- by 660 nm, 532 nm, and 405 nm lasers in the MAC-E filter without the influence of the RF field.

and $d = 4$ mm. Results of these simulations are shown in figure 29. The first important thing to notice is that some electrons gain energy in the RF field and are able to pass through the retarding barrier high above the expected electron energy. This is especially pronounced for electrons produced by the red laser from the larger $d = 4$ mm source. These electrons have the initial energy only slightly above the axial barrier used for ion trapping. In particular, at ring electrode voltage 100 V, the axial barrier voltage is about 320 mV. Therefore, some electrons with small axial velocity can be trapped in the octopole as in a Penning trap until they gain enough energy from the RF field to leave the trap. The acceleration of electrons by the RF field is—as expected—stronger at the higher radii.

Significant broadening, which reduces the expected resolution to approximately 20 %, is also visible. This resolution is still sufficient to resolve the major features of the associative detachment spectra shown in figures 2 and 4.

Seeking the explanation of experimental observations of lines with relative line width significantly above 20 % motivated us to investigate the possible effect of mechanical or electric imperfections of the octopole on the measured spectra. A rough estimate of the field of a slightly displaced octopole rod can be obtained by varying the potential of a correctly placed rod. The rod potential decreases by approximately 20 % at a distance of 0.2 mm from the rod surface in the direction to the trap center. Therefore, increasing the voltage on the rod by 20 % has similar consequences for the field in the trap center as moving the rod by 0.2 mm closer to the trap center.

A simulation of spectra with a 20 % increase of RF amplitude on one of the rods is shown in figure 30. The simulation shows that the

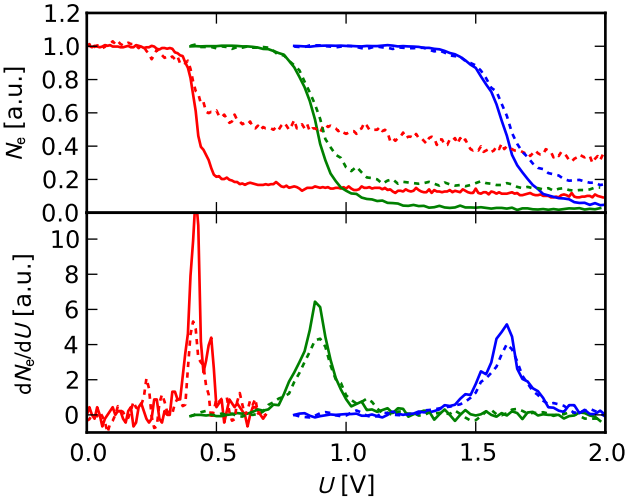

Figure 29: Influence of the RF field of octopole at $\Omega/2\pi = 6$ MHz, $V_0 = 10$ V on the electron spectra. Simulated spectra of electrons produced by the photodetachment of O^- by 660 nm, 532 nm, and 405 nm lasers. The simulations for electron source diameter 2 mm and 4 mm are shown in solid and dashed lines respectively.

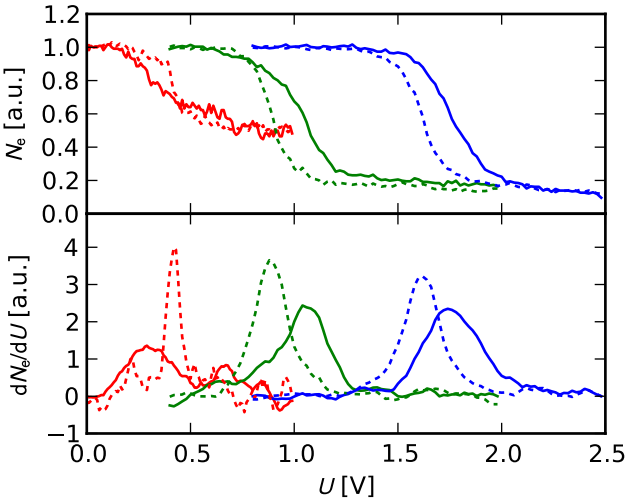

Figure 30: Influence of the imperfections of the RF field—simulated spectra of electrons produced by the photodetachment of O^- by 660 nm, 532 nm, and 405 nm lasers. The simulations for electron source diameter 4 mm with ideal octopole field and with 20 % higher amplitude on one of the rods are shown in dashed and solid lines respectively.

effects of such perturbation can vary with electron energy. The distribution of low energy electrons is very strongly broadened, which causes the peak to almost disappear. However, the peaks corresponding to blue and green laser are systematically shifted to higher energies with only moderate broadening. This means that the mechanical accuracy of the trap and symmetricity of the RF field are essential for successful operation of the ES-MPT apparatus. Fortunately, the production of electrons by photodetachment provides an ideal tool to reveal the possible sources of error.

6.5.1 *Electron Transmission of the Spectrometer*

An important parameter of the spectrometer is the transmission function as a function of the electron energy. Knowledge of this function is essential for obtaining correct electron energy distribution function. We loosely define the transmission function of monoenergetic electrons as the integral of the peak area divided by the emitted number of electrons. Thanks to the integral character of the retarding spectrum, the peak area for electrons with energy $\mathcal{E}$ is easily obtained as the difference $N_e(U_{max}(\mathcal{E})) - N_e(U_{min}(\mathcal{E}))$, where U_{min} and U_{max} limits are chosen to contain only the steeply decreasing part of the retarding spectrum (the peak). This way the electrons accelerated by the RF field are excluded from the transmission function. We have found an appropriate choice of limits $qU_{min} = 0.75\mathcal{E}$ and $qU_{max} = 1.25\mathcal{E}$, which includes the peak widths observed in the relevant simulations.

In principle, the transmission function of the MAC-E filter should be independent of energy. However, in our experiment the electrons are flying from the trap with electrostatic potential barriers. Only electrons with high enough component of the parallel velocity can escape from the trap. Since the magnetic field inside the trap is approximately constant, the transmission of electrons from the trap can be obtained from equation (129) by replacing the ratio of magnetic fields with unity, which leads to

$$T(\mathcal{E}, U_B) = 1 - \sqrt{\frac{qU_B}{\mathcal{E}}}, \tag{146}$$

where U_B is the potential of the axial barrier for ion trapping.

The numerically calculated transmission of the ES-MPT for various conditions in comparison with the above theoretical expression is shown in figure 31. The barrier potential was 0.32 V as obtained from the numerical simulation (ring electrode voltage was 100 V). Both the idealized case without the RF and the case with RF field are close the theoretical prediction. They differ only by a constant factor close to unity as indicated in figure 31. In the case of the more extended electron source with diameter 4 mm, the transmission is much lower, which means that most of the electrons on the higher radii is lost due

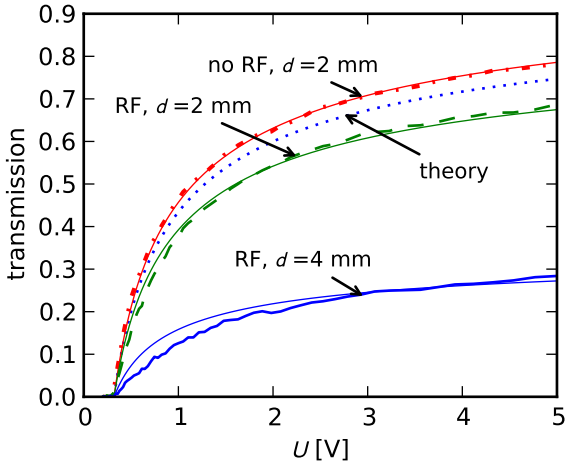

Figure 31: Calculated transmission of the MAC-E filter for ion trapping barrier 320 mV. Cases with and without RF field and with source diameters 2 mm and 4 mm are indicated in the figure. The thin solid lines overlaid over the simulations are the theoretical curves normalized to match the simulation.

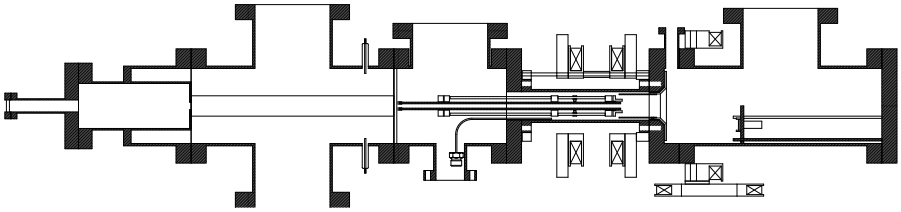

Figure 32: Configuration of the ES-MPT apparatus for testing the ion and electron detection. Compare with the full configuration shown in figure 12

to the RF field. The agreement of the simulation with the theoretical curve is satisfying in all cases. For the most accurate calibration it is recommended to select the electrons from the central area of the trap using a focused reactant beam or an aperture for electrons on the trap exit.

6.6 EXPERIMENTAL RESULTS

Before building in the spectrometer, the ES-MPT apparatus was set up to test the confinement of ions in the magnetic field and the extraction and detection of the electrons from the trap. The major differences in comparison to the full configuration in figure 12 are the absence of the filtering electrodes and placement of the detector with associated coils closer to the octopole exit. The test configuration is shown in figure 32.

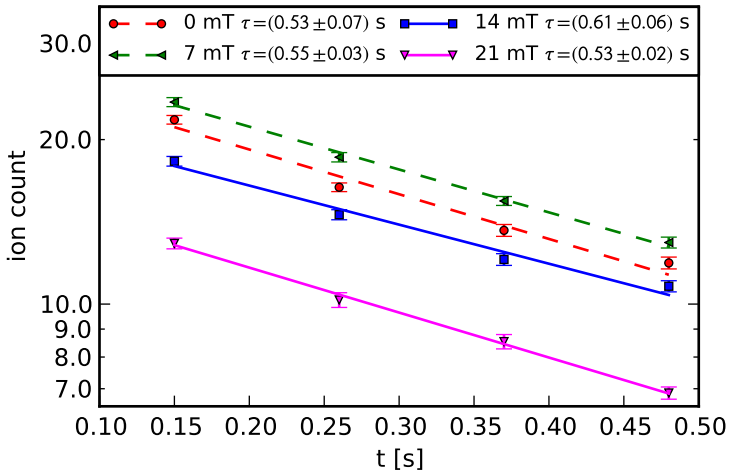

Figure 33: Measured influence of the magnetic field on the O^- trapping. The storage time is independent on the magnetic field.

6.6.1 *Ion Storage in the Magnetic Field*

The O^- ions produced by the electron bombardment of the nitrous oxide (N_2O) precursor gas (Lee and Grabowski, 1992) were stored in the octopole at operating conditions $\Omega/2\pi = 7$ MHz, $V_0 = 20.5$ V. The background pressure in the trap chamber was $5{\cdot}10^{-9}$ mbar. The number of stored ions was measured as a function of time for different values of current through the Helmholtz coils. The magnetic field intensities corresponding to these currents were calculated using the 3D simulation and are shown in figure 33. Obtaining the storage time from the experimental data by fitting the data with exponential decay curves reveals that the storage time is independent on the magnetic field within the range of experimental error for fields up to 21 mT. The differences in the total number of trapped ions are caused by varying detection efficiency for the ions due to the magnetic field. This confirms our expectation that the storage of ions should not be greatly influenced by the magnetic field.

6.6.2 *Detection of Electrons*

For tests of the electron detection, again the O^- ions were used with the same operating conditions $\Omega/2\pi = 7$ MHz, $V_0 = 20.5$ V. Electromagnet currents were 2 A on the axial coils and 1.6 A on the bending coil, which corresponds to 14 mT field in the trap.

A 660 nm laser beam from a laser diode was used detach the electrons from the trapped ions. The 200 mW laser beam was going through the apparatus along the trap axis.

The laser beam was switched on for 145 ms with a 18 ms delay after filling the trap. The electrons were detected using the MCP detector

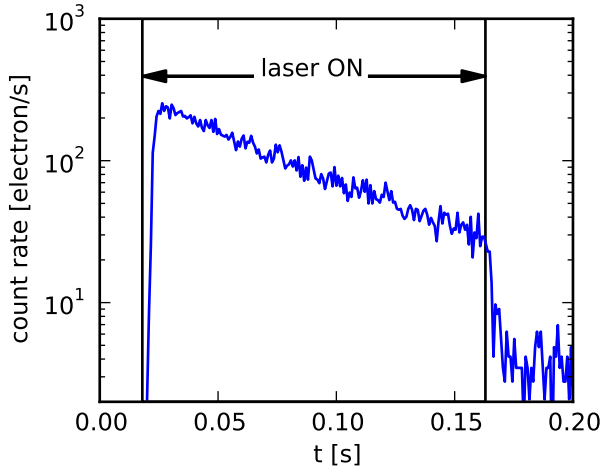

Figure 34: Detection of the photodetached electrons using a multichannel scaler

and their arrival times were recorded using the multichannel analyzer in the multichannel scaler mode. (see section 6.1 for description of the detection system). The recorded electron production rate is shown in figure 34. The electrons were produced at a rate exceeding 100 electrons per second, which is more than two orders of magnitude above the dark count of our detection system.

Under the same conditions, the ion signal was also measured by the conventional method of extracting the ions to the detector with variable time delays. The ion counts with and without the laser beam are shown in figure 35. The exponential decay rates R_{on} and R_{off} for ions with and without laser were obtained from exponential fits. The expected number of produced electrons is then given by

$$[e^-] = [O^-]_0 \frac{R_{on}}{R_{on} + R_{off}} \left(1 - \exp(-(R_{on} + R_{off})t)\right), \tag{147}$$

where $[O^-]_0$ is the initial number of O^- at the time of switching on the laser. This expected quantity is plotted in figure 35 in comparison with the electron signal. The electron signal in the plot is multiplied by 0.5 to account for the detection efficiency, but the slope of the curve is in a very good agreement with the prediction.

6.6.3 *Measured Spectra*

After the test measurements confirmed that the electron detection and ion confinement in the magnetic field work as expected, the machine was assembled into its full configuration. The retarding electrodes (ES2, ES3, and ES4, see figure 10) were mounted according to the figure 12. Electrons from the laser photodetachment of O^- were used for our calibration tests. The laser wavelengths and corresponding electron energies used in our tests are summarized in the table 2.

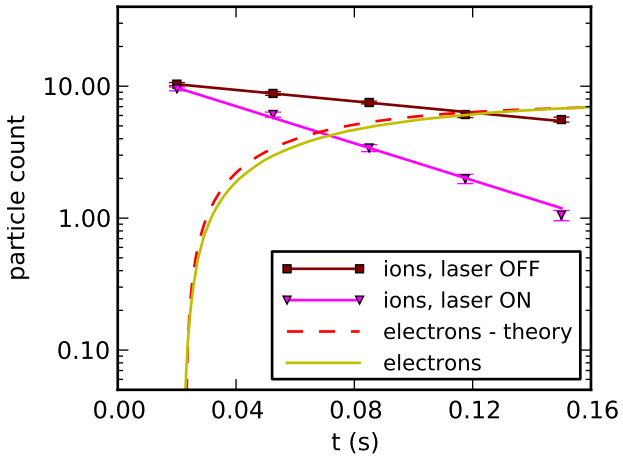

Figure 35: Combined measurement of ion loss and electron production. Theoretical electron production obtained from the ion decays is indicated by the dashed line. the cumulative sum of detected electrons (figure 34) is multiplied by a factor accounting for the different detection efficiency.

Our experimental procedure starts with extracting the ions from the ion source and filling the trap with ions. After a 50 ms delay (thermalization phase), the laser beam is switched on for another 100 ms (photodetachment phase). The detection system is gated and only the signal produced during the photodetachment phase is counted. The exact timing was varied and only the typical values are given. This procedure is repeated with a typical repetition frequency 2 Hz. The typical count rates of detached electrons are in the range 50–500 per second.

The voltages applied to the electrodes are in accordance with the design described in the section 6.2: $U_{ES2} = 0.3 \cdot U_B$, $U_{ES3} = U_B$, and $U_{ES1} = U_{ES4} = 0$ V. The reference "zero" voltage of the spectrometer can be varied. For the simplicity of the further discussion, we define the barrier potential relative to the octopole DC potential, so that it corresponds to the electron energy.

The initial measurements of the electron spectra were carried out at the same RF operating conditions as the test measurements for ion confinement and electron detection, i. e., $\Omega/2\pi = 7$ MHz, $V_0 = 20.5$ V. However, at these conditions, the spectrum obtained by differentiation of the retarding curve was strongly distorted. The peaks from the red and green laser were wider than 1 V. It was suspected that this broadening is caused by the interaction of the electrons with the RF field of the trap. In order to decrease the RF amplitude as much as possible, while still being able to store the ions, we had to decrease also the RF frequency according to the adiabatic theory (see section 5.1.3). The spectra obtained after decreasing the RF frequency to 6 MHz and the RF amplitude to 12.8 V are shown in figure 36. The

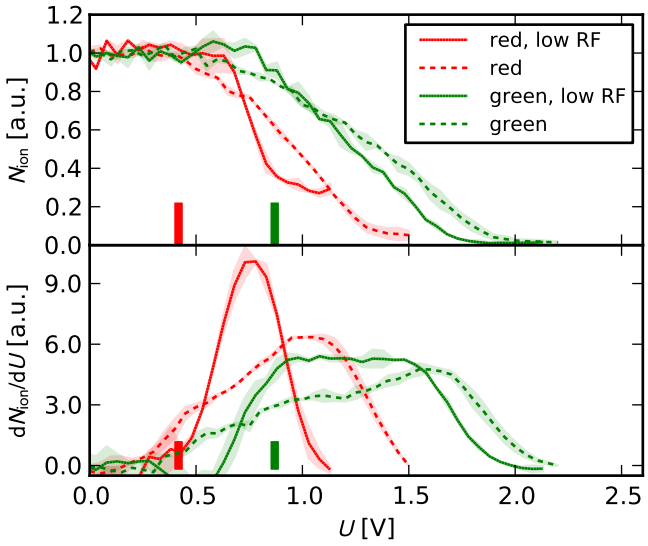

Figure 36: Effects of RF amplitude on the photodetached electron spectra from O^-. The measurements with amplitudes $V_0 = 12.8$ V and $V_0 = 10$ V are indicated by the dashed and solid lines respectively. RF frequency $\Omega/2\pi = 6$ MHz was used for both measurements. The theoretical positions of the peaks are indicated by the colored bars.

effective potential produced by the RF field with amplitudes below 12.8 V was not strong enough to trap the initially hot ions injected from the ion source. In order to decrease the amplitude further, a modulation of the RF amplitude was implemented, which allows us to use a higher amplitude in the initial thermalization phase and a lower amplitude in the photodetachment phase. Decreasing the amplitude further, slightly below 10 V, lead to a significant improvement in the resolution of the measured spectra, as indicated in figure 36.

Another effect observed in our preliminary measurements is the influence of the laser pointing on the shape of the spectrum. This effect in general indicates that the location of the electron formation influences the measured electron energy. Small variations on the order of $\lesssim 100$ mV can be attributed to static patch fields on the surface of the octopole electrodes as discussed in the section 6.5. However, the large effects on the scale of 1 V, which are shown in figure 37 are most likely caused by the interaction of the electrons with the RF field. Comparing the retarding curves in figure 37 indicates that at one position (the dashed line), there is a population of electrons with energies high above the expected energy—even above our measurement range. Changing the laser focus position reduced the energy of these electrons significantly (solid line in figure 37). These accelerated electrons now appear as a second peak in the electron spectrum at ≈ 2.3 V. Similar acceleration of electrons to high energies by the RF is observed in our simulated spectra in figures 29 and 30.

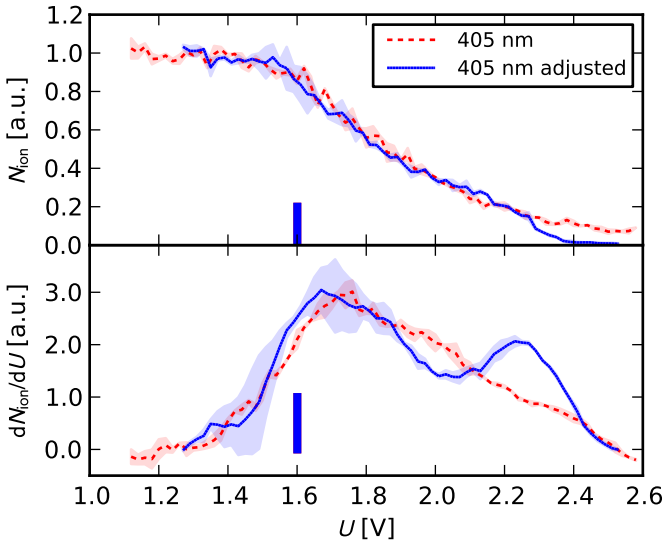

Figure 37: Effects of adjusting the laser focus position. Two spectra of photodetached electrons which differ in the laser focus position are shown. Otherwise identical operating conditions are used: $V_0 = 9.6$ V; $\Omega/2\pi = 6$ MHz.

Finally, the spectra of the photodetached electrons produced by the three available wavelengths (see table 2) are compared in figure 38. The figure demonstrates that the current energy resolution is approximately 20 %. The offset of the peaks in comparison with the theoretical positions is caused by the interaction of the electrons with the RF field with a possible contribution of the contact potential between the octopole and the electrostatic filter.

6.7 CONCLUSION

In this chapter we have shown the design of a novel apparatus for measuring the energy of electrons produced in the RF trap. The electron spectrometer was designed to match our current ion trapping equipment. The possibility of combining the RF ion trap with the magnetic field of the spectrometer was predicted by numerical simulations and experimentally confirmed. The electromagnetic fields of the spectrometer were also designed with help of computer models. The first detection of electrons and measurements of electron spectra prove the feasibility of our goals. The energy resolution of our preliminary measurements is limited to approximately 20 %. Comparing the measured spectra with our simulations indicates that the electron energy is influenced by the RF field. There are several strategies available to improve the energy resolution. The symmetricity of the RF field on the rods has already been verified. Further plans consist of mounting a new exit electrode–aperture on the octopole, which will

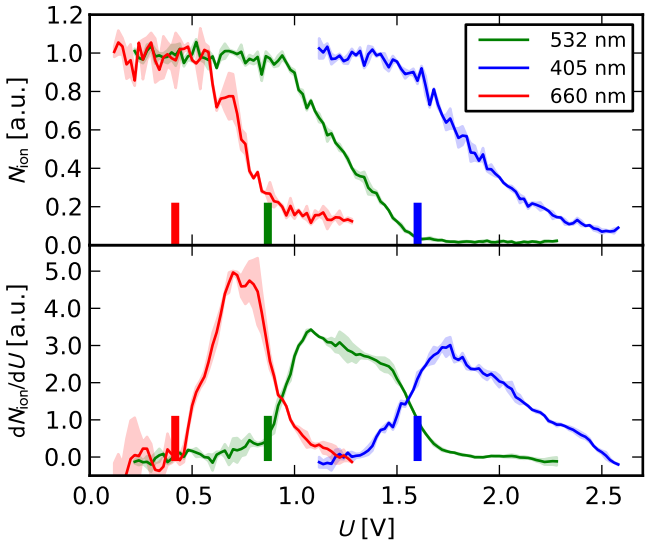

Figure 38: Comparison of the measured electron spectra from the O^- photodetachment by lasers with three different wavelengths. The theoretical positions of the peaks are indicated by the colored bars.

select only the less disturbed electrons close to the axis. An additional effect of this electrode will be the shielding of the RF field from the end of the octopole. Furthermore, an inspection of the mechanical accuracy and possibly also a mechanical cleaning of the octopole rods (see Gerlich, 1992, p. 75) will be carried out. Ideally, using a higher order multipole trap should reduce the sensitivity of the electrons to the RF field. However, the construction of such an apparatus would be significantly more difficult. There are no plans for switching to a higher order multipole trap, because the present resolution is sufficient to resolve the major characteristics of the electron spectra from the associative detachment and study the possible isotopic effects.

7

MEASUREMENT OF THE $H^- + H$ RATE COEFFICIENT

This chapter describes the measurement of the reaction rate coefficient of the $H^- + H$ associative detachment

$$H^- + H \rightarrow H_2 + e^- \,. \tag{4}$$

The results of the experiment and the description of the experimental setup are published by Gerlich et al., 2012. Additional measurements used for the absolute and relative calibration of the measurement are presented by Roučka et al., 2011; Jusko et al., 2011b. Here, only a brief review of the experiment and auxiliary measurements is presented. For more information, refer to the publications.

7.1 EXPERIMENTAL

Our experimental setup is based on a 22-pole RF ion trap (Gerlich, 1992; Gerlich and Horning, 1992; Gerlich, 1995) in combination with an effusive beam source of atomic hydrogen. The machine is called AB-22PT, which stands for *atomic beam combined with 22-pole trap*. This apparatus was built at the Chemnitz University of Technology and is described in publications by Borodi et al., 2009; Plasil et al., 2011; Gerlich et al., 2011. The configuration used in our experiment is presented schematically in figure 39. The ion trap is shown in more detail in figure 40.

The H^- ions are produced in a storage ion source (Gerlich, 1992) by the electron bombardment of the the H_2 precursor gas. After thermalization in the ion source to energies of the order of 100 meV, the ions are mass selected using a quadrupole mass filter and injected into the

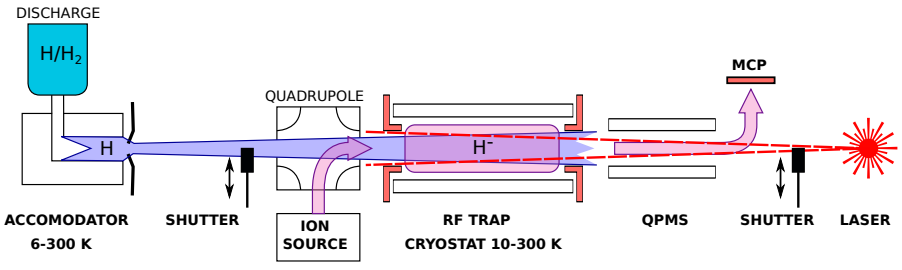

Figure 39: Schematic drawing of the AB-22PT apparatus. Components from left to right: discharge source of H, ion source, ion trap, ion detection system, laser for photodetachment experiments. The dimensions are not to scale.

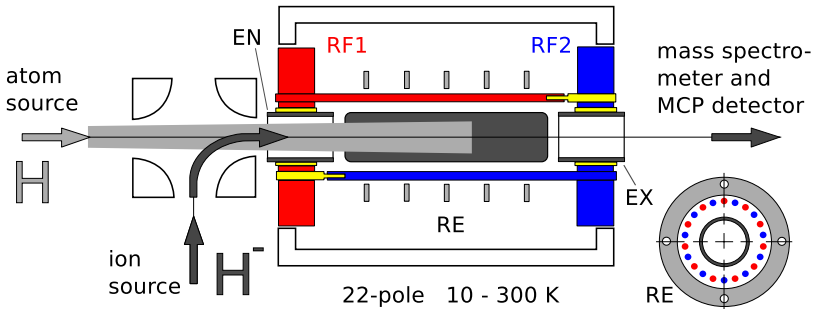

Figure 40: Detailed view of the interaction region, reprinted from Gerlich et al., 2012

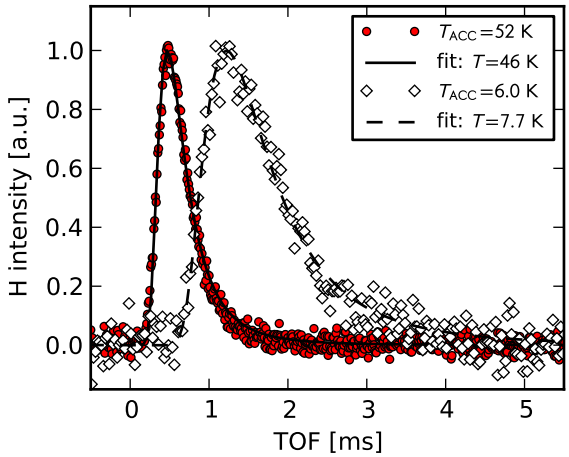

Figure 41: TOF distributions of H atoms at different accommodator temperatures in comparison with the Maxwell distribution.

22-pole trap. The ion trap temperature T_{22PT} is variable in the range 10 K $< T_{22PT} <$ 300 K. Ions are cooled down close to the trap temperature by collisions with the H_2 buffer gas. The agreement between the trap temperature and the ion temperature was studied by action spectroscopy for heavier ions (Glosík et al., 2006) and by numerical simulations for ions with mass 1 amu (Asvany and Schlemmer, 2009). We estimate the upper limit for ion temperature to be 5 K above the trap temperature.

The H atoms are produced by the dissociation of the H_2 in an RF discharge. A cold effusive beam is then formed by flowing the partially dissociated hydrogen through a cold nozzle (accommodator) with temperature in the range 6 K $< T_{ACC} <$ 300 K. The energy distribution of the hydrogen atoms was obtained by measuring the *time of flight* (TOF) distribution of a chopped H beam. The measured distributions displayed in figure 41 are in a good agreement with the maxwellian distribution. The fitting functions for the analysis of the TOF spectra were obtained by convolving the ideal maxwellian TOF distribution with a function representing the opening of the shutter.

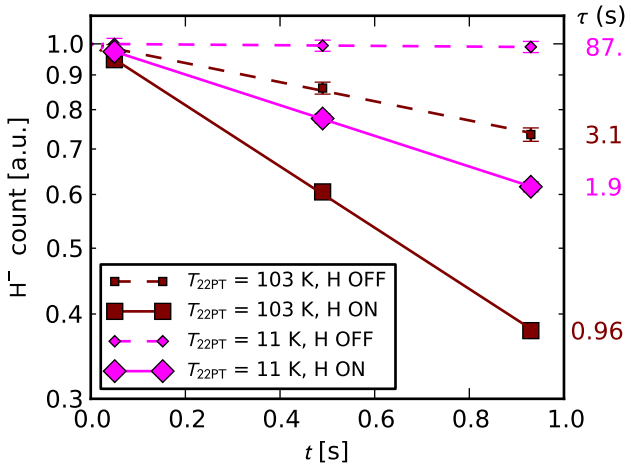

Figure 42: Examples of measured decays and corresponding exponential fits at $T_{ACC} = 50$ K. The smaller symbols and dashed lines indicate measurements and fits with the H beam off, whereas the larger symbols and solid lines correspond to measurements with the H beam on. The decay time τ obtained from each fit is displayed on the right side of the graph. Statistical errors indicated by the error bars are smaller than the symbol size in some cases.

The temperature of the beam differs from the accommodator temperature by up to 20 % at low temperatures, which defines the accuracy of determining the beam temperature during measurements. At higher temperatures, the accuracy of the analysis is limited by the accuracy and resolution of the chopper timing, which causes a slight underestimate of the temperature displayed in the figure 41. A mechanical shutter was used for switching the H beam during measurements.

7.2 MEASUREMENT PROCEDURE

A standard experimental procedure for examining the ion-neutral reactions in the trap was used (see e.g. Gerlich, 1992; Gerlich and Horning, 1992; Gerlich, 1995). It starts with a pulsed extraction of the primary ions from the storage ion source. Ions of the desired mass are then selected using a quadrupole mass filter and injected into the 22-pole trap. The trap is closed by pulsing an electrostatic entrance electrode (EN, see figure 40). After a certain trapping time, the ions are extracted from the trap using a pulsed exit electrode (EX) and analysed using a second quadrupole mass filter. This procedure is applied repeatedly for different trapping times and product masses tuned on the second quadrupole until a sufficient signal is accumulated.

The measurements are always carried out with the H atom beam ON and OFF as illustrated in the figure 42. The loss rates R are obtained from exponential fits to the data. The decay time ($\tau = 1/R$) of

H^- ions in the trap when the H beam is OFF is determined mainly by reactions with impurities. At higher temperatures ($T_{22PT} \approx 100$ K) the residence time is of the order of seconds, whereas at lower temperatures ($T_{22PT} \lesssim 40$ K), it is of the order of minutes—much longer than the typical 1 s trapping time used in the present experiment. The reaction rate is then obtained by subtracting the loss rate with the H beam OFF from the loss rate with the H beam ON.

7.3 INTERACTION TEMPERATURE

In our experiment we study the interaction of two ensembles of particles with temperatures T_1 and T_2. We will show that this is equivalent to a thermal ensemble at a single temperature. Let us define the three-dimensional normal distribution centered at zero with variance σ^2 as

$$\mathcal{N}(\boldsymbol{x}|\sigma^2) = \frac{1}{(2\pi\sigma^2)^{3/2}} \exp\left(-\frac{x^2}{2\sigma^2}\right). \tag{148}$$

The Maxwell velocity distribution of particles with mass m_1 and temperature T_1 is then $f(\boldsymbol{v}) = \mathcal{N}(\boldsymbol{v}|k_B T_1/m_1)$. The relative velocity distribution f_{rel} is a convolution of the velocity distributions

$$f_{rel}(\boldsymbol{v}_{rel}) = \mathcal{N}\left(\boldsymbol{v}_{rel}\middle|\frac{k_B T_1}{m_1}\right) * \mathcal{N}\left(\boldsymbol{v}_{rel}\middle|\frac{k_B T_2}{m_2}\right) \tag{149}$$

Convolving two normal distributions produces a normal distribution with a sum of variances, i. e.,

$$f_{rel}(\boldsymbol{v}_{rel}) = \mathcal{N}\left(\boldsymbol{v}_{rel}\middle|\frac{k_B T_1}{m_1} + \frac{k_B T_2}{m_2}\right). \tag{150}$$

If $T_1 = T_2 = T$, the resulting variance is $\sigma^2 = k_B T(m_1 + m_2)/m_1 m_2$. The equation (150) can be formally rewritten into the same form:

$$f_{rel}(\boldsymbol{v}_{rel}) = \mathcal{N}\left(\boldsymbol{v}_{rel}\middle|k_B T_{kin}\left(\frac{m_1 + m_2}{m_1 m_2}\right)\right), \tag{151}$$

where T_{kin} defines the interaction temperature

$$T_{kin} = \frac{T_1 m_2 + T_2 m_1}{m_1 + m_2}. \tag{152}$$

The velocity distribution of the effusive beam can be understood as a conical subset of the Maxwell distribution. Thanks to the spherical symmetry of the Maxwell distribution, the conclusion applies also to the interaction of the trapped particles with the effusive beam. As discussed earlier, the H^- and H temperatures are close to the trap and accommodator temperatures respectively. Therefore, we can write the interaction temperature of the $H^- + H$ reaction as

$$T_{kin} = \frac{T_{ACC} + T_{22PT}}{2}. \tag{153}$$

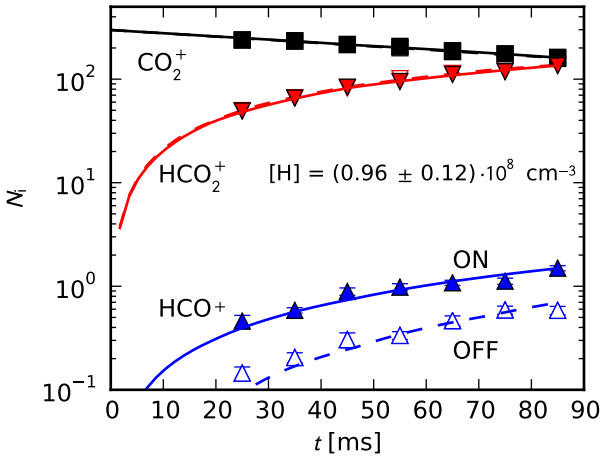

Figure 43: Reaction of CO_2^+ with H_2 and H. The full and open symbols denote the measurements with the H beam ON and OFF. The difference is visible only in the signal of HCO^+.

7.4 H BEAM CALIBRATION

The rate of reaction $R = \dot{N}_i/N_i$ is given by $\int_{\mathbf{r}} k(T_{kin}) n_i(\mathbf{r}) n_H(\mathbf{r})\, d\mathbf{r}/N_i$, where N_i is the number of ions in the trap, $k(T)$ is the thermal rate coefficient, and n_H and n_i are the hydrogen and ion densities respectively. Factoring out the rate coefficient, we can express the rate as

$$R = k(T_{kin}) N_H\,, \qquad N_H = \int_{\mathbf{r}} n_H(\mathbf{r}) \frac{n_i(\mathbf{r})}{N_i}\, d\mathbf{r}\,, \tag{154}$$

where N_H is the effective H atom density determined by the spatial overlap between the atomic beam and the ion distribution. A standard method for determination of N_H is the chemical probing with CO_2^+ (see Borodi et al., 2009). The CO_2^+ ion reacts with H and H_2 mainly by these reactions (Borodi et al., 2009):

$$CO_2^+ + H \rightarrow HCO^+ + O, \quad k_1 = 4.5{\cdot}10^{-10}\ \mathrm{cm^3\ s^{-1}}, \tag{155}$$

$$CO_2^+ + H_2 \rightarrow HCO_2^+ + H, \quad k_2 = 9.5 \left(\frac{T}{300\ \mathrm{K}}\right)^{-0.15} {\cdot}10^{-10}\ \mathrm{cm^3\ s^{-1}}. \tag{156}$$

To determine the effective H density, we measure the rate of HCO^+ production with the atomic beam ON and OFF (blocked by the shutter) as indicated in the figure 43. The H density is obtained by a least squares fit of the data with a numerical solution of the chemical kinetics equations. The fitting parameters are $[H_2]$, $[CO_2^+]_0$, N_H, and loss due to impurities. This procedure is also described by Jusko et al., 2011b.

When applying the calibrated H atom density to the analysis of measurements at different conditions, such as using the CO_2^+ calibration for measurements with H^-, one has to account for the sensitivity

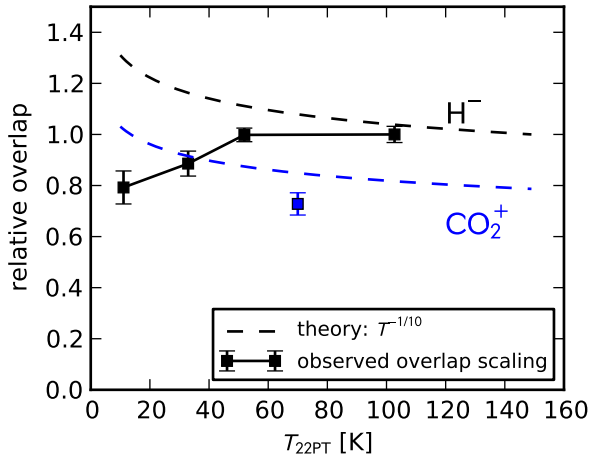

Figure 44: The experimentally determined overlap factor in comparison with theory.

of N_H on the shape of the ion cloud. In our configuration, the radius of the H beam, r_H, is limited by the trap entrance electrode and is smaller than the diameter of the ion cloud d_i. Due to the nature of the 22-pole effective potential, we can assume that the beam passes through a radially homogeneous part of the cloud.

The relative ion density on axis n_i/N_i is inversely proportional to the ion cloud cross section area. Therefore, as the ion cloud radius is varied, the overlap with the beam changes and the effective H atom density is proportional to d_i^{-2}. It follows from equation (118) that the theoretical scaling with our experimental parameters is

$$N_H \sim \frac{1}{d_i^2} \sim \left(\frac{T_i m_i}{V_0^2}\right)^{-\frac{1}{10}}, \tag{157}$$

where T_i is the ion temperature, m_i is the ion mass, and V_0 is the RF amplitude. The scaling with amplitude was confirmed experimentally and then used to correct the N_H determined by the chemical probing with CO_2^+ for the effect of the different ion masses and RF amplitudes. However, it was observed in our measurements that the scaling with temperature deviates strongly from the theory. The scaling was determined experimentally by two independent procedures, which are described by Roučka et al., 2011 in detail. First, by comparing the AD rate measurements carried out at the same interaction temperature T_{kin} with different combinations of T_{22PT} and T_{ACC}. Second, by measuring the temperature dependence of the photodetachment rate with a broad laser beam, which should have the same overlap scaling as the atomic beam. Examples of the experimentally determined scaling in comparison with the theoretical curve are shown in figure 44. The discrepancy can be qualitatively explained by the presence of patch fields on the electrode surfaces. See the attached paper (Roučka et al., 2011) for details.

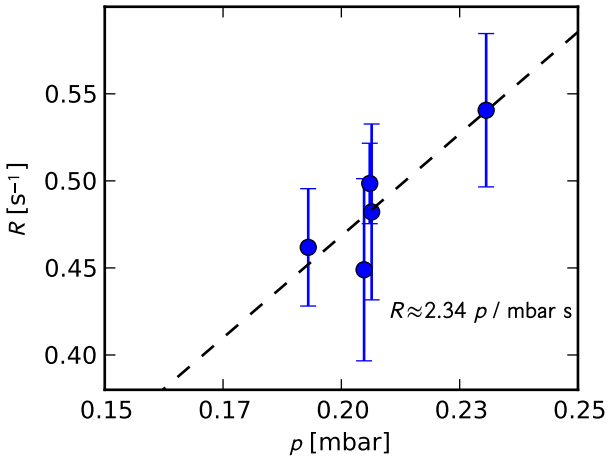

Figure 45: Linear dependence of the H^- decay rate on the discharge pressure.

The calibration measurement was carried out at a single temperature interaction temperature of approximately 50 K. After applying the correction for different masses to the N_H measured by the chemical probing with CO_2^+, we have obtained the effective H atom density in the H^- cloud as

$$N_H = (1.3 \pm 0.6) \cdot 10^8 \, cm^{-3} \, . \tag{158}$$

The 45 % error estimate is determined mainly by the 40 % uncertainty in the known rate coefficient k_1 for production of HCO^+ (Borodi et al., 2009). The additional experimental uncertainty 20 % is obtained by adding in squares the standard deviation of multiple measurements and the estimated reproducibility of the hydrogen beam density.

7.5 AUXILIARY MEASUREMENTS

During the measurements, multiple precautions were taken to avoid any systematic errors. The stability of the RF discharge for the production of atomic hydrogen was checked by continuous monitoring of the intensity of the optical emission lines. In our experimental conditions, a linear dependence of the effective hydrogen density on the discharge pressure was observed as indicated in the figure 45. Therefore, the discharge pressure was kept stable within few percent. Small variations, which were unavoidable due to the thermal sensitivity of the leak valve, were corrected by normalizing the data with the discharge pressure, which was measured for each rate data point.

The short term stability of the experimental conditions was verified by a statistical analysis of the measured data. The number of detected ions under certain stable experimental conditions is randomly distributed according to the Poisson distribution. In our experiment,

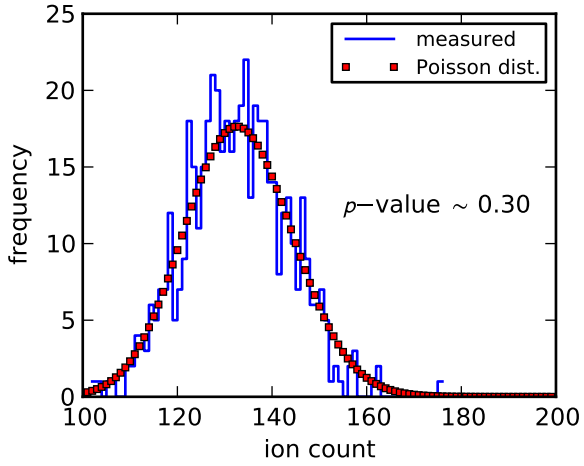

Figure 46: The measured ion count distribution (510 measurements) in comparison with the Poisson distribution. Compatibility with the Poisson distribution tested by the two-sided Pearson's χ^2-test with resulting p-value $p = 0.30$.

every point is measured repeatedly to accumulate the sufficient data. This allows us to check the compatibility of the measured particle counts with the Poisson distribution by the Pearson's χ^2 test. An example of the measured ion count distribution compared to the Poisson distribution is shown in figure 46. The two-sided p-value of all our measurements was calculated and it was verified that the p-value is uniformly distributed in the interval $[0, 1]$. This further confirms that there are no significant drifts or oscillations during a single measurement.

7.6 DATA ANALYSIS AND RESULTS

The temperature dependence of the reaction rate coefficient was measured by varying the 22-pole temperature in a range $10\ \mathrm{K} < T_{22PT} < 150\ \mathrm{K}$ with fixed accomodator temperature. The upper limit on T_{22PT} is caused by the presence of impurities at higher temperatures. Due to the kinematic averaging, a reaction temperature range of 70 K can be measured at a single T_{ACC}. The total measurement range was extended by measuring at three different T_{ACC}: 10 K, 50 K, and 120 K. This way, a number of uncalibrated datasets was obtained, each spanning a temperature range of 70 K. The correction of the overlap scaling, described in section 7.4, was applied to all the datasets. Using the chemical probing, the N_H for two of our datasets was obtained. These directly calibrated datasets are shown in the figure 47. Then, all the datasets were reduced by binning, which is indicated in the figure 48. A multiplicative factor which minimizes the squared differences between the uncalibrated and calibrated data was found for

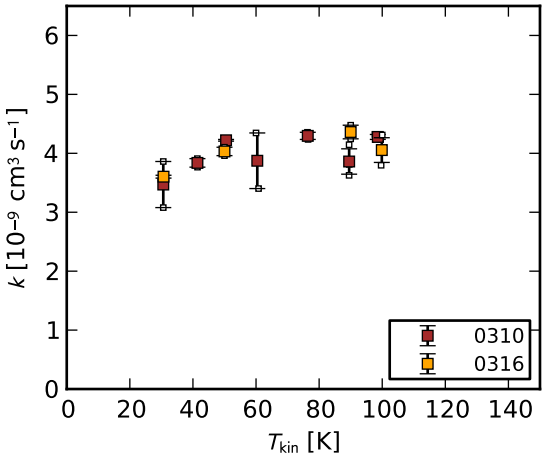

Figure 47: Calibrated datasets measured at the same conditions as the calibration reaction in figure 43.

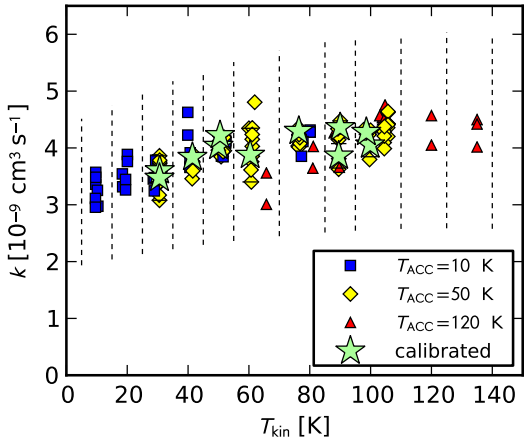

Figure 48: Overview of all measured data. The binning of the data used in the analysis is indicated

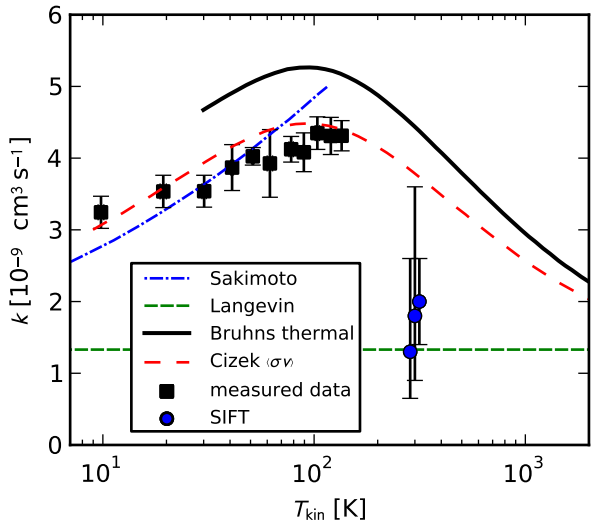

Figure 49: Measured data (squares) in comparison with thermal rate coefficient calculated from merged beam data by Kreckel et al., 2010; Bruhns et al., 2010 (error estimate 26 %,multiplied by 1.086 to account for later calibration improvements by Miller et al., 2011). Round points indicate (from left to right) the flow tube measurements at 300 K by Schmeltekopf et al., 1967, Fehsenfeld et al., 1973, and Martinez et al., 2009 respectively (points are shifted in temperature for better readability). Our statistical error is indicated by error-bars. Theoretical results of Čížek et al., 1998 and Sakimoto, 1989 and the Langevin limit are shown for comparison.

each uncalibrated dataset. This way, the calibration was extended to the range of collision temperatures $T_{kin} = 10$–135 K.

The calibrated data were reduced by binning. The final results in comparison with previous measurements and theory are plotted in the figure 49. The error-bars represent the standard deviation of our data points. The figure shows that our results are in a good agreement with the theory of Čížek et al., 1998. At higher temperatures, where the theory of Čížek et al., 1998 differs significantly from the theory of Sakimoto, 1989, our data support the theory of Čížek et al., 1998. This was expected, because the theory of Sakimoto, 1989 is specialized for low energies ($< 10^{-2}$ eV).

Although our measurements cannot be directly compared to the flow tube measurements due to the different temperatures, our agreement with the theory and the merged beam experiment in the overlapping temperature range suggests that the merged beam results are correct also at 300 K. This indicates a possible systematic error in the flow tube measurements. It has been pointed out that a possible source of this systematic error is the rate constant of the AD reaction of $H + Cl^-$, which was used for calibration of the H concentration by the flow tube measurements. However, Martinez et al., 2009 used

the AD reaction of $H + OH^-$ as a complementary calibration method with a result $k = (1.7 \pm 0.2) \cdot 10^{-9}$ cm^3 s^{-1}.

7.7 CONCLUSION

We have independently measured the absolute value of the thermal rate coefficient in a yet unexplored temperature range. Our results are in a good agreement with theories of Čížek et al., 1998 and Sakimoto, 1989. In the overlapping temperature range our results agree within the systematic error with the results of Kreckel et al., 2010. However, the presented values are slightly lower than those of Kreckel et al., 2010 and the current systematic uncertainty in combination with the limited temperature range do not allow us to rule out the flow-tube results completely. Further measurements with a more accurate calibration reaction in a broader temperature range are planned as described by Gerlich et al., 2012. Further studies of the $H^- + H$ AD are planned, including measurements of the isotopic effects and product energy distributions.

8

ELECTRON KINETICS IN THE AFTERGLOW PLASMA

There are two plasmatic afterglow experiments being operated in the Laboratory of elementary processes in plasma at the Charles University in Prague. These experiments are used to investigate the process of electron-ion recombination at low temperatures. In this work, we analyze the methods used to produce the thermal plasma at temperatures T = 40–300 K. We will pay special attention to the processes involved in the cooling of electrons and to their possible influence on the mechanism of collisional radiative recombination.

One of the experiments involved is the flowing afterglow with Langmuir probe (FALP) experiment, which is schematically shown in figure 50. In the FALP, the plasma is produced by a microwave discharge in a glass tube upstream from the metallic flow tube. The decaying plasma (afterglow) is then carried by a carrier gas through the flow tube and the electron density is measured by a Langmuir probe along the tube. The tube is cooled by a liquid nitrogen bath or by a closed cycle helium refrigerator in the newer design (See Kotrík et al., 2011a; Kotrík et al., 2011b for description of the relevant experiments).

The other experiment is the stationary afterglow with cavity ring-down spectrometer (SA-CRDS). There, a pulsed microwave discharge is ignited directly inside a liquid-nitrogen-cooled glass tube. The experiment is schematically displayed in figure 51. Thanks to the higher initial electron concentrations and the smaller diameter of the tube, the time scale of the afterglow is much shorter than in the FALP. Therefore, the afterglow can be considered stationary, despite the similarity of the gas velocities to the FALP apparatus. The evolution of concentrations of ions is monitored by the cavity ring-down spectrometer (CRDS) (Macko et al., 2004), which is a highly sensitive absorption spectrometer capable of determining the absolute densities of ions in specific rotational states.

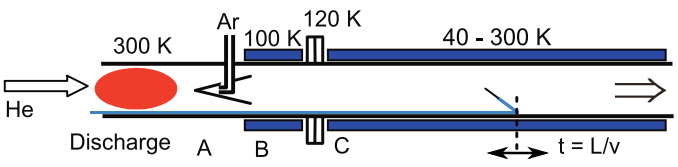

Figure 50: Schematic drawing of the FALP experiment

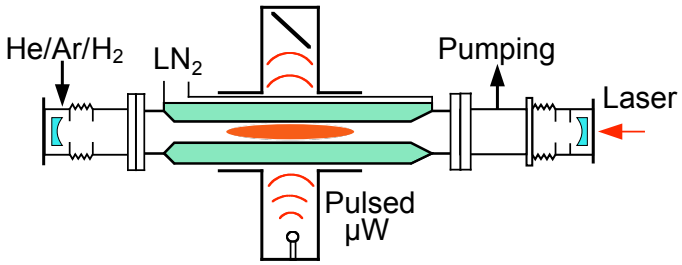

Figure 51: Schematic drawing of the SA-CRDS experiment

The results of both FALP and SA-CRDS are analyzed by fitting the measured decays of electron density with a theoretical curve, which is a solution to the balance equation

$$\frac{dn}{dt} = -K_3 n^3 - \alpha_{eff} n^2 - \frac{n}{\tau_D} . \tag{159}$$

The n stands for the number density of ions or electrons, K_3 and α_{eff} are effective ternary and binary recombination rate coefficients, and τ_D is the effective diffusion time constant. The validity of this equation is discussed in section 8.2.

In particular, in our studies of H_3^+ recombination in helium buffer gas, it was observed that the K_3 is zero within the margin of error (see section 8.5). The effective diffusion time constant is determined from the ambipolar diffusion time and from the rate of effective unary reactions with impurities as described by equation (173). The effective binary coefficient of H_3^+ recombination can be expressed as (Glosík et al., 2009)

$$\alpha_{eff} = \alpha_{bin} + K_{He}[He] , \tag{160}$$

where α_{bin} is the true binary recombination coefficient and K_{He} is the ternary helium-assisted recombination coefficient. Recently, the dependence of the recombination coefficients on the nuclear spin state was studied and state-specific recombination coefficients of ortho- and para-H_3^+ were measured for the first time using the SA-CRDS apparatus (Dohnal et al., 2012b; Dohnal et al., 2012a; Varju et al., 2011). The coefficients were obtained by comparing the results of the measurements obtained in the *normal* and *para-enriched* hydrogen. For details of the experiment refer to Dohnal et al., 2012a; Hejduk et al., 2012.

8.1 COOLING OF THE CARRIER GAS

The first step necessary for producing a cold afterglow plasma consists of cooling down the carrier gas, which in our experiments is helium. In the FALP experiment, the flow velocity v in the cold region is typically several meters per second. At these conditions, the

symbol	value	unit	description
ρ		$\mathrm{kg\,m^{-3}}$	gas density
v		$\mathrm{m\,s^{-1}}$	flow velocity
d		m	tube diameter
μ	ρv	$\mathrm{Pa\,s}$	dynamic viscosity
ν		$\mathrm{m^2\,s^{-1}}$	kinematic viscosity
β		$\mathrm{K^{-1}}$	volumetric thermal expansivity
T_g		K	gas temperature
T_w		K	wall temperature
g		$\mathrm{m\,s^{-2}}$	standard gravity
k		$\mathrm{W\,m^{-1}\,K^{-1}}$	thermal conductivity
C_p		$\mathrm{J\,kg^{-1}\,K^{-1}}$	isobaric specific heat capacitance
$\mathbf{q}$		$\mathrm{W\,m^{-2}}$	heat flux
h		$\mathrm{J\,m^{-3}}$	volumetric enthalpy density

Table 3: Parameters of the gas cooling model.

flow time of the gas over the dimension of the flow tube is of similar magnitude as the thermalization time. Therefore, the forced flow needs to be included in the model of gas cooling.

The symbols of physical quantities used in the further discussion are shown in table 3. The character of the gas behavior can be qualitatively estimated from several dimensionless numbers (see for example Pitts and Sissom, 1998, p. 125 or any textbook on heat transfer for details). The *Reynolds number*, defined as

$$\mathrm{Re} = \frac{\rho v d}{\mu} \sim \frac{\text{inertial force}}{\text{viscous force}} \tag{161}$$

is used to determine, whether the gas flow is laminar or turbulent. For gas flowing in a pipe, the flow is laminar if $\mathrm{Re} \lesssim 2000$.

The onset of the natural convection, which is caused by the buoyancy forces, is described by the *Grashof number*, defined for a cylindrical pipe as

$$\mathrm{Gr} = \frac{g\beta(T_g - T_w)d^3}{\nu^2} \sim \frac{\text{buoyancy force}}{\text{viscous force}}\,. \tag{162}$$

In order to make a model of the gas cooling in the flow tube, it is necessary to determine whether the natural convection contributes significantly to the heat transfer in comparison with the forced convection. A criterion for estimating the influence of natural convection is based on comparing the Reynolds and Grashof numbers in a ratio

$$\frac{\mathrm{Gr}}{\mathrm{Re}^2} \sim \frac{\text{buoyancy force}}{\text{inertial force}}\,. \tag{163}$$

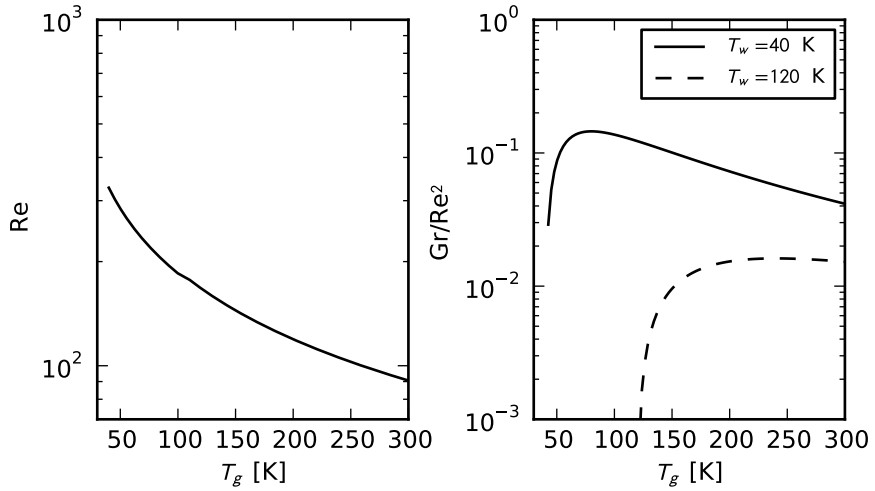

Figure 52: Dimensionless quantities Re and Gr/Re^2 as a function of the gas temperature. The Gr/Re^2 number is shown for two different wall temperatures.

The forced convection dominates the heat transport if $Gr/Re^2 \ll 1$ (Pitts and Sissom, 1998, p. 231).

The Reynolds and Grashof numbers were evaluated for the typical conditions in the flow tube. In the evaluation of the Grashof number, the isobaric value of the thermal expansion coefficient $\beta_p = 1/T$ is used. The temperature dependent quantities are evaluated at the average temperature $(T_g + T_w)/2$. The helium properties obtained from the NIST database (Lemmon et al., 2012) were used in the evaluation. The Reynolds number is plotted in the left panel of figure 52. The typical pressure of 300 Pa and a high flow velocity $v_0 = 10\ \mathrm{m\,s^{-1}}$ at $T_0 = 40$ K were used in the calculation. The tube diameter $d = 5$ cm. The velocity is scaled as $v(T) = v_0 T/T_0$, so that the curve corresponds to a constant gas flow. The typical flow velocities are smaller than this, therefore, the flow is always laminar in the FALP apparatus.

The ratio Gr/Re^2 is shown in the right panel of figure 52. Constant flow curves for low velocity flow at $v_0 = 10\ \mathrm{m\,s^{-1}}$ at $T_0 = 40$ K are shown. Two different wall temperatures T_w are shown. As can be seen from the figure, even at this low velocity the heat transport is still dominated by the forced convection, because $Gr/Re^2 \ll 1$.

Now that we know that the flow regime is laminar with a negligible natural convection, we can construct a simple model of the heat transport. The assumption of negligible convection can be made even stronger by completely neglecting the component of velocity perpendicular to the tube axis. In principle, a small component of perpendicular velocity can be present due to the thermal expansion of the warmer gas at the center against the colder gas close to the walls. This effect can only be expected to slightly speed up the cooling, be-

cause it would transport the heat towards the walls and slow down the propagation of the warm gas along the axis.

Neglecting this contribution in comparison to the faster forced convection leads to a significant simplification of the model. The velocity field can now be easily determined just from a requirement to match the known parabolic velocity profile in the isothermal regions far from the temperature transition. It is useful to express the velocity in terms of the mass flow $v\rho$, which is independent on temperature. The velocity of a fluid element with temperature T on radius r from the tube axis is then given by

$$v(r,T)\rho(T) = 2v_0\rho_0\left(1-\frac{4r^2}{d}\right), \tag{164}$$

where v_0 is a prescribed axial velocity and ρ_0 is the corresponding gas density at certain temperature and pressure.

The heat flux $\mathbf{q}$ in a static medium is given by the Fourier's law

$$\mathbf{q} = -k\nabla T\,. \tag{165}$$

In the Eulerian description of the flow, the heat transport by convection equals $\boldsymbol{v}h$, where the enthalpy h is given as $\rho C_p T$. Adding this term to the Fourier's law yields the governing equation of our problem

$$\mathbf{q} = -k\nabla T + \boldsymbol{v}\rho C_p T\,. \tag{166}$$

Since no major heat sources are present in the gas, we can apply the continuity equation for energy $\nabla\cdot\mathbf{q} = 0$, which leads to

$$\nabla\cdot(\boldsymbol{v}\rho C_p T) - \nabla\cdot(k\nabla T) = 0\,. \tag{167}$$

Now, in analogy to the methods for electromagnetism described in section 3, this equation is converted to the weak form. The solution $T \in V$ is defined as a function which satisfies the equation

$$\int_\Omega u\nabla\cdot(\boldsymbol{v}\rho C_p T)\,d\mathbf{r} + \int_\Omega \nabla u\cdot(k\nabla T)\,d\mathbf{r} = 0 \tag{168}$$

for all the test functions $u \in \hat{V}$, where the test and trial function spaces are defined as

$$\hat{V} = \{v \in H^1(\Omega) : v = 0 \text{ on } \partial\Omega\}, \tag{169}$$

$$V = \{v \in H^1(\Omega) : v = T_w \text{ on } \partial\Omega\}, \tag{170}$$

where T_w is the wall temperature. Since the thermal conductivity depends on temperature, this equation is nonlinear. It is solved iteratively using the Picard iteration with a constant temperature as initial estimate.

This equation was solved using the FEniCS software on a 3D cylindrical domain with the velocity field given by equation (164). The

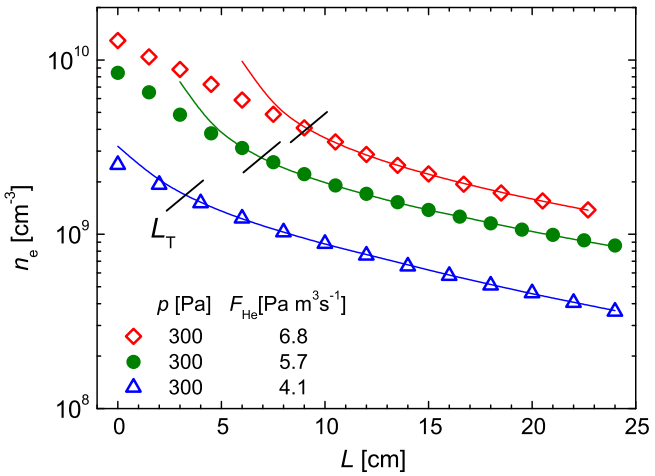

Figure 53: Measured electron density decay along the FALP flow tube at different flow rates. The flow rate is defined at 300 K as $F = p\Delta V/\Delta t$, where $\Delta V/\Delta t$ is the volumetric flow rate. The corresponding axial velocities at 77 K are 3.8 $m\,s^{-1}$, 5.3 $m\,s^{-1}$, and 6.1 $m\,s^{-1}$. Reprinted from Kotrík et al., 2011b.

boundary conditions were determined using an independent 2D thermal model of the flow tube (Kotrík, 2012).

The first calculations were motivated by the measurements of the Ar^+ collisional radiative recombination (CRR). Details of the CRR process will be described later in this chapter, but for now we just need to know that the CRR reaction coefficient is strongly dependent on temperature. Therefore, a good thermalization of the gas is necessary to obtain accurate measurement. Thanks to the strong thermal dependence of the rate coefficient, the onset of thermal conditions can be estimated in the data analysis—the measured data agree with the theoretical model (159) only in a range downstream from a certain point in the flow-tube. This fact is illustrated in figure 53 from Kotrík et al., 2011b: the points where the recombination starts to follow the theoretical curve move downstream with the increasing flow velocity.

This model was set up to confirm our hypothesis that the observed behavior is caused by a higher temperature of the carrier gas upstream. A simulation was prepared with parameters corresponding to the experimentally obtained data. The flow velocity on axis was calibrated by measuring the propagation of inhomogeneities in the plasma using the Langmuir probe (Kotrík et al., 2011b). The result of the simulation is shown in figure 54. The points where the gas thermalizes to the wall temperature with less than 10 % difference were obtained from the simulation as indicated in the figure 54. Positions of these points are also shown in figure 53 with the experimental data. The choice of the 10 % was quite arbitrary. However, the resulting spacing of the points does not strongly depend on this choice. The points obtained from the simulation coincide with the positions

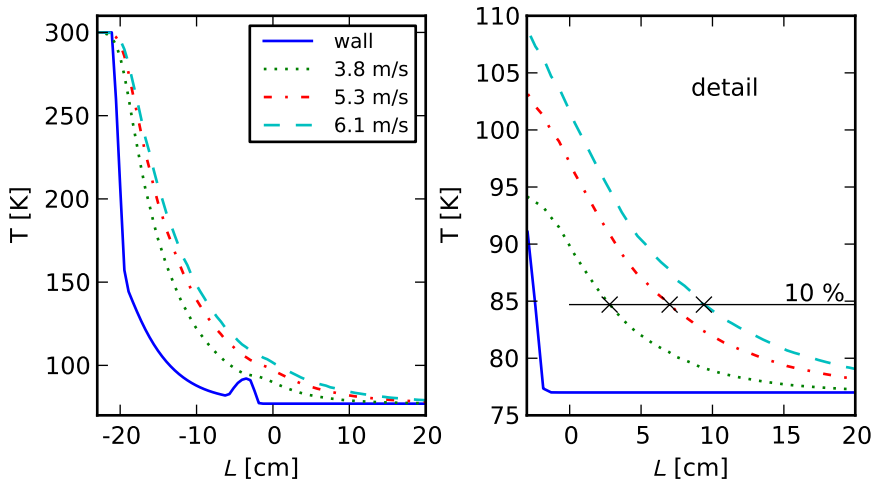

Figure 54: Calculated temperature of the carrier gas on axis. Axial flow velocities correspond to figure 53.

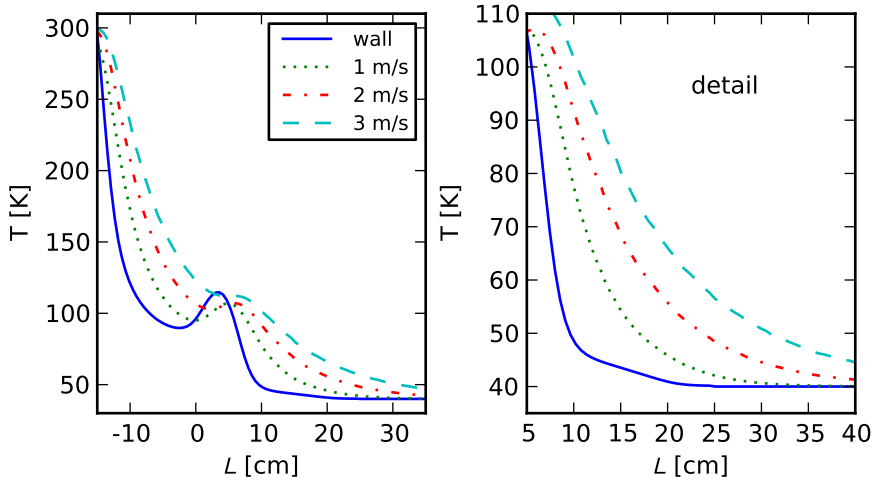

Figure 55: Calculated temperature of the carrier gas on axis for different axial flow velocities. Minimal wall temperature 40 K.

where the experimental curves merge with the fits. This indicates that the uneven gas temperature is a good explanation of the observed behavior.

The same model was also applied to the conditions of the newly built Cryo-FALP apparatus with helium refrigerator, where the flow tube can be cooled down to 40 K. At such conditions, the thermal conduction slows down significantly—the thermal conductivity data for helium from Lemmon et al., 2012 are well approximated by a power function of temperature with proportionality $k \sim T^{0.68}$. The model data obtained for some typical flow velocities are shown in figure 55. The model shows that low flow velocities about 2 $m\,s^{-1}$ are needed to achieve a reasonable thermalization of the gas. This is in a qualitative agreement with the observed behavior. However, the

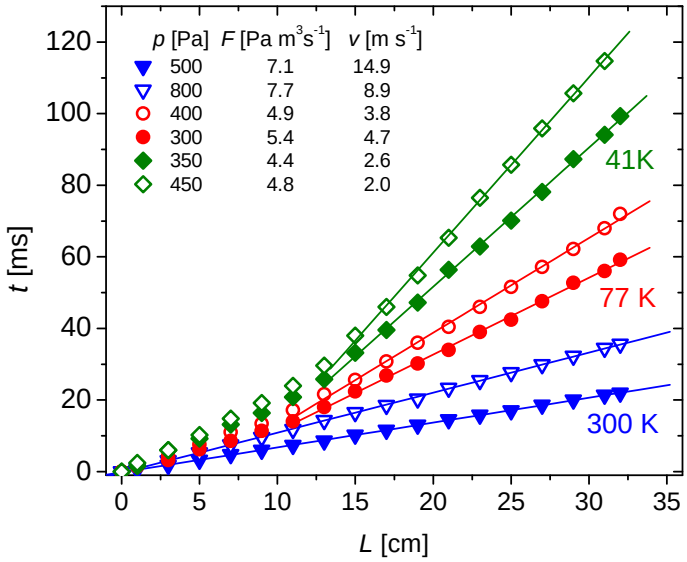

Figure 56: Velocity profiles measured at different temperatures of the flow tube. Reprinted from (Kotrík et al., 2011a).

measurements of the gas flow velocity indicate that the thermalization is achieved earlier than the model predicts. The thermalization can be estimated from the measurements of propagation of a plasma produced by a short discharge pulse. The measured time delays of the pulse along the flow tube are shown in figure 56. The measured velocity is stabilized (i. e., the delay is linear with L) approximately at $L > 15$ cm, whereas in the model the temperature is still very high. At these low temperatures and strong temperature gradients, the difference between the temperature on axis from the wall temperature is so big and the thermal conductivity so small that the heat transport associated with expansion of the warmer gas and compression of the cold gas at the walls becomes non-negligible. Nevertheless, our model provides a reasonable upper estimate of the temperature.

Finally, the cooling of gas in the SA-CRDS instrument was analyzed using our model. The thin glass discharge tube is immersed in liquid nitrogen bath from outside. The inner diameter of the tube is 12.8 mm. Results of the calculation for a relatively high flow velocity 10 $\mathrm{m\,s^{-1}}$ are shown in figure 57. The figure shows that the gas is perfectly thermalized in the discharge area, which starts approximately at $L = 15$ cm from the beginning of the cooled part. Actually, thanks to the small diameter of the tube, the gas is very well thermalized in less than 10 cm.

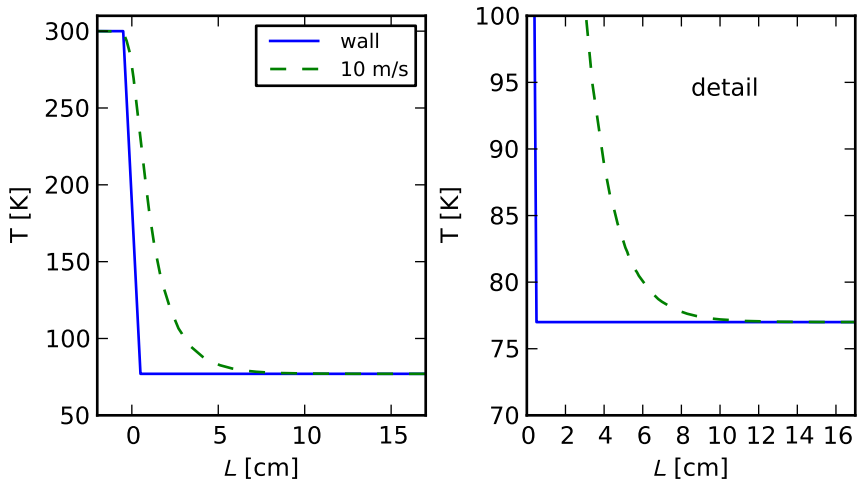

Figure 57: Calculated gas temperature along the SA-CRDS tube. The wall temperature is indicated by the solid line. The temperature on axis of the flowing gas is indicated by the dashed line.

8.2 DESCRIPTION OF THE ELECTRON RECOMBINATION

The evolution of the electron density n in the afterglow is given by the continuity equation with a source term and a diffusion term

$$\frac{\partial n}{\partial t} = S + \nabla \cdot D\nabla n\,, \tag{171}$$

where S is the source term and D is the coefficient of ambipolar diffusion. Assume that D is homogeneous and the recombination is driven by the effective ternary, binary, and unary processes:

$$\frac{\partial n}{\partial t} = -K_3 n^3 - \alpha_{\text{eff}} n^2 - \frac{n}{\tau_R} + D\Delta n\,. \tag{172}$$

The meaning of the ternary and binary coefficients K_3 and α_{eff} was explained in the description of the equation (159). The unary losses characterized by the time constant τ_R can be caused by reactions with impurities which produce quickly recombining species. If we further assume that only the principal diffusion mode is present ($\Delta n = -n/\Lambda^2$), the electron density on axis of the discharge tube is given by an ordinary differential equation (ODE) equivalent to equation (159)

$$\frac{dn_a}{dt} = -K_3 n_a^3 - \alpha_{\text{eff}} n_a^2 - \frac{n_a}{\tau_D}; \qquad \frac{1}{\tau_D} = \frac{1}{\tau_{\text{dif}}} + \frac{1}{\tau_R}\,, \tag{173}$$

where n_a denotes the value of n on the axis and τ_{dif} is the characteristic diffusion time given by $\tau_{\text{dif}} = \Lambda^2/D$. The true diffusion time is indicated by τ_{dif} to distinguish it from the effective diffusion time τ_D, which can be directly measured in our experiments. The distinction between n_a and n is used only in this section. In other sections we implicitly assume that n is evaluated on the axis.

The validity of assuming only the principal diffusion mode in converting the PDE to ODE will be verified by comparing the numerical solution of the equation (172) to the analytic solution of the equation (173). Pure binary recombination ($K_3 = 0$) will be assumed, because of its relevance to the analysis of our experimental data. Both equations can be rewritten into dimensionless variables

$$n' = \alpha_{\text{eff}} \tau_D n; \quad t' = t/\tau_D; \quad x' = x/\Lambda; \quad \Lambda = r/J_{0,0}\,, \tag{174}$$

where $J_{0,0}$ is the first root of the Bessel function J_0 and Λ is chosen as the eigenvalue of the principal diffusion mode in the cylindrical tube with radius r. By this substitution we obtain dimensionless equations

$$\frac{\partial n'}{\partial t'} = -n'^2 - n' \frac{\tau_D}{\tau_R} + \Delta' n' \frac{\tau_D}{\tau_{\text{dif}}}; \qquad \frac{dn'_a}{dt'} = -n'^2_a - n'_a\,. \tag{175}$$

The analytic solution of the ODE is

$$n'_a(t') = \frac{n'_{a0}}{n'_{a0}(\exp(t') - 1) + \exp(t')}\,. \tag{176}$$

For comparison, the PDE is solved numerically by the finite difference method. We use a simple and stable fully implicit scheme for solving the diffusion equation described by Press et al., 2002, sec. 19-2 in combination with the differentiation of the Laplacian in the cylindrical coordinates by Birdsall and Langdon, 1991 (see section 3.1.1 in this work). Our model has one spatial dimension r. The Bessel profile with very high number density is used as the initial density distribution.

The transition of the afterglow from the recombination-dominated ($n'_a \gtrsim 1$) to the diffusion-dominated ($n'_a \lesssim 1$) regime is illustrated in figure 58. The calculation assumes that the unary losses are pure diffusion, i. e., $\tau_D = \tau_{\text{dif}}$, $\tau_R = 0$. The density profiles are fully characterized by the dimensionless parameter $n'_a = n_a \alpha_{\text{eff}} \tau_{\text{dif}}$ if the initial density is sufficiently high.

To estimate the validity of our data analysis, we apply the same procedures to the data obtained from our model. In the SA-CRDS experiment, the pure diffusion losses are comparable to the losses due to effective unary reactions (ternary association $H_3^+ + H_2 + He$ and reactions with impurities which produce quickly recombining species). Therefore, we illustrate the results on two models. One contains only the pure diffusion and the other, more realistic, assumes a loss time constant $\tau_R = \tau_{\text{dif}}$.

First, we demonstrate the analysis using the reciprocal electron number density plot (see, e. g., figure 9 by Dohnal et al., 2012a). In this procedure, the rate coefficient is obtained from the slope of the initial linear part of the curve. The results of the models in comparison with the theoretical linear slope and with the formula (176) are shown in figure 59. The figure demonstrates that the model results

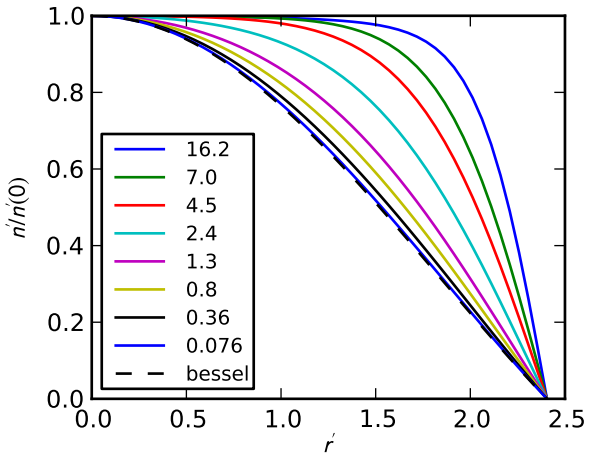

Figure 58: Radial electron density profiles in the afterglow calculated for different values of $n(0)\alpha_{eff}\tau_D$, which are indicated in the legend. The figure illustrates the transition from the recombination dominated to the diffusion dominated regime.

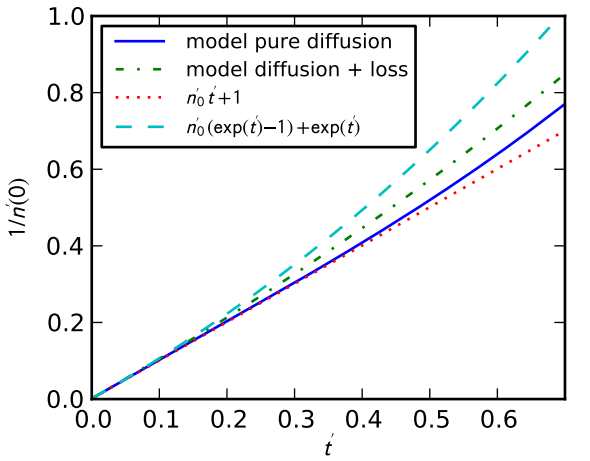

Figure 59: Analysis of the reaction rate coefficient from the slope of the $1/n$ plot applied to the simulated data.

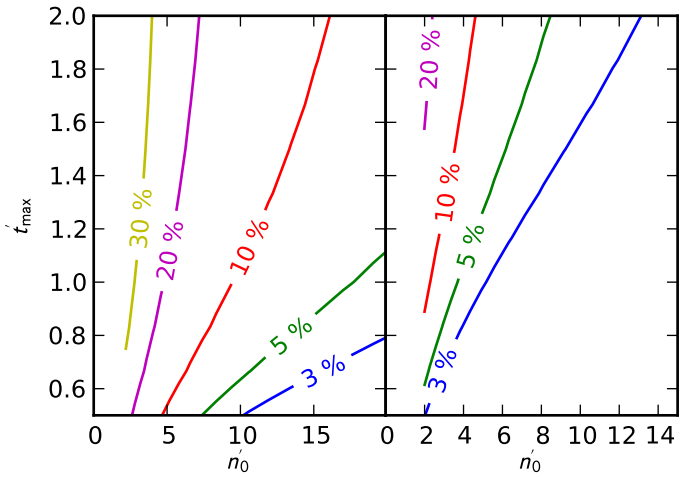

Figure 60: Deviation of the fitted α_{eff} from the correct value as a function of the initial number density $n'_0 = n_0 \alpha_{eff} \tau_D$ and maximal time included in the fit $t'_{max} = t_{max}/\tau_D$. The cases with the pure diffusion ($\tau_R = 0$) and with the unary losses ($\tau_R = \tau_{dif}$) are shown in the left and right panel respectively.

are actually closer to the linear slope than the approximate solution (176). Therefore, the analysis using the $1/n$ plot is perfectly valid.

The second method of data analysis employs the least squares fitting of the measured data with the curve (176). The result of the fitting procedure depends on the position of the start- and end-point of the measured curve. Hence, we applied the fits to the model data with various initial concentrations n'_0 and maximal fitting times t'_{max}. The deviation of the fitted α_{eff} from the correct value as a function of these fitting limits is shown in figure 60. In the typical SA-CRDS data, $t'_{max} \approx 1$. The figure shows that it is generally necessary to start the fit at high enough concentration $n'_0 > 1$ in order to obtain reasonably accurate results. In the case with $\tau_{dif} = \tau_R$, which roughly corresponds to the recent experiment, the accuracy is much better even at low values of $n' \approx 1$. Nevertheless, the fitting procedure must be used with care to avoid significant systematic errors.

8.3 COLLISIONAL RADIATIVE RECOMBINATION

This section discusses the results obtained in the SA-CRDS study of the electron-H_3^+ recombination with regard to the *collisional radiative recombination* (CRR). The CRR is a multi-step process characterized by cascading of electrons from the free continuum states towards the ground state through a sequence of intermediate Rydberg states. The transitions of the Rydberg states with the principal quantum value above a certain n_{cr} are driven mainly by collisions with electrons as a third body, whereas the transitions in the lower states are mainly

radiative. Hence the name collisional radiative recombination. An important implication of this combination of collisional and radiative transitions is that the energy of recombination from the collisional transitions is transfered to the electron gas, whereas the energy from the radiative transitions is radiated away from an optically thin plasma. The n_{cr} is approximately 10 with corresponding heating energy $\Delta\mathcal{E} = 0.136$ eV for plasma at $T = 77$ K and $n_e = 2{\cdot}10^{10}\,\mathrm{cm}^{-3}$ (Kotrík et al., 2011b; Byron et al., 1962). The rate of CRR is limited by the so-called bottleneck, which is a set of states with the principal quantum number around $n_b \geqslant n_{cr}$, where the cascading is the slowest. The population of the states above the bottleneck is close to the thermal equilibrium with the surrounding electron gas.

There are numerous theoretical studies of this process in atomic ions (D'Angelo, 1961; Bates and Kingston, 1964; Stevefelt et al., 1975) and the experimental studies of various atomic ions were able to confirm these theories with success over many orders of magnitude (Collins et al., 1972; Skrzypkowski et al., 2004)—including the results obtained in our group by Kotrík et al., 2011b; Kotrík et al., 2011a.

However, the situation with molecular ions is complicated by the presence of dissociative states. For many molecular ions, the neutral counterpart does not even exist in the stable form, which means that the cascading process is truncated by dissociation at some point. Nevertheless, the theory of atomic ions should be applicable to simple molecular ions as He_2^+ (Stevefelt et al., 1975). The experimental research in the field of CRR of molecular ions has been limited to the He_2^+ ion only, where the experimental studies of Robertson, 1965 and Deloche et al., 1976 at temperatures $T > 300$ K agree with the theory by Stevefelt et al., 1975. To distinguish the CRR from the binary or helium-assisted ternary recombination in our work, we define the CRR as a process with the rate proportional to the squared electron number density.

8.3.1 *CRR in the SA-CRDS Experiment*

The theoretical rate coefficient α_{crr} of the CRR is concisely expressed in the form of an approximate formula given by Stevefelt et al., 1975

$$\begin{aligned}\alpha_{crr}(T_e[\mathrm{K}], n_e[\mathrm{cm}^{-3}]) = 1.55{\cdot}10^{-10}\,T_e^{-0.63} + \\ + 6.0{\cdot}10^{-9}\,T_e^{-2.18}\,n_e^{0.37} + 3.8{\cdot}10^{-9}\,T_e^{-4.5}\,n_e\ \mathrm{cm}^3\mathrm{s}^{-1}\,,\end{aligned} \quad (177)$$

where T_e and n_e denote the electron temperature and number density respectively. In the conditions of the SA-CRDS experiment, where $T \lesssim 100$ K and $n_e \gtrsim 10^9$ cm^{-3}, the first two terms are negligible. The third term—the so called *collisional term*—dominates the recombination, which means that the bottleneck is located among the collisionally recombining states, i. e., $n_b > n_{cr}$ and the process is effectively three-body recombination. Since the theory has not been developed

for H_3^+ ions, it is plausible that the pre-factor $3.8{\cdot}10^{-9}$ is different, but the scaling with temperature should remain the same. In particular, recent calculations of collisional transitions by Pohl et al., 2008 indicate that the numerical coefficient for ultracold plasmas should be $2.77{\cdot}10^{-9}$ instead. Therefore, we describe the CRR in our analysis using a three body reaction coefficient with a variable coefficient A_{crr}

$$K_{crr} = \frac{\alpha_{crr}}{n_e} = A_{crr} T_e^{-4.5}\,, \tag{178}$$

where the value by Stevefelt et al., 1975 is $A_{crr} = 3.8{\cdot}10^{-9}\,K^{4.5}\,cm^6\,s^{-1}$.

Apart from the CRR, the electrons in the afterglow are destroyed by the effective binary recombination with a rate coefficient α_{eff} and by diffusion to the walls and other unary loss processes with an effective diffusion time τ_D. The electron concentration in the bulk plasma is then approximately described by the balance equation (159) (see the discussion in section 8.2).

$$\frac{dn_e}{dt} = -K_{crr}(T_e(n_e))n_e^3 - \alpha_{eff} n_e^2 - \frac{n_e}{\tau_D}\,. \tag{179}$$

We explicitly write the dependence of K_{crr} on n_e to indicate the influence of electron gas heating by recombination. To calculate the electron temperature as a function of electron concentration in this equation, we have to consider the heat balance between the heating by CRR and cooling by elastic or inelastic collisions with neutrals and ions. This will be the subject of the following section.

8.4 ELECTRON TEMPERATURE IN THE AFTERGLOW

First, let us introduce the conditions in the afterglow and the processes that are significant for the electron heat balance. The quasineutral plasma consists of electrons and H_3^+ ions with initial number density $n_e \approx 10^{11}\mathrm{cm}^{-3}$. Helium gas at densities $[\mathrm{He}] \lesssim 10^{18}\mathrm{cm}^{-3}$ was used as a buffer gas, with a small admixture of argon and hydrogen negligible for cooling. The evolution of the mean energy per particle U of the electron gas is symbolically described by an equation in the form

$$\frac{dU}{dt} = Q_{crr} + Q_{elastic} + Q_{e\text{-}i} + Q_{rot}\,, \tag{180}$$

where the terms Q_{crr}, $Q_{elastic}$, $Q_{e\text{-}i}$, and Q_{rot} account for the heating by CRR, cooling by elastic collisions with neutrals, cooling by Coulombic collisions with ions, and cooling by the rotational excitation of ions. When applicable, the energy transfer terms Q will be written in the form of temperature relaxation time ${}^{\epsilon}\tau$ defined as

$${}^{\epsilon}\tau = \frac{\Delta\mathcal{E}}{Q} = \frac{3}{2}k_B\frac{T - T_e}{Q}\,, \tag{181}$$

where T is the temperature of the interacting species.

8.4.1 *Recombination*

As discussed earlier in section 8.3, the CRR adds on average $\Delta\mathcal{E}_{crr} \approx 0.136$ eV to the electron gas per single recombined electron. Using the ternary rate defined by equation (178), the heating by CRR can be expressed as

$$Q_{crr} = \Delta\mathcal{E}_{crr} K_{crr} n_e^2 \,. \tag{182}$$

We define for reference also the mean lifetime of electrons before CRR recombination as

$$\tau_{crr} = \frac{1}{K_{crr} n_e^2} = \frac{1}{A_{crr} T_e^{-4.5} n_e^2} \,. \tag{183}$$

The strong temperature dependence of K_{crr} is written explicitly above using equation (178).

8.4.2 *Elastic Collisions*

The mean time between elastic collisions with helium τ_{en} (see equation 79) is given by

$$\tau_{en} = \frac{1}{\nu_{en}} = \frac{1}{[He] \left\langle \sigma_{en}(v) v \right\rangle} \,, \tag{184}$$

where the average $\langle\rangle$ is taken over the distribution of relative velocities. Because of the large mass ratio and slowly varying cross section, a good approximation is obtained by evaluating τ_{en} for constant cross section σ_{en} and negligible motion of neutrals, which results

$$\tau_{en} = \frac{1}{[He]\sigma(\langle v_e \rangle) \langle v_e \rangle} \,, \qquad \langle v_e \rangle = \sqrt{\frac{8 k_B T_e}{\pi m_e}} \,. \tag{185}$$

When neglecting the motion of neutrals, the average electron energy loss per collision is $\Delta\mathcal{E} = -2 m_e E \cdot 10/m_g$. For comparable electron and ion temperatures, a more accurate formula, which accounts for the thermal motion of neutrals, is given by Cravath, 1930 as $\Delta\mathcal{E} = -\frac{8}{3} m_e \mathcal{E}/m_g$, where we neglect the electron mass in comparison to the mass of neutral particles. The characteristic time for electron thermalization close to equilibrium is

$${}^{\epsilon}\tau_{en} = \frac{3 m_g}{8 m_e} \frac{1}{[He]\sigma \langle v_e \rangle} \,. \tag{186}$$

The cross section for collisions of electrons with helium at energies $\mathcal{E} \lesssim 0.015$ eV is

$$\sigma_{e\text{-}He} = 5 \cdot 10^{-16} \,\mathrm{cm}^2 \tag{187}$$

with accuracy better than 5 % according to Phelps, 2001; Crompton and McIntosh, 1968.

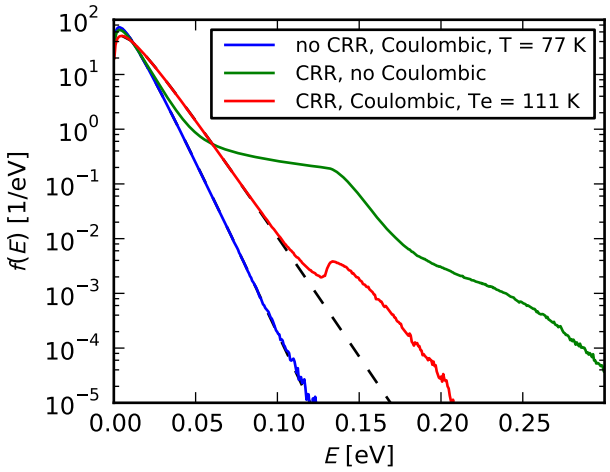

Figure 61: Electron energy distribution function calculated by the Monte Carlo method. Figure illustrates thermalization of hot electrons by the electron-electron Coulombic collisions.

8.4.3 *Coulombic Collisions*

The cross section of the Coulombic collisions, which was given in equation (94) of section 4.3.2, is

$$\sigma_c(v) = \pi\Lambda^2 \ln\frac{\lambda_D}{\Lambda}, \tag{188}$$

where Λ is the impact parameter for $\pi/2$ scattering and λ_D is the Debye length. Although the electron-electron Coulombic collisions do not contribute to the heating, they are very efficient at redistributing the energy among the electrons. The maxwellization of the electrons is faster than the other energy-changing processes, which makes it possible to properly define the electron temperature.

This effect is illustrated in figure 61, which shows the Monte Carlo simulation of electron energy distribution in a helium buffer gas at $[He] \approx 4{\cdot}10^{17}\,cm^{-3}$, $T_{He} = 77$ K. The electron number density $n_e = 10^{11}\,cm^{-3}$. An artificial collision process was included in the model, which increases the electron energy by $\Delta\mathcal{E}_{crr}$ with rate $\nu_{crr} = K_{crr} n_e^2$. In reality, the effect of CRR will be much smaller, because the cascading proceeds in steps and the electrons will be more uniformly heated. The figure shows that this process causes a strong deformation of the energy distribution when the Coulombic collisions are neglected. However, including the Coulombic collisions in the model leads to a good internal thermalization of the electron gas with resulting temperature significantly above T_{He}.

The Coulombic collisions of electrons with ions can contribute significantly to the cooling at higher electron densities. The time con-

stant for equipartition of energy by Coulombic collisions with ions given by Dougal and Goldstein, 1958 is

$$ {}^{\epsilon}\tau_{ei} = \frac{6\sqrt{2m_e}\epsilon_0^2(\pi k_B T_e)^{3/2}}{n_e q^4 \lambda_c} \frac{m_i}{2m_e}, \tag{189} $$

where m_i is the ion mass and λ_c is the Coulomb logarithm. The electron temperature has to be close to the ion temperature. The approximate value by Huba, 2011 for electron thermalization rate

$$ {}^{\epsilon}\tau'_{ei} = \frac{m_e[\text{amu}](T_e[\text{eV}])^{3/2}}{3.2{\cdot}10^{-9}\,\lambda_c n_e[\text{cm}^{-3}]}\ \text{s} \tag{190} $$

agrees with the expression by Dougal and Goldstein, 1958 within few percent. The Coulomb logarithm definition used in this work, i. e., $\lambda_c = \ln(\lambda_D/\Lambda)$ (see section 4.3.2) is again in agreement with the formula given by Huba, 2011 for the conditions of our experiment

$$ \lambda_c = 23 - \ln\left(\sqrt{n_e[\text{cm}^{-3}]}\,(T_e[\text{eV}])^{-3/2}\right). \tag{191} $$

8.4.4 *Rotational Excitation of Ions*

The rotational transition of H_3^+ with the lowest excitation energy is the transition between the two lowest rotational states $(1,1)$ and $(2,1)$ of para-H_3^+. Its excitation energy is

$$ \frac{\Delta_{1,2}}{k_B} = \frac{\mathcal{E}_{(2,1)} - \mathcal{E}_{(1,1)}}{k_B} = 249\ \text{K}. \tag{192} $$

The states are identified using the rotational quantum numbers (J, K) with the nomenclature of Kokoouline et al., 2010. For brevity, we will label the states with italic numbers as $1 \equiv (1,1)$ and $2 \equiv (2,1)$. This excitation energy is accessible for a considerable fraction of electrons even at $T_e \approx 100$ K. Therefore, we include the possible effect of electron cooling by this transition.

The rate of energy transfer by rotational (de-)excitation between the states 1 and 2 is

$$ Q_{rot} = \Delta_{1,2}(n_2\alpha_{2\to1} - n_1\alpha_{1\to2}), \tag{193} $$

where $\Delta_{1,2}$ is the energy difference between the states, n_1 and n_2 are the populations of 1 and 2 respectively, and $\alpha_{2\to1}$ and $\alpha_{1\to2}$ are the (de-)excitation rates. A recently calculated formula for the (de-)excitation rates by Kokoouline et al., 2010 is

$$ \alpha_{1\to2} = \frac{1}{\sqrt{T_e}} \exp\left(-\frac{\Delta_{1,2}}{k_B T_e}\right) P_{1\to2}(\ln(T_e[\text{K}]))\,\text{cm}^3\,\text{s}^{-1}, \tag{194} $$

$$ P_{1\to2}(x) = a_0 + a_1 x + a_2 x^2 + a_3 x^3, \tag{195} $$

where the coefficients $a = (a_0, a_1, a_2, a_3)$ for the excitation and de-excitation of states $1 = (1, 1)$ and $2 = (2, 1)$ are given by Kokoouline et al., 2010 as

$$a^{1\to2} = (1.51{\cdot}10^{-5}, 4.6{\cdot}10^{-7}, -3.96{\cdot}10^{-7}, 3.00{\cdot}10^{-8}), \quad (196)$$

$$a^{2\to1} = (8.81{\cdot}10^{-6}, 4.08{\cdot}10^{-7}, -2.62{\cdot}10^{-7}, 1.94{\cdot}10^{-8}). \quad (197)$$

The number density of ions in a state (J, K) with a nuclear spin degeneracy g is

$$n_{(J,K)}(T_{rot}) = n_i \frac{(2J+1)g}{z(T_{rot})} \exp\left(-\frac{\mathcal{E}_{(J,K)}}{k_B T_{rot}}\right), \quad (198)$$

where $z(T_i)$ is the partition function calculated relative to the same energy as $\mathcal{E}_{(J,K)}$. This equation defines the rotational temperature of ions, T_{rot}. In this work we use the partition function calculated by Ramanlal and Tennyson, 2004.

After inserting the concentrations and reaction rates into the equation (193), we obtain

$$Q_{rot} = \Delta_{1,2} \frac{n_i}{z(T_{rot})} \left[(2J_2+1)g_2 \exp\left(-\frac{\mathcal{E}_2}{k_B T_{rot}}\right) \frac{P_{2\to1}(\ln(T_e))}{\sqrt{T_e}} - (2J_1+1)g_1 \exp\left(-\frac{\mathcal{E}_1}{k_B T_{rot}} - \frac{\Delta_{1,2}}{k_B T_e}\right) \frac{P_{1\to2}(\ln(T_e))}{\sqrt{T_e}}\right]. \quad (199)$$

From the principle of detailed balance ($Q_{rot}(T_e = T_{rot}) = 0$), we can deduce a relationship between the excitation and de-excitation rates:

$$(2J_1+1)g_1 P_{2\to1}(T_e) = (2J_2+1)g_2 P_{1\to2}(T_e). \quad (200)$$

Finally, the equation (199) can be simplified to

$$Q_{rot} = \Delta_{1,2} \frac{(2J_1+1)g_1 P_{1\to2}(T_e) n_i}{z(T_{rot})\sqrt{T_e}} \exp\left(-\frac{\mathcal{E}_2}{k_B T_{rot}}\right) \left[1 - \exp\left(-\frac{\Delta_{1,2}(T_{rot} - T_e)}{k_B T_{rot} T_e}\right)\right]. \quad (201)$$

For further reference, we define the characteristic rotational cooling time

$$^{\epsilon}\tau_{rot} = \frac{3}{2} k_B \frac{(T_{rot} - T_e)}{Q_{rot}}. \quad (202)$$

8.4.5 *Ambipolar Field and Diffusion Cooling*

A question arose, whether the ambipolar field, which confines the electron gas in the flow tube, can cause some heating of the electrons. In theory, the ambipolar field just repels the electrons from the walls of the discharge tube and it should not cause any heating

of the electrons. This assumption was verified using our 2D Cartesian particle in cell (PIC) model of the discharge tube. Furthermore, the PIC model also investigates the possible contribution of the diffusion cooling (Robson, 1976). Since the cross section for the elastic collisions of the electrons with helium is nearly constant, the faster electrons have higher diffusion coefficient, which can lead to cooling. However, we expect that no cooling effect will be observed due to the short thermalization time in comparison with the diffusion time (cf. table 4),

The model uses the finite difference Poisson equation solver of section 3.1.1 combined with the Verlet integrator and Monte Carlo collisions (see sections 4.2 and 4.3 for details). Linear interpolation is used for charge weighting and force interpolation (the cloud-in-cell (CIC), see Birdsall and Langdon, 1991). Description of some aspects of our model is given by Roučka and Hrach, 2011. The model plane was oriented perpendicular to the discharge tube axis. A coarse mesh spacing $\Delta x = 3.2{\cdot}10^{-4}\,\mathrm{m}$ was used to limit the numerical heating. Time step $\Delta t = 1{\cdot}10^{-11}$. In our simplified model, only elastic collisions were included. The heat balance equation (180) in terms of temperature then reduces to

$$\frac{dT_e}{dt} = \frac{T_g - T_e}{\tau_{en}} = \frac{m_g}{2m_e}\frac{T_g - T_e}{[He]\sigma(\langle v_e\rangle)\langle v_e\rangle}, \qquad \langle v_e\rangle = \sqrt{\frac{8k_B T_e}{\pi m_e}}, \tag{203}$$

where T_g denotes the neutral gas kinetic temperature. We use the factor 2 instead of 8/3 in equation (186) for τ_e to account for the initial high energy of electrons after switching off the discharge. The initial conditions for simulation are Bessel density distribution of electrons and ions with $n_e = n_i = 10^{11}\,\mathrm{cm}^{-3}$ on axis, temperatures $k_B T_e^0 = 1$ eV, $T_g^0 = 77$ K. The boundary conditions simulate immediate recombination on the walls.

It is a difficult task, to calculate the electron temperature with the required accuracy of 1 K due to the numerical heating. Because of this requirement, the statistical noise in the ambipolar field should be approximately below 10^{-4} V to limit the influence on the electrons. The number of macroparticles used was $N < 2{\cdot}10^6$ to keep the calculation time of the order of days on a regular personal computer. An additional smoothing operator had to be applied to the potential to further reduce the heating. It was found that the smoothing scheme HCIC (hollow particle smoothing) of Hockney, 1971 is unstable with respect to a specific type of checkerboard oscillations. Therefore, a new stable scheme was developed, which convolves the potential with a square of dimensions $2\Delta x \times 2\Delta x$. Repeated application of this smoothing operator allowed us to reach a sufficient accuracy for the price of low spatial resolution. The typical results of our simulations are shown in figure 62. The left panel shows the temperature evolu-

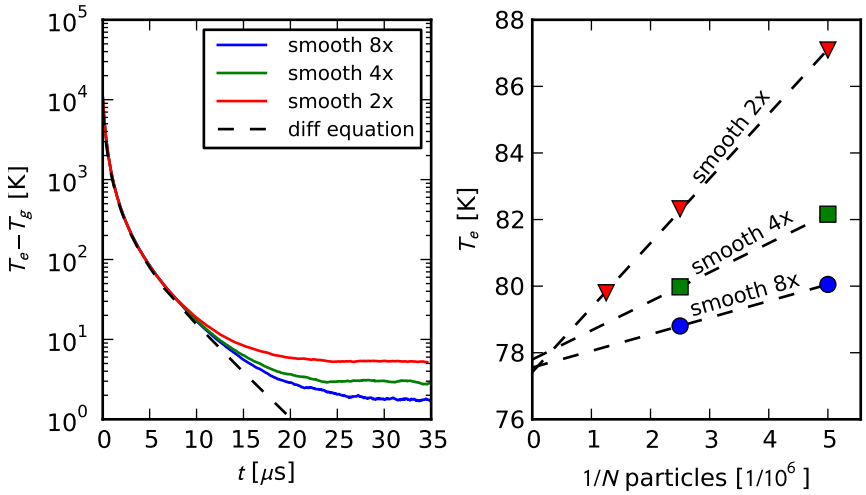

Figure 62: Results of the particle-in-cell model of the afterglow. The left panel shows the temperature evolution of electrons and the right panel illustrates the calculation of the equilibrium temperature.

tions calculated for $8{\cdot}10^6$ macroparticles in comparison with the exact solution of the equation (203). Calculations with different levels of smoothing are shown. The results are in a very good agreement down to $T_e - T_g \approx 10$ K. The variations at low temperatures demonstrate the effect of non-physical numerical heating. According to Hockney, 1971, the heating effect can be described by an additional term in the energy balance equation

$$Q_H = \frac{T_e}{\tau_H}, \tag{204}$$

where the heating time constant τ_H, which is defined by this equation, differs by a factor $\ln 2$ from the τ_H defined by Hockney, 1971. Neglecting all the constant parameters of a given physical problem, the proportionality of τ_H is

$$\tau_H \sim \frac{N(\lambda_D^2 + \Delta x^2)}{\Delta x^2}, \tag{205}$$

where λ_D is the Debye length. Thanks to the simple linear relationship, the heating effect can be calculated for different numbers of particles and linearly extrapolated in the $1/N$ graph for $N \to \infty$. This is demonstrated in the right panel of figure 62, where the equilibrium temperatures obtained under different model parameters are extrapolated for $N \to \infty$. All the extrapolations agree within 1 K with the ion temperature $T_g = 77$ K, which demonstrates that the smoothing does not influence the extrapolated temperature.

One of the conclusions of this section is that it is problematic to achieve ≈ 1 K accuracy with the PIC model due to the numerical noise. Our results confirm the observation of Hockney, 1971, although

reactants	process	symbol	τ[μs]	equation
$e + He$	elastic scattering	τ_{en}	0.0008	(184)
$e + e$	Coulombic scattering	τ_{ee}	0.004	(94)
$e + He$	elastic cooling	${}^{\epsilon}\tau_{en}$	2.6	(186)
$e + H_3^+$	Coulombic cooling	${}^{\epsilon}\tau_{ei}$	3.4	(189)
$e + e + H_3^+$	CRR	τ_{crr}	43.	(183)
$e + H_3^+$	rotational cooling	${}^{\epsilon}\tau_{rot}$	140.	(202)
$e + H_3^+ + He$	ternary recombination	τ_{He}	200.	(160)
$e + H_3^+$	binary recombination	τ_{bin}	250.	(160)
e + wall	ambipolar diffusion	τ_D	400.	(159)

Table 4: Overview of the processes in the H_3^+ afterglow plasma. Typical time scales of these processes are evaluated under conditions $n_e = n_i = 5{\cdot}10^{10}\,\mathrm{cm}^{-3}$, $T_g = T_i = T_{rot} = 77$ K, $[He] = 5{\cdot}10^{17}\,\mathrm{cm}^{-3}$. The recombination and diffusion times are obtained from experimental data by Dohnal et al., 2012a as $\tau_{bin} = 1/\alpha_{bin} n_i$ and $\tau_{He} = 1/K_{He}[He]n_i$. The time between Coulombic collisions is estimated as $\tau_{ee} = 1/n_e \sigma_c(\langle v\rangle)\langle v\rangle$.

his smoothing scheme was found to be unstable at very low temperatures. The coarse grid in combination with the smoothing operators does not allow for accurate representation of the field in the sheath, but this is expected to be repulsive for the electrons. Nevertheless, our PIC model proves that the analytical formula (203) is accurate in the range of validity of the PIC model. No physical heating or diffusion cooling effects were observed, which was expected. Finally, the results in figure 62 show that the electrons are thermalized with 1 K accuracy in the first 20 μs of the afterglow.

8.4.6 *Equilibrium temperature*

Now that we have defined the relaxation times of the relevant cooling processes, the heat balance equation (180) can be rewritten in terms of temperatures as

$$\frac{dT_e}{dt} = \frac{2\Delta\mathcal{E}_{crr}/3k_B}{\tau_{crr}} + \frac{T_g - T_e}{{}^{\epsilon}\tau_{en}} + \frac{T_i - T_e}{{}^{\epsilon}\tau_{ei}} + \frac{T_{rot} - T_e}{{}^{\epsilon}\tau_{rot}}\,. \tag{206}$$

To simplify this equation, we need to consider the time scale of the thermalization in comparison with the time scale of evolution of the afterglow. The relevant processes are summarized in table 4. We can see from the table that in our experimental conditions, the temperature relaxation processes have time constants typically ${}^{\epsilon}\tau < 10$ μs, whereas the decay processes of recombination and diffusion have time constants $\tau \gtrsim 100$ μs. Therefore, we can assume that the electron temperature is close to equilibrium during the afterglow, i. e., the

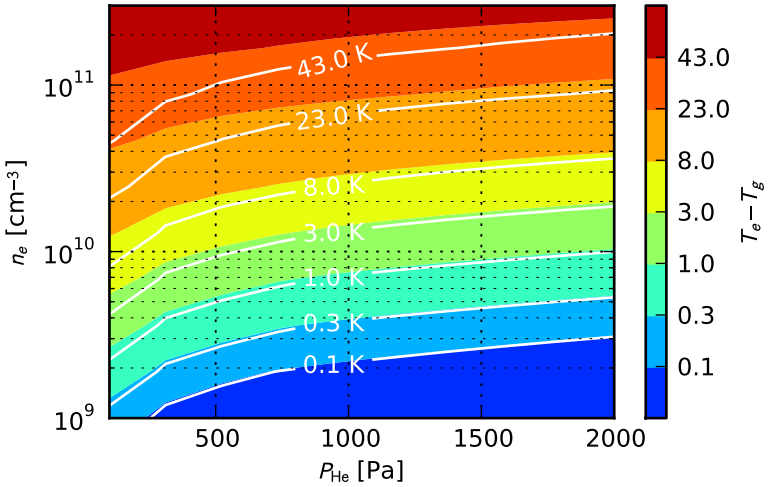

Figure 63: Temperature of electrons determined from equation (207) as a function of helium pressure p_{He} and electron number density n_e. Calculated for $T_g = 77$ K with assumption $A_{crr} = 3.8{\cdot}10^{-9}$ K$^{4.5}$ cm^6 s^{-1}. The color map shows the solution of the full equation (207), whereas the white lines indicate the effect of neglecting the electron-ion collisions.

time derivative term in equation (206) can be neglected. The electron temperature is then obtained by numerically solving the equation

$$\frac{2\Delta\mathcal{E}_{crr}/3k_B}{\tau_{crr}} + \frac{T_g - T_e}{\epsilon\tau_{en}} + \frac{T_i - T_e}{\epsilon\tau_{ei}} + \frac{T_{rot} - T_e}{\epsilon\tau_{rot}} = 0\,. \tag{207}$$

The electron temperature given by this equation is a complicated function of the variable parameters $n_e, n_i, [He], T_i, T_g, T_{rot}$, and also of the unknown A_{crr}. For the typical conditions of our experiment, the electron temperature is shown in figure 63. The temperatures in the figure are calculated using the $A_{crr} = 3.8{\cdot}10^{-9}$ K$^{4.5}$ cm^6 s^{-1} given by Stevefelt et al., 1975.

8.5 RECOMBINATION KINETICS - EXPERIMENTAL RESULTS

The results of the previous section were used to solve the equation (179) with electron temperature given as a function of electron concentration and other experimental parameters. We repeat the equation here for reference

$$\frac{dn_e}{dt} = -K_{crr}(T_e(n_e))n_e^3 - \alpha_{eff}n_e^2 - \frac{n_e}{\tau_D}\,. \tag{179}$$

An example of the solution is shown in figure 64. The parameters used in the calculation closely follow the experimental conditions (cf. figure caption and table 4). The figure clearly shows a strong contribution of the CRR in the initial—recombination dominated—phase of

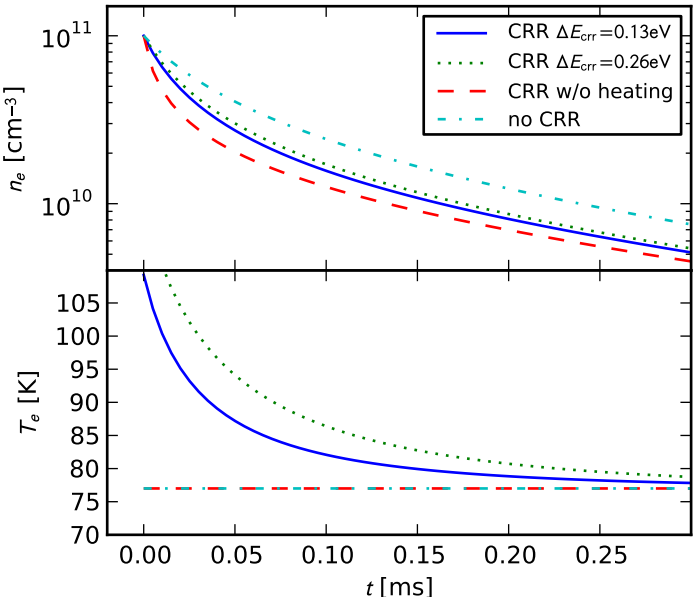

Figure 64: Electron kinetics obtained as a solution of the equation (179). Electron number density and the corresponding temperature are shown in the upper and lower panel respectively. Parameters used: $T_g = 77$ K, $[He] = 5{\cdot}10^{17}$ cm^{-3}, $n_e^0 = 10^{11}$ cm^{-3}, $\tau_D = 0.4$ ms, $\alpha_{eff} = 2.5{\cdot}10^{-7}$ cm^3 s^{-1}. The solid line shows the full solution with $A_{crr} = 3.8{\cdot}10^{-9}$ K$^{4.5}$ cm^6 s^{-1}. The dashed line shows the effect of neglected heating by the CRR, i. e., $T_e = 77$ K. The effect of completely neglecting the CRR is shown by the dash-dotted line.

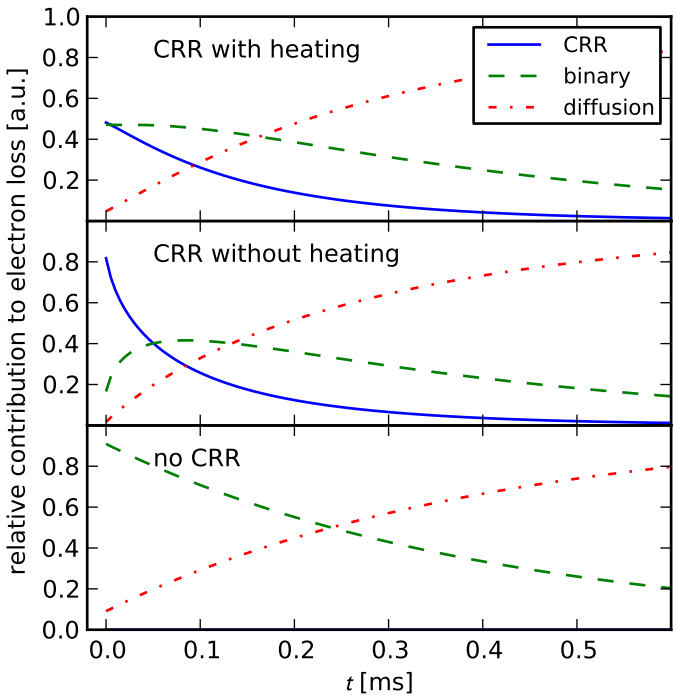

Figure 65: Relative Contributions of particular loss terms in equation (179). Each panel corresponds to a different model described in figure 64.

the afterglow. The importance of the heating effects for the afterglow kinetics is demonstrated by comparing the results with a simulation where the electron temperature is fixed at $T_e = 77$ K. The sensitivity of the model to the exact value of $\Delta\mathcal{E}_{crr}$ was also investigated by carrying out the simulation with $\Delta\mathcal{E}_{crr} = 0.26$ eV, i. e., twice bigger than the expected value. The value of $\Delta\mathcal{E}_{crr}$ has a strong influence on the electron temperature, but not on the electron density evolution. The lower panel with the corresponding electron temperature shows that—in the presence of CRR—the electron temperature stabilizes within 10 K at 50 µs, in accordance with figure 63.

The contributions of individual terms in equation (179) are illustrated by figure 65. The plotted data are obtained by dividing the corresponding loss term of equation (179) by dn_e/dt. The figure again shows that including the heating effects slows the CRR down significantly.

The theoretical decay curves were fitted with various parameters to the experimentally obtained curves. For a thorough description of the measured data refer to Dohnal et al., 2012a. For the purpose of this analysis, it is sufficient to know that the time evolution of the electron, para-H_3^+, and ortho-H_3^+ densities was obtained by monitoring the density of particular rotational states of H_3^+ with the CRDS. Only the measurements carried out at the lowest temperature, $T_g = 77$ K,

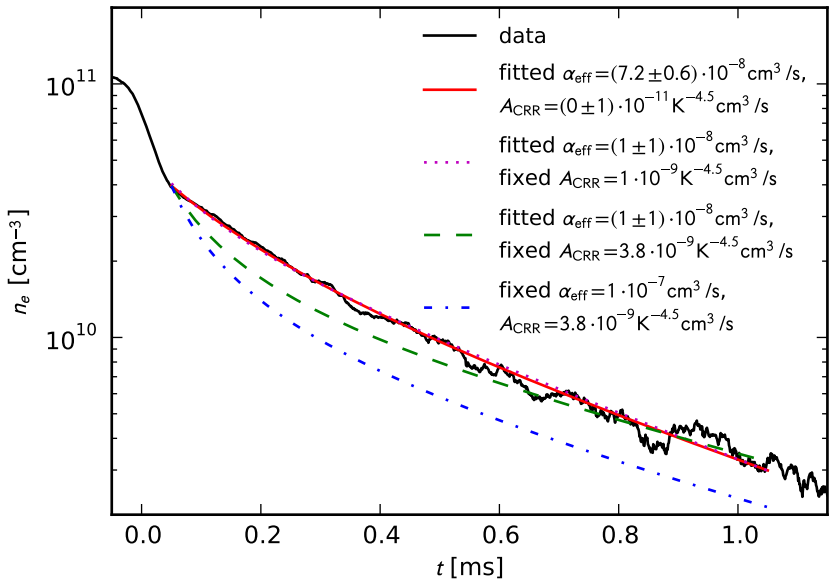

Figure 66: Measured electron number density decay in comparison with models. The solid red line shows the least squares fit of a model with A_{crr} and α_{eff} as free parameters. The dotted and dashed lines show fits with α_{eff} as a free parameter and A_{crr} fixed at a hypothetical values $1{\cdot}10^{-9}\,K^{4.5}\,cm^6\,s^{-1}$ and $3.8{\cdot}10^{-9}\,K^{4.5}\,cm^6\,s^{-1}$ respectively. Finally, the dash-dotted line shows the model for fixed values of α_{eff} and A_{crr} as indicated in the legend. In all fits, the initial number of electrons, n_e, and τ_D are also treated as free parameters. Measurements was carried out at a helium pressure $p_{He} = 608$ Pa.

are considered in our analysis. The measurements at the higher temperatures ($T_g \geqslant 140$ K) should not be significantly influenced by CRR thanks to the strong $T^{-4.5}$ temperature dependence.

Two examples of experimentally obtained electron density decays are shown in the figures 66 and 67. The measurements were carried out at moderate pressures around 600 Pa. In both cases, the unconstrained fit results basically zero value of A_{crr} in comparison with the theoretical value of Stevefelt et al., 1975. Using a hypothetical fixed value of $A_{crr} = 10^{-9}\,K^{4.5}\,cm^6\,s^{-1}$ results in a fit which is still in a good agreement with the data. However, the small value of α_{eff} obtained from this fit is not consistent with the independent measurements of H_3^+ recombination by Glosík et al., 2009. The fits which use the fixed value $A_{crr} = 3.8{\cdot}10^{-9}\,K^{4.5}\,cm^6\,s^{-1}$ are not able to reproduce the measured data.

The analysis by fitting with the unconstrained model was applied to a number of measured decay curves in the normal hydrogen and para-enriched hydrogen at various pressures. A summary of the A_{crr} values obtained from measurements at different pressures is shown in the figure 68. The weighted average values of A_{crr} are

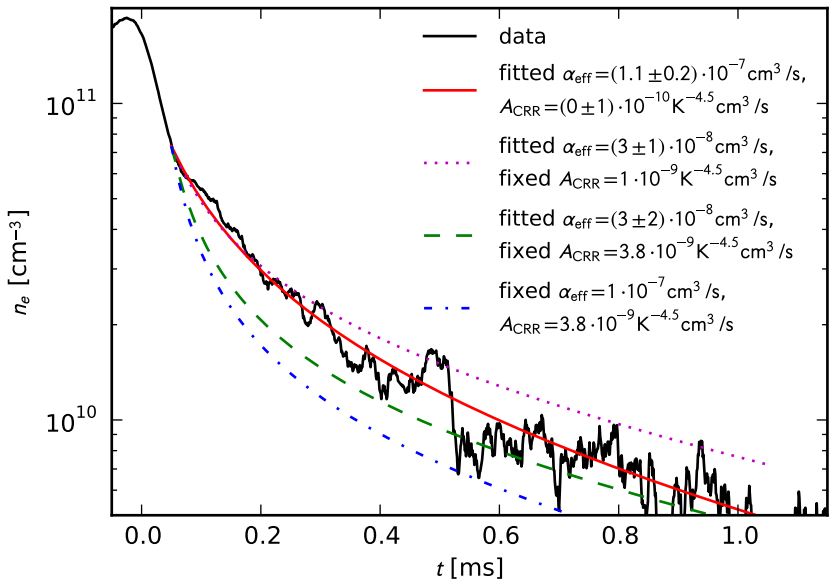

Figure 67: Measured electron number density decay obtained at a helium pressure $p_{He} = 613$ Pa. Refer to the caption of the figure 66 for description of the theoretical lines.

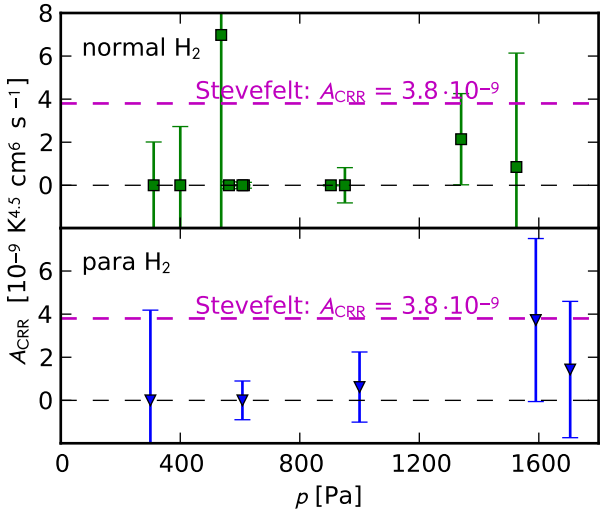

Figure 68: The A_{crr} values obtained by fitting the measured decays in the normal and para-enriched H_2.

$$A_{crr}^{normal} = (0 \pm 0.02 \pm 2)\cdot 10^{-9}\,K^{4.5}\,cm^6\,s^{-1}, \quad (208)$$

$$A_{crr}^{para} = (0.3 \pm 0.7 \pm 1.4)\cdot 10^{-9}\,K^{4.5}\,cm^6\,s^{-1}, \quad (209)$$

where the first error estimate is obtained from the fit errors and the second, more reliable, error estimate is the standard deviation of the fitted values.

8.6 CONCLUSION

We have studied several aspects of the afterglow plasmas which are used in our laboratory. We have developed a numerical model of cooling of the carrier gas which can be used to estimate the plasma temperature along the flow tube. At the lowest wall temperatures ($T \approx 40$ K), the model gives the upper estimate of the temperature. At the higher temperature ($T \approx 77$ K), a good agreement with the experimental results from the FALP instrument is obtained.

The heating of the electrons in the afterglow plasma by the energy released from the CRR was investigated using a model of the energy balance. The model includes the heating by the CRR and the cooling by the elastic collisions with ions, by the elastic collisions with neutrals, and by the rotational excitation of ions.

The electron temperature obtained from the heat balance model was coupled to a solver of chemical kinetics equations. The experimental data from the SA-CRDS experiment were analyzed by fitting with the results of the numerical model. The conclusion of our data analysis is that there is no measurable contribution of the CRR to the reaction kinetics. There are two possible explanations of the negligible value of A_{crr} obtained from our fits, which is in contradiction with the theory of CRR for atomic ions. First, there could be some unknown heating mechanism, which further increases the electron temperature by several K and suppresses the CRR. Second, the theory is not directly applicable to the recombination of H_3^+.

The study of the electron heat balance and reaction kinetics was motivated by the experimental investigation of the H_3^+ dissociative recombination. For the measurements of the ternary and binary recombination, it is important to know that the measurements are not influenced by the CRR. The conclusion of our analysis that there is no significant contribution of the CRR is supported by the experimental observation of the strong nuclear spin sensitivity of the reaction rate coefficients. The CRR contribution should not depend on the nuclear spin configuration and therefore it should not exceed the smallest measured binary recombination rate coefficient. That is the extrapolated rate coefficient of the ortho-H_3^+ recombination, $\alpha_{eff} \lesssim 5\cdot 10^{-8}\,cm^3\,s^{-1}$ (Dohnal et al., 2012a). Furthermore, the experimental results are in agreement with independent measurements using the FALP apparatus, which could not be influenced by the CRR

due to the lower electron number density (see Dohnal et al., 2012a for details on the experimental results).

9 SUMMARY AND OUTLOOK

This work shows several experimental techniques for studying ion chemistry and the applications of computer models in these studies are demonstrated.

A major part of this work consists of the description of a novel apparatus for studying the energy of the electrons produced in the RF trap—the ES-MPT. The machine is built upon an ion trap, which was originally constructed in the group of prof. Gerlich in Germany. The electron spectrometer capable of extracting the electrons from the trap without disturbing the trapped ions was designed using numerical simulations which are described by *Roučka et al., 2009; Roučka et al., 2010* [1]. First experimental tests have confirmed the validity of our design. Electrons from the laser photodetachment were successfully detected. The measured energy resolution of the spectrometer is sufficient to observe the most prominent features of expected spectrum from the $O^- + H_2$ and $H^- + H$ associative detachment. Experiments are in progress, which should further improve the energy resolution by decreasing the RF amplitude and selecting only the undisturbed electrons using a mechanical aperture. The results of the initial tests were presented by *Jusko et al., 2012a*. A publication describing the apparatus and the first results is in preparation *(Jusko et al., 2012b)*. Further plans consist of measuring the electron spectra from the $O^- + H_2$ and $O^- + D_2$ associative detachment reactions. The measurement with H_2 will verify the previously measured data by Mauer and Schulz, 1973. Measuring the, yet unknown, spectra from the reaction with D_2 will provide information about the isotopic effects, which are tightly related to the quantum-mechanical features of the interaction (see section 2.2.2 for more details).

The temperature dependence of the reaction rate coefficient of the $H^- + H$ associative detachment reaction was measured using the AB-22PT apparatus. Our measurements provided the value of the reaction rate coefficient in a range of temperatures 10–135 K which was not accessed before. Our results published by *Gerlich et al., 2012* confirm the theory of Čížek et al., 1998 and also the experimental results of Kreckel et al., 2010 in the overlapping temperature range. Details of the calibration measurements and data analysis are described by *Roučka et al., 2011; Jusko et al., 2011a*. Further experiments are planned to reduce the systematic error of our measurement and to study the isotopic effects in the reactions $D^- + H$ and $H^- + D$.

1 Publications coauthored by Š. Roučka which partly contain the results of this thesis are printed in *italics*

The process of thermalization of the plasma in the low-temperature afterglow experiments was investigated using mathematical models. A simple model of cooling of the carrier gas was developed and used to verify the thermalization in the FALP experiment, which was measuring the collisional radiative recombination of Ar^+. The results of the model are published by *(Kotrík et al., 2011b; Kotrík et al., 2011a)*. Improvements to the accuracy of the model are planned. The accuracy of empirical formulas will be investigated and ultimately the compressible Navier–Stokes equations will be applied.

Another model was developed to calculate the temperature of electrons in the afterglow plasma. The model was used for the analysis of the results from the SA-CRDS experiment. The conclusion of the analysis is that the collisional radiative recombination does not influence the measurement of the effective binary recombination of H_3^+ in the experiments *(Dohnal et al., 2012a; Dohnal et al., 2012b)*. The absence of the CRR effects will be further investigated, seeking for possible corrections of our understanding of CRR of molecular ions and also for other electron heating processes, which could suppress the CRR.

The computer models used in this thesis are based on the computer algorithms for particle in cell simulations at moderate pressures which were developed for the master's thesis of the author *(Roučka, 2008)*. The description of the collision model in combination with the particle in cell model was published by *Roučka and Hrach, 2011*.

A

IMPLEMENTATION OF THE MAGNETIC FIELD SOLVER

This appendix contains a fully working simple example of magnetostatic problem solution. The geometry consisting of an electromagnetic coil and a coil-shaped ferromagnetic body is defined in the NETGEN *constructive solid geometry* (CSG) language in listing 1. For description of the NETGEN language, refer to the NETGEN manual (Schöberl, 2003).

Listing 1: Geometry definition, file `MAC.geo`

```
algebraic3d
solid box_outer = sphere (0, 0, 320e-3; 1000e-3) -bc=1;

#electromagnet coil
solid coil1 = cylinder (0, 0, -60e-3; 0, 0, -50e-3; 70e-3)
        and not cylinder  (0, 0, -60e-3; 0, 0, -50e-3; 40e-3)
        and plane (0, 0, -50e-3; 0, 0, 1)
        and plane (0, 0, -60e-3; 0, 0, -1) -bc=3 -maxh=10e-3;

#ferromagnetic shield
solid shield1 = cylinder (0, 0, 0e-3; 0, 0, 100e-3; 70e-3)
        and not cylinder  (0, 0, 0e-3; 0, 0, 100e-3; 40e-3)
        and plane (0, 0, 100e-3; 0, 0, 1)
        and plane (0, 0, 0e-3; 0, 0, -1) -bc=3 -maxh=10e-3;

solid air =  box_outer and not coil1 and not shield1 -bc=3;

tlo coil1 -col=[0, 1, 0];       #solid number 1
tlo shield1 -col=[1, 0, 0];     #solid number 2
tlo air  -col=[0, 0, 1] -transparent;
```

The weak formulation of the magnetostatic problem and its subsequent solution are implemented in the python programming language using the dolfin interface to the FEniCS library. The implementation is shown in listing 2. For description of this library, see Logg et al., 2012.

Listing 2: Problem definition and solution, file `curl.py`

```
from dolfin import *

mesh = Mesh("MAC.xml")
subdomains = MeshFunction("uint", mesh, "MAC_mat.xml")

P0 = FunctionSpace(mesh, "Nedelec 1st kind H(curl)", 1)
```

```
P1 = FunctionSpace(mesh, "Lagrange", 1)
PN = MixedFunctionSpace((P0, P1))

(v0, q0) = TestFunctions(PN)
(u0, p0) = TrialFunctions(PN)

# Define functions
ZeroVector = Constant((0.0, 0.0, 0.0))
ZeroScalar = Constant(0.0)

# Dirichlet boundary
class DirichletBoundary(SubDomain):
    def inside(self, x, on_boundary):
        return on_boundary

# Boundary condition
# Fields are truncated on the distant boundary
bc1 = DirichletBC(PN.sub(0), ZeroVector, DirichletBoundary())
bc2 = DirichletBC(PN.sub(1), ZeroScalar, DirichletBoundary())
bcs = [bc1, bc2]

#define the current density field
class CurrentExpression0(Expression):
    def eval_cell(self, values, x, ufc_cell):
        index = subdomains[ufc_cell.index]
        x, y, z = x[0:3]
        if index == 1:              #solid number 1
            SC = 10e-3*30e-3        #coil cross section
            AT = 300*2.9            #number of ampere-turns
            J = AT/SC
            r = sqrt(x**2 + y**2)
            values[0] = -y/r*J
            values[1] = x/r*J
            values[2] = 0.0
        else:
            values[0] = 0.0
            values[1] = 0.0
            values[2] = 0.0

    def value_shape(self):
        return (3,)
J = CurrentExpression0()

#define the permitivity field
class MuExpression0(Expression):
    def eval_cell(self, value, x, ufc_cell):
        mu0 = 4*pi*1e-7
        index = subdomains[ufc_cell.index]
        if index == 2:              #solid number 2
            value[0] = mu0*2333
            #permitivity of 1117 steel according to FEMM
        else:
```

```
            value[0] = mu0

    def value_shape(self):
        return ()
Mu = MuExpression0()

#define the problem - left and right hand side of the equations
a = (inner(curl(v0), curl(u0)/Mu) + inner(v0, grad(p0)) +\
        inner(grad(q0), u0))*dx
L = -inner(J, v0)*dx

#solve the problem
U = Function(PN)
problem = LinearVariationalProblem(a, L, U, bcs)
solver = LinearVariationalSolver(problem)
solver.solve()

#obtain the vector potential
u, p = split(U)

# calculate curl(u)
V = VectorFunctionSpace(mesh, "CG", 1)
g = project(curl(u), V)

# obtain the axial values of B
import numpy as N
nsampl = 200
length = 650e-3
x = N.zeros((nsampl, 3))
x[:,2] = N.arange(nsampl)*length/nsampl

values = N.zeros((nsampl, 3))
for i in N.arange(len(x)):
    values[i] = g(x[i])
axial_table = N.c_[x[:,2], values]

#save the axial values
N.savetxt("axial1.txt", axial_table)

#save the full solution
outfile = File("MAC1.pvd")
outfile << g
```

The mesh generation and problem solution is done by the following commands in listing 3 (assuming that the geometry definition and problem definition are stored in files `MAC.geo` and `curl.py` respectively. The solver produces files `axial1.txt` and `MAC1.pvd`. The file `axial1.txt` contains the tabulated values of the magnetic field on the axis of the model. The file `MAC1.pvd` contains the full solution in

the VTK format (*VTK: The Visualization Toolkit*). The VTK file can be visualized using the ParaView[1] or Mayavi[2] software.

Listing 3: Shell commands for running the solver

```
# generate the mesh
netgen -geofile=MAC.geo -meshfile=MAC.grid\
    -meshfiletype="DIFFPACK Format" -batchmode
dolfin-convert MAC.grid MAC.xml

# run the solver
python curl.py
```

1 http://www.paraview.org/
2 http://code.enthought.com/projects/mayavi/

BIBLIOGRAPHY

Abel, T., G. Bryan, and M. Norman (Jan. 2002). "The Formation of the First Star in the Universe." In: *Science* 295, pp. 93–98 (cit. on p. 4).
DOI: 10.1126/science.295.5552.93.
arXiv:astro-ph/0112088v1.

Agúndez, M., J. Cernicharo, M. Guélin, C. Kahane, E. Roueff, J. Kłos, F. Aoiz, F. Lique, et al. (July 2010). "Astronomical identification of CN^-, the smallest observed molecular anion." In: *Astronomy & Astrophysics* 517, p. L2 (cit. on p. 2).
DOI: 10.1051/0004-6361/201015186.
arXiv:1007.0662 [astro-ph.GA].

Asvany, O. and S. Schlemmer (2009). "Numerical simulations of kinetic ion temperature in a cryogenic linear multipole trap." In: *International Journal of Mass Spectrometry* 279.2-3, pp. 147 –155 (cit. on pp. 53, 70).
DOI: 10.1016/j.ijms.2008.10.022.

Balbus, S. and J. Hawley (July 1991). "A powerful local shear instability in weakly magnetized disks. I - Linear analysis. II - Nonlinear evolution." In: *The Astrophysical Journal* 376, pp. 214–233 (cit. on p. 3).
DOI: 10.1086/170270.

Balser, D., T. Bania, R. Rood, and T. Wilson (Jan. 1999). "^{3}He in the Milky Way Interstellar Medium: Abundance Determinations." In: *The Astrophysical Journal* 510, pp. 759–783 (cit. on p. 4).
DOI: 10.1086/306598.

Bartmess, J. (2012). "NIST Chemistry WebBook, NIST Standard Reference Database Number 69." In: ed. by P. Linstrom and W. Mallard. retrieved May 28, 2012. Gaithersburg MD, 20899: National Institute of Standards and Technology. Chap. Negative Ion Energetics Data (cit. on p. 58).
URL: http://webbook.nist.gov.

Bates, D. R. and A. E. Kingston (1964). "Collisional-radiative recombination at low temperatures and densities." In: *Proceedings of the Physical Society* 83.1, p. 43 (cit. on p. 92).
DOI: 10.1088/0370-1328/83/1/307.

Baumjohann, W. and R. A. Treumann (2012). *Basic space plasma physics*. Imperial College Press (cit. on p. 49).

Beamson, G., H. Q. Porter, and D. W. Turner (1980). "The collimating and magnifying properties of a superconducting field photoelectron spectrometer." In: *Journal of Physics E: Scientific Instruments* 13.1, p. 64 (cit. on p. 36).
DOI: doi:10.1088/0022-3735/13/1/018.

Bieniek, R. and A. Dalgarno (Mar. 1979). "Associative detachment in collisions of H and H^-." In: *The Astrophysical Journal* 228, pp. 635–639 (cit. on pp. 6, 8).
DOI: 10.1086/156889.

Birdsall, C. K. and A. B. Langdon (1991). *Plasma Physics via Computer Simulation*. Philadelphia: IOP Publishing (cit. on pp. 12, 14, 25, 26, 89, 98).

Borodi, G., A. Luca, and D. Gerlich (2009). "Reactions of CO_2^+ with H, H_2 and deuterated analogues." In: *International Journal of Mass Spectrometry* 280.1-3, pp. 218 –225 (cit. on pp. 69, 73, 75).
DOI: 10.1016/j.ijms.2008.09.004.

Bossavit, A. (1998). *Computational Electromagnetism*. Boston: Academic Press (cit. on p. 12).

Bruhns, H., H. Kreckel, K. A. Miller, X. Urbain, and D. W. Savin (Oct. 2010). "Absolute energy-resolved measurements of the $H^- + H \rightarrow H_2 + e^-$ associative detachment reaction using a merged-beam apparatus." In: *Physical Review A: General Physics* 82.4, p. 042708 (cit. on pp. 7, 78).
DOI: 10.1103/PhysRevA.82.042708.

Byron, S., R. C. Stabler, and P. I. Bortz (May 1962). "Electron-Ion Recombination by Collisional and Radiative Processes." In: *Physical Review Letters* 8 (9), pp. 376–379 (cit. on p. 92).
DOI: 10.1103/PhysRevLett.8.376.

Callen, J. D. (2006). *Fundamentals of Plasma Physics*. online textbook, retrieved June 2012 (cit. on p. 31).
URL: http://homepages.cae.wisc.edu/~callen/book.html.

CDMS (2012). online. The Cologne Database for Molecular Spectroscopy (cit. on p. 2).
URL: http://www.astro.uni-koeln.de/cdms.

Chen, F. F. (1974). *Introduction to Plasma Physics*. New York: Plenum Press (cit. on pp. 19, 31, 49).

Čížek, M., J. Horáček, and W. Domcke (June 1998). "Nuclear dynamics of the H collision complex beyond the local approximation: associative detachment and dissociative attachment to rotationally and vibrationally excited molecules." In: *Journal of Physics B: Atomic, Molecular and Optical Physics* 31, pp. 2571–2583 (cit. on pp. 6–8, 78, 79, 108).
DOI: 10.1088/0953-4075/31/11/018.

Collins, C. B., H. S. Hicks, W. E. Wells, and R. Burton (Oct. 1972). "Measurement of the Rate Coefficient for the Recombination of He^+ with Electrons." In: *Physical Review A: General Physics* 6 (4), pp. 1545–1558 (cit. on p. 92).
DOI: 10.1103/PhysRevA.6.1545.

Cravath, A. M. (July 1930). "The Rate at Which Ions Lose Energy in Elastic Collisions." In: *Physical Review* 36 (2), pp. 248–250 (cit. on p. 94).
DOI: 10.1103/PhysRev.36.248.

Crompton, R. W. and A. I. McIntosh (1968). "Electron Drift and Diffusion in Parahydrogen at 77 K." In: *Australian Journal of Physics* 21, pp. 637–648 (cit. on p. 94).
DOI: 10.1071/PH680637.

D'Angelo, N. (Jan. 1961). "Recombination of Ions and Electrons." In: *Physical Review* 121 (2), pp. 505–507 (cit. on p. 92).
DOI: 10.1103/PhysRev.121.505.

Darling, T. W., F. Rossi, G. I. Opat, and G. F. Moorhead (Jan. 1992). "The fall of charged particles under gravity: A study of experimental problems." In: *Reviews of Modern Physics* 64.1, pp. 237–257 (cit. on p. 55).
DOI: 10.1103/RevModPhys.64.237.

Davis, T. A. (June 2004a). "A column pre-ordering strategy for the unsymmetric-pattern multifrontal method." In: *ACM Transactions on Mathematical Software* 30.2, pp. 165–195 (cit. on p. 15).
DOI: 10.1145/992200.992205.

— (June 2004b). "Algorithm 832: UMFPACK V4.3—an unsymmetric-pattern multifrontal method." In: *ACM Transactions on Mathematical Software* 30.2, pp. 196–199 (cit. on p. 15).
DOI: 10.1145/992200.992206.

Davis, T. A. and I. S. Duff (Mar. 1999). "A combined unifrontal/multifrontal method for unsymmetric sparse matrices." In: *ACM Transactions on Mathematical Software* 25.1, pp. 1–20 (cit. on p. 15).
DOI: 10.1145/305658.287640.

Dehmelt, H. G. and F. L. Walls (July 1968). ""Bolometric" Technique for the rf Spectroscopy of Stored Ions." In: *Physical Review Letters* 21 (3), pp. 127–131 (cit. on p. 32).
DOI: 10.1103/PhysRevLett.21.127.

Deloche, R., P. Monchicourt, M. Cheret, and F. Lambert (Mar. 1976). "High-pressure helium afterglow at room temperature." In: *Physical Review A: General Physics* 13 (3), pp. 1140–1176 (cit. on p. 92).
DOI: 10.1103/PhysRevA.13.1140.

Dodin, I. Y. and N. J. Fisch (2005). "Approximate integrals of radio-frequency-driven particle motion in a magnetic field." In: *Journal of Plasma Physics* 71.03, pp. 289–300 (cit. on p. 47).
DOI: 10.1017/S0022377804003174.

Dodin, I. and N. Fisch (2006). "Nonadiabatic ponderomotive potentials." In: *Physics Letters A* 349.5, pp. 356 –369 (cit. on p. 47).
DOI: 10.1016/j.physleta.2005.09.049.

Dohnal, P., M. Hejduk, J. Varju, P. Rubovič, Š. Roučka, T. Kotrík, R. Plašil, J. Glosík, et al. (2012a). "Binary and ternary recombination of para- and ortho-H_3^+ with electrons; State selective study at 77–

200 K." In: *Journal of Chemical Physics* 136.24, 244304, p. 244304 (cit. on pp. 1, 81, 89, 100, 103, 106, 107, 109).
DOI: 10.1063/1.4730162.
URL: http://link.aip.org/link/?JCP/136/244304/1.

Dohnal, P., M. Hejduk, J. Varju, P. Rubovič, Š. Roučka, T. Kotrík, R. Plašil, R. Johnsen, et al. (2012b). "Binary recombination of para- and ortho-H_3^+ with electrons at low temperatures." In: *Philos. Trans. R. Soc. London, Ser. A*. in print (cit. on pp. 1, 81, 109).

Dougal, A. A. and L. Goldstein (Feb. 1958). "Energy Exchange between Electron and Ion Gases through Coulomb Collisions in Plasmas." In: *Physical Review* 109 (3), pp. 615–624 (cit. on pp. 31, 96).
DOI: 10.1103/PhysRev.109.615.

Elmer. Open Source Finite Element Software for Multiphysical Problems (cit. on pp. 17, 45).
URL: http://www.csc.fi/english/pages/elmer.

Esaulov, V. A., R. L. Champion, J. P. Grouard, R. I. Hall, J. L. Montmagnon, and F. Penent (1990). "Reactive scattering and electron detachment in O^- collisions with H_2. Nascent product energy distributions." In: *Journal of Chemical Physics* 92.4, pp. 2305–2309 (cit. on pp. 9–11).
DOI: 10.1063/1.457971.

Fehsenfeld, F. C., C. J. Howard, and E. E. Ferguson (1973). "Thermal energy reactions of negative ions with H atoms in the gas phase." In: *Journal of Chemical Physics* 58, pp. 5841–5842 (cit. on pp. 7, 8, 78).
DOI: 10.1063/1.1679215.

Fitzpatrick, R. (2011). *Plasma Physics*. online textbook, retrieved June 2012 (cit. on p. 19).
URL: http://farside.ph.utexas.edu/teaching/plasma/plasma.html.

Gerlich, D. (1992). "Inhomogeneous RF fields: a versatile tool for the study of processes with slow ions." In: *Advances in Chemical Physics* 82.1 (cit. on pp. 32, 34, 35, 42, 48, 68, 69, 71).

— (1995). "Ion-neutral collisions in a 22-pole trap at very low energies." In: *Physica Scripta* 1995.T59, p. 256 (cit. on pp. 69, 71).
URL: http://stacks.iop.org/1402-4896/1995/i=T59/a=035.

Gerlich, D., G. Borodi, A. Luca, C. Mogo, and M. A. Smith (2011). "Reactions between Cold CH_x^+ and Slow H and H_2." In: *Zeitschrift für Physikalische Chemie* 225, pp. 475–492 (cit. on p. 69).
DOI: 10.1524/zpch.2011.0118.

Gerlich, D. and S. Horning (1992). "Experimental investigation of radiative association processes as related to interstellar chemistry." In: *Chemical Reviews* 92.7, pp. 1509–1539 (cit. on pp. 69, 71).
DOI: 10.1021/cr00015a003.

Gerlich, D., P. Jusko, Š. Roučka, I. Zymak, R. Plašil, and J. Glosík (Apr. 2012). "Ion Trap Studies of $H^- + H \rightarrow H_2 + e^-$ between 10 and 135 K." In: *The Astrophysical Journal* 749, 22, p. 22 (cit. on pp. 1, 69, 70, 79, 108).
DOI: 10.1088/0004-637X/749/1/22.

Geuzaine, C. and J.-F. Remacle (2009). "Gmsh: A 3-D finite element mesh generator with built-in pre- and post-processing facilities." In: *International Journal for Numerical Methods in Engineering* 79.11, pp. 1309–1331 (cit. on p. 17).
DOI: 10.1002/nme.2579.
URL: http://geuz.org/gmsh/gmsh_paper_preprint.pdf.

Glosík, J., R. Plašil, I. Korolov, T. Kotrík, O. Novotný, P. Hlavenka, P. Dohnal, J. Varju, et al. (May 2009). "Temperature dependence of binary and ternary recombination of H_3^+ ions with electrons." In: *Physical Review A: General Physics* 79 (5), p. 052707 (cit. on pp. 81, 104).
DOI: 10.1103/PhysRevA.79.052707.

Glosík, J., P. Hlavenka, R. Plašil, F. Windisch, D. Gerlich, A. Wolf, and H. Kreckel (2006). "Action spectroscopy of and D_2H^+ using overtone excitation." In: *Philos. Trans. R. Soc. London, Ser. A* 364.1848, pp. 2931–2942 (cit. on p. 70).
DOI: 10.1098/rsta.2006.1866.

Glover, S. (Mar. 2008). "Chemistry and Cooling in Metal-Free and Metal-Poor Gas." In: *First Stars III*. Ed. by B. O'Shea and A. Heger. Vol. 990. American Institute of Physics Conference Series, pp. 25–29 (cit. on p. 5).
DOI: 10.1063/1.2905558.
arXiv:0708.3086.

Glover, S. C. O. (2011). "The Chemistry of the Early Universe." In: *Proceedings of the International Astronomical Union* 7.Symposium S280, pp. 313–324 (cit. on pp. 4, 40).
DOI: 10.1017/S1743921311025075.
arXiv:1107.3314v1.

Glover, S. C., D. W. Savin, and A.-K. Jappsen (Apr. 2006). "Cosmological Implications of the Uncertainty in H^- Destruction Rate Coefficients." In: *The Astrophysical Journal* 640.2, pp. 553–568 (cit. on pp. 5, 8).
DOI: 10.1086/500166.

Haase, G., M. Kuhn, and U. Langer (2001). "Parallel multigrid 3D Maxwell solvers." In: *Parallel Computing* 27.6, pp. 761 –775 (cit. on p. 17).
DOI: 10.1016/S0167-8191(00)00106-X.

Hejduk, M., P. Dohnal, J. Varju, P. Rubovič, R. Plašil, and J. Glosík (2012). "Nuclear spin state-resolved cavity ring-down spectroscopy diagnostics of a low-temperature H_3^+-dominated plasma."

In: *Plasma Sources Science and Technology* 21.2, p. 024002 (cit. on p. 81).
DOI: 10.1088/0963-0252/21/2/024002.

Hockney, R. (1971). "Measurements of collision and heating times in a two-dimensional thermal computer plasma." In: *Journal of Computational Physics* 8.1, pp. 19–44 (cit. on pp. 98, 99).
DOI: 10.1016/0021-9991(71)90032-5.

Hockney, R. W. and J. W. Eastwood (1988). *Computer Simulation Using Particles*. Bristol: Adam Hilger (cit. on p. 12).

Huba, J. D. (2011). *NRL Plasma Formulary*. Naval Research Laboratory, Washington, D.C. (cit. on p. 96).
URL: http://wwwppd.nrl.navy.mil/nrlformulary/.

Jusko, P., D. Roučka Š. Mulin, R. Plašil, and J. Glosík (2011a). "Atomic Beam Calibration for the $H^- + H$ Experiment." In: *WDS'11 Proceedings of Contributed Papers: Part II - Physics*. Prague, Czech Republic: Matfyzpress, pp. 165–168 (cit. on p. 108).

Jusko, P., Š. Roučka, D. Mulin, R. Plašil, and J. Glosík (2011b). "Atomic Beam Calibration for the $H^- + H$ Experiment." In: *WDS' Proceedings of Contributed Papers: Part II - Physics*. Prague, Czech Republic: Matfyzpress, pp. 158–164 (cit. on pp. 69, 73).

Jusko, P., Š. Roučka, R. Plašil, D. Gerlich, and J. Glosík (2012a). "Electron Spectrometer – Multipole Trap: First Experimental Results." In: *WDS'12*. (May 29–31, 2011). poster presentation. Prague, Czech Republic (cit. on p. 108).

— (2012b). "Electron Spectrometer – Multipole Trap: First Experimental Results." In: *Acta Universitatis Carolinae, Mathematica et Physica*. in preparation (cit. on p. 108).

KATRIN collaboration (2005). *KATRIN Design Report 2004*. Tech. rep. NPI ASCR Řež (cit. on p. 36).
URL: http://bibliothek.fzk.de/zb/berichte/FZKA7090.pdf.

Kokoouline, V., A. Faure, J. Tennyson, and C. H. Greene (2010). "Calculation of rate constants for vibrational and rotational excitation of the H_3^+ ion by electron impact." In: *Monthly Notices of the Royal Astronomical Society* 405.2, pp. 1195–1202 (cit. on pp. 96, 97).
DOI: 10.1111/j.1365-2966.2010.16522.x.

Kotrík, T., P. Dohnal, P. Rubovič, R. Plašil, Š. Roučka, S. Opanasiuk, and J. Glosík (2011a). "Cryo-FALP study of collisional-radiative recombination of Ar^+ ions at 40–200 K." In: *The European Physical Journal - Applied Physics* 56.02, p. 24011 (cit. on pp. 1, 80, 87, 92, 109).
DOI: 10.1051/epjap/2011110158.

Kotrík, T. (2012). PhD thesis. Charles University in Prague, Faculty of Mathematics and Physics (cit. on p. 85).

Kotrík, T., P. Dohnal, Š. Roučka, P. Jusko, R. Plašil, J. Glosík, and R. Johnsen (Mar. 2011b). "Collisional-radiative recombination

$Ar^+ + e + e$: Experimental study at 77–180 K." In: *Physical Review A: General Physics* 83 (3), p. 032720 (cit. on pp. 1, 80, 85, 92, 109).
DOI: 10.1103/PhysRevA.83.032720.

Kreckel, H., H. Bruhns, M. Čížek, S. C. O. Glover, K. A. Miller, X. Urbain, and D. W. Savin (2010). "Experimental Results for H_2 Formation from H^- and H and Implications for First Star Formation." In: *Science* 329.5987, pp. 69–71 (cit. on pp. 7, 8, 78, 79, 108).
DOI: 10.1126/science.1187191.

Le Bourlot, J., G. Pineau des Forets, and D. R. Flower (1999). "The cooling of astrophysical media by H_2." In: *Monthly Notices of the Royal Astronomical Society* 305.4, pp. 802–810 (cit. on p. 4).
DOI: 10.1046/j.1365-8711.1999.02497.x.

Lee, J. and J. J. Grabowski (1992). "Reactions of the atomic oxygen radical anion and the synthesis of organic reactive intermediates." In: *Chemical Reviews* 92.7, pp. 1611–1647 (cit. on p. 63).
DOI: 10.1021/cr00015a007.

Lee, S. T. and J. M. Farrar (1999). "Vibrational state-resolved study of the O^- + H_2 reaction: Isotope effects on the product energy partitioning." In: *Journal of Chemical Physics* 111.16, pp. 7348–7358 (cit. on pp. 8, 9, 11).
DOI: 10.1063/1.480057.

Lemmon, E., M. McLinden, and D. Friend (2012). "Thermophysical Properties of Fluid Systems." In: *NIST Chemistry WebBook, NIST Standard Reference Database Number 69*. Ed. by P. Linstrom and W. Mallard. retrieved June 2, 2012. Gaithersburg MD, 20899: National Institute of Standards and Technology (cit. on pp. 83, 86).
URL: http://webbook.nist.gov.

Logg, A., K.-A. Mardal, G. N. Wells, et al. (2012). *Automated Solution of Differential Equations by the Finite Element Method*. Springer (cit. on pp. 12, 16, 17, 44, 110).
DOI: 10.1007/978-3-642-23099-8.

Logg, A. and G. N. Wells (Apr. 2010). "DOLFIN: Automated finite element computing." In: *ACM Transactions on Mathematical Software* 37 (2), 20:1–20:28 (cit. on pp. 17, 44).
DOI: 10.1145/1731022.1731030.

Macko, P., G. Bánó, P. Hlavenka, R. Plašil, V. Poterya, A. Pysanenko, O. Votava, R. Johnsen, et al. (2004). "Afterglow studies of $H_3^+(v = 0)$ recombination using time resolved cw-diode laser cavity ring-down spectroscopy." In: *International Journal of Mass Spectrometry* 233.1–3. Special Issue: In honour of Tilmann Mark, pp. 299–304 (cit. on p. 80).
DOI: 10.1016/j.ijms.2003.12.035.

Manura, D. (2007). *Collision Model HS1*. Tech. rep. Scientific Instrument Services, Inc. (cit. on pp. 27, 28).
URL: http://simion.com/info/collision_model_hs1.html.

Martín, A., N. Bordel, R. Pereiro, and A. Bogaerts (2008). "Monte Carlo analysis of the electron thermalization process in the afterglow of a microsecond dc pulsed glow discharge." In: *Spectrochimica Acta Part B: Atomic Spectroscopy* 63.11, pp. 1274 –1282 (cit. on p. 31).
DOI: 10.1016/j.sab.2008.09.012.

Martinez, O., Z. Yang, N. B. Betts, T. P. Snow, and V. M. Bierbaum (2009). "Experimental Determination of the Rate Constant for the Associative Detachment Reaction $H^- + H \rightarrow H_2 + e^-$ at 300 K." In: *The Astrophysical Journal* 705.2, p. L172 (cit. on pp. 7, 8, 78).
DOI: 10.1088/0004-637X/705/2/L172.

Mauer, J. L. and G. J. Schulz (Feb. 1973). "Associative Detachment of O^- with CO, H_2, and O_2." In: *Physical Review A: General Physics* 7 (2), pp. 593–605 (cit. on pp. 9–11, 40, 108).
DOI: 10.1103/PhysRevA.7.593.

McCarthy, M. C., C. A. Gottlieb, H. Gupta, and P. Thaddeus (2006). "Laboratory and Astronomical Identification of the Negative Molecular Ion C_6H^-." In: *The Astrophysical Journal* 652.2, p. L141 (cit. on p. 2).
DOI: 10.1086/510238.

McFarland, M., D. Albritton, F. Fehsenfeld, E. Ferguson, and A. Schmeltekopf (Dec. 1973). "Flow-drift technique for ion mobility and ion-molecule reaction rate constant measurements. III. Negative ion reactions of O^- with CO, NO, H_2, and D_2." In: *Journal of Chemical Physics* 59, pp. 6629–6635 (cit. on p. 9).
DOI: 10.1063/1.1680043.

Meeker, D. C. (2009). *Finite Element Method Magnetics*. Version 4.2 (01Apr2009 Build) (cit. on pp. 17, 43).
URL: http://www.femm.info.

Miller, K., H. Bruhns, J. Eliášek, M. Čížek, H. Kreckel, X. Urbain, and D. Savin (Nov. 2011). "Associative detachment of $H^- + H \rightarrow H_2 + e^-$." In: *Physical Review A: General Physics* 84.5, 052709, p. 052709 (cit. on pp. 6, 7, 78).
DOI: 10.1103/PhysRevA.84.052709.
arXiv:1110.0683 [physics.atom-ph].

Molinari, S., B. Swinyard, J. Bally, M. Barlow, J.-P. Bernard, P. Martin, T. Moore, A. Noriega-Crespo, et al. (Mar. 2010). "Hi-GAL: The Herschel Infrared Galactic Plane Survey." In: *The Publications of the Astronomical Society of the Pacific* 122, pp. 314–325 (cit. on p. 3).
DOI: 10.1086/651314.
arXiv:1001.2106 [astro-ph.GA].

Müller, H., F. Schlöder, J. Stutzki, and G. Winnewisser (May 2005). "The Cologne Database for Molecular Spectroscopy, CDMS: a useful tool for astronomers and spectroscopists." In: *Journal of Molecular Structure* 742, pp. 215–227 (cit. on p. 2).
DOI: 10.1016/j.molstruc.2005.01.027.

Müller, H., S. Thorwirth, D. Roth, and G. Winnewisser (Apr. 2001). "The Cologne Database for Molecular Spectroscopy, CDMS." In: *Astronomy & Astrophysics* 370, pp. L49–L52 (cit. on p. 2).
DOI: 10.1051/0004-6361:20010367.

Nanbu, K. and Y. Kitatani (1995). "An ion-neutral species collision model for particle simulation of glow discharge." In: *Journal of Physics D: Applied Physics* 28.2, p. 324 (cit. on p. 30).
DOI: 10.1088/0022-3727/28/2/015.

Pagel, B. (1959). "Note on the collisional dissociation of the Hˆ- Ion in the solar atmosphere." In: *Monthly Notices of the Royal Astronomical Society* 119, pp. 609–+ (cit. on p. 6).
URL: http://adsabs.harvard.edu/abs/1959MNRAS.119..609P.

Palla, F., E. Salpeter, and S. Stahler (Aug. 1983). "Primordial star formation - The role of molecular hydrogen." In: *The Astrophysical Journal* 271, pp. 632–641 (cit. on pp. 4, 5).
DOI: 10.1086/161231.

Paul, W. (July 1990). "Electromagnetic traps for charged and neutral particles." In: *Reviews of Modern Physics* 62 (3), pp. 531–540 (cit. on p. 32).
DOI: 10.1103/RevModPhys.62.531.

Pekárek, Z., M. Lahuta, and R. Hrach (2007). "Improving performance of multi-dimensional Particle-In-Cell codes for modelling of medium pressure plasma." In: *Journal of Physics: Conference Series* 63.1, p. 012009 (cit. on p. 14).
DOI: 10.1088/1742-6596/63/1/012009.

Petschek, H. and S. Byron (1957). "Approach to equilibrium lonization behind strong shock waves in argon." In: *Annals of Physics* 1.3, pp. 270–315 (cit. on p. 31).
DOI: 10.1016/0003-4916(57)90012-X.

Phelps, A. V. (2001). "Compilation of Electron Cross Sections." online (cit. on p. 94).
URL: http://jilawww.colorado.edu/~avp/collision_data/.

Pitts, D. and L. E. Sissom (1998). *Schaum's Outline of Theory and Problems of Heat Transfer*. 2nd ed. McGraw-Hill Professional (cit. on pp. 82, 83).

Planck Collaboration, P. Ade, N. Aghanim, M. Arnaud, M. Ashdown, J. Aumont, C. Baccigalupi, M. Baker, et al. (Dec. 2011). "Planck early results. I. The Planck mission." In: *Astronomy & Astrophysics* 536, A1, A1 (cit. on p. 2).
DOI: 10.1051/0004-6361/201116464.
arXiv:1101.2022 [astro-ph.IM].

Plasil, R., T. Mehner, P. Dohnal, T. Kotrik, J. Glosik, and D. Gerlich (2011). "Reactions of cold trapped CH^+ ions with slow H atoms." In: *The Astrophysical Journal*. Submitted (cit. on p. 69).

Pohl, T., D. Vrinceanu, and H. R. Sadeghpour (June 2008). "Rydberg Atom Formation in Ultracold Plasmas: Small Energy Transfer

with Large Consequences." In: *Physical Review Letters* 100 (22), p. 223201 (cit. on p. 93).
DOI: 10.1103/PhysRevLett.100.223201.

Press, W. H., S. A. Teukolsky, W. T. Vetterling, and B. P. Flannery (2002). *Numerical Recipes in C*. second. Cambridge: Cambridge university press (cit. on p. 89).

Ramanlal, J. and J. Tennyson (2004). "Deuterated hydrogen chemistry: partition functions, equilibrium constants and transition intensities for the H+3 system." In: *Monthly Notices of the Royal Astronomical Society* 354.1, pp. 161–168 (cit. on p. 97).
DOI: 10.1111/j.1365-2966.2004.08178.x.

Robertson, W. W. (1965). "Collisional-Radiative Recombination of He_2^+ into Dissociative States." In: *Journal of Chemical Physics* 42.6, pp. 2064–2070 (cit. on p. 92).
DOI: 10.1063/1.1696248.

Robson, R. E. (Apr. 1976). "Diffusion cooling of electrons in a finite gas." In: *Physical Review A: General Physics* 13 (4), pp. 1536–1542 (cit. on p. 98).
DOI: 10.1103/PhysRevA.13.1536.

Rossi, F. and G. I. Opat (1992). "Observations of the effects of adsorbates on patch potentials." In: *Journal of Physics D: Applied Physics* 25.9, p. 1349 (cit. on p. 55).
DOI: 10.1088/0022-3727/25/9/012.

Roučka, Š. (2008). "Studium interakce plazma-pevná látka při středních tlacích." MA thesis. Charles University in Prague, Faculty of Mathematics and Physics (cit. on p. 109).
URL: http://www.roucka.eu/diplomka.

Roučka, Š. and R. Hrach (Nov. 2011). "Extending PIC Models to Higher Pressures - Enhanced Model of Collisions." In: *Plasma Science, IEEE Transactions on* 39.11, pp. 3244 –3250 (cit. on pp. 25, 98, 109).
DOI: 10.1109/TPS.2011.2164789.

Roučka, Š., P. Jusko, I. Zymak, D. Mulin, R. Plašil, and J. Glosík (2011). "Influence of the 22-pole Trap Imperfections on the Interaction of Ions with a Neutral Beam." In: *WDS' Proceedings of Contributed Papers: Part II - Physics*. Prague, Czech Republic: Matfyzpress, pp. 158–164 (cit. on pp. 69, 74, 108).

Roučka, Š., A. Podolník, P. Jusko, T. Kotrík, R. Plašil, and J. Glosík (2009). "Combination of a 22-pole Trap with an Electron Energy Filter – Study of Associative Detachment $H^- + H \rightarrow H_2 + e^-$." In: *WDS'09 Proceedings of Contributed Papers: Part II - Physics*. Prague, Czech Republic: Matfyzpress, pp. 121–128 (cit. on pp. 43, 108).

— (2010). "Study of Capture and Cooling of H^- Ions in RF Octopole with superimposed Magnetic Field." In: *WDS'09 Proceedings of Contributed Papers: Part II - Physics*. Prague, Czech Republic: Matfyzpress, pp. 105–111 (cit. on pp. 44, 55, 108).

Sakimoto, K. (1989). "Ion-molecule reactions at extremely low energies: $H^- + H \rightarrow H_2 + e$." In: *Chemical Physics Letters* 164.2-3, pp. 294 –298 (cit. on pp. 6, 7, 78, 79).
DOI: DOI:10.1016/0009-2614(89)85032-8.

Schmeltekopf, A., F. Fehsenfeld, and E. Ferguson (1967). "Laboratory measurement of the rate constant for $H^- + H \rightarrow H_2 + e$." In: *The Astrophysical Journal* 148, p. L155 (cit. on pp. 7, 8, 78).
DOI: 10.1086/180035.

Schöberl, J. (May 2003). *NETGEN - 4.3* (cit. on p. 110).
URL: www.hpfem.jku.at/netgen/ng4.pdf.

Schöberl, J. (1997). "NETGEN An advancing front 2D/3D-mesh generator based on abstract rules." In: *Computing and Visualization in Science* 1 (1), pp. 41–52 (cit. on pp. 17, 44).
DOI: 10.1007/s007910050004.

Schöberl, J. (2009). "Numerical Methods for Maxwell Equations." Lecture notes, retrieved March 2012 (cit. on p. 17).
URL: http://www.asc.tuwien.ac.at/~schoeberl/wiki/index.php/Lecture_Notes.

Semenov, D., Y. Pavlyuchenkov, T. Henning, S. Wolf, and R. Launhardt (Feb. 2008). "Chemical and Thermal Structure of Protoplanetary Disks as Observed with ALMA." In: *The Astrophysical Journal Letters* 673, pp. L195–L198 (cit. on p. 3).
DOI: 10.1086/528795.
arXiv:0801.1463.

Skrzypkowski, M., R. Johnsen, R. Rosati, and M. Golde (2004). "Flowing-afterglow measurements of collisional radiative recombination of argon ions." In: *Chemical Physics* 296.1, pp. 23 –27 (cit. on p. 92).
DOI: 10.1016/j.chemphys.2003.09.032.

Skullerud, H. R. (Nov. 1968). "The stochastic computer simulation of ion motion in a gas subjected to a constant electric field." In: *Journal of Physics D: Applied Physics* 1.11, p. 1567 (cit. on p. 28).
DOI: 10.1088/0022-3727/1/11/423.

Smith, M. A. and S. R. Leone (1983). "Product vibrational state distributions in thermal energy associative detachment reactions: F^-+H, D $\rightarrow$ HF(v), DF(v)+e^-." In: *Journal of Chemical Physics* 78.3, pp. 1325–1334 (cit. on pp. 6, 11, 40).
DOI: 10.1063/1.444870.

Stevefelt, J., J. Boulmer, and J.-F. Delpech (Oct. 1975). "Collisional-radiative recombination in cold plasmas." In: *Physical Review A: General Physics* 12 (4), pp. 1246–1251 (cit. on pp. 92, 93, 101, 104).
DOI: 10.1103/PhysRevA.12.1246.

Takizuka, T. and H. Abe (1977). "A binary collision model for plasma simulation with a particle code." In: *Journal of Computational Physics* 25.3, pp. 205 –219 (cit. on p. 31).
DOI: 10.1016/0021-9991(77)90099-7.

Turk, M. J., P. Clark, S. C. O. Glover, T. H. Greif, T. Abel, R. Klessen, and V. Bromm (2011). "Effects of Varying the Three-body Molecular Hydrogen Formation Rate in Primordial Star Formation." In: *The Astrophysical Journal* 726.1, p. 55 (cit. on p. 5).
DOI: 10.1088/0004-637X/726/1/55.

Vahedi, V. and M. Surendra (1995). "A Monte Carlo collision model for the particle-in-cell method: applications to argon and oxygen discharges." In: *Computer Physics Communications* 87.1-2. Particle Simulation Methods, pp. 179–198 (cit. on p. 28).
DOI: 10.1016/0010-4655(94)00171-W.

Vangioni-Flam, E., M. Casse, and J. Audouze (Aug. 2000). "Lithium-beryllium-boron: origin and evolution." In: *Physics Reports* 333, pp. 365–387 (cit. on p. 4).
DOI: 10.1016/S0370-1573(00)00030-2.
eprint: arXiv:astro-ph/9907171.

Varju, J., M. Hejduk, P. Dohnal, M. Jílek, T. Kotrík, R. Plašil, D. Gerlich, and J. Glosík (May 2011). "Nuclear Spin Effect on Recombination of H_3^+ Ions with Electrons at 77 K." In: *Physical Review Letters* 106 (20), p. 203201 (cit. on p. 81).
DOI: 10.1103/PhysRevLett.106.203201.

VTK: The Visualization Toolkit (cit. on pp. 56, 113).
URL: http://www.vtk.org/.

Walker, T., G. Steigman, H.-S. Kang, D. Schramm, and K. Olive (July 1991). "Primordial nucleosynthesis redux." In: *The Astrophysical Journal* 376, pp. 51–69 (cit. on p. 3).
DOI: 10.1086/170255.

Wardle, M. (Oct. 2007). "Magnetic fields in protoplanetary disks." In: *Astrophysics and Space Science* 311, pp. 35–45 (cit. on p. 3).
DOI: 10.1007/s10509-007-9575-8.
arXiv:0704.0970.

Weinheimer, C. (2002). "KATRIN, a next generation tritium β decay experiment in search for the absolute neutrino mass scale." In: *Progress in Particle and Nuclear Physics* 48.1, pp. 141 –150 (cit. on p. 36).
DOI: 10.1016/S0146-6410(02)00120-5.

Woodall, J., M. Agúndez, A. Markwick-Kemper, and T. Millar (May 2007). "The UMIST database for astrochemistry 2006." In: *Astronomy & Astrophysics* 466, pp. 1197–1204 (cit. on p. 3).
DOI: 10.1051/0004-6361:20064981.

Yao, W.-M. et al. (2006). "Review of Particle Physics." In: *Journal of Physics G: Nuclear and Particle Physics* 33.1. All tables, listings, and reviews (and errata) are also available on the Particle Data Group website., p. 1 (cit. on p. 4).
DOI: 10.1088/0954-3899/33/1/001.
URL: http://pdg.lbl.gov.

Zivanov, S., M. Cizek, J. Horacek, and M. Allan (2003). "Electron spectra for associative detachment in low-energy collisions of Cl- and Br- with H and D." In: *Journal of Physics B: Atomic, Molecular and Optical Physics* 36.16, p. 3513 (cit. on p. 40).
DOI: 10.1088/0953-4075/36/16/312.

Zwier, T. S., M. M. Maricq, C. J. S. M. Simpson, V. M. Bierbaum, G. B. Ellison, and S. R. Leone (Apr. 1980). "Direct Detection of the Product Vibrational-State Distribution in the Associative Detachment Reaction $Cl^- + H \rightarrow HCl(v) + e$." In: *Physical Review Letters* 44 (16), pp. 1050–1053 (cit. on p. 40).
DOI: 10.1103/PhysRevLett.44.1050.

LIST OF FIGURES

LIST OF TABLES

ACRONYMS

AB-22PT	atomic beam combined with 22-pole trap
AD	associative detachment
BBN	Big Bang nucleosynthesis
BVP	boundary value problem
CRDS	cavity ring-down spectrometer
CRR	collisional radiative recombination
CSG	constructive solid geometry
DC	direct current
DE	dissociation energy
EA	electron affinity
EEDF	electron energy distribution function
ES-MPT	electron spectrometer with a multipole trap

FDM	finite difference method
FEM	finite element method
FALP	flowing afterglow with Langmuir probe
FWHM	full width at half maximum
HARHA	half acceleration, rotation, half acceleration
MCP	microchannel plate
MAC-E	magnetic adiabatic collimator with electrostatic filter
ODE	ordinary differential equation
PDE	partial differential equation
PIC	particle in cell
QPMS	quadrupole mass spectrometer
RF	radio-frequency
SA-CRDS	stationary afterglow with cavity ring-down spectrometer
SIFT	selected ion flow tube
SIS	storage ion source
TOF	time of flight
UMFPACK	unsymmetric multifrontal sparse LU factorization package

ATTACHED PUBLICATIONS

ION TRAP STUDIES OF $H^- + H \rightarrow H_2 + e^-$ BETWEEN 10 AND 135 K

Bibliographic record of the attached publication:

Gerlich, D., P. Jusko, Š. Roučka, I. Zymak, R. Plašil, and J. Glosík (Apr. 2012). "Ion Trap Studies of $H^- + H \rightarrow H_2 + e^-$ between 10 and 135 K." In: *The Astrophysical Journal* 749, 22, p. 22. DOI: 10.1088/0004-637X/749/1/22.

The Astrophysical Journal, 749:22 (6pp), 2012 April 10 doi:10.1088/0004-637X/749/1/22
© 2012. The American Astronomical Society. All rights reserved. Printed in the U.S.A.

ION TRAP STUDIES OF $H^- + H \rightarrow H_2 + e^-$ BETWEEN 10 AND 135 K

Dieter Gerlich[1,2], Pavol Jusko[1], Štěpán Roučka[1], Illia Zymak[1], Radek Plašil[1], and Juraj Glosík[1]
[1] Faculty of Mathematics and Physics, Charles University, 18000 Prague, Czech Republic
[2] Faculty of Natural Science, Technical University, 09107 Chemnitz, Germany
Received 2011 December 7; accepted 2012 January 26; published 2012 March 19

ABSTRACT

Thermal rate coefficients for forming H_2 via associative detachment in $H^- + H$ collisions were determined using the combination of a 22-pole ion trap (22PT) with a skimmed effusive beam of atomic hydrogen penetrating the ion cloud. The temperature of both reactants have been varied independently (ion trap: $T_{22PT} = 10$–150 K, neutral beam accommodator $T_{ACC} = 10, 50, 120$ K). Using various combinations, the temperature range between 10 and 135 K has been accessed for the first time experimentally. The effective number density of H (typically some 10^8 cm^{-3}) is determined in situ via chemical probing with CO_2^+ ions. With decreasing temperature, the measured thermal rate coefficients decrease slowly from 5.5×10^{-9} cm^3 s^{-1} at 135 K to 4.1×10^{-9} cm^3 s^{-1} at 10 K. The relative error is 10%, while the absolute values may deviate systematically by up to 40%, due to uncertainties in the calibration reaction. Significant improvements of the versatile and sensitive experiment are possible, e.g., by using electron transfer from H to D^+ as calibration standard.

Key words: astrochemistry – atomic processes – early Universe – methods: laboratory – molecular processes

Online-only material: color figures

1. INTRODUCTION

The evolution of matter in the early universe toward the formation of the first stars is determined by atomic and molecular processes involving mainly hydrogen (H, D), helium (^{3}He, ^{4}He), electrons, and radiation. Traces of lithium and beryllium are assumed to play only a minor role. Since the elemental composition remains unchanged during this period, one could expect that primordial chemistry is rather simple. However, up to 200 reactions can contribute to the abundance of 23 atomic and molecular species as pointed out by Lepp et al. (2002). Important for star formation is the role of molecules as coolants, i.e., the conversion of translational energy into internal degrees of freedom via inelastic or reactive collisions, followed by radiative transitions.

There has been significant progress in improving the models which predict abundances of molecules and their role as coolants; however, in all these models, most chemical reactions are described just by simple temperature-dependent rate coefficients whereas, in principle, one would need state-to-state cross sections (or elementary rate coefficients) for describing the non-equilibrium chemistry. An example of central importance is the scrambling reaction of H^+ with H_2 and isotopic variants. This collision system is very efficient in converting kinetic energy into internal excitation of the product molecule. Important for the spectrum of the emitted radiation is that not only does vibration play a role but that also rotational states are populated very efficiently to the limit given by the available energy. A recent extensive comparison between theoretical and experimental results for collisions of $H^+ + D_2$ and $D^+ + H_2$ corroborates this statement (Jambrina et al. 2012).

Several specific uncertainties in the reaction network describing the primordial chemistry have been discussed in recent years. A special problem is the efficiency to form H_2, the most abundant molecule, and HD, which is important because it has a dipole moment (Glover et al. 2006). But also molecules such as H_3^+ and its isotopic variants or HeH^+ are considered to be important trace molecules and coolants (Glover & Abel 2008; Puy & Signore 2007). An interesting case is the HeH^+ ion. This ion (or He_2^+) is the first molecule ever formed in the primordial universe and, in sequential collisions with H atoms, first H_2^+ and then H_2 is formed. A new ab initio calculation for the proton transfer rate coefficient in $HeH^+ + H$ recently led to the conclusion that the abundance of HeH^+ is more than one order of magnitude higher than previously predicted (Bovino et al. 2011).

Formation of a hydrogen molecule from two H atoms under early universe conditions requires a catalytic gas phase reaction such as $H^+ + H \rightarrow H_2^+ + h\nu$ followed by $H_2^+ + H \rightarrow H_2 + H^+$. Besides the proton, an efficient catalyst is the electron, as soon as conditions are such that the lifetime of H^- gets long enough. The sequence is radiative attachment $e^- + H \rightarrow H^- + h\nu$ followed by associative detachment (AD)

$$H^- + H \rightarrow H_2 + e^- \quad (1)$$

Due to bound–free, free–bound, and free–free transitions, the (H–e^-) system plays an important role in the universe, for example for the continuum opacity of late-type stars or in establishing a thermal equilibrium in the photosphere of a star. Despite its abundance, H^- not yet has been observed directly via a specific transition (in the UV; see Ross et al. 2008 and references therein).

The central role of H^- in the primordial chemistry and consequences of uncertainties in several rate coefficients have been discussed by Glover et al. (2006) and Glover & Abel (2008). Theoretical calculations for reaction (1) disagreed among each other in the range of (1–5) $\times 10^{-9}$ cm^3 s^{-1} (Sakimoto 1989; Launay et al. 1991; Cizek et al. 1998). A few years ago, the only experimental results have been from flow tubes operated at room temperature and using two different schemes for producing the H atoms (Schmeltekopf et al. 1967; Fehsenfeld et al. 1973; Martinez et al. 2009).

Meanwhile, the situation has changed due to new experimental and theoretical activities. At Columbia University, D. W. Savin and coworkers have constructed a dedicated instrument based on the merged beams principle. Using a 10 keV fast H^- beam and converting a fraction of the ions into neutral atoms

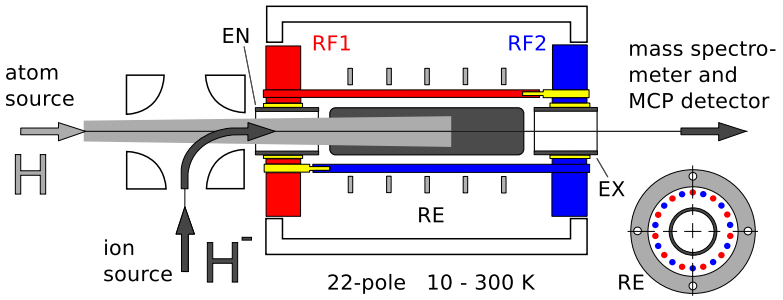

Figure 1. Detailed drawing of the central part of the 22-pole ion trap apparatus. H^- ions are injected into the trap via the electrostatic quadrupole bender. To the right, ions move via the quadrupole mass spectrometer towards the detector. The cold effusive H-atom beam comes from the left. The gray shaded areas indicate the overlap between the ion cloud and the neutral beam. For photodetachment studies, a laser beam is injected from the right.

(A color version of this figure is available in the online journal.)

via photodetachment (PD), reaction (1) could be studied at collision energies between 4 meV and 1 eV (Bruhns et al. 2010). Recently an extension to 4.8 eV has been reported by Miller et al. (2011). Despite the fact that the merged beams technology is rather complex and that the precise detection of the neutral H_2 products from reaction (1) is a challenge, rate coefficients have been determined with rather high accuracy, the total systematic error has been estimated to be only ±24% (Kreckel et al. 2010; Bruhns et al. 2010; Miller et al. 2011).

The merged beams results are in very good agreement with calculated cross sections (Cizek et al. 1998) but there is still a discrepancy, not only with the above-mentioned old flow tube measurements but also with recent rate coefficients determined at the University of Colorado, Boulder, with a tandem flowing afterglow–selected ion flow tube (Martinez et al. 2009). The old and new flow tube measurements agree with each other; however, they are a factor of 2.2 ± 0.9 smaller than the recently slightly correct merged beams results (Miller et al. 2011). It has been suspected in Bruhns et al. (2010) that the discrepancy may be due to an error in the AD calibration reaction $Cl^- + H$ used for determining the H-atom density in the flow tube. Looking at the recent activities related to the specific reaction (1) and realizing that there are certainly more uncertainties in the models simulating the processes in the pregalactic era, it becomes obvious that more dedicated experimental activities are needed.

In the following, we report first results for reaction (1) obtained with an ion trapping instrument, a versatile method which is complementary to the two experimental methods mentioned above and which allows us to extend the temperature range down to 10 K. After a short description of the ion trap and the effusive H-atom beam, new data are presented with emphasis on the accuracy of the absolute values, achieved so far and on planned improvements, especially concerning the determination of the effective number density of the reactants. In the outlook we will mention other primordial reactions which can be studied using temperature variable ion traps and give a short summary to ongoing activities for detecting the electrons produced by reaction (1).

2. EXPERIMENTAL

2.1. 22PT Ion Trap

The instrument used in this study was developed at the Chemnitz University of Technology and is now operated successfully at the Charles University in Prague. It is based on the combination of a radio-frequency (rf) 22-pole ion trap with an effusive beam source for atomic hydrogen (AB-22PT). The method of using inhomogeneous rf fields for storing ions has been summarized in Gerlich (1992). Technical details of the present experimental setup can be found in Borodi (2008) and Borodi et al. (2009). Previous studies of the interaction of stored CH_n^+ ions with H atoms have been reported in Gerlich et al. (2011) and Plasil et al. (2011).

The geometry of the region where the trapped ion cloud and the neutral beam interact is shown in some detail in Figure 1. The importance of determining the effective volume where the reactants overlap is discussed below. Primary H^- ions are produced by electron bombardment of H_2 precursor gas in a storage ion source (Gerlich 1992). After prethermalization in the source, the ions are mass selected using a quadrupole filter, bent by 90° using an electrostatic quadrupole and injected into the 22-pole trap. In the radial direction, the ions are confined by the rf field created by two sets of 11 poles (RF1 and RF2) precisely mounted on both sides. The potential inside the trap can be corrected locally using the five ring electrodes (RE). The entrance and exit electrode (EN and EX) are used to open and close the trap with electrostatic barriers of some tens of meV. After various storage times the exit electrode is opened, the ions leave the trap, pass through the QP mass spectrometer, and they are converted into a short current pulse using a micro channel plate detector (MCP assembly F4655-12, Hamamatsu). The pulses are accumulated in a 100 MHz counter.

The standard sequence (1) filling the trap repetitively with a well-defined number of primary ions, (2) storing them for various times, and (3) detecting them is averaged over many iterations, for reducing the statistical errors. For comparison, the number of ions, $N_i(t)$, is normalized to one iteration or normalized to the total number of ions. In general, there is no loss of ions, i.e., the total *number per filling* remains constant. In the present experiment, the charged products from the AD reaction are electrons which cannot be detected in the current experimental setup. A method to guide them out from the rf field by superimposing a suitable magnetic field is under development.

The temperature of the ion trap, T_{22PT}, can be varied between 10 K and 300 K. Ions are cooled to the trap temperature by collisions with H_2 buffer gas. For relaxing the kinetic energy of H^-, a few collisions are sufficient. As discussed by Gerlich (1992) and emphasized in Gerlich (2008a), the influence of the micromotion driven by the oscillating confining field—effects referred to as radio frequency heating—is negligible if high

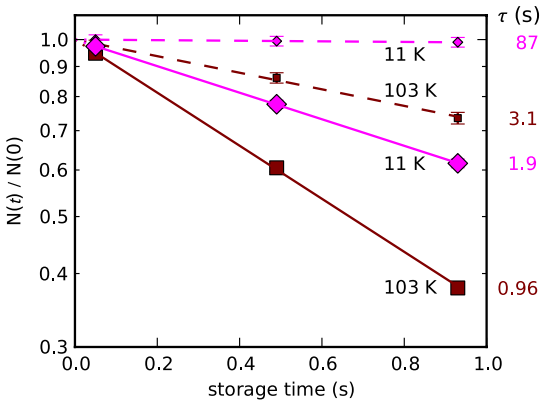

Figure 2. Relative number of H^- ions per filling as a function of storage time (ion trap temperature: $T_{22PT} = 11$ and 103 K, hydrogen beam temperature $T_{ACC} = 50$ K, small and large symbols correspond to H-atom beam OFF and ON, respectively. The statistical errors are in the order of or smaller than the size of the symbols. Fitting the data with $\exp(-t/\tau)$ (solid and dashed lines) leads to the time constants τ shown on the right.

(A color version of this figure is available in the online journal.)

enough frequencies are used. Problems may be caused by potential distortions or parasitic low frequency fields.

2.2. Atomic Beam

H atoms are produced by dissociation of H_2 in an rf discharge operating at 0.2 mbar and a gas flow of 5×10^{-3} mbar l s^{-1}. For slowing down the gas emerging from the hot discharge, an accommodator is used the temperature of which can be tuned to 6 K $< T_{ACC} <$ 300 K. It consists of a channel in a copper block (2 mm diameter, length 22 mm) which is coated with a $\sim$50 μm thick layer of PTFE for reducing recombination. A mechanical shutter can block the H beam (beam ON or OFF). The geometrical arrangement of apertures and differential pumping ensures that a well-collimated beam (divergence $< 1^\circ$) passes through the trap without hitting any surface. The gray shaded areas in Figure 1 indicate the overlap between the ion cloud and the neutral beam. The volume of the ion cloud is $\sim$1.5 cm^3, the interaction volume is about one quarter.

The actual velocity distributions of atoms and molecules emerging from the accommodator have been determined using time-of-flight measurements. The obtained distributions are in a good agreement with Maxwellians the actual temperatures of which are very close to the accommodator temperature. Deviations are less than 2 K or a few percent, whichever is larger. In deviation from the description in Borodi et al. (2009), all measurements of this study have been performed without hexapole magnets for focusing the beam of H atoms. Although this leads to a much lower effective number density in the trap (about one order of magnitude; see Borodi et al. 2009), it has the advantage that one can use flux conservation for absolute calibration, i.e., the total number of H flowing through the accommodator (as atom or in a molecule) remains unchanged if the discharge is switch on or off.

2.3. Typical Raw Data

Figure 2 shows a typical set of raw data. Plotted is the relative number of H^- ions per filling, $N(t)/N(0)$, as a function of trapping time. The repetition period was set to 1 s. The number of initially injected ions, typically 100 H^- per filling, is checked after 20 ms, when most of them have already been thermalized in collisions with ambient hydrogen. Typically H_2 densities have been 10^{12} cm^{-3}, mainly from the ion source gas. Higher densities have also been tested without any effect. Extracting the ions at later times reveals a more or less slow loss, depending on the temperature of the trap and on the presence of the H-atom beam (small symbols and dashed lines: beam OFF, large symbols and solid lines: beam ON). The data have been fitted with exponential functions, resulting in time constants τ longer than 1 minute and shorter than 1 s (see numbers on the right side of Figure 2). Without H atoms the slow loss of primary ions is caused by reactions with ambient background gas. At 11 K, cryopumping inside the trap leads to long storage times. For extending the measurements toward higher temperatures, better vacuum conditions are needed. The rate coefficients for reaction (1) are simply determined from the difference of the rates with the H beam ON and OFF and the effective number density of the H atoms.

Table 1
Diameter of the Ion Cloud (d_1 for H^- and d_2 for CO_2^+ for Different Kinetic Energies E of the Ions Calculated from the Effective Potential (Gerlich 1992)

E (meV)	d_1 (mm)	d_2 (mm)	$(d_1/d_2)^2$
100	9.21	8.17	1.271
10	8.21	7.28	1.272
1	7.32	6.49	1.272

Notes. The 22-pole has been operated with $\Omega/2\pi = 18$ MHz and $V_0 = 50$ V and 25 V for mass 44 and 1, respectively. Note that the inner free diameter of the 22-pole is 10 mm. Assuming that the kinetic energy distributions of CO_2^+ and H^- are the same, the volume of the CO_2^+ cloud is about 1.27 times the volume of the H^- ions as can be seen from $(d_1/d_2)^2$, the ratio of the areas.

2.4. Effective Number Density

In order to extract absolute rate coefficients from the experiment, one has to account for the spatial distribution of the reactants and for their velocity distributions. Special aspects concerning kinematic averaging in neutral beam–ion trap arrangements can be found in Gerlich (2008a, 2008b) and Gerlich & Borodi (2009). For determining the distribution of the relative velocity, it is safe to assume in the present arrangement that we have two ensembles, thermalized to T_{22PT} and T_{ACC}. In such a case the temperature (in the center-of-mass frame) is the mass-weighted average of the two temperatures. For reaction (1) one gets

$$T = (T_{22PT} + T_{ACC})/2. \quad (2)$$

Note that in our beam-trap arrangement reactions occur only in the nearly field-free region, since the target density goes to zero in regions of large amplitude micromotion. As indicated in Figure 1, it is straightforward to account for the spatial overlap, at least under ideal conditions, i.e., a well-skimmed neutral beam with a diameter of 4 mm, an angular divergence of 0.°7 and a homogeneous density in the region of overlap, and an ion cloud the distribution of which is determined by the effective potential and the temperature of the ions. Some parameters relevant for trapping H^- can be found in Table 1. In the axial direction, the electrodes EN and EX are used to close the trap with dc voltages. A few tens of mV are sufficient for confining the ions.

In reality the potential of the ion trap may be influenced by geometrical effects, by perturbations of the surface potential, or by other stray fields. Related experimental tests and strategies to avoid or reduce such effects have been discussed in Gerlich

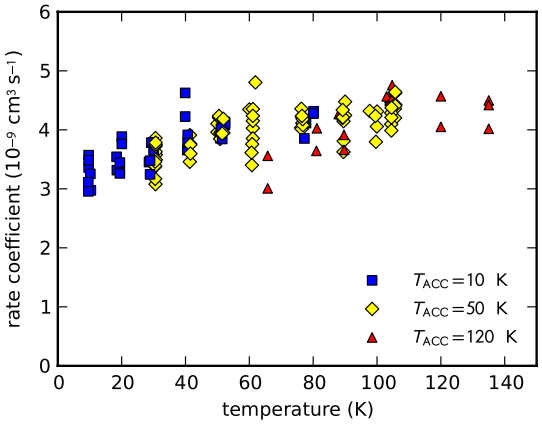

Figure 3. Measured rate coefficients, shown as a function of the translational temperature. The data shown as squares, diamonds, and triangles have been measured at $T_{ACC} = 10$, 50, and 120 K, respectively. Variation of T_{22PT} between 10 and 150 K covers each time a range of 70 K (in the center-of-mass system).

(A color version of this figure is available in the online journal.)

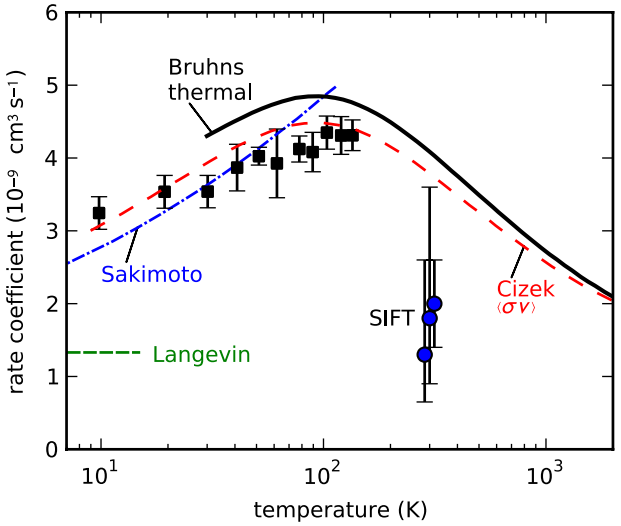

Figure 4. Comparison of our ion trap results (squares; bars indicate the statistical errors; the systematic uncertainty is larger; see the text) with previous measurements and results from theory. The solid line indicates the thermal rate coefficient $k(T)$, derived from the merged beams data published by Bruhns et al. (2010). The theoretical results of Sakimoto (1989) and Cizek et al. (1998) are in good overall accord agreement, while the Langevin limit and the 300 K flow tube measurements are significantly smaller (from left to right: Schmeltekopf et al. 1967; Fehsenfeld et al. 1973; Martinez et al. 2009; shifted for better readability).

(A color version of this figure is available in the online journal.)

(1992, 2008a). An odd situation has been reported by Otto et al. (2009). The spatial distribution of the ion cloud on a 22-pole, imaged by PD, showed 10 intensity maxima close to the rods. The origin of this effect can be explained by the superposition of a dipolar field, caused by a misalignment of the two sets of electrodes against each other. In our trap (see Figure 1), all 22 rods are localized rather precisely on each end. Nonetheless we observed that, at lower temperatures, the ions spend more time close to the rods than predicted from calculations. Some tests have been performed via PD with a 660 nm laser beam. Going from 100 to 10 K the PD rate dropped by 20% instead of an increase of 30% expected from the fact that colder ions are confined closer to the axis of the trap. This indicates that there are some forces attracting the ions toward the electrodes. Improvements are possible by cleaning or also by using the RE (see Figure 1), if the perturbations are localized. An alternative solution is to use a reaction for calibrating the effective overlapping volume as described in the following.

Since it cannot be excluded that the ion distribution is affected by perturbations or that some H atoms were hitting the surface of the entrance or exit electrode in the present experiment, we decided to determine the effective number density via chemical probing with CO_2^+. This method has the advantage that it accounts automatically for the real overlap integral of the spatial distributions of ions and neutrals. As described by Borodi et al. (2009), collisions of CO_2^+ with molecular hydrogen lead to HCO_2^+ while collisions with H atoms produce HCO^+. The rate coefficients for the last reaction are independent on the temperature of the CO_2^+ ions and on the velocity of the atoms. Borodi et al. (2009) recommend a value of $k(T) = 4.6 \times 10^{-10}$ cm^3 s^{-1} for H as target, and 2.2×10^{-10} cm^3 s^{-1} for D. The uncertainty was conservatively estimated to be 40%.

In the present experiment the H-atom density was measured routinely between several runs at an accommodator temperature $T_{ACC} = 50$ K, using the probing reaction. Depending on the conditions of the discharge tube, typical values of some 10^8 cm^{-3} have been obtained. The results have been corrected for the mass dependence of the effective potential which scales with $V_0{}^2/(m\Omega^2)$. Selected ion trap parameters used for CO_2^+ and H^- are given in Table 1.

3. RESULTS AND DISCUSSION

Rate coefficients for reaction (1) have been measured in several iterations and under various conditions as described above. Usually data were collected by holding the accommodator temperature fixed and by varying the 22-pole temperature between 10 and 150 K. Higher trap temperatures could not be used because of ion loss due to reactions with gas impurities. Figure 3 shows a collection of typical sets of data as a function of translational temperature, each of them covering a range of 70 K. As indicated, the different symbols correspond to $T_{ACC} = 10$, 50, and 120 K. The 50 K values are absolute based on the calibration reaction while the two other sets of measurements have been matched to them using the region where the data overlap. Higher temperatures T_{ACC} are possible; however, the dissociation degree of the H-atom source decreases (Borodi 2008). The overall trend is well reproduced accounting for the statistical uncertainties of each data point. All individual data were reduced by binning leading to the result plotted in Figure 4. The error bars represent the standard deviation of each data point. Not shown is the fact that there is a systematic uncertainty of 40%. As discussed above it is caused by the calibration reactions. Below 20 K the actual ion temperature may be higher by up to 5 K, at higher temperatures the error is less than 2%.

In the overlapping regime, our results are in good accordance with the results from Bruhns et al. (2010). For better comparison, their experimental results which have a total systematic uncertainty of 24% are represented just by the solid curve taken from Figure 10 of Bruhns et al. (2010). Note that this curve, showing the derived thermal rate coefficients, should be shifted up by 8.6% according to a recent new evaluation (Miller et al. 2011). For solving the discrepancy with the flow measurements, it is mandatory to extend the ion trap experiments to higher temperatures. This is possible by improving the vacuum conditions,

e.g., by mounting the trap on a different support such that it can be baked. Alternatively, there is the possibility to create a fast beam of H atoms.

Inspection of Figure 4 reveals the good agreement of our data with the low temperature prediction of the two theories (Sakimoto 1989; Cizek et al. 1998). They are both based on the same interaction potential from Senekowitsch et al. (1984) which is significantly more attractive than the polarization potential. A recent new calculation of the potential curve (Pichl 2005) agrees well and it is stated that further improvements have to account for correlation effects in the electron and proton motion. Sakimoto (1989) discussed convincingly the fact that at energies below 0.1 eV the rate coefficient for reaction (1) is determined just by a simple capture condition at large distances. During the succeeding approach of the two atoms, the probability to detach the electron is close to unity. From this point of view, our data may indicate that the potential is even more attractive at distances which are probed by 1 meV collisions (partial waves up to $l = 10$, turning point at distances larger than 10 a_0).

For such conclusions, we have to reduce the uncertainties in the determination of absolute rate coefficients and in our temperature scale. This is possible by better characterizing the flux of the H-atom beam (see discussion by Borodi et al. 2009) and by characterizing the ion cloud using PD. The ions can be influenced by varying the effective potential and shifted with the correction electrodes. Cleaning the electrodes (stainless steel) always has some effect on potential distortions. Since a calibration reaction has a lot of advantages, it is also planned to establish the exothermic electron transfer from H to D^+ as one. Since this one-electron system is much better understood from first principles than the three-electron reaction (1), it is ideal for determining the effective H density. Also the reverse process, the 3.70 meV endothermic electron transfer from D to H^+ is well characterized by theory (Esry et al. 2000). The threshold onset is a critical test of the instrument.

A final remark has to be made regarding reaction (1). Measured absolute integral cross sections (or rate coefficients) are in general a critical test for theory; however, in the present case the outcome of the H^- + H collision is rather insensitive to the actual AD process occurring at distances of a few a_0. A more sensitive experiment is to observe the competition between electron transfer and AD in H^- + D and D^- + H collisions. Corresponding work is in progress. Most information on the details of the dynamics can be obtained by determining how the exothermicity of 3.724 eV is distributed among the degrees of freedom of the products, i.e., the kinetic energy of the electron and the rovibrational population of H_2. The population of the rotational states is mainly determined by conservation of total angular momentum since only p-electrons are ejected. From this it can be concluded that, for example at a collision energy of a few meV (corresponding to $J_{MAX} \sim 20$), more than 1 eV goes into rotation of H_2. The actual population of the vibrational states depends on the coupling in the collision complex. Interesting predictions already have been made by Cizek et al. (1998; see Figure 5). Such information is certainly also of importance for cooling early universe matter.

4. CONCLUSION AND OUTLOOK

Using the rf ion trapping technique and by exposing an H^- ion cloud to a cold effusive beam of hydrogen atoms, thermal rate coefficients for reaction (1) have been measured in a temperature range so far unexplored. The temperature dependence is in accordance with simple theoretical predictions based on capture via the long-range attraction. In the overlapping energy range, there is good agreement with the merged beams results reported by Kreckel et al. (2010), Bruhns et al. (2010), and Miller et al. (2011). Due to our rather large systematic uncertainty, caused by the calibration reaction, our present results cannot solve the discrepancy between merged beams and flow tube results at 300 K (Martinez et al. 2009). Improving the accuracy of our instrument and going to higher temperatures will solve this problem. Work is in progress to use the electron transfer in D^+ + H collisions as calibration standard.

The versatile instrument opens up new possibilities to study reactions which are of interest for early universe chemistry or which are of central importance for testing fundamental theories. The need to determine state specific rate coefficients for HeH^+ ($v = 0$, j) + H, which was mentioned in Section 1. Radiative association of two atoms, especially with H, is an experimental challenge. With today's technologies, it should be possible to detect HeH^+ from H^+ + He. Storing H^- and operating the beam source with deuterium will allow us to study the competition between electron transfer and AD in H^- + D. Also mutual neutralization of H^- and H^+ can be studied in a trap since the effective potential is proportional to the square of the charge, i.e., the rf field confines simultaneously positive and negative ions.

A challenge for theoretical predictions for reaction (1) is an experiment which can determine the kinetic energy of the detached electrons and which provides information on the rovibrational population of the H_2 product. Simulations show that one can superimpose an rf field and a suitable magnetic field such that electrons are guided out of the trap and that one can detect them. Moreover, the integration of an electron spectrometer using magnetic adiabatic collimation should be possible. Corresponding work is in progress.

The AB-22PT instrument has been developed in Chemnitz with contributions from S. Schlemmer, G. Borodi, and A. Luca and the help from many other people. Financial support of the Deutsche Forschungsgemeinschaft (DFG) via the Forschergruppe FOR 388 "Laboratory Astrophysics" is gratefully acknowledged. Since 2010 the instrument has been operated in the Faculty of Mathematics and Physics of the Charles University in Prague, also within the COST Action CM0805 (The Chemical Cosmos). We thank the Chemnitz University of Technology and the DFG for making this transfer possible. This work is a part of the research plan MSM 0021620834 and grant OC10046 financed by the Ministry of Education of the Czech Republic. It was also partly supported by GACR (202/07/0495, P209/12/0233, 205/09/1183, 202/09/0642) and by GAUK 25709, GAUK 406011, GAUK 388811.

REFERENCES

Borodi, G. 2008, PhD thesis, TU Chemnitz, http://nbn-resolving.de/urn:nbn:de:bsz:chl-200900932
Borodi, G., Luca, A., & Gerlich, D. 2009, Int. J. Mass Spectrom., 280, 218
Bovino, S., Tacconi, M., Gianturco, F. A., & Galli, D. 2011, A&A, 529, A140
Bruhns, H., Kreckel, H., Miller, K. A., Urbain, X., & Savin, D. W. 2010, Phys. Rev. A, 82, 042708-1
Cizek, M., Horacek, J., & Domcke, W. 1998, J. Phys. B: At. Mol. Opt. Phys., 31, 2571
Esry, B. D., Sadeghpour, H. R., Wells, E., & Ben-Itzhak, I. 2000, J. Phys. B: At. Mol. Opt. Phys., 33, 5329
Fehsenfeld, F. C., Howard, C. J., & Ferguson, E. E. 1973, J. Chem. Phys., 58, 5841
Gerlich, D. 1992, Adv. Chem. Phys., 82, 1

Gerlich, D. 2008a, in Low Temperatures and Cold Molecules, ed. I. W. M. Smith (Singapore: Imperial College Press), 121
Gerlich, D. 2008b, in Low Temperatures and Cold Molecules, ed. I. W. M. Smith (Singapore: Imperial College Press), 295
Gerlich, D., & Borodi, G. 2009, Faraday Discuss., 142, 57
Gerlich, D., Borodi, G., Luca, A., Mogo, C., & Smith, M. 2011, Z. Phys. Chem., 252, 475
Glover, S., & Abel, T. 2008, MNRAS, 388, 1627
Glover, S., Savin, D. W., & Jappsen, A.-K. 2006, ApJ, 640, 553
Jambrina, P. G., Alvarino, J. M., Gerlich, D., et al. 2012, Phys. Chem. Chem. Phys., 14(10), 3346
Kreckel, H., Bruhns, H., Čížek, M., et al. 2010, Science, 329, 69
Launay, J. M., Le Dourneuf, M., & Zeippen, J. 1991, A&A, 252, 842
Lepp, S., Stancil, P. C., & Dalgarno, A. 2002, J. Phys. B: At. Mol. Opt. Phys., 35, R57
Martinez, O., Yang, Z., Betts, N. B., Snow, T. P., & Bierbaum, V. M. 2009, ApJ, 705, L172
Miller, K. A., Bruhns, H., Eliasek, J., et al. 2011, Phys. Rev. A, 84, 052709
Otto, R., Hlavenka, P., Trippel, S., et al. 2009, J. Phys. B: At. Mol. Opt. Phys., 42, 154007-1
Pichl, L. 2005, Czech. J. Phys., 55, 167
Plasil, R., Mehner, T., Dohnal, P., et al. 2011, ApJ, 737, 60
Puy, D., & Signore, M. 2007, New Astron., 51, 411
Ross, T., Baker, E., Snow, T. P., et al. 2008, ApJ, 684, 358
Sakimoto, K. 1989, Chem. Phys. Lett., 164, 294
Schmeltekopf, A. L., Fehsenfeld, F. C., & Ferguson, E. E. 1967, ApJ, 118, L155
Senekowitsch, J., Rosmus, P., Domcke, W., & Werner, H.-J. 1984, Chem. Phys. Lett., 111, 211

CRYO-FALP STUDY OF COLLISIONAL-RADIATIVE RECOMBINATION OF Ar^+ IONS AT 40–200 K

Bibliographic record of the attached publication:

Kotrík, T., P. Dohnal, P. Rubovič, R. Plašil, Š. Roučka, S. Opanasiuk, and J. Glosík (2011). "Cryo-FALP study of collisional-radiative recombination of Ar^+ ions at 40–200 K." In: *The European Physical Journal - Applied Physics* 56.02, p. 24011.
DOI: 10.1051/epjap/2011110158.

Eur. Phys. J. Appl. Phys. **56**, 24011 (2011)
DOI: 10.1051/epjap/2011110158

THE EUROPEAN PHYSICAL JOURNAL
APPLIED PHYSICS

Regular Article

Cryo-FALP study of collisional-radiative recombination of Ar^+ ions at 40–200 K

T. Kotrík[a], P. Dohnal, P. Rubovič, R. Plašil, Š. Roučka, S. Opanasiuk, and J. Glosík

Department of Surface and Plasma Physics, Faculty of Mathematics and Physics, Charles University, V Holešovičkách 2, Praha 18000, Czech Republic

Received: 14 April 2011 / Received in final form: 26 July 2011 / Accepted: 25 August 2011
Published online: 28 October 2011 – © EDP Sciences 2011

Abstract. New flowing afterglow apparatus, Cryo-FALP, was built to study ternary Collisional-Radiative Recombination (CRR) of Ar^+ ions with electrons in He/Ar afterglow plasma at temperatures 40–200 K. The obtained ternary recombination rate coefficient at 57 K is $K_{CRR} = (3\pm1)\times10^{-17}\,cm^6\,s^{-1}$. It is the first time that the K_{CRR} was measured below 77 K. The measured temperature dependence $K_{CRR} \sim T^{(-4.5\pm0.4)}$ is in a good agreement with theoretical prediction.

1 Introduction

A binary recombination of singly charged atomic cations with electrons is slow process comparing to a dissociative recombination (DR) of molecular ions (like O_2^+ or H_3^+, etc.). In low temperature plasma an overall recombination process can be enhanced by a ternary process where part of the recombination energy is transferred to a third particle (neutral or charged). When plasma electrons act as energy-removing third bodies, the process is referred to as collisional-radiative recombination, CRR. Schematically, the mechanism of collisional-radiative recombination can be described by the formula:

$$A^+ + e + e \xrightarrow{\alpha_{CRR}} A + e, \tag{1}$$

where A^+ denotes positive ion in general, e indicates electron and α_{CRR} corresponds to the effective binary recombination rate coefficient of CRR. The theory of CRR was originally developed by Bates et al. [1] and Mansbach and Keck [2]. The analytical formula derived by Stevefelt et al. [3] for the effective binary rate coefficient of CRR has the form:

$$\begin{aligned}\alpha_{CRR} &= 3.8\times10^{-9}T_e^{-4.5}n_e + 1.55\times10^{-10}T_e^{-0.63} \\ &\quad + 6\times10^{-9}T_e^{-2.18}n_e^{0.37}\,cm^3\,s^{-1},\end{aligned} \tag{2}$$

where T_e is the electron temperature given in K and n_e is the electron number density given in cm^{-3}. The first term belongs to the pure recombination through a collision with electron (note strong temperature dependence), the second term corresponds to the radiative recombination, where the exceeding energy is carried away by an emitted photon, and the third term accounts for the coupling between the collisional and radiative recombination. As only higher-order Rydberg states participate in the CRR process, formula (2) holds more or less for all atomic and to some extent also molecular ions (for details see Ref. [3] and references therein). This formula was confirmed also by the quantum mechanical calculations [4–6]. At our experimental conditions ($n_e \sim 10^9\,cm^{-3}, T_e < 200\,K$) the first term (pure recombination through collision with electron) is dominant and the other two terms can be neglected. Then the recombination process can be described by the simpler ternary recombination rate coefficient: $K_{CRR} = \alpha_{CRR}/n_e = 3.8\times10^{-9}T_e^{-4.5}\,cm^6\,s^{-1}$.

Previous experimental studies have been carried out mostly at higher electron temperatures (1000–4000 K, see compilation in [4]) and in only few cases also at 300 K [7–10]. It is not obvious that the Stevefelt formula holds also at low temperatures (below 300 K). Only very recently CRR was studied in our laboratory at temperatures below 200 K and K_{CRR} was obtained for temperatures from 77 up to 200 K [11]. Process of CRR has been studied also in ultracold plasmas in connection with the formation of neutral antihydrogen, where it is expected that at high positron number density the production of antihydrogen via recombination of positrons with antiprotons can be enhanced by CRR process. Nevertheless in these experiments CRR is influenced by the presence of strong magnetic field confining the plasma and neutralization process can have different character [12–14].

To study CRR in low temperature plasma we constructed a new flowing afterglow apparatus, Cryo-FALP, where afterglow plasma can be cooled down to 40 K. In this paper we present the first results of the study of recombination in plasma dominated by Ar^+ ions in the temperature range of 40–77 K. It is the first FALP apparatus ever built to operate at temperatures below the boiling point of liquid nitrogen.

[a] e-mail: kotrik.tomas@gmail.com

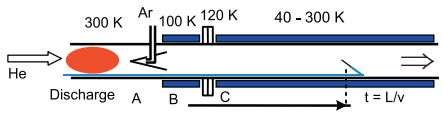

Fig. 1. (Color online) Scheme of the Cryo-FALP apparatus. The temperatures of sections A and B are fixed at 300 and 100–120 K respectively. The temperature of section C can be adjusted to a required value in the range of 40–300 K. The plasma decay time is given by the position in the flow tube. The axially movable Langmuir probe is used to monitor plasma decay along the flow tube, decay time $t = L/v_{\mathrm{PLASMA}}$.

2 Experiment

Modified version of the Flowing Afterglow with Langmuir Probe (FALP, for original design see Ref. [15]) apparatus – Cryo-FALP (for details on the previous versions of FALP apparatuses operating at higher pressure see Refs. [16–19]) was built and used to study CRR at temperatures down to 40 K. Scheme of the Cryo-FALP is shown in Figure 1. Helium buffer gas (300–800 Pa) is flowing through a glass discharge tube into a stainless steel flow tube. Plasma, consisting of helium ions (He^+, He_2^+), helium metastables (He^m) and electrons, is created in pure He by a microwave discharge (2.54 GHz, 10–20 W) ignited in a cavity attached to the glass discharge tube. Plasma is then driven along the flow tube by the flow of helium buffer gas. Downstream from the discharge region argon gas is added to the flow tube and Ar^+ dominated plasma is formed in the sequence of ion-molecule reactions:

$$\begin{aligned}
&He^+ + 2He \longrightarrow He_2^+ + He,\\
&He^m + He^m \longrightarrow He_2^+ + e,\\
&He^+ + Ar \longrightarrow Ar^+ + He,\\
&He^m + Ar \longrightarrow Ar^+ + He + e,\\
&He_2^+ + Ar \longrightarrow Ar^+ + 2He. \qquad (3)
\end{aligned}$$

In order to set the optimal experimental conditions (He pressure and flow, Ar number density) at which Ar^+ ion is the dominant ion in afterglow plasma, a chemical kinetics model was developed and numerically solved (for details on reaction kinetics and the kinetics model see Refs. [16,17,20]).

The flow tube is divided into three sections with different temperature regime. The upstream section A of the flow tube, in which the microwave discharge is ignited, is kept at 300 K. The section further downstream, B, is cooled by liquid nitrogen to 100–120 K. The following section C is placed in a large insulating vacuum chamber and is connected via copper braids to a cold head of helium closed-cycle refrigerator (Sumitomo). The temperature of section C can be adjusted to a value between 40 and 300 K. Further details on the design and construction will be given in a separate publication.

Plasma, created in section A, undergoes many collisions with neutral particles. Through the collisions, after a short period of time outside of the discharge region (∼ms), electrons and ions thermalize to the temperature

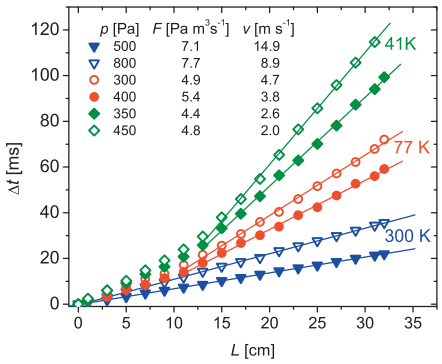

Fig. 2. (Color online) The measurements of plasma velocity. The microwave discharge is modulated and the dependence of the time delay (Δt) of the response is measured as a function of the probe position (L).

of the neutral species (i.e., temperature of the walls). The thermodynamic equilibrium is reached and instead of the temperature of electrons (T_e), ions (T_i) and neutrals (T_n) only one temperature can be used: $T = T_e = T_i = T_n$ (for details and discussion on plasma species thermalization in afterglow plasma see Refs. [11,21–23]). At the beginning of section B plasma is precooled via collisions with helium buffer gas to 100–120 K and in section C to the desired temperature adjusted in the range 40–300 K (see discussion later on). Temperature of the wall is monitored by sensors (silicon diodes, thermocouples type T) mounted along the wall of the flow tube.

Recombination rate coefficients are derived from the electron density decay monitored along section C by the axially movable cylindrical Langmuir probe [17,24]. While gas flow velocity (v) (i.e., plasma flow velocity) is known, spatial position (L) of the Langmuir probe along the flow tube can be transformed into the time (t) passed since the plasma creation by the relation $t = L/v$. The decay of the electron density due to CRR and diffusion in quasineutral plasma ($[Ar^+] = n_e$) is described by the balance equation:

$$\frac{\mathrm{d}n_e}{\mathrm{d}t} = -K_{\mathrm{CRR}}\,[Ar^+]\,n_e^2 - \frac{n_e}{\tau_D} = -K_{\mathrm{CRR}}\,n_e^3 - \frac{n_e}{\tau_D}, \qquad (4)$$

where τ_D is characteristic diffusion time. K_{CRR} and τ_D can be obtained from the fit of the measured electron density decay under the assumption of K_{CRR} and τ_D being constant (for details on the data analysis see Ref. [11]).

Because of the temperature variation along sections B and C, gas density and flow velocity are changing along the flow tube. Plasma velocity v_{PLASMA} necessary for determination of the decay time is measured by the modulation of the discharge and by monitoring the time delay of the distortion along the flow tube (see Fig. 2). Plasma velocity depends on temperature (T), on gas flow (F) and on pressure (p). Because gas flow and pressure are constant along the flow tube, gas velocity is proportional to temperature (T). When the gas temperature relaxes to the wall temperature, velocity is constant (see linear fits in Fig. 2). In this region with constant temperature, from the decay of

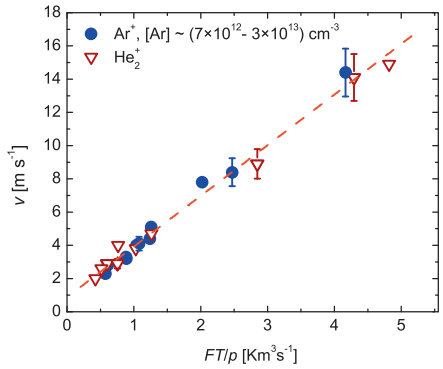

Fig. 3. (Color online) The measured dependence of plasma velocity on the "similarity parameter" $\phi = FT/p$, where F is the gas flow rate, T is the temperature and p is the pressure of the buffer gas. Indicated is dominant ion in the plasma.

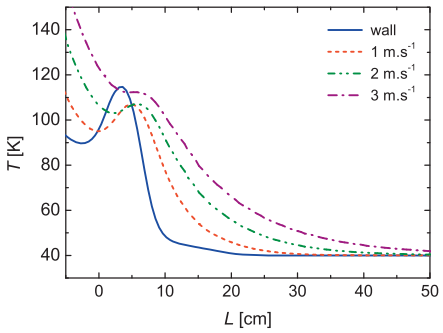

Fig. 4. (Color online) Evolution of buffer gas temperature in section C calculated for different flow velocities. Solid line denotes calculated temperature of the flow tube wall, the flow tube construction, materials and heat transfers are considered.

electron density, the effective recombination rate coefficient is obtained. Because of very strong temperature dependence of CRR, the measurements of the plasma velocity dependence on the flow parameters are very important in order to define conditions in which plasma is thermalized to the temperature of the flow tube wall. Measured dependence of the plasma velocity on "similarity parameter" $\phi = FT/p$ in Ar^+ and He_2^+ dominated plasma is plotted in Figure 3. To better understand the thermalization of buffer gas and plasma with the flow tube walls, a simple computer model of heat transport inside the flow tube was developed and numerically solved (the details on the computer model will be given in separate publication). The examples of gas temperature evolution calculated for different gas velocities at temperature of the flow tube ∼40 K are plotted in Figure 4. The calculated buffer gas (and plasma) thermalization agrees well with the experimental insight gained from the plasma flow velocity measurements (linear fits in Fig. 2) and from the measurements of the diffusion losses (see Ref. [11]).

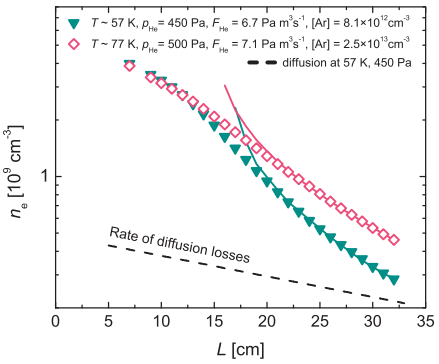

Fig. 5. (Color online) Examples of the electron decay curves measured at 57 and 77 K (temperature of section C). Experimental conditions are listed in the plot. From the fits of the plots in the region of constant plasma temperature (solid lines), the coefficients K_{CRR} are obtained. The dashed line indicates diffusion losses at 57 K, 450 Pa.

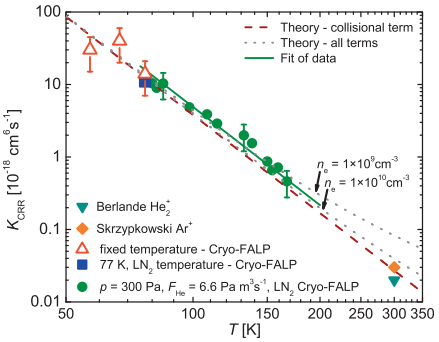

Fig. 6. (Color online) Measured K_{CRR} coefficient as a function of temperature. Dashed line corresponds to the theoretical value calculated from the collisional (first) term of equation (2). Dotted lines indicate the theoretical values of K_{CRR} for two electron densities calculated using all terms of relation (2). Closed square and triangle are data measured by Skrzypkowski et al. [8] and by Berlande et al. [10].

3 Results and conclusions

The examples of the measured electron density decay curves at particular experimental conditions are plotted in Figure 5. Measurements of the electron density decays were performed at various experimental conditions in order to control and verify the thermalization of plasma with the flow tube wall. At low temperatures and high enough argon number densities argon clusters Ar_2^+ with fast binary recombination rate coefficients ($\sim 10^{-6}\,cm^3\,s^{-1}$) can be created. As the present version of FALP apparatus is not equipped with a mass spectrometer, one needs to follow the optimal conditions suggested by the chemical kinetics model and/or examine the dependence of α_{eff} on [Ar] in order to exclude the formation of fast recombining Ar_2^+ ions. Such measurements were performed (the details on the results and discussion will be published in separate publication) and after careful examination of the results, the eventual electron assisted ternary recombination rate coefficient K_{CRR} of Ar^+ ion obtained at particular

temperature in the range 50–170 K is plotted in Figure 6. Open triangles denote experimental values obtained in the present version of FALP apparatus, full circles and squares correspond to values measured in the previous FALP experiment, where the flow tube was cooled by liquid nitrogen (for details see Ref. [11]). The theoretical dependence equation (2) is plotted by dashed line (collisional term only). Dotted lines denote theoretical K_{CRR} obtained from the formula $K_{\mathrm{CRR}} = \alpha_{\mathrm{eff}}/n_{\mathrm{e}}$ for two different electron number densities when all terms of equation (2) are involved in α_{eff} calculation. The results show an excellent agreement of the measured K_{CRR} with the theory down to 50 K. Further studies of CRR in Ar^+ dominated plasma are in progress.

This work is a part of the research plan MSM 0021620834 and Grant No. OC10046 financed by the Ministry of Education of the Czech Republic and was partly supported by GACR (202/07/0495, 202/08/H057, 205/09/1183, 202/09/0642), by GAUK 92410, GAUK 353811, GAUK 54010 and by COST Action CM0805 (The Chemical Cosmos).

References

1. D.R. Bates, A.E. Kingston, R.W.P. Mcwhirter, Proc. Roy. Soc. A **267**, 297 (1962)
2. P. Mansbach, J. Keck, Phys. Rev. **181**, 275 (1969)
3. J. Stevefelt, J. Boulmer, J.-F. Delpech, Phys. Rev. A **12**, 1246 (1975)
4. G.J. Pert, J. Phys. B: At. Mol. Opt. Phys. **23**, 619 (1990)
5. S.X. Hu, Phys. Rev. Lett. **98**, 133201-1 (2007)
6. T. Pohl, D. Vrinceanu, H.R. Sadeghpour, Phys. Rev. Lett. **100**, 223201 (2008)
7. M. Tsuji, T. Matsuzaki, T. Tsuji, Chem. Phys. **285**, 335 (2002)
8. M.P. Skrzypkowski, R. Johnsen, R.E. Rosati, M.F. Golde, Chem. Phys. **296**, 23 (2004)
9. G.E. Veatch, H.J. Oskam, Phys. Rev. A **1**, 1498 (1970)
10. J. Berlande, M. Cheret, R. Deloche, A. Gonfalone, C. Manus, Phys. Rev. A **1**, 887 (1970)
11. T. Kotrik, P. Dohnal, S. Roucka, P. Jusko, R. Plasil, J. Glosik, Phys. Rev. A **83**, 032720 (2011)
12. R.S. Fletcher, X.L. Zhang, S.L. Rolston, Phys. Rev. Lett. **99**, 145001-1 (2007)
13. S.X. Hu, D. Vrinceanu, S. Mazevet, L.A. Collins, Phys. Rev. Lett. **95**, 163402-1 (2005)
14. M. Amoretti et al., Phys. Lett. B **583**, 59 (2004)
15. D. Smith, N.G. Adams, A.G. Dean, M.J. Church, J. Phys. D **8**, 141 (1975)
16. J. Glosik, O. Novotny, A. Pysanenko, P. Zakouril, R. Plasil, P. Kudrna, V. Poterya, Plasma Sources Sci. Technol. **12**, 117 (2003)
17. I. Korolov, O. Novotný, J. Varju, T. Kotrík, R. Plašil, M. Hejduk, J. Glosík, Contrib. Plasma Phys. **48**, 521 (2008)
18. J. Glosík, R. Plašil, I. Korolov, T. Kotrík, O. Novotný, P. Hlavenka, P. Dohnal, J. Varju, V. Kokoouline, C.H. Greene, Phys. Rev. A **79**, 052707 (2009)
19. T. Kotrík, P. Dohnal, I. Korolov, R. Plašil, Š. Roučka, J. Glosík, C.H. Greene, V. Kokoouline, J. Chem. Phys. **133**, 034305 (2010)
20. R. Plasil, J. Glosik, V. Poterya, P. Kudrna, J. Rusz, M. Tichy, A. Pysanenko, Int. J. Mass Spectrom. **218**, 105 (2002)
21. H.J. Oskam, Philips Res. Rep. **13**, 335 (1958)
22. I. Korolov, T. Kotrik, P. Dohnal, O. Novotny, J. Glosik, Contrib. Plasma Phys. **48**, 461 (2008)
23. R. Plasil, I. Korolov, T. Kotrik, P. Dohnal, G. Bano, Z. Donko, J. Glosik, Eur. Phys. J. D **54**, 391 (2009)
24. J.D. Swift, M.J.R. Schwar, *Electrical Probes for Plasma Diagnostics* (Illiffe Books, London, 1970)

EXTENDING PIC MODELS TO HIGHER PRESSURES—ENHANCED MODEL OF COLLISIONS

Bibliographic record of the attached publication:

Roučka, Š and R. Hrach (Nov. 2011). "Extending PIC Models to Higher Pressures - Enhanced Model of Collisions." In: *Plasma Science, IEEE Transactions on* 39.11, pp. 3244 –3250.
DOI: 10.1109/TPS.2011.2164789.

Extending PIC Models to Higher Pressures—Enhanced Model of Collisions

Štěpán Roučka and Rudolf Hrach

***Abstract*—This paper treats the problems of the particle-in-cell (PIC) models at higher pressures. We discuss the influence of the time discretization on the results of a model of a highly collisional plasma using a simplified analytical model. A new algorithm is proposed that calculates the collisions independently of the simulation time step, thus eliminating the errors introduced by the time discretization. The benchmarks at the pressure of the neutral gas of 665 Pa show that the presented algorithm is approximately seven times faster than a classical PIC model with the same accuracy.**

***Index Terms*—Collision processes, modeling, particle collisions, plasmas, simulation.**

I. Introduction

THE USE OF plasmas at higher pressures is now widely adopted in various technological applications like the destruction of volatile organic compounds [1], disinfection or destruction of tissue in medicine [2], or surface processing at atmospheric pressure [3]. However, the processes at medium to high pressures are not yet clearly understood, which complicates the development of new applications and the optimization of present techniques.

For the purpose of this paper, we define the medium pressure as a pressure on the order of several hundreds of pascals in a nonequilibrium low-temperature plasma, where the charged particles collide mostly with neutrals. However, our algorithm should be applicable to any type of plasma.

The theoretical approach in this field of plasma physics is complicated by the high amount of collisions and complex geometries. It is usually not usable for quantitative analysis, which is needed for technological applications.

Methods of computational fluid dynamics have problems mainly with incorporating the nonequilibrium energy distribution of charged particles that depends on local conditions. In order to include this important feature of nonthermal plasmas, the fluid model can be coupled with a simple particle simulation into a so-called hybrid model [4], [5].

The particle models are still the most reliable source of information about plasma because of their straightforward implementation of kinetic processes in plasmas. The main problem of particle models are their high computational demands. In this paper, we deal with particle-in-cell (PIC) models, where the computational requirements are proportional to the number of simulated macroparticles times the number of time steps. The number of particles is related to various size scales in the model that need to be correctly represented, while the number of time steps or time step length is determined by the time scale of various processes in combination with the Courant–Friedrichs–Lewy condition

$$\Delta t \lesssim \Delta x / v \tag{1}$$

which gives a relation between the time step Δt, the grid spacing or the smallest characteristic dimension of the system Δx, and the particle velocity v. This paper deals with highly collisional plasmas where the mean time between collisions τ is much shorter than the characteristic times of other processes in plasma, including the Courant–Friedrichs–Lewy limit. We will show that, in order to keep the errors small, the time step of the simulation must be much shorter than the mean time between collisions. For pressures above several hundreds of pascals, this presents a serious limitation on the time step, and the computational requirements grow in proportion to pressure. A method to reduce this limitation of PIC models is presented in the last section of this paper.

II. Model of Collisions

There are various approaches to the modeling of collisions by the Monte Carlo method. The simplest one consists in generating a random-free path between collisions with a mean value given by $\lambda = 1/\sigma n$, where σ is the integral cross section and n is the concentration of scattering centers. This method is valid for nonmoving scattering centers, and therefore, it is not generally applicable to collisions in plasmas, where the scattering centers are formed by moving plasma particles.

For the simulation of collisions in gases, it is useful to speak in terms of the mean time between collisions τ instead of the free path. For a particle with position $\boldsymbol{x}$ and velocity $\boldsymbol{v}$ moving in a gas with velocity distribution $f(\boldsymbol{x}, \boldsymbol{v}')$, the frequency of collisions ν with gas particles from the element of phase space $d\boldsymbol{v}'$ is given by

$$\nu(\boldsymbol{x}, \boldsymbol{v}, \boldsymbol{v}')d\boldsymbol{v}' = f(\boldsymbol{x}, \boldsymbol{v}')n(\boldsymbol{x})g\sigma(g)d\boldsymbol{v}' \tag{2}$$

where $g = |\boldsymbol{v} - \boldsymbol{v}'|$ is the relative velocity, $n(\boldsymbol{x})$ is the concentration of particles, and the distribution function is normalized

Manuscript received November 30, 2009; revised August 31, 2010 and March 3, 2011; accepted July 6, 2011. Date of publication September 19, 2011; date of current version November 9, 2011. This work was supported by the Ministry of Education of the Czech Republic under Grant MSM0021620834 and by the Grant Agency of Charles University Prague under Project GAUK-51808/2008.

The authors are with the Faculty of Mathematics and Physics, Charles University, 121 16 Prague, Czech Republic (e-mail: Stepan.Roucka@mff.cuni.cz; rudolf.hrach@mff.cuni.cz).

Digital Object Identifier 10.1109/TPS.2011.2164789

0093-3813/$26.00 © 2011 IEEE

to unity $\int f(\boldsymbol{x},\boldsymbol{v}')d\boldsymbol{v}'=1$. The total collision frequency ν is then obtained by integration over velocity space

$$\nu(\boldsymbol{x},\boldsymbol{v})=\frac{1}{\tau(\boldsymbol{x},\boldsymbol{v})}=\int f(\boldsymbol{x},\boldsymbol{v}')n(\boldsymbol{x})g\sigma(g)d\boldsymbol{v}'. \quad (3)$$

This complicated velocity- and position-dependent expression can be transformed into a constant expression $\nu(\boldsymbol{x},\boldsymbol{v})=\nu_{\max}$ by a mathematical transformation called *null collision method* [6], [7]. This transformation is equivalent to adding a fictive interaction—null collision—to the model, which does not change particle velocity. The cross section of the null collision $\sigma_0(g,\boldsymbol{x})$ is chosen so that the integral in (3) is independent of the velocity and position of the studied particle, e.g., $(\sigma(g)+\sigma_0(g,\boldsymbol{x}))gn(\boldsymbol{x})\equiv\nu_{\max}$. The value of $\nu_{\max}$ is calculated from $\nu_{\max}=\max_g\{\sigma(g)g\}\max_{\boldsymbol{x}}\{n(\boldsymbol{x})\}$ either globally for the whole simulation [7] or locally for each collision [6]. In our model, the global approach is used, which is suitable in case of nonnegligible temperature of neutrals.

We can therefore model any collision operator for which $\sigma(g)g+n(\boldsymbol{x})$ is bounded over relevant velocities as a homogeneous Poisson process with constant frequency $\nu_{\max}$.

During the collision event, we pick a random particle from the interacting gas and choose randomly between the null collision and real collision with respective probabilities $\sigma_0(g,\boldsymbol{x})gn(\boldsymbol{x})/\nu_{\max}$ and $\sigma(g)gn(\boldsymbol{x})/\nu_{\max}$ [7]. Collisions selected by this procedure exactly satisfy the fundamental equation for collision frequency (2).

A different method for collision selection is presented in [8]. The author calculates that, for a particle starting at time $t=0$ with a random collision time t_c' chosen using the null collision method, the probability of a nonnull collision is given by

$$\frac{\text{Prob}\left\{T_c\left(\nu(\boldsymbol{x},v)\right)<t_c'\right\}}{\text{Prob}\left\{T_c(\nu_{\max})<t_c'\right\}}=\frac{1-\exp\left(-\int_0^{t_c'}\nu\left(\boldsymbol{x}(t),v(t)\right)dt\right)}{1-\exp\left(-\nu_{\max}t_c'\right)} \quad (4)$$

where $\text{Prob}\{(T_c(\nu(t))<t_c'\}$ is the probability that at least one event of the process with frequency $\nu(t)$ occurs in the time interval $(0,t_c')$. This expression takes into account the previous trajectory of the particle, which is in contradiction to the nature of collisions as a Poisson process. The collision occurring at t_c' depends only on the local conditions, not on the history, i.e., the conditional probability at $T_c\in(t_c',t_c'+dt)$ has to be used to get a correct result in agreement with [7]

$$\frac{\text{Prob}\left\{T_c\left(\nu(\boldsymbol{x},v)\right)\in(t_c',t_c'+dt)\right\}}{\text{Prob}\left\{T_c(\nu_{\max})\in(t_c',t_c'+dt)\right\}}=\frac{\nu\left(\boldsymbol{x}\left(t_c'\right),v\left(t_c'\right)\right)}{\nu_{\max}}. \quad (5)$$

Up to now, we discussed the mathematical model of collisions without reference to any particular numerical method. However, incorporating collisions into the PIC model requires some kind of time discretization of the collision process. A simple and accurate method is presented in [9], where particles collide on integer multiples of time step Δt with probability $P=n(\boldsymbol{x})g\sigma(g)\Delta t$, where the g is calculated relative to a randomly selected neutral particle. This algorithm does not employ a null collision method and is efficient only for the Langevin collision process. It is computationally expensive in case of variable collision frequency because P has to be recalculated for each particle time step. In a more efficient approach employing the null collision method [7], particles collide with constant probability

$$P_1=1-\exp\left(-\frac{\Delta t}{\tau}\right) \quad (6)$$

which is the probability that the particle undergoes at least one collision during the time step. The process of collision selection is not affected by the time discretization.

III. Errors Introduced by Time Discretization

In this section, the influence of the finite time step Δt on the behavior of a model system will be studied analytically. This will allow us to estimate the Δt required for calculating the energy or velocity of particles with specified accuracy.

Our model system consists of charged particles in constant homogeneous electric field. This assumption is approximately valid for a highly collisional plasma because the particle undergoes many collisions before the electric field changes significantly.

Charged particles collide with particles of a neutral background gas with mean time between collisions τ independent of particle velocity. The collision is simulated by stopping the charged particle. This simple model approximates the resonant charge transfer interaction of ions with cold neutrals.

A. Amount of Collisions

In a classical PIC model, the particles collide on integer multiples of the time step with probability P_1. However, in the model system, there are $\Delta t/\tau$ collisions on average during time Δt. Hence, the amount of collisions neglected by the PIC model per particle time step is given by

$$r=\Delta t/\tau-P_1. \quad (7)$$

The number of neglected collisions is also calculated by Vahedi and Surendra [7] with a different result $r=P_1^2/(1-P_1)$. The discrepancy is present because, in [7], the probability of n collisions in a time step is incorrectly assumed to be P_1^n, whereas the real probability is given by the Poisson distribution.

The number of neglected collisions (7) can be set to zero by choosing collision probability

$$P_2=\Delta t/\tau \quad (8)$$

instead of P_1 (see [9] for example use of probability P_2 outside of the null collision framework, i.e., the probability is recalculated after each time step). A simplified model presented in this section demonstrates a decrease in the accuracy of calculated parameters when using P_2. Only minor differences between using P_1 and P_2 were observed in the realistic example study in Section V. For clarity, only the results for P_1 are presented.

B. Drift Velocity

Let us assume that the external electric field accelerates the studied particles with constant acceleration a. The velocity of a particle at time T since the last collision is given by $v(T) = aT$. The distribution of times since the last collision is exponential

$$f(T)dT = \frac{1}{\tau}\exp\left(-\frac{T}{\tau}\right)dT. \tag{9}$$

Now, we can simply obtain the mean velocity in the model ensemble by integration

$$\langle v\rangle = \int_0^\infty v(T)f(T)dT = a\tau. \tag{10}$$

The situation in the ensemble with a discrete time axis is, however, more complicated. The problem is that the mean velocity of particles is not constant in the stationary state. In each time step, the ensemble first acquires energy from the electric field during the integration of Newton equations, and then, it suddenly looses part of its energy due to collisions. Therefore, we define three different average values in order to obtain a comprehensive picture of the studied system. The first average $\langle v\rangle_{\mathrm{T}}$ is simply defined as an average over the ensemble of particles over the whole time step. The second $\langle v\rangle_{\mathrm{B}}$ is defined as the ensemble average before computing the Monte Carlo collisions (MCCs), and the third one $\langle v\rangle_{\mathrm{A}}$ is the ensemble average after collisions.

Now, we shall compute the average value $\langle v\rangle_{\mathrm{A}}$. The probability that the particle collided and then propagated n steps without collision is PQ^n, where $Q = 1 - P$ is the probability that a particle does not collide in one time step. The average value of a variable A_i that depends on the number of time steps since the last collision i can be expressed as

$$\langle A\rangle = P\sum_{i=0}^{\infty} Q^i A_i. \tag{11}$$

The mean velocity over one time step of a particle that collided i time steps before is given by

$$\langle v\rangle_i = \frac{1}{\Delta t}\int_{i\Delta t}^{(i+1)\Delta t} atdt = a\Delta t\left(i+\frac{1}{2}\right). \tag{12}$$

As a next step, we can average the $\langle v\rangle_i$ over i by plugging it into (11)

$$\langle v\rangle_{\mathrm{T}} = P\sum_{i=0}^{\infty} Q^i\langle v\rangle_i = Pa\Delta t\left(\sum_{i=1}^{\infty} Q^i i + \frac{1}{2}\sum_{i=0}^{\infty} Q^i\right). \tag{13}$$

The second sum in (13) is a geometric series, and the first sum can be expressed as a derivation of a geometric series. After evaluating these series, we obtain the average velocity

$$\langle v\rangle_{\mathrm{T}} = a\Delta t(Q/P + 1/2). \tag{14}$$

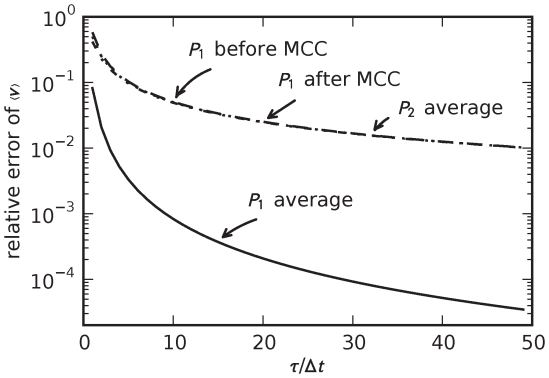

Fig. 1. Average error of velocity in the model with discrete time axis for collisions versus the ratio of mean time between collisions to the simulation time step. The lines representing $\langle v\rangle_{\mathrm{B}}$ (before MCC) and $\langle v\rangle_{\mathrm{A}}$ (after MCC) computed using the collision probability P_1 and the average error $\langle v\rangle_{\mathrm{T}}$ computed using probability P_2 are almost identical. The average error in simulation using the collision probability P_1 is much smaller than that with collision probability P_2.

In order to determine the mean velocity before MCC $\langle v\rangle_{\mathrm{B}}$, we can just replace the average $\langle v\rangle_i$ in the previous procedure by the actual velocity before collisions $v((i+1)\Delta t) = (i+1)a\Delta t$ to get

$$\langle v\rangle_{\mathrm{B}} = a\Delta t/P. \tag{15}$$

Finally, the mean velocity after collisions $\langle v\rangle_{\mathrm{A}}$ could be obtained by plugging $ia\Delta t$ into the aforementioned procedure, but this is equivalent to multiplying $\langle v\rangle_{\mathrm{B}}$ by Q in the averaging sum (11)

$$\langle v\rangle_{\mathrm{A}} = Q\langle v\rangle_{\mathrm{B}} = a\Delta tQ/P. \tag{16}$$

As we can see, none of these values in the discrete-time approximation is equal to the value in our model system. The differences are plotted in Fig. 1. If we use the collision probability P_1 in our computation, the error in velocity before computing the MCC is almost equal to the error after computing the MCC, but is of opposite sign. Hence, the average error is much smaller. When using the P_2 collision probability, the error in velocity before collisions is zero, but the error after collisions is larger and the average error is by orders of magnitude larger than that in the case of P_1.

C. Energy

The analysis of the mean energy of particles in the simulation with discrete time axis is, in principle, equivalent to the analysis of mean velocities. In order to simplify our expressions, we will speak in terms of v^2 instead of energy.

The mean squared velocity in the model system is equal to

$$\langle v^2\rangle = 2a^2\tau^2. \tag{17}$$

In analogy to the analysis of velocity, we define three different values of mean energy: $\langle v^2\rangle_{\mathrm{B}}$ and $\langle v^2\rangle_{\mathrm{A}}$ as the mean values before and after collisions, respectively, and $\langle v^2\rangle_{\mathrm{T}}$ as the mean value over the whole time step.

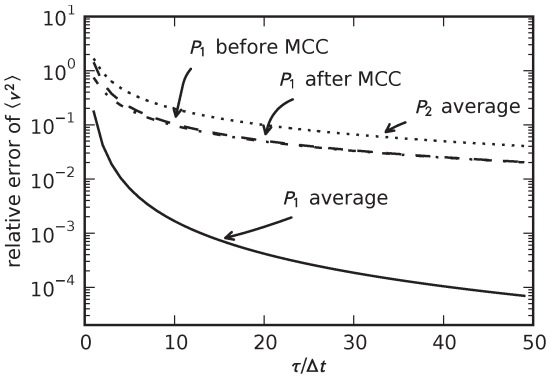

Fig. 2. Average error of square velocity in the model with discrete time axis for collisions versus the ratio of mean time between collisions to the simulation time step. The lines representing $\langle v^2\rangle_{\rm B}$ (before MCC) and $\langle v^2\rangle_{\rm A}$ (after MCC) computed using the collision probability P_1 are almost identical. The average error in simulation using the collision probability P_1 is much smaller than that with collision probability P_2.

The average squared velocity for a particle that collided i time steps before is given by

$$\langle v^2\rangle_i = \frac{1}{\Delta t}\int_{i\Delta t}^{(i+1)\Delta t} a^2t^2dt = a^2\Delta t^2\left(i^2+i+\frac{1}{3}\right). \quad (18)$$

After inserting this value into the averaging formula (11), we obtain

$$\langle v^2\rangle_{\rm T} = Pa^2\Delta t^2\left(\sum_{i=0}^{\infty}Q^ii^2+\sum_{i=0}^{\infty}Q^ii+\frac{1}{3}\sum_{i=0}^{\infty}Q^i+\right). \quad (19)$$

These series can again be easily evaluated by converting them to a geometric series with a result

$$\langle v^2\rangle_{\rm T} = a^2\Delta t^2\left(\frac{Q(1+Q)}{P^2}+\frac{Q}{P}+\frac{1}{3}\right). \quad (20)$$

The mean values of v^2 before and after computing collisions are given by

$$\langle v^2\rangle_{\rm B} = a^2\Delta t^2\frac{1+Q}{P^2}, \qquad \langle v^2\rangle_{\rm A} = a^2\Delta t^2\frac{Q(1+Q)}{P^2}. \quad (21)$$

The differences between these mean values and the model system are plotted in Fig. 2. The average value computed using the collision probability P_2 is again much larger than the value computed using the collision probability P_1. An important fact that can be observed in this graph is that the mean error in $\langle v^2\rangle_{\rm B}$ (energy before MCC) decreases relatively slowly with decreasing time step. For time steps ten times smaller than τ, the error in energy is still around 10%. This could seriously influence the result of computation if the collision cross sections have strong dependence on energy.

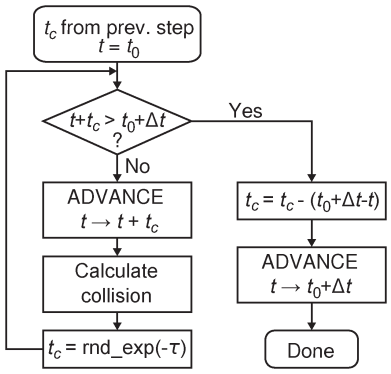

Fig. 3. Flow diagram representing a single global time step Δt of a single particle. The *ADVANCE* step integrates the equations of motion and increases the value of t. The rnd_exp function generates a random sample from exponential distribution.

IV. Elimination of Discretization Errors

It was shown in the simplified model that the discretization of the time axis used for the computation of collisions introduces a significant discrepancy in the computed energy even if the time step is ten times shorter than the mean time between collisions. A similar behavior can be expected for more realistic collision operators used in PIC models and will be demonstrated in Section V.

We now define a simple modification of the PIC model that completely eliminates this type of error. Our method computes collisions independently of the PIC time steps, which makes the time axis of collisional processes effectively continuous. We replace the integration of equations of motion by a more general solution of a transport problem. The PIC simulation has then basically two different time steps. One time step that we call *global* defines the time between updating the fields, whereas the second time step is not constant and is individual for each particle. Every particle has an additional variable t_c that stores its time to the next collision in seconds. The t_c is initialized as a random sample from the exponential distribution (9) at the program start-up and after each collision. The mean value of t_c is a constant $\tau = 1/\nu_{\max}$ determined by the null collision method (see Section II). During the simulation of a single global time step, the position of a particle in the phase space is repeatedly advanced in time by t_c seconds until the time of the next collision is beyond the time of the next global time step (see Fig. 3). The effects of each collision are computed using the appropriate model.

This modification slightly complicates the numerical integration of the equations of motion because the time step of integration is now random. It prevents us from employing the widely used leap-frog algorithm. We considered using the first-order Euler scheme because the motion of particles in our simulations is dominated by collisions and the accuracy of the integration of motion equations is not crucial. However, our benchmarks show that the velocity Verlet scheme gives significantly better results in this application. Technically, our scheme is different from the velocity Verlet scheme because we assume that the force exerted on the particle is constant during the global time step. Therefore, we compute the force $\boldsymbol{F}$ at the

beginning of the global time step and then repeatedly advance the position $\boldsymbol{x}$ and velocity $\boldsymbol{v}$ from one collision to another as expressed by the equations

$$\boldsymbol{x}^{k+1} = \boldsymbol{x}^k + \boldsymbol{v}^k t_{c,k} + \frac{\boldsymbol{F}}{2m} t_{c,k}^2,$$
$$\boldsymbol{v}^{k+1} = \boldsymbol{v}^k + \frac{\boldsymbol{F}}{m} t_{c,k}. \quad (22)$$

The time between subsequent collisions is given by $t_{c,k}$.

A. Our Method in Context of Other Null Collision Models

A common feature of most null collision models is that the process of collisions is transformed from a nonhomogeneous Poisson process into a homogeneous Poisson process. In this sense, the null collision method used in our algorithm is identical with the methods of Skullerud [6] and Vahedi and Surendra [7].

The method of Skullerud [6] is developed with the assumption of negligible velocity of gas particles. It does not deal with discrete time axis—it is not embedded in the PIC method. The $\nu_{\max}$ is recalculated after each collision.

The null collision method introduced by Vahedi and Surendra [7] includes time discretization by calculating collisions at integer multiples of the time step. The $\nu_{\max}$ is calculated globally for all possible velocities, which is an efficient approach when the velocity of neutrals is not negligible. This method is optimal for use in PIC models with relatively small amount of collisions.

Our method is an extension of these approaches. We calculate $\nu_{\max}$ globally like in [7]. The time between collisions is continuous as in [6]. In contrast to [6], we include the collisions in a PIC model with discrete time axis, which requires using two independent time axes as described in Section IV.

V. Numerical Benchmarks

In order to prove the advantages of the new algorithm in a real-world application with more complicated collision operators, we performed a series of PIC simulations with different Δt. In these simulations, several macroscopic quantities were observed. Our computations show that the results of all methods converge for small Δt. This common limit defines a "correct" value of the observed quantity. When increasing Δt, we can observe the growth of error for both methods.

A. Model Description

Our benchmarking models are 2-D PIC models with a Cartesian grid. The Poisson equation is solved using LU decomposition implemented in the UMFPACK library [10]. We use the cloud-in-cell weighting scheme for the particle–mesh interaction [11]. Because we are modeling the steady state, we applied a speedup method based on using a longer time step for ions. This effectively means that the time flows faster for ions. We used 1000 times longer ion time step in all our simulations.

All modules of our PIC code were thoroughly tested with special attention paid to the accuracy of the MCC code. Efficient random number generators (RNGs) were used [12], and the independence of the results on the underlying RNG was checked. Apart from comparisons with analytical solutions, the accuracy of the MCC code and motion equation integrator was verified by comparing our results to that of a direct solver of the Boltzmann equation, i.e., the ELENDIF [13]. The calculated electron energy distribution functions show good agreement over several orders of magnitude, and the differences are on the level of accuracy of the numerical method used in ELENDIF.

The model was used to simulate the interaction of a cylindrical Langmuir probe of infinite length with a low-temperature plasma. Our working area is a square with 1-cm size perpendicular to the probe axis. The probe is situated in the center of our working area. The boundary conditions for potential are as follows: linear dependence at the outer boundary (external field) and a fixed value at the probe surface. Particles are injected from outside from a coupled non-self-consistent simulation of the undisturbed plasma. We model an argon plasma consisting of electrons, Ar and Ar^+. The concentration of electrons is $n = 10^{15}$ m^{-3}. Only collisions of charged particles with neutrals are considered—the elastic collision, ionization, and excitation to the $^3P_2$ state for electrons and the elastic collision and resonant charge transfer for ions. The velocity-dependent cross sections were taken from [14]. The collisions are modeled as isotropic scattering in the center of mass system, and the resulting velocity is determined by momentum and energy conservation. The external electric field is set to 500 V/m.

The grid size used in our simulations is 200 $\times$ 200, and we simulated $4 \cdot 10^5$ particles in total. The computation times were estimated using the Intel Core 2 T5500 at 1.66-GHz processor with 3-GB DDR2 667-MHz RAM without parallelization.

B. Results

In the first set of simulations, the probe with a diameter of 0.1 mm is biased to -5 V. The neutral gas pressure is 266 Pa. The macroscopic parameters obtained from both models are plotted in Fig. 4. In order to compare the two models of collisions, we specify a certain relative error (5%) in the macroscopic parameters, and then, we find the time step needed to achieve this error.

The panel (a) of Fig. 4 shows the energy of the ions hitting the probe surface. For the classical PIC algorithm, the error grows to 5% at $\Delta t \approx 10^{-12}$ s. The new algorithm reaches this error at $\Delta t \approx 10^{-8}$ s. This could allow us to use ten times longer time step with the new algorithm.

The ion probe current normalized to a probe length of 1 cm is plotted in the panel (b). The new algorithm shows here virtually no dependence on the Δt. The error of the classical PIC model grows to almost 10% for $\Delta t = 2 \cdot 10^{-12}$ s; hence, the required Δt is again 10^{-12} s.

The results for the electron probe current in Fig. 4(c) do not show a significant difference between the two algorithms. The required Δt for both methods is below 10^{-11} s.

Fig. 4(d) shows the computation time needed to simulate 1 s of electron time. We concluded that, in order to keep the error below 5%, we have to use $\Delta t \lesssim 10^{-12}$ s in the classical PIC. On the other hand, the new algorithm allows time steps above

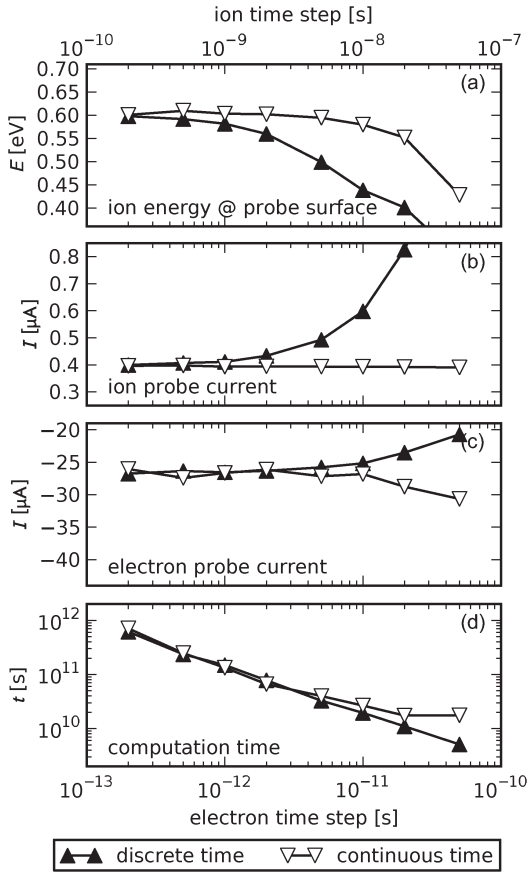

Fig. 4. Results of a simulation of a cylindrical Langmuir probe in a plasma at 266 Pa as a function of the simulation time step. The full triangles denote the classical PIC model, whereas the white triangles denote the results of the algorithm with continuous time step for collisions.

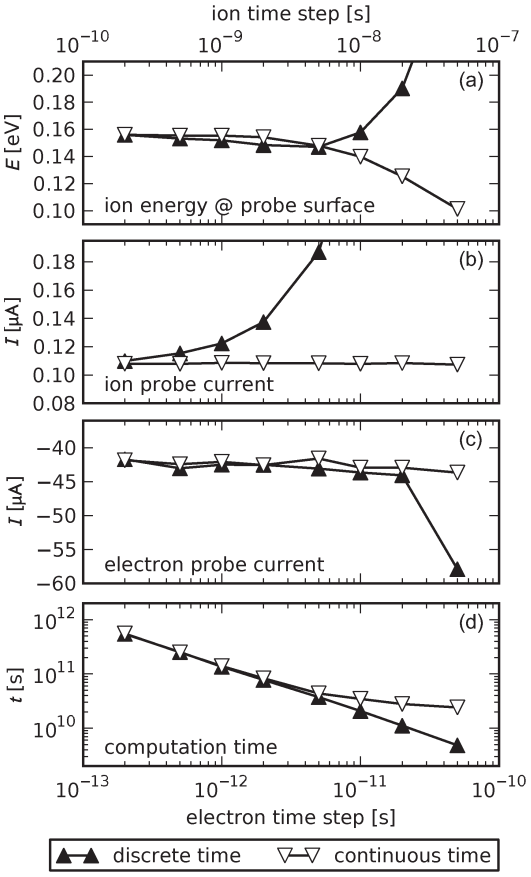

Fig. 5. Results of a simulation of a cylindrical Langmuir probe in a plasma at 665 Pa as a function of the simulation time step. The full triangles denote the classical PIC model, whereas the white triangles denote the results of the algorithm with continuous time step for collisions.

$5 \cdot 10^{-12}$ s. This corresponds to four times shorter computation times with the new algorithm.

In the second set of simulations, plotted in Fig. 5, the probe has a diameter of 0.2 mm and is biased to -5 V. The neutral gas pressure is 665 Pa.

After repeating the same analysis as in the case of 266-Pa pressure, we can see that the Δt of the new algorithm is limited below $5 \cdot 10^{-12}$ s because of the error in the computed energy of the ions at the probe surface. The biggest difference between the two algorithms is in the computed ion probe current. The classical PIC algorithm requires $\Delta t < 5 \cdot 10^{-13}$ s, whereas the results of the new algorithm are independent of the choice of the time step. From Fig. 5(d), it can be read that using $\Delta t = 5 \cdot 10^{-12}$ s in the new algorithm and $\Delta t = 5 \cdot 10^{-13}$ s in the classical PIC algorithm corresponds to roughly seven times faster computation using the new algorithm.

VI. Conclusion

We estimated analytically the errors introduced by the time discretization of collision processes in the PIC models with a simple collision operator. We proposed a modification of the PIC algorithm that eliminates this important source of errors. Our benchmarks with realistic collision operators show that the modified PIC model reaches the same accuracy of observed parameters as the classical PIC model in four times shorter time at 266 Pa and in seven times shorter time at 665 Pa.

References

[1] H. Grossmannová, M. Cigánek, and F. Krčma, "High-molecular products analysis of VOC destruction in atmospheric pressure discharge," *J. Phys., Conf. Ser.*, vol. 63, no. 1, p. 012 011, 2007.

[2] M. Laroussi and X. Lu, "Room-temperature atmospheric pressure plasma plume for biomedical applications," *Appl. Phys. Lett.*, vol. 87, no. 11, p. 113 902, Sep. 2005.

[3] H. Baránková and L. Bárdoš, "Fused hollow cathode cold atmospheric plasma," *Appl. Phys. Lett.*, vol. 76, no. 3, pp. 285–287, Jan. 2000.

[4] T. J. Sommerer and M. J. Kushner, "Numerical investigation of the kinetics and chemistry of RF glow discharge plasmas sustained in He, N_2, 0_2, $He/N_2/0_2$, $He/CF_4/0_2$, and SiH_4/NH_3 using a Monte Carlo-fluid hybrid model," *J. Appl. Phys.*, vol. 71, no. 4, pp. 1654–1673, Feb. 1992.

[5] I. Kolev and A. Bogaerts, "Numerical models of the planar magnetron glow discharges," *Contrib. Plasma Phys.*, vol. 44, no. 7/8, pp. 582–588, Nov. 2004.

[6] H. R. Skullerud, "The stochastic computer simulation of ion motion in a gas subjected to a constant electric field," *J. Phys. D, Appl. Phys.*, vol. 1, no. 11, p. 1567, Nov. 1968.

[7] V. Vahedi and M. Surendra, "A Monte Carlo collision model for the particle-in-cell method: Applications to argon and oxygen discharges," *Comput. Phys. Commun.*, vol. 87, no. 1/2, pp. 179–198, May 1995.

[8] K. Nanbu, "Probability theory of electron–molecule, ion–molecule, molecule–molecule, and Coulomb collisions for particle modeling of materials processing plasmas and cases," *IEEE Trans. Plasma. Sci.*, vol. 28, no. 3, pp. 971–990, Jun. 2000.

[9] K. Nanbu and Y. Kitatani, "An ion-neutral species collision model for particle simulation of glow discharge," *J. Phys. D, Appl. Phys.*, vol. 28, no. 2, pp. 324–330, Feb. 1995.
[10] T. A. Davis, "Algorithm 832: UMFPACK, an unsymmetric-pattern multifrontal method," *ACM Trans. Math. Softw.*, vol. 30, no. 2, pp. 196–199, Jun. 2004.
[11] R. W. Hockney and J. W. Eastwood, *Computer Simulation Using Particles*. Bristol, U.K.: IOP, 1988.
[12] G. Marsaglia and W. W. Tsang, "The Ziggurat method for generating random variables," *J. Statist. Softw.*, vol. 5, no. 8, pp. 1–7, Oct. 2000.
[13] W. L. Morgan and B. M. Penetrante, "ELENDIF: A time-dependent Boltzmann solver for partially ionized plasmas," *Comput. Phys. Commun.*, vol. 58, no. 1/2, pp. 127–152, Feb./Mar. 1990.
[14] A. V. Phelps, *Compilation of Electron Cross Sections*. [Online]. Available: http://jila.colorado.edu/~avp/collision_data/

Štěpán Roučka, photograph and biography not available at the time of publication.

Rudolf Hrach, photograph and biography not available at the time of publication.

BINARY AND TERNARY RECOMBINATION OF PARA- AND ORTHO-H_3^+ WITH ELECTRONS; STATE SELECTIVE STUDY AT 77–200 K

Bibliographic record of the attached publication:

Dohnal, P., M. Hejduk, J. Varju, P. Rubovič, Š. Roučka, T. Kotrík, R. Plašil, J. Glosík, et al. (2012). "Binary and ternary recombination of para- and ortho-H_3^+ with electrons; State selective study at 77–200 K." In: 136.24, 244304, p. 244304.
DOI: 10.1063/1.4730162.
URL: http://link.aip.org/link/?JCP/136/244304/1.

Binary and ternary recombination of para-H_3^+ and ortho-H_3^+ with electrons: State selective study at 77–200 K

Petr Dohnal,[1] Michal Hejduk,[1] Jozef Varju,[1] Peter Rubovič,[1] Štěpán Roučka,[1] Tomáš Kotrík,[1] Radek Plašil,[1] Juraj Glosík,[1] and Rainer Johnsen[2]
[1]*Department of Surface and Plasma Science, Faculty of Mathematics and Physics, Charles University, Prague 18000, Czech Republic*
[2]*Department of Physics and Astronomy, University of Pittsburgh, Pittsburgh, Pennsylvania 15260, USA*

(Received 13 April 2012; accepted 1 June 2012; published online 26 June 2012)

Measurements in H_3^+ afterglow plasmas with spectroscopically determined relative abundances of H_3^+ ions in the para-nuclear and ortho-nuclear spin states provide clear evidence that at low temperatures (77–200 K) para-H_3^+ ions recombine significantly faster with electrons than ions in the ortho state, in agreement with a recent theoretical prediction. The cavity ring-down absorption spectroscopy used here provides an *in situ* determination of the para/ortho abundance ratio and yields additional information on the translational and rotational temperatures of the recombining ions. The results show that H_3^+ recombination with electrons occurs by both binary recombination and third-body (helium) assisted recombination, and that both the two-body and three-body rate coefficients depend on the nuclear spin states. Electron-stabilized (collisional-radiative) recombination appears to make only a small contribution. © *2012 American Institute of Physics*. [http://dx.doi.org/10.1063/1.4730162]

I. INTRODUCTION

The present experiments were motivated by the fundamental character of the recombination of H_3^+ ions,[1] its relevance to modeling of astrophysical diffuse clouds,[2] and electrical discharges in hydrogen. In cold diffuse clouds (temperatures from 50 to 100 K), H_3^+ ions are formed by cosmic-ray ionization of H_2, followed by the reaction $H_2^+ + H_2 \rightarrow H_3^+ + H$.[3] The H_3^+ ions subsequently either recombine by dissociative recombination (DR) with electrons or transfer protons to other atoms or molecules.[4] The recombination of H_3^+ ions competes with the rate of molecule formation in diffuse clouds and plays a pivotal role in the chemical evolution. Even though H_3^+ is the "simplest" triatomic ion, its recombination is a rather subtle process that has challenged theorists and experimentalists for many years. It has become clear in recent years that the ortho-modifications and para-modifications of H_3^+, distinguished by their nuclear spins and allowed rotational states, may recombine differently at low temperatures. The experiments described in this paper focus on this question. Unlike other previous experiments, they incorporate *in situ* spectroscopic identification of the recombining ion species in the recombining medium.

The spin dependence of H_3^+ recombination also plays a role in the interpretation of spectra observed in astrophysical clouds. For instance, a recent analysis by Crabtree *et al.*[5] of several diffuse molecular clouds suggests that the observed differences between the rotational excitation temperatures of H_2 and H_3^+ (denoted as $T_{(01)}(H_2)$ and $T(H_3^+)$) can be explained by a kinetic model that includes both reactive collisions of H_3^+ or para-H_3^+ with H_2 and recombination with electrons. The model makes specific allowance for the dependence of all relevant reaction rates on the ortho/para states of both H_2 and H_3^+. Surprisingly, reasonable agreement between observed and calculated excitation temperatures was found only when the DR rate coefficients of para-H_3^+ (nuclear spin $I = 1/2$) and H_3^+ (nuclear spin $I = 3/2$) were assumed to be nearly equal, which, however, is in conflict with the theoretical prediction[6] that the low-temperature DR rate coefficient of para-H_3^+ is considerably larger than that of H_3^+.

The history of H_3^+ recombination studies has been extensively covered in a number of reviews[7–12] and in the book by Larsson and Orel.[13] Many of the once puzzling disagreements among measured recombination coefficients have either been resolved or can be rationalized by invoking third-body stabilized recombination processes that occur in plasmas but not in beam-type experiments. Also, earlier serious discrepancies between experimental results and theory were largely resolved in 2001 when it was shown that the Jahn–Teller mechanism can account for the observed magnitude of dissociative recombination rates of H_3^+ ions.[14] Subsequent improvements of the theory[15] yielded a thermal rate coefficient of the dissociative recombination at 300 K of $\alpha_{DR} = 5.6 \times 10^{-8}$ cm^{3}s^{-1} which comes close to the magnitude of many experimental values. Theoretical predictions also agree quite well with the temperature dependence of the thermal rate coefficients inferred from ion-storage-rings (ISR) experiments. The more recent ISR studies employed ion sources specifically designed to produce rotationally cold ions ("cold ion sources")[16–18] and the results supported the theoretical thermal rate coefficients.[19] At that time it appeared that a satisfactory solution to the "H_3^+ enigma," the often-cited term coined by Bates *et al.* in 1993,[20] had been found. However, it proved difficult to verify experimentally that the H_3^+ ions circulating in the storage rings were truly rotationally cold

 © 2012 American Institute of Physics

Downloaded 28 Jun 2012 to 195.113.25.123. Redistribution subject to AIP license or copyright; see http://jcp.aip.org/about/rights_and_permissions

and this problem has not been entirely solved. It had been assumed that the "cold" rotational distributions inferred from spectroscopic observations in the ion source survived extraction into the storage ring and were not altered further in the ring, but recent experiments using high-resolution storage-rings indicate that these assumptions were not necessarily correct.[21,22] The problem awaits clarification by further experiments. Also, high-resolution storage rings data exhibit resonances at particular collision energies that have not been clearly assigned to specific recombination paths and are not predicted by theory.[22] Thus, a truly satisfactory convergence of theory and experiment has not been achieved. Petrignani *et al.*[22] summed up the current situation of storage-ring experiments: *"Presently no rate coefficient measurement with a confirmed temperature below 300 K exists."* Plasma afterglow measurements at reduced temperatures have been made, but those, as will be discussed later, have their own set of complications. Paraphrasing Bates *et al.*[20] and Larsson *et al.*,[19] we can sum up the state of the art today in the words: *"... the saga of the* H_3^+ *enigma continues...."*

Recent theoretical calculations[6] predict that the low-temperature DR rate coefficients for para-H_3^+ are larger than those for H_3^+ ions, by a factor of about ten at temperatures below 10 K. This prediction has been qualitatively confirmed at low electron-ion collision energies in storage-ring experiments using para-enriched H_3^+,[17,23] but, as has been mentioned before, the actual para/ortho abundance ratio of the recombining ions was not experimentally verified. This problem, of course, is closely linked to that of the rotational populations. Further progress will require direct *in situ* determination of the para/ortho ratio and rotational excitation of the stored H_3^+ ions. Experimental photodissociation measurements on H_3^+ ions in the ring may be one feasible approach (see discussion in Refs. 24 and 25).

The experiments described here make use of the plasma afterglow technique but add spectroscopic capabilities. Here, the ion densities are many orders of magnitude larger than those in storage rings which enables *in situ* spectroscopic absorption measurements of rotational populations of H_3^+ ions under recombination-controlled conditions. The feasibility of such experiments was demonstrated by us in a recent study in which we measured binary recombination rate coefficients for para-H_3^+ and ortho-H_3^+ ions ($^{\mathrm{p}}\alpha_{\mathrm{bin}}$ and $^{\mathrm{o}}\alpha_{\mathrm{bin}}$) at buffer gas temperature ~77 K.[26,27] The present study extends this work and provides recombination rate coefficients for pure para-H_3^+ and pure ortho-H_3^+ over a wider range of temperatures from 77 K to 200 K. As before, the experiments were carried out in a stationary afterglow (SA) in conjunction with a near-infrared cavity-ring-down absorption spectrometer (NIR–CRDS) for direct *in situ* determination of the kinetic temperature, the rotational temperature, and the spin states of the ions.

In a SA experiment[28] electrons and ions undergo multiple collisions with buffer gas atoms (here He and Ar) and reagent molecules (here H_2) prior to their recombination. The early phase of the afterglow is dominated by ion-formation and ion-conversion reactions, electron thermalization, and equilibration of internal degrees of freedom of the ions. Ideally, this early phase should be completed rapidly so that the only relevant processes during the recombination phase are binary electron-ion recombination and ambipolar diffusion of ions and electrons. However, the neutral constituents (He, H_2, and Ar in our case) and ambient electrons and ions can affect the overall recombination process as well as the para/ortho ratio and this requires careful consideration. There are two known ternary recombination processes that contribute to the plasma decay, ternary neutral-assisted recombination (largely due to the helium buffer),[29] and ternary electron-assisted collisional radiative recombination (CRR).[30–32] We have recently studied the ternary helium-assisted recombination of H_3^+ and D_3^+ ions with electrons at conditions similar to those of the present experiments[8,33–37] and found that H_3^+ ions recombine by both the binary process with rate coefficient α_{bin} and by ternary ("He-assisted") process with ternary rate coefficient K_{He}. The observed plasma decay yields an "effective" rate coefficient α_{eff} given by the sum $\alpha_{\mathrm{eff}} = \alpha_{\mathrm{bin}} + K_{\mathrm{He}}[\mathrm{He}]$ that can be decomposed into its parts by measuring the dependence of α_{eff} on helium density [He].

The role of electron-assisted CRR is less clear because experimental data and theoretical calculations exist only for atomic ions but not for molecular ions. For atomic ions the predicted very strong negative temperature dependence, $\alpha_{\mathrm{CRR}} \sim n_{\mathrm{e}} T^{-4.5}$, of the CRR rate coefficient, has been confirmed for temperatures above 300 K,[30,38,39] and recently also for Ar^+ ions at temperatures below 300 K.[32,40] In low-temperature plasmas most molecular ions are removed by fast dissociative recombination (see, e.g., book by Larsson and Orel[13]) and the contribution from collisional radiative recombination is usually negligible. However, at temperatures approaching 77 K the effective binary rate of CRR (Refs. 38 and 39) becomes comparable to typical DR rate coefficients for electron densities $>10^{10}$ cm^{-3}. Somewhat surprisingly, the H_3^+ afterglow studies of Amano[41,42] at gas temperatures near 77 K and electron densities $>10^{11}$ cm^{-3} seemed to indicate that CRR did not play a significant role. However, as Bates[20] pointed out, the occurrence of CRR is "inevitable," and to make matters worse, the observed plasma decay due to CRR can give the appearance of binary recombination since the energy released by CRR can lead to a time-dependent electron temperature. A quantitative re-analysis of Amano's experiments is beyond the scope of this paper. It is far from obvious that CRR made only a negligible contribution. It is also difficult to accept the author's conclusion that clustering of H_3^+ to form fast recombining H_5^+ ions was entirely absent.

In our flowing afterglow (FA, FALP (Ref. 34)) and stationary afterglow (SA (Refs. 26 and 43)) experiments we can measure at gas temperatures close to 77 K and cover a wide range of electron and ion densities, from 10^8 to 10^{11} cm^{-3}. This makes it possible to separate binary and helium-assisted ternary recombination of H_3^+ ions from CRR. We will conclude (see Appendix) that CRR may have a slight effect at the lowest temperature (77 K), but most likely it is completely negligible at higher temperatures.

II. EXPERIMENTAL METHODS

The basic methods of measuring recombination rates in afterglow plasmas are well known and will not be

Downloaded 28 Jun 2012 to 195.113.25.123. Redistribution subject to AIP license or copyright; see http://jcp.aip.org/about/rights_and_permissions

discussed here in great detail. This section focuses on the interconversion processes between para-H_3^+ and ortho-H_3^+ ions, and their recombination. Technical details of the experiments will be presented in Sec. III.

A. Afterglow processes in para-H_3^+ and ortho-H_3^+ dominated plasma

In the following upper left indices p, o, n, and e denote "para," "ortho," "normal," and "para-enriched" hydrogen (e.g., ${}^{\mathrm{p}}H_2$, ${}^{\mathrm{o}}H_2$, ${}^{\mathrm{n}}H_2$, and ${}^{\mathrm{e}}H_2$) and ${}^{\mathrm{p}}f_2$ and ${}^{\mathrm{o}}f_2$ denote their fractions. Para-H_3^+ and ortho-H_3^+ ions denote ${}^{\mathrm{p}}H_3^+$ and ${}^{\mathrm{o}}H_3^+$, while ${}^{\mathrm{p}}f_3$ and ${}^{\mathrm{o}}f_3$ stand for their fractions (i.e., ${}^{\mathrm{p}}f_3 = [{}^{\mathrm{p}}H_3^+]/[H_3^+]$ and ${}^{\mathrm{o}}f_3 = [{}^{\mathrm{o}}H_3^+]/[H_3^+]$ with ${}^{\mathrm{p}}f_3 + {}^{\mathrm{o}}f_3 = 1$). Absence of an index implies that the spin modification is not specified.

In a low-temperature afterglow plasma in a gas mixture of helium (the "buffer gas") with small additions of argon and hydrogen the principal processes affecting the densities of ${}^{\mathrm{p}}H_3^+$ and ${}^{\mathrm{o}}H_3^+$ are recombination, ambipolar diffusion, para/ortho conversion in reactions with H_2, and formation of H_5^+ in ternary association, i.e.:

$$ {}^{\mathrm{p}}H_3^+ + e^- \xrightarrow{{}^{\mathrm{p}}\alpha_{\mathrm{eff}}} \text{neutral products}, \tag{1a} $$

$$ {}^{\mathrm{o}}H_3^+ + e^- \xrightarrow{{}^{\mathrm{o}}\alpha_{\mathrm{eff}}} \text{neutral products}, \tag{1b} $$

$$ {}^{\mathrm{p}}H_3^+ + H_2 \xrightarrow{\nu_{\mathrm{po}}} {}^{\mathrm{o}}H_3^+ + H_2, \tag{1c} $$

$$ {}^{\mathrm{o}}H_3^+ + H_2 \xrightarrow{\nu_{\mathrm{op}}} {}^{\mathrm{p}}H_3^+ + H_2, \tag{1d} $$

$$ {}^{\mathrm{p}}H_3^+ + H_2 + He \xrightarrow{{}^{\mathrm{p}}\tau_{\mathrm{R}}} H_5^+ + He, \tag{1e} $$

$$ {}^{\mathrm{o}}H_3^+ + H_2 + He \xrightarrow{{}^{\mathrm{o}}\tau_{\mathrm{R}}} H_5^+ + He, \tag{1f} $$

where ${}^{\mathrm{p}}\alpha_{\mathrm{eff}}$ and ${}^{\mathrm{o}}\alpha_{\mathrm{eff}}$ stand for effective (apparent binary) recombination rate coefficients of pure para-H_3^+ and pure ortho-H_3^+ ions, respectively. ν_{po} and ν_{op} are the frequencies of para-H_3^+/ortho-H_3^+ conversion due to reactions with H_2. The spin state of the neutral hydrogen molecule in reactions (1c) and (1d) will change also, but because the neutral hydrogen is far more abundant than the ions, the resulting change in ${}^{\mathrm{p}}f_2$ can be neglected. ${}^{\mathrm{p}}\tau_{\mathrm{R}}$ and ${}^{\mathrm{o}}\tau_{\mathrm{R}}$ are time constants for ternary association, later we will assume that ${}^{\mathrm{p}}\tau_{\mathrm{R}} = {}^{\mathrm{o}}\tau_{\mathrm{R}}$ for simplification. The continuity equations for the ion densities $[{}^{\mathrm{p}}H_3^+]$ and $[{}^{\mathrm{o}}H_3^+]$ during the afterglow are:

$$ \frac{\mathrm{d}[{}^{\mathrm{p}}H_3^+]}{\mathrm{d}t} = -{}^{\mathrm{p}}\alpha_{\mathrm{eff}}[{}^{\mathrm{p}}H_3^+]n_{\mathrm{e}} - \frac{[{}^{\mathrm{p}}H_3^+]}{\tau_{\mathrm{D}}} - \nu_{\mathrm{po}}[{}^{\mathrm{p}}H_3^+] + \nu_{\mathrm{op}}[{}^{\mathrm{o}}H_3^+] - \frac{[{}^{\mathrm{p}}H_3^+]}{{}^{\mathrm{p}}\tau_{\mathrm{R}}}, \tag{2} $$

$$ \frac{\mathrm{d}[{}^{\mathrm{o}}H_3^+]}{\mathrm{d}t} = -{}^{\mathrm{o}}\alpha_{\mathrm{eff}}[{}^{\mathrm{o}}H_3^+]n_{\mathrm{e}} - \frac{[{}^{\mathrm{o}}H_3^+]}{\tau_{\mathrm{D}}} + \nu_{\mathrm{po}}[{}^{\mathrm{p}}H_3^+] - \nu_{\mathrm{op}}[{}^{\mathrm{o}}H_3^+] - \frac{[{}^{\mathrm{o}}H_3^+]}{{}^{\mathrm{o}}\tau_{\mathrm{R}}}, \tag{3} $$

where n_{e} is electron density and τ_{D} is the time constant for ambipolar diffusion, assumed to be equal for both spin modification of H_3^+. Three-body association of H_3^+ with H_2 to form H_5^+ is at the hydrogen and helium densities used in the present experiments relatively slow in comparison with the rate of the recombination (for details see Refs. 9, 34, and 44) and we can conclude $[H_5^+] \ll [H_3^+]$. Assuming that the plasma is quasineutral and that it contains no ions other than H_3^+ (i.e., $n_{\mathrm{e}} = [{}^{\mathrm{p}}H_3^+] + [{}^{\mathrm{o}}H_3^+]$), the continuity equation for the electron density (obtained by summing Eqs. (2) and (3)) becomes

$$ \frac{\mathrm{d}n_{\mathrm{e}}}{\mathrm{d}t} = -({}^{\mathrm{p}}f_3\,{}^{\mathrm{p}}\alpha_{\mathrm{eff}} + {}^{\mathrm{o}}f_3\,{}^{\mathrm{o}}\alpha_{\mathrm{eff}})n_{\mathrm{e}}^2 - \frac{n_{\mathrm{e}}}{\tau_{\mathrm{D}}} - \frac{n_{\mathrm{e}}}{\tau_{\mathrm{R}}}. \tag{4a} $$

The experimental data (see Sec. V) show that the fractions ${}^{\mathrm{p}}f_3$ and ${}^{\mathrm{o}}f_3$ are nearly constant during the afterglow. This implies that the para/ortho ratio is maintained by reactions (1c) and (1d) on a time scale that is short compared to the recombination time scale. In that case, one can define an overall effective (apparent binary) recombination rate coefficient for a given mixture of ortho and para ions by $\alpha_{\mathrm{eff}} = {}^{\mathrm{p}}f_3\,{}^{\mathrm{p}}\alpha_{\mathrm{eff}} + {}^{\mathrm{o}}f_3\,{}^{\mathrm{o}}\alpha_{\mathrm{eff}}$. Equation (4a) then simplifies to

$$ \frac{\mathrm{d}n_{\mathrm{e}}}{\mathrm{d}t} = -\alpha_{\mathrm{eff}}n_{\mathrm{e}}^2 - \frac{n_{\mathrm{e}}}{\tau_{\mathrm{L}}}, \tag{4b} $$

where $1/\tau_{\mathrm{L}} = 1/\tau_{\mathrm{D}} + 1/\tau_{\mathrm{R}}$. The time constant τ_{L} characterizes losses due to diffusion and reactions (1e) and (1f).

A measurement of α_{eff} for two or more different values of ${}^{\mathrm{p}}f_3$, but under otherwise identical conditions (temperature and density of He and H_2), then permits a determination of the individual recombination rate coefficients ${}^{\mathrm{p}}\alpha_{\mathrm{eff}}$ and ${}^{\mathrm{o}}\alpha_{\mathrm{eff}}$. These rate coefficients still do not necessarily represent purely binary recombination. In earlier work we observed that H_3^+ recombination in low-temperature (<300 K) helium-buffered afterglows occurs not only by binary recombination but also by ternary helium-assisted recombination.[8,33,34,36] In those studies ${}^{\mathrm{n}}H_2$ was used as a precursor gas to form H_3^+. It was then found that the effective recombination coefficient α_{eff} varies linearly with helium density [He], i.e.,

$$ \alpha_{\mathrm{eff}}(T, [\mathrm{He}]) = \alpha_{\mathrm{bin}}(T) + K_{\mathrm{He}}[\mathrm{He}], \tag{5} $$

where α_{bin} and K_{He} are the binary and ternary recombination rate coefficients. Previous experiments at 77 K (Ref. 27) showed that the same linear relation holds for the state-selected effective recombination rate coefficients ${}^{\mathrm{p}}\alpha_{\mathrm{eff}}$ and ${}^{\mathrm{o}}\alpha_{\mathrm{eff}}$. Hence, least-square fits to data of α_{eff} as a function of the helium density for two different values of ${}^{\mathrm{p}}f_3$ can be analyzed to obtain α_{bin} and K_{He} for each of the two spin states of H_3^+.

In experiment, ${}^{\mathrm{p}}f_3$ can be enhanced from about 0.5 to 0.8 by substituting para-enriched hydrogen for normal hydrogen. This was tested by a preliminary set of experiments, to be discussed next. Technical details of the para H_2 generator and the optical absorption measurements will be presented in Sec. III.

Downloaded 28 Jun 2012 to 195.113.25.123. Redistribution subject to AIP license or copyright; see http://jcp.aip.org/about/rights_and_permissions

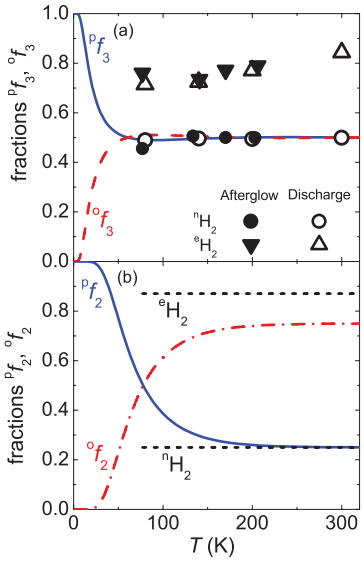

FIG. 1. Panel (a): Calculated temperature variation of the fractions $^pf_3$ and $^of_3$ in thermal equilibrium, compared to measured values of $^pf_3$ during the discharge phase (open triangles) and during the afterglow (closed circles and triangles) in experiments with either $^nH_2$ or $^eH_2$. Panel (b): Calculated thermal-equilibrium fractions $^pf_2$ and $^of_2$. The dashed horizontal lines indicate the values of $^pf_2$ in experiments with either $^nH_2$ or $^eH_2$ (measured by NMR).

B. Method of controlling the relative abundance of para-H_3^+ and ortho-H_3^+

In the experiment, normal $^nH_2$ is obtained by cooling normal hydrogen from 300 K to lower temperatures without ortho–para conversion, i.e., in a container without a catalyst. Hence, $^nH_2$ will have fraction $^pf_2 = 1/4$ and $^of_2 = 3/4$. Para-enriched H_2 is produced by cooling normal hydrogen to cryogenic temperatures in the presence of a catalyst and then letting it warm up without the catalyst to the desired temperature. Our experiments confirmed earlier findings that an increase of $^pf_3$ in hydrogen discharges can be achieved by using $^eH_2$ instead of $^nH_2$ (see, e.g., Refs. 45 and 46), and that the increase of $^pf_3$ observed during the microwave discharge persists into afterglow phase.[26,27,43]

Figure 1 shows the equilibrium values $^pf_3$ and $^of_3$ and $^pf_2$ and $^of_2$ for temperatures from 0 to 300 K, calculated using published energy levels.[47,48] The same graph shows our experimental values of $^pf_3$ and $^of_3$. In normal H_2 measured $^pf_3$ approach 0.5 at temperatures above ~77 K, this is the value corresponding to thermal equilibrium at these temperatures. When para-enriched H_2 is used, measured $^pf_3$ becomes significantly larger (~0.8).

III. EXPERIMENTAL APPARATUS

A. Stationary afterglow

The plasma is generated in a pulsed microwave discharge in a fused silica tube (inner diameter ~ 1.5 cm) cooled by liquid nitrogen to nearly 77 K or by pre-cooled nitrogen gas for measurements in the range 80–220 K. The tube contains a mixture of He/Ar/H_2 with a typical composition

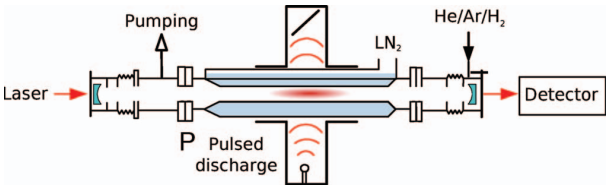

FIG. 2. Schematic diagram (not to scale) of the discharge tube and the optical resonator (cw–CRDS). The discharge tube at the center (containing a He/Ar/H_2 gas mixture) is immersed in liquid or pre-cooled gaseous nitrogen. The light signal exiting the optical cavity is measured by a photodetector (InGaAs avalanche photodiode).

$10^{17}/10^{14}/10^{14}$ cm^{-3} (details of the ion formation reactions are given in Refs. 8, 9, 34, 37, 44, and 49. The gas handling system includes a "para H_2 generator," used to prepare samples of para-enriched H_2, indicated here as $^eH_2$.[43] The microwave generator 2.45 GHz is equipped with an external fast high voltage switch to cut off the power to the magnetron within a fall time of < 30 μs. A fairly low microwave power in the range 5–15 W, with ~50% duty cycle, was used to avoid excessive heating of the gas during the discharge.

B. CRDS spectroscopy

The principal diagnostic technique employs cavity ring down absorption spectroscopy in the continuous wave modification (cw-CRDS), based on the configuration described by Romanini *et al.*[50] The instrument used here was fabricated in our laboratory for spectroscopic time-resolved studies of elementary processes in plasmas, such as ion-electron recombination (see, e.g., Refs. 43 and 51–54). The light source is a fiber-coupled distributed feedback (DFB) laser diode with a central wavelength of 1381.55 nm, linewidth <2 MHz, and maximum output optical power of 20 mW. The wavelengths are measured by a wavemeter and a Fabry–Perot etalon. The ring-down signal exiting the optical cavity is detected by an InGaAs avalanche photodiode. A schematic picture of the apparatus is shown in Fig. 2.

The cw-CRDS instrument in conjunction with associated data processing electronics records the time-dependent optical absorption signals during the discharge and the afterglow. The observed absorption strengths are then converted to ion concentrations. By tuning the wavelength of the laser diode one can also determine the kinetic temperatures of the H_3^+ ions from the Doppler-broadened absorption line profiles, and their evolution during the discharge and in the early afterglow.

All spectroscopic absorption measurements were performed on the second overtone transitions originating from the ground vibrational level of H_3^+. The lowest rotational levels (1,0) (ortho) and (1,1) (para) of the vibrational ground state were monitored routinely, but the higher lying level (3,3) (ortho) was probed only occasionally. These first two transitions were chosen for routine scanning because they have closely spaced frequencies that can be covered by a single DFB laser. This made it possible to switch quickly from observing one to the other H_3^+ spin state. Figure 3 shows the relevant rotational levels and Table I lists the transitions. The

Downloaded 28 Jun 2012 to 195.113.25.123. Redistribution subject to AIP license or copyright; see http://jcp.aip.org/about/rights_and_permissions

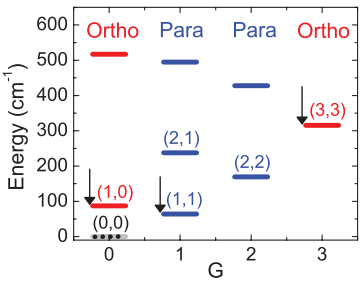

FIG. 3. Rotational energy levels of the ground vibrational state of H_3^+. The energy levels (J,G) are labeled by quantum numbers J and G.[55] The zero of the energy scale is taken at the forbidden (0,0) level, indicated by a dashed line. The rotational states, (1,0), (1,1), and (3,3) observed in the present study are indicated by arrows. Compiled from the data in Ref. 56.

energy levels are labeled (J,G) by their quantum numbers J and G.[55]

C. Para H_2 generator

Normal hydrogen gas at 300 K is a mixture of 1/4 para-hydrogen and 3/4 ortho-hydrogen (i.e., ${}^{\mathrm{p}}f_2 = 0.25$ and ${}^{\mathrm{o}}f_2 = 0.75$, see Fig. 1). It is well known that the composition changes extremely slowly when the hydrogen is cooled or heated, unless the gas is in contact with a suitable paramagnetic catalyst that facilitates re-alignment of the proton spins. By using a catalyst and cooling to low temperatures, nearly pure samples of para-hydrogen in the lowest rotational state ($J = 0$, $v = 0$) can be produced. When the catalyst is then removed and the gas is reheated, the hydrogen retains its low-temperature para/ortho composition for a sufficiently long time to carry out experiments with para-enriched hydrogen.

We produced para-enriched hydrogen in a closed-cycle helium cryostat that cools hydrogen in a conversion chamber[57] filled with the catalyst Fe_2O_3. Nuclear magnetic resonance (NMR) was used to check the actual para/ortho ratio in the enriched para-hydrogen ${}^{\mathrm{e}}H_2$. The experimental setup for measurement of para-hydrogen enrichment was similar to the one used in study by Tom.[58] The NMR measurements indicated (87 ± 5)% content of para-hydrogen, i.e., ${}^{\mathrm{p}}f_2 = 0.87$,[59] which is adequate for our experiments. In the following text we will use this value of ${}^{\mathrm{p}}f_2$ without explicitly mentioning its error. It suffices to enrich the hydrogen to a level where the fraction of para-H_3^+ significantly exceeds the value ${}^{\mathrm{p}}f_3 = 0.5$ in normal hydrogen. Figure 1 shows experimental data on the para-enrichment of H_3^+ measured in the discharge and in the afterglow for ${}^{\mathrm{e}}H_2$ and for ${}^{\mathrm{n}}H_2$.

IV. TEMPERATURES IN THE H_3^+ AFTERGLOW PLASMA

The different particles in a plasma afterglow and their internal degrees of freedom are not necessarily in complete thermal equilibrium with each other and with the walls of the plasma container. For instance, the electron temperature T_e can significantly exceed that of the ions T_{Kin} and gas atoms T_G because the energy transfer in electron collisions with heavy particles is inefficient. Also, the ion's rotational temperature T_{Rot} and vibrational temperature T_{Vib} do not have to be equal to the ion's translational temperature.

A. Ion and neutral gas kinetic temperatures

Since the exchange of translational energy between ions and neutral gas atoms is very efficient, the kinetic temperature of the H_3^+ ions during the afterglow should be nearly the same as the gas temperature, provided that the plasma is free of macroscopic electric fields that, in principle, can heat the ions. The ambipolar electric field is too weak to cause a significant heating. This expectation was confirmed by time-resolved scans of the Doppler-broadened absorption lines of H_3^+ ions over the experimental temperature range from 77 K to 220 K. The inferred temperatures of the H_3^+ ions during the discharge and the afterglow were equal to the wall temperature within ~10 K (see also Figs. 3 and 4 in Ref. 43). This also confirmed that the gas temperature in the discharge region approaches that of the walls. Previous afterglow studies in this lab performed under similar conditions,[60] but using absorption lines of H_2O rather than of H_3^+, led to the same conclusion.

B. Electron temperature T_e

The electron temperature T_e was not measured in these experiments. In previous FALP experiments[61–63] we used Langmuir probes to determine the electron energy distribution function in He and He/Ar buffered afterglow plasmas under conditions similar to those in the present study. It was found that the electrons gained a Maxwellian distribution with the gas temperature very quickly after the metastable helium atoms from the microwave discharge had been depleted by Penning ionization of argon atoms.[64] The electron cooling time constant at typical helium densities can also be estimated as the product of the electron-helium collision frequency (>1 GHz) and the mass ratio $2m_e/m_{He}$, which yields a cooling time of $\tau_\varepsilon < 10\ \mu$s.[65] We indirectly observed fast cooling of electrons by monitoring visible light emissions from the discharge and in the very early afterglow.[51] These estimates

TABLE I. Transitions monitored in the present study. For details on the spectroscopic notation see Ref. 55. Energy levels were taken from Ref. 56.

Wavenumber (cm^{-1})	Spin	Low. lvl. (cm^{-1})	Up. lvl. (cm^{-1})	Transition
7234.957	o	315.349	7550.316	$3\nu_2^1(4,3) \leftarrow 0\nu_2^0(3,3)$
7237.285	p	64.1234	7301.4084	$3\nu_2^1(2,1) \leftarrow 0\nu_2^0(1,1)$
7241.245	o	86.9591	7328.2041	$3\nu_2^1(2,0) \leftarrow 0\nu_2^0(1,0)$

Downloaded 28 Jun 2012 to 195.113.25.123. Redistribution subject to AIP license or copyright; see http://jcp.aip.org/about/rights_and_permissions

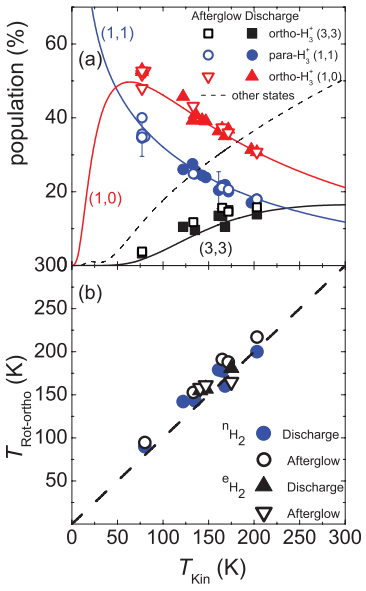

FIG. 4. Rotational temperatures of H_3^+ ions. Panel (a): Relative populations of H_3^+ ions in ortho (1,0) and (3,3) and para (1,1) states versus kinetic temperature of the ions measured in the experiments with normal H_2. The data obtained during the discharge (before switching it off) and during the afterglow (at ~ 150 μs) are indicated by the filled and the open symbols, respectively. The full lines indicate the calculated populations of the indicated states for ions in thermal equilibrium at temperatures equal to T_{Kin}. The dashed line indicates joint population of all other states. Panel (b): The measured rotational temperature of ortho manifold ($T_{Rot-ortho}$) versus measured kinetic temperature (T_{Kin}). The data were obtained in experiments with $^nH_2$ and with $^eH_2$. The dashed straight line indicates equality $T_{Rot-ortho} = T_{Kin}$.

need to be refined when the plasma contains energy sources that heat the electron gas, for instance, recombination of ions by collisional radiative recombination. It is shown in Appendix that this heating mechanism at used electron densities can elevate the electron temperature slightly in the early afterglow at gas temperatures near 77 K, but becomes unimportant at higher gas temperatures and lower electron densities.

C. Vibrational excitation of the H_3^+ ions

We expect that all excited vibrational states of H_3^+ are quenched in collisions with He, Ar, and H_2. The reaction $H_2^+ + H_2$ can produce H_3^+ ions with vibrational excitation up to $v = 5$ but the ions with internal energies above 0.57 eV are rapidly destroyed by proton transfer with Ar, leaving only ions in $v \leq 2$ (for details see Refs. 23 and 53). There is also a high probability that the vibrational excitation of H_3^+ will be quenched in collision with H_2. Kim *et al.*[66] obtained a rate coefficient 3×10^{-10} cm^{3}s^{-1} for vibrational relaxation of H_3^+ ions in H_2. At $[H_2] \sim 10^{14}$ cm^{-3} this leads to vibrational relaxation within 30 μs (see also discussion and references in Ref. 67). We conclude that at Ar and H_2 densities of the order of $\sim 10^{14}$ cm^{-3} vibrational excitation will be quenched within 30 μs after ion formation. Collisions with He atoms are more frequent by at least by three orders of magnitude, but vibrational quenching by helium can be very low, as it is, e.g., in collisions of He with vibrationally excited N_2^+ ions (see, e.g., Ref. 68). To estimate the rate of formation of H_3^+ ions (in reactions with H_2, Ar, and He) we studied the processes at very early afterglow at several He densities and at low H_2 and Ar densities ($[H_2]$, $[Ar] \sim 10^{12}$ cm^{-3}) in our previous study[69] and we found qualitative agreement with results obtained from kinetic model.

D. Rotational and nuclear spin states of the H_3^+ ions

The determination of the spin-dependent recombination rate coefficients of H_3^+ ions relies on accurate knowledge of the relative abundance of ions in the ortho-states and para-states and corresponding rotational states. In this experiment these quantities were measured by optical absorption, rather than by modeling the kinetic processes, but we will briefly describe the reactions of relevance.

The probability of changing the nuclear spin alignment by radiation is very low and likewise collisions with He or Ar atoms are inefficient in causing spin changes. The principal rotational equilibration and spin scrambling process is the proton-hopping or exchange reaction of H_3^+ with H_2 that proceeds via a short-lived $(H_5^+)^*$ reaction complex. The reaction has been studied in great detail.[5,27,70–75] It has been found that the ratio of $[^pH_3^+]/[^oH_3^+]$ in plasmas containing H_2 is constrained by nuclear spin selection rules and depends on the relative concentrations of $^pH_2$ and $^oH_2$ (Refs. 70–75) and on temperature. Rotational-state changes without changing the nuclear spin state, i.e., within the para or ortho manifold, are possible by radiation and in collisions with He or Ar. Electron collisions can change the rotational states within the para or the ortho manifold with rates approximately ten times faster than the rate of the dissociative recombination (for details see Ref. 76) which means than on average an H_3^+ ion has ten thermalizing collisions with electrons prior to its recombination at our conditions. For this reason, we expect that ions are rotationally thermalized within the para and ortho manifolds.

Rotational temperatures of the ions were inferred from measurements of absolute densities of ions in three rotational states. Panel (a) of Fig. 4 shows the populations of two ortho-states and one para-state, measured during the discharge and during the afterglow in experiments with normal H_2 at temperatures 77–200 K. The relative populations of the ortho- and para-states were computed by dividing the measured absolute ion densities in a given state by the density of all H_3^+ ions, assuming a thermal rotational state distribution. At temperatures where two H_3^+ absorption lines were observable, the rotational temperature $T_{Rot-ortho}$ within the ortho manifold was obtained also. The relation between the rotational temperature ($T_{Rot-ortho}$) and the kinetic temperature (T_{Kin}) of the ions is shown in panel (b) of Fig. 4. The data plotted in panel (b) were obtained in experiments with $^nH_2$ and with $^eH_2$. The agreement between $T_{Rot-ortho}$ and T_{Kin} is very good ($|T_{Rot-ortho} - T_{Kin}| < 15$ K). During the discharge, a slightly higher rotational temperature $T_{Rot-ortho}$ compared to the kinetic temperature T_{Kin} is expected since the ions are produced with higher rotational excitation and then relax by collisions to lower states. During the afterglow, the lifetime of the H_3^+ ions is longer (because ambipolar diffusion is slower) and

Downloaded 28 Jun 2012 to 195.113.25.123. Redistribution subject to AIP license or copyright; see http://jcp.aip.org/about/rights_and_permissions

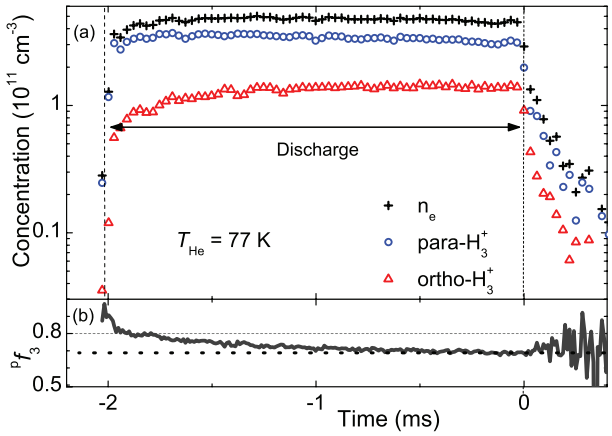

FIG. 5. Panel (a): Evolution of $[^pH_3^+]$, $[^oH_3^+]$, and n_e measured in experiments with enriched hydrogen, $^eH_2$, at $T_{He}\sim$ 77 K and [He] = 4 × 10^{17} cm^{-3}, $[^eH_2] = 3 \times 10^{14}$ cm^{-3}, [Ar] = 6 × 10^{13} cm^{-3}. The decay in the early afterglow is caused by recombination. Panel (b): Evolution of $^pf_3$. The final value of $^pf_3 \sim 0.7$ during the late discharge and in the early afterglow exceeds the equilibrium value of $^pf_3 \sim 0.5$ in normal hydrogen.

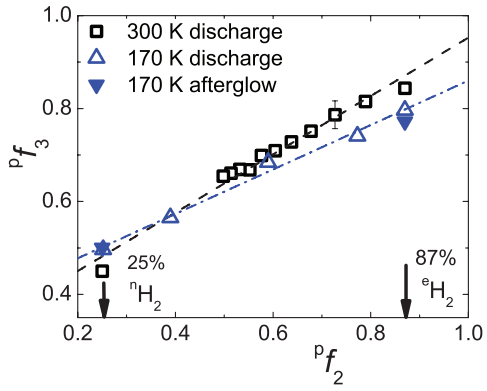

FIG. 6. Dependence of $^pf_3$ on $^pf_2$ measured in a He/Ar/H_2 mixture at 300 K (discharge) and 170 K (discharge and afterglow). Arrows point to the values of $^pf_2$ in $^nH_2$ and $^eH_2$ that were used in the recombination studies. Open symbols: Values in the discharge ($\tau_{Disch} \sim 2$ ms). Filled symbols: Values during the afterglow ($\tau_{Afterglow} \sim 150$ μs).

more time is available for rotational relaxation. Some production of rotationally excited H_3^+ ions may occur in very early afterglow. Therefore, in the determination of $T_{Rot-ortho}$ we excluded data obtained during the first $\sim$ 150 μs after switching off the discharge.

We concluded that the ions under study were kinetically and internally thermalized in plasmas containing $^nH_2$, within the experimental uncertainties of $T_{Rot-ortho}$, T_{Kin}, and $^pf_3$(see Figs. 1 and 4). In plasmas containing $^eH_2$, we also found that $T_{Rot-ortho} \sim T_{Kin} \sim T_{He}$ (see panel (b) of Fig. 4), but in this case the relative abundances of para-H_3^+ and ortho-H_3^+ ($^pf_3$ and $^of_3$) are not in thermal equilibrium (see panel (a) of Fig. 1). The enrichment of para-H_3^+ will be discussed next.

E. H_3^+ para to ortho ratio

We measured absolute densities $[^pH_3^+]$ and $[^oH_3^+]$ during the discharge and during the afterglow to determine the dependence of the para-H_3^+ and ortho-H_3^+ fractions on experimental conditions. The time resolution in our experiment suffices to record the temporal evolution during the discharge and during the early afterglow. Typical evolutions of $[^pH_3^+]$, $[^oH_3^+]$ and electron densities are plotted in panel (a) of Fig. 5 for the case where $^eH_2$ was the precursor gas. The electron density n_e is taken as the sum $[^pH_3^+] + [^oH_3^+]$. Panel (b) of Fig. 5 shows the measured fraction $^pf_3$ of $[^pH_3^+]$. After the rapid change in the early discharge the variation during the discharge becomes slow. The faster change of $^pf_3$ at the beginning reflects the transition from the nascent H_3^+, formed by proton transfer from ArH^+ or H_2^+ to H_2, to the steady state established in subsequent reactions with H_2. A thorough discussion of the reactions is contained in two recent papers by Crabtree *et al.*[45,46]). During the discharge, the para/ortho composition of H_2 ($^pf_2$) changes slowly as a consequence of H_2 dissociation and recombination and hence $^pf_3$ also changes during the discharge. When we refer to values (e.g., $T_{Rot-ortho}$, T_{Kin}) measured "during the discharge" we mean values measured shortly before switching off the discharge ($\tau_{Disch} \sim 2$ ms), unless stated otherwise (see also discussion in Ref. 43).

Our systematic measurements of the evolution of the para/ortho composition show that, under the conditions of this set of experiments, the fraction $^pf_3$ remains nearly constant during the afterglow, and that it can be varied by using normal or para enriched hydrogen. We also measured the dependence of $^pf_3$ on $^pf_2$ which was varied from $^pf_2$= 0.25 to ~0.87 by mixing $^nH_2$ with $^eH_2$, while keeping the overall hydrogen density ($[^nH_2] + [^eH_2]$) constant. The dependence of $^pf_3$ on $^pf_2$ measured at 300 K and at 170 K (see Fig. 6) is linear and the same was found to be true at other temperatures (for details see Ref. 43). The linearity is a consequence of the spin-scrambling reaction with hydrogen.[70–73] Crabtree *et al.*[45,46] have recently discussed in great detail the general dependence of $^pf_3$ on $^pf_2$ and other experimental conditions. For the present study of H_3^+ recombination a quantitative understanding of the reaction kinetics is not required; it is only important that $^pf_3$ is known and can be varied over a significant range.

V. EXPERIMENTAL RESULTS – STATE SELECTIVE RECOMBINATION

The measured electron-density decay curves were analyzed to obtain apparent binary recombination rate coefficients for two particular values of $^pf_3$(see Eqs. (2)—(4)). Further details can also be found in Ref. 27. We carried out a systematic set of measurements which differed only in the value of $^pf_2$, but employed otherwise very similar conditions. The densities of para (1,1), ortho (1,0), and ortho (3,3) states of H_3^+ were monitored. Examples of data measured at 170 K with $^nH_2$ and with $^eH_2$ are plotted in Figs. 7 and 8, respectively. Note the large difference in measured populations of particular rotational states of H_3^+ in both experiments (see panels (b) of both figuers). In this set of experiments we obtained $^pf_3 \sim 0.5$ for $^nH_2$ and $^pf_3 \sim 0.7$–0.8 for $^eH_2$ (see panels (c) of both figures). Note also that in both experiments the values of $^pf_3$ are nearly constant during the afterglow.

Downloaded 28 Jun 2012 to 195.113.25.123. Redistribution subject to AIP license or copyright; see http://jcp.aip.org/about/rights_and_permissions

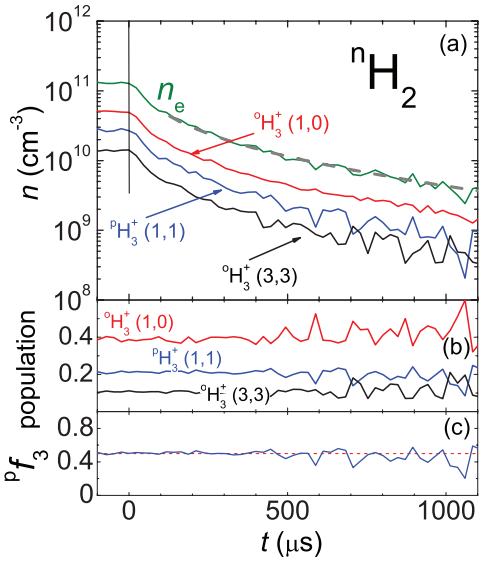

FIG. 7. Panel (a): Example of decay curves of densities of ions in para (1,1), ortho (1,0), and ortho (3,3) states of H_3^+, measured during the afterglow in a He/Ar/$^{n}H_2$ gas mixture at 170 K, 1440 Pa of He, $[H_2] = 1 \times 10^{14}$ cm^{-3}, and $[Ar] = 2 \times 10^{14}$ cm^{-3}. Time is set to zero at the beginning of the afterglow. The vertical bar shows the end of the discharge period and the beginning of the afterglow. Electron density is obtained as a sum of ion densities. Panel (b): The measured relative populations of para (1,1), ortho (1,0), and ortho (3,3) states of H_3^+, note the nearly constant values during whole afterglow. Panel (c): Measured fraction $^{p}f_3$ of para-H_3^+.

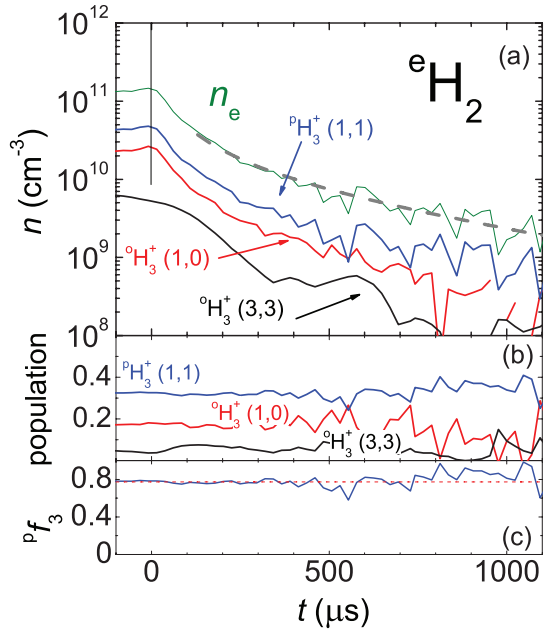

FIG. 8. Panel (a): Example of decay curves of densities of ions in para (1,1), ortho (1,0), and ortho (3,3) states of H_3^+, measured during the afterglow in a He/Ar/$^{e}H_2$ gas mixture at 170 K, 1550 Pa of He, $[H_2] = 1 \times 10^{14}$ cm^{-3}, and $[Ar] = 2 \times 10^{14}$ cm^{-3}. The vertical bar shows the end of the discharge period and the beginning of the afterglow. Panel (b): The measured relative populations of para (1,1), ortho (1,0), and ortho (3,3) states of H_3^+. Panel (c): Measured fraction $^{p}f_3$ of para-H_3^+.

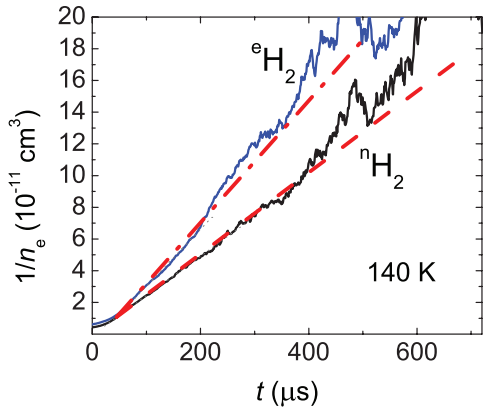

FIG. 9. Examples of the evolutions of the reciprocal number density $1/n_e$ during the afterglow when using normal $^{n}H_2$ or para-enriched $^{e}H_2$ at otherwise identical conditions. The effective (apparent) binary recombination rate coefficient is given by the slope of the linear part of the plot.

From the densities of the ions in (1,1) and (1,0) states we calculated, assuming thermal equilibrium (TDE) within the para-manifolds and ortho-manifolds, the total densities $[^{p}H_3^+]$ and $[^{o}H_3^+]$ and their sum, i.e., the electron density. The electron-density decay curves can be approximately analyzed by graphing $1/n_e$ versus decay time. The slope of the linear part of the plot yields the effective (apparent) binary recombination rate (for details see Ref. 61). Examples of such graphs of data obtained with $^{n}H_2$ and $^{e}H_2$ are shown in Fig. 9.

This simple form of analysis demonstrates that recombination in afterglows containing para-enriched hydrogen $^{e}H_2$, i.e., with higher relative population of para-H_3^+, is faster than when normal hydrogen is used. However, it neglects ambipolar diffusion and eventual reactive losses characterized in Eqs. (2) and (3). Hence, we used the more advanced "integral analysis" of the measured electron density decay curves (for details of "integral analysis" see Refs. 61 and 77). This analysis can separate α_{eff} from τ_L and minimize influence of ternary association (1e) and (1f) on determination of α_{eff}. The first 50–150 μs of the afterglow decay were excluded because probably new ions were still being formed (for details see Refs. 8, 27, 43, and 69. At 77 K special attention was paid to analysis of the decay curves because of a possible influence of the CRR process, which is discussed in Appendix.

The dependences of $^{n}\alpha_{eff}$ and $^{e}\alpha_{eff}$ on He density measured at 170 K are shown in panel (a) of Fig. 10. Panel (c) shows values of the corresponding fractions $^{p}f_3$. Note that the fractions $^{p}f_3$ are different in $^{n}H_2$ and in $^{e}H_2$, but are independent on helium density [He]. Both, $^{n}\alpha_{eff}$ and $^{e}\alpha_{eff}$ increase linearly with increasing [He]. Therefore (see Eq. (5)), we can obtain separate binary and ternary recombination rate coefficients for known para/ortho ratios. The values obtained with normal hydrogen refer to the thermal equilibrium H_3^+ with $^{p}f_3 \sim 0.5$. In our previous FALP experiments using $^{n}H_2$ we assumed but did not prove that $^{p}f_3 = 0.5$. The present experiments with $^{n}H_2$ confirmed that $^{p}f_3 = 0.5$ and $T_{Rot-ortho} = T_{Kin}$. In other words, the values of α_{bin} and K_{He} recombination rate coefficients obtained in our previous FALP experiments were the values appropriate for thermal equilibrium.[8,33–37]

Downloaded 28 Jun 2012 to 195.113.25.123. Redistribution subject to AIP license or copyright; see http://jcp.aip.org/about/rights_and_permissions

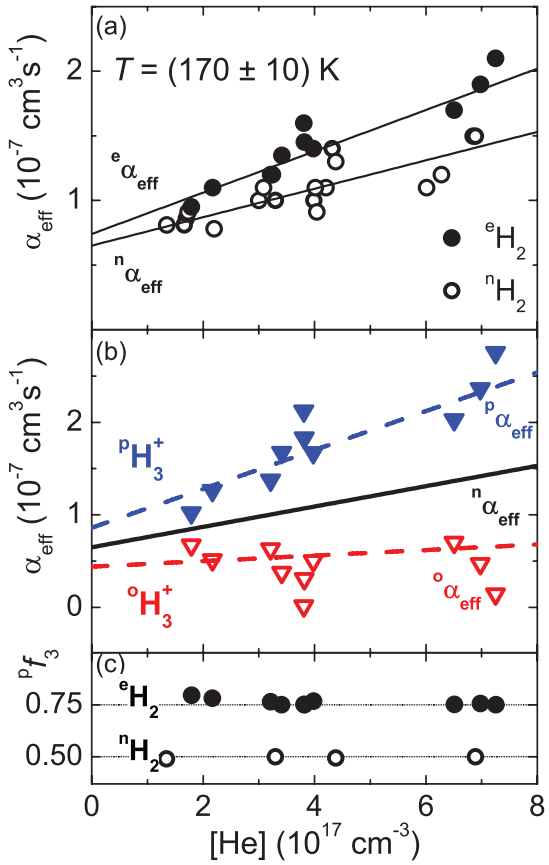

FIG. 10. Measured dependence of effective recombination rate coefficients α_{eff} on He density at 170 K. Panel (a): The values α_{eff} measured using $^{n}H_2$ as the precursor gas ($^{n}\alpha_{\text{eff}}$, open circles) and the values measured using $^{e}H_2$ ($^{e}\alpha_{\text{eff}}$, filled circles). Panel (b): The calculated values $^{p}\alpha_{\text{eff}}$ and $^{o}\alpha_{\text{eff}}$ for pure para-H_3^+ (filled triangles) and pure H_3^+ (open triangles), respectively. For comparison straight line obtained by fit of values $^{n}\alpha_{\text{eff}}$ in panel (a) is also plotted. Panel (c): The $^{p}f_3$ fractions of para-H_3^+ measured in the experiments with $^{n}H_2$ and $^{e}H_2$.

We measured the dependences of $^{n}\alpha_{\text{eff}}$ and $^{e}\alpha_{\text{eff}}$ on [He] for temperatures in the range 77–200 K. From the dependences of $^{n}\alpha_{\text{eff}}$ and $^{e}\alpha_{\text{eff}}$ on [He] and the corresponding values of $^{p}f_3$ we calculated values $^{p}\alpha_{\text{eff}}$ and $^{o}\alpha_{\text{eff}}$ for pure para-H_3^+ and for pure ortho-H_3^+, respectively. In these calculations, linear fits to the data measured with $^{n}H_2$ were used as a reference (the full lines in panels (a) and (b) of the Fig. 10 indicated as $^{n}\alpha_{\text{eff}}$). The obtained negative values of $^{o}\alpha_{\text{eff}}$ were truncated to zero and the corresponding values of $^{p}\alpha_{\text{eff}}$ were corrected accordingly. By fitting the data $^{p}\alpha_{\text{eff}}$ and $^{o}\alpha_{\text{eff}}$ (panel (b) of Fig. 10) with a linear dependence (Eq. (5)) we obtained the corresponding binary ($^{p}\alpha_{\text{bin}}$ and $^{o}\alpha_{\text{bin}}$) and ternary ($^{p}K_{\text{He}}$ and $^{o}K_{\text{He}}$) recombination rate coefficients for pure para-H_3^+ and for pure ortho-H_3^+. This form of data analysis is also described in Ref. 27.

VI. RESULTS—TERNARY HE ASSISTED RECOMBINATION OF PARA-H_3^+ AND ORTHO-H_3^+

The present SA–CRDS experiments cover a range of pressures from 200 to 1600 Pa, corresponding to maximum He densities of 1.6×10^{18} cm^{-3} at 77 K and $\sim 6 \times 10^{17}$ cm^{-3} at 200 K. The ability to vary the He density over a large range of nearly a factor of 10 improves the accuracy of the inferred ternary rate coefficients. The dependences of α_{eff} on [He] were measured at four temperatures (77, 140, 170, and 200 K) using $^{n}H_2$ and $^{e}H_2$. The dependences of $^{p}\alpha_{\text{eff}}$ and $^{o}\alpha_{\text{eff}}$ on helium density obtained for 170 K are shown in panel (b) of Fig. 10 and dependences obtained for 77 K and for 140 K can be found in our previous papers[27,78] and are shown in Fig. 11 (the values of $^{p}\alpha_{\text{eff}}$ were omitted in Fig. 11 for better clarity). From the dependences of $^{p}\alpha_{\text{eff}}$ and $^{o}\alpha_{\text{eff}}$ on [He] we obtained (using Eq. (5)) the corresponding binary and ternary recombination rate coefficients α_{bin} and K_{He}. In spite of the fairly large scatter in the data it is clear that ternary recombination depends on the spin state of recombining ions (on $^{p}f_3$). This large scatter is mirrored in error bars of the values shown in Figs. 12 and 13. As can be seen from Fig. 11, zero values of extrapolated $^{o}\alpha_{\text{bin}}$ cannot be excluded at the lowest temperatures. For all three temperatures the ternary helium-assisted recombination of para-H_3^+ is faster than the recombination of H_3^+.

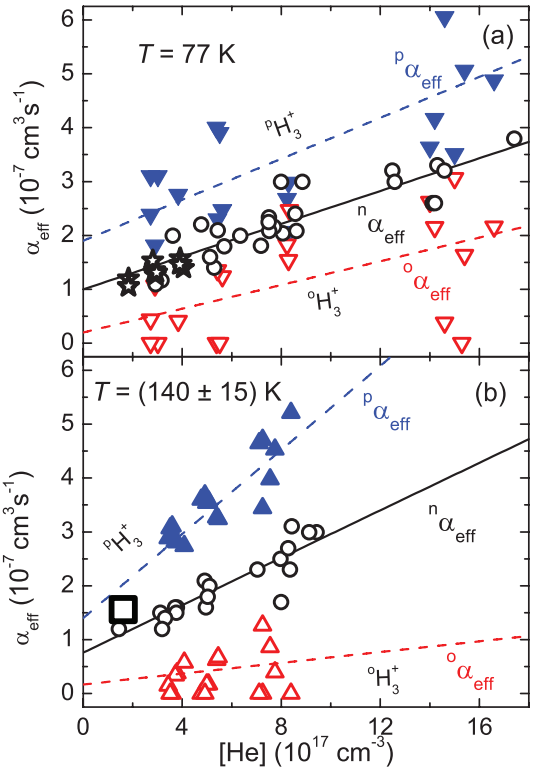

FIG. 11. Measured effective recombination rate coefficients $^{p}\alpha_{\text{eff}}$ and $^{o}\alpha_{\text{eff}}$ (closed and open triangles, respectively) as a function of He density at 77 K (panel (a), for details see also Ref. 27) and at 140 K (panel (b)). The full lines indicate $^{n}\alpha_{\text{eff}}$. The stars in panel (a) are data measured in previous FALP experiment at 77 K (Ref. 34) and the large square in panel (b) represents data measured in previous FALP and stationary afterglow experiments at 130 K.[34,79] The slopes of the straight-line fits yield the corresponding ternary recombination rate coefficients (K_{He}) while the intercept for [He] → 0 gives the corresponding α_{bin}.

Figure 12 shows the ternary recombination rate coefficients $^{p}K_{\text{He}}$ and $^{o}K_{\text{He}}$ as a function of temperature, as

Downloaded 28 Jun 2012 to 195.113.25.123. Redistribution subject to AIP license or copyright; see http://jcp.aip.org/about/rights_and_permissions

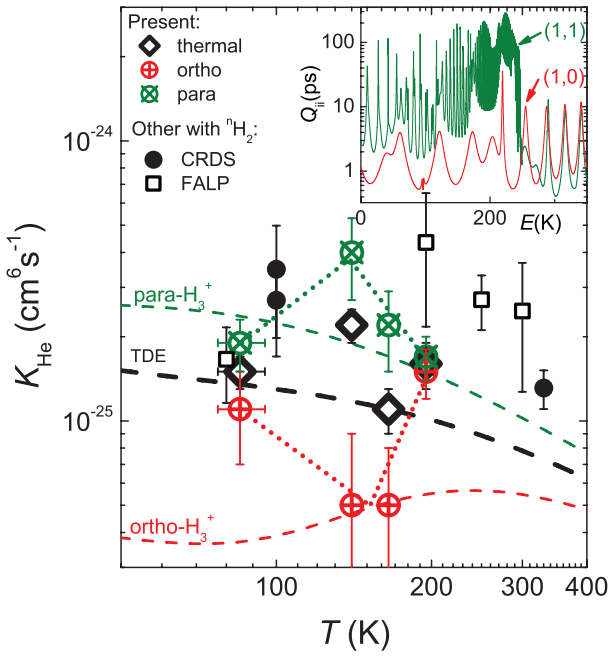

FIG. 12. Ternary recombination rate coefficients $^pK_{He}$, $^oK_{He}$, and $^nK_{He}$. The data obtained in previous CRDS (closed circles) and FALP/SA (open squares) experiments[33,34] are also shown. The dotted lines drawn through the para and ortho data are only meant to guide the eye. In the insert diagonal elements Q_{ii} of lifetime Matrix **Q** for the two lowest initial rotational states of H_3^+ are plotted. Each curve is labeled with the corresponding quantum numbers (J,G).[8,34]

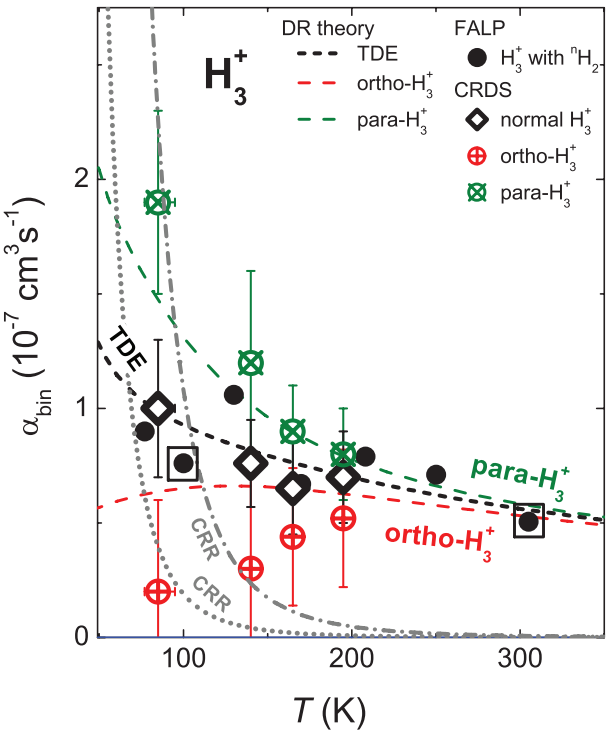

FIG. 13. Measured temperature dependences of the binary recombination rate coefficients $^n\alpha_{bin}$, $^p\alpha_{bin}$, and $^o\alpha_{bin}$ for normal-H_3^+ (measured in experiments with $^nH_2$), para-H_3^+, and ortho-H_3^+, respectively (see also Ref. 78). Previous FALP data[8,33,34] measured with $^nH_2$ are indicated by full circles. Combined SA–CRDS/FALP data at 100 K and 305 K (Refs. 8 and 34) are indicated by a full circle in a square. The temperature T in the SA–CRDS experiments is given by T_{Kin}, while in the FALP it is the temperature of the flow tube. That is why we use $T = 82$ K for data obtained in experiment made with discharge tube (SA–CRDS) immersed in liquid nitrogen, otherwise we indicate it as 77 K (e.g., in Fig. 5). Error bars (present CRDS data) represent statistical errors (see linear fits in Figs. 10 and 11). The dashed lines indicate the theoretical rate coefficients for para-H_3^+, ortho-H_3^+, and for H_3^+ ions in the thermal equilibrium (TDE).[6] The curves labeled CRR are the effective binary rate coefficients of collisional radiative recombination (CRR) calculated from the Stevefelt formula (see Refs. 31, 32, and 38) for electron densities $n_e = 5 \times 10^9$ cm^{-3} (dotted line) and $n_e = 3 \times 10^{10}$ cm^{-3} (dash-dotted line). For details see the Appendix.

obtained from the slopes of graphs of the kind shown in Figs. 10 and 11. The values $^nK_{He}$ corresponding to thermal equilibrium at 77, 140, 170, and 200 K (open rhomboids in Fig. 12) were obtained in the same way from $^n\alpha_{eff}$ (see Figs. 10 and 11). Particular attention was paid to experiments at 77 and 140 K (see Fig. 11) where we obtained high accuracy by measuring at larger helium density range (when comparing current CRDS data to FALP data, see Fig. 11). The CRDS data at 100 and 330 K (closed circles in Fig. 12) and FALP data at 200 K were measured in previous experiments and were obtained from the measured dependences of $^n\alpha_{eff}$ on hydrogen number density in the "saturated region." For details see Ref. 34. Values of K_{He} at 250 K and 300 K were obtained from the slopes of the linear dependence on helium number density from the data collection of SA and FALP data.[34] Because of the lower electron density in FALP experiment plasma decay is longer and formation of H_5^+ can influence the decay at higher helium densities. We have taken this effect into the account by enlarging error bars of the FALP data. Having in mind high He density and low temperature we used kinetic models to verify our assumptions on influence of H_5^+ formation on plasma decay and on determination of α_{eff}. Note that H_5^+ formed in association (1e) and (1f) is in used experimental conditions removed from plasma within $\sim 10\,\mu$s and the association is loss determining process. Possible error caused by H_5^+ formation is within statistical error of the data, as was confirmed by the chemical kinetics model. In Fig. 12 we did not include the data previously measured in "continuous regime" where FALP was first cooled to 77 K and after stopping cooling effective rate coefficients were measured at continuously increasing temperature (for details see Ref. 8). The accuracy of data obtained in "continuous regime" is lower when comparing with accuracy of present data obtained from dependences on helium density (Figs. 10 and 11).

In our previous studies[8,33,34] of recombination of H_3^+ with electrons we discussed the ternary recombination rate coefficient K_{He} in terms of the lifetimes of excited metastable Rydberg states H_3^* formed in collision of H_3^+ ion with electron.[8,33,34] At low collision energies the calculated values of the lifetimes depend on the spin state of the recombining ions and on collision energy. In the inset in Fig. 12 the calculated diagonal elements Q_{ii} of the lifetime Matrix **Q** for the two lowest initial rotational states of H_3^+ are plotted. The calculated lifetimes are long enough to enable l-changing collision of H_3^* molecule with helium buffer gas atom. The calculated ternary recombination rate coefficients[34] for para-H_3^+ and ortho-H_3^+, shown as dashed lines in Fig. 12,

Downloaded 28 Jun 2012 to 195.113.25.123. Redistribution subject to AIP license or copyright; see http://jcp.aip.org/about/rights_and_permissions

are in qualitative agreement with measured values. ${}^{p}K_{He}$ is greater than ${}^{o}K_{He}$ due to the longer lifetimes of para-H_3^* Rydberg resonances. Although some rather rough assumptions were made in the theoretical calculations (mainly the independence of the rate coefficient of *l*-changing collision on temperature) the overall agreement with the measured data is quite good in comparison with older theories of ternary assisted recombination.[29,80] An alternative explanation of ternary recombination of H_3^+ has been suggested by Johnsen and Guberman.[12]

More accurate theory should address decrease of ternary rate coefficients at temperature decreasing towards 77 K and also observed small difference between ${}^{p}K_{He}$ and ${}^{o}K_{He}$ at 77 K (see also Ref. 27), which are in contradiction with calculated dependences.

VII. RESULTS—BINARY RECOMBINATION OF PARA-H_3^+ AND ORTHO-H_3^+

The values of ${}^{p}\alpha_{bin}$ and ${}^{o}\alpha_{bin}$ for pure para-H_3^+ and pure ortho-H_3^+ and values of ${}^{n}\alpha_{bin}$ measured in the present experiment are plotted versus temperature in Fig. 13. Plotted are also values ${}^{n}\alpha_{bin}$ for H_3^+ ions in thermal equilibrium obtained in our previous FALP experiments.[8,33,34] The theoretical rate coefficients for pure para-H_3^+, pure ortho-H_3^+, and for H_3^+ ions in thermal equilibrium[6] are also shown in Fig. 13. The agreement between experimental and theoretical binary recombination rate coefficients ${}^{n}\alpha_{bin}$, ${}^{p}\alpha_{bin}$, and ${}^{o}\alpha_{bin}$ is very good. Also, the agreement between the present ${}^{n}\alpha_{bin}$ values and those obtained in our earlier FALP experiments using Langmuir probes is very good over the whole temperature range, even though in the present experiments the electron densities in the early afterglow were higher by at least a factor of 20.[34] The agreement at higher temperatures (140, 170, and 200 K) indicates that the measured rate coefficients at 77 K do not depend on electron density (see overlap of FALP and CRDS data plotted in Fig. 11), which means that CRR has little effect on the binary recombination rate coefficients ${}^{p}\alpha_{bin}$ and ${}^{o}\alpha_{bin}$ (for details see discussion in the Appendix).

VIII. POSSIBLE CONTRIBUTION OF CRR

The afterglow experiments described here had to be performed at high ion and electron densities (approaching 10^{11} cm^{-3}) in order to obtain adequate optical absorption. Hence, we were concerned that electron-stabilized recombination (CRR) might contribute to the recombination loss, especially at the lowest gas temperature of 77 K. The dominant term in the "classical" treatment of CRR for atomic ions by Stevefelt *et al.*[30,38] yields a three-body CRR rate coefficient $K_{CRR} = 3.8 \times 10^{-9}\ T_e^{-4.5}$ cm^{6}s^{-1}. The formula (hereinafter referred to as the "Stevefelt formula") has been experimentally verified for recombination of atomic argon ions at temperatures down to 60 K (Refs. 32 and 40)). Its validity for molecular ions seems plausible but has not been tested.

An uncritical application of the commonly used "Stevefelt formula"[38] results in an effective binary CRR rate coefficient of 3×10^{-7} cm^{3}s^{-1} (at $T_e = 77$ K and an electron density $n_e = 3 \times 10^{10}$ cm^{-3}, see Fig. 13), larger than the binary H_3^+ recombination coefficient measured in normal H_2 at the same temperature. At later afterglow times, e.g., when the electron density has dropped below 5×10^9 cm^{-3}, the contribution of CRR becomes much smaller (see Fig. 13). However, the real situation is more complicated because the electrons that are captured by CRR transfer energy to other electrons, thereby raise the temperature of the electron gas, and reduce the rate of the strongly temperature-dependent CRR. The estimates of the electron heat balance described in the Appendix indicate that the electron temperature in the very early afterglow may be as high as 100 K, when the gas temperature is 77 K. This would reduce the contribution of CRR considerably but not make it entirely negligible. The model calculations described in the Appendix suggest that the effect of CRR is negligible, even at 77 K.

The fact that the present data for normal hydrogen are very close to those measured by us in flow tubes (FALP) at ten times smaller electron densities[34] supports our conclusion that CRR makes only a small contribution to recombination. While the exact contribution of CRR is difficult to determine, our main conclusion, namely that para-H_3^+ and ortho-H_3^+ recombine with different rates, remains unaffected since CRR should not distinguish between nuclear spin states, however this question is in need of further clarification. Under preparation is the SA–CRDS experiment where wall temperature will be below liquid nitrogen temperature, i.e., below 77 K.

IX. DISCUSSION AND CONCLUSION

Our investigations show that the low-temperature recombination of H_3^+ ions depends strongly on the nuclear spin states of the ions. CRDS proved eminently capable of quantifying the populations of para-H_3^+ and ortho-H_3^+ in the discharge and during the afterglow and to verify that the afterglow plasma was in thermal equilibrium with the He buffer gas. By adding normal and para enriched hydrogen to He buffer gas we were able to form plasmas with different partial populations of para-H_3^+ (fractions, ${}^{p}f_3$) and ortho-H_3^+ (fractions, ${}^{o}f_3$) and to deduce both binary and ternary (He-assisted) recombination rate coefficients for pure para-H_3^+ and ortho-H_3^+ ions. The rate coefficients were measured at temperatures from 77 to 200 K. As far as applications to astrophysical clouds are concerned, the binary rate coefficients are the most important. Applications to laboratory hydrogen plasmas will have to include the ternary coefficients as well. It is worth mentioning here that the recent observation of laser lines in hydrogen/rare gas discharge was explained by three-body recombination of H_3^+.[81]

This is the first time that binary and ternary recombination rate coefficients have been determined for H_3^+ ions with *in situ* measured abundances of the para and ortho nuclear spin state and actual kinetic and rotational temperature. The results support theoretical predictions and are compatible with the partial results obtained in storage-ring experiments.

ACKNOWLEDGMENTS

We would like to thank Mgr. Mojmir Jilek for the design of para-H_2 generator and RNDr. Jan Lang, Ph.D. for

Downloaded 28 Jun 2012 to 195.113.25.123. Redistribution subject to AIP license or copyright; see http://jcp.aip.org/about/rights_and_permissions

TABLE II. Electron processes and corresponding characteristic times calculated for a plasma at $T_{He} = T_{Kin} = T_{Rot} = 77$ K, $T_e = 82$ K, $n_e = 5 \times 10^{10}$ cm^{-3}, and [He] $= 5 \times 10^{17}$ cm^{-3} ($\sim$500 Pa). Definition of symbols: v: electron velocity; $\sigma_{e/He}(v)$: tabulated cross section of electron-He elastic scattering; $\langle \ldots \rangle$: average over relative velocity distribution; λ_D: Debye length; Λ: impact parameter for 90° coulombic scattering; m_{He}: mass of He atom; m_e: electron mass; λ: coulombic logarithm; $\Delta_{1,2}$: energy difference between rotational states (1,1) and (2,1); n_1, n_2: number density of H_3^+ ions in rotational states (1,1) and (2,1); α_{21}, α_{12}: rate coefficients for electron (de)excitation between the states 2 $\rightarrow$ 1 and vice versa; K_{He}: ternary rate coefficient of helium assisted dissociative recombination; α_{bin}: rate coefficient of binary dissociative recombination.

Reactants	Process	τ [μs]	Remark	Reference
$e + He$	Elastic scattering	0.0008	${}^c\tau_{e/He} = 1/[He]\langle\sigma_{e/He} \cdot v\rangle$	85
$e + e$	Coulombic scattering	0.004	${}^c\tau_{e/e} = 1/n_e\langle v\pi\Lambda^2 \ln(\lambda_D/\Lambda)\rangle$	83,84
$e + He$	Elastic cooling	2.9	${}^\varepsilon\tau_{e/He} = {}^c\tau_{e/He}(m_{He}/2m_e)$	65
$e + H_3^+$	Coulombic cooling	3.4	${}^\varepsilon\tau_{e/i} = \frac{6\sqrt{2m_e}\varepsilon_0^2(\pi k_B T_e)^{3/2}}{n_e e^4 \lambda} \frac{m_i}{2m_e}$	86
$e + e + H_3^+$	CRR	43	$\tau_{CRR} = 1/n_e^2 K_{CRR}$	38
$e + H_3^+$	Rotational cooling	140	${}^\varepsilon\tau_{Rot} = \frac{3}{2}\frac{k_B(T_{Rot} - T_e)}{\Delta_{1,2}(n_2\alpha_{21} - n_1\alpha_{12})}$	76,87
$e + H_3^+ + He$	Ternary recombination	200	$\tau_{ternary} = 1/K_{He}[He]n_e$	34
$e + H_3^+$	Binary recombination	250	$\tau_{bin} = 1/\alpha_{bin} n$	34

NMR measurements of para enrichment of ${}^eH_2$ gas. This work was partly financed by the research Grant No. OC10046 from the Ministry of Education of the Czech Republic and was partly supported by GACR (205/09/1183, P209/12/0233), SV 265 302, GAUK 92410, GAUK 353811, GAUK 54010, and COST Action CM0805 (The Chemical Cosmos).

APPENDIX A: ELECTRON HEATING AND EFFECT OF COLLISIONAL RADIATIVE RECOMBINATION

In this appendix we consider the heat balance for electrons in low temperature plasma. First we consider the heat balance between the heat released by CRR and heat transfer to ions and neutrals and the resulting increase of the electron temperature. In the second step we consider the effect of electron heating on the afterglow decay.

We denote characteristic times between electron collisions as ${}^c\tau$ (left superscript c) and characteristic times for equipartition of energy as ${}^\varepsilon\tau$ (left superscript ε). Right subscript will be used to denote collision partners. For example, the characteristic time for electron/He collisions is denoted as ${}^c\tau_{e/He}$ and the electron temperature relaxation time due to electron/He collisions is denoted as ${}^\varepsilon\tau_{e/He}$. Both quantities are related by the equation: ${}^\varepsilon\tau_{e/He} = {}^c\tau_{e/He}(m_{He}/2m_e)$.[65]

In these calculations we do not distinguish between the para and ortho nuclear spin states of H_3^+. In this approximation we treat the interactions as spin independent. The relevant collision processes are listed in Table II together with calculated characteristic times for conditions typical in our experiment: $T_{He} = T_{Kin} = T_{Rot} = 77$ K, $T_e = 82$ K, $n_e = 5 \times 10^{10}$ cm^{-3}, and [He] $= 5 \times 10^{17}$ cm^{-3} ($\sim$500 Pa). Collisional radiative recombination adds ΔE_{CRR} to the internal energy of the electron gas. We assume that this energy is of the order of $\Delta E_{CRR} = 0.13$ eV per recombined electron. This corresponds to the ionization potential of the lowest Rydberg state recombining predominantly by collisions rather than radiative transitions.[38,82] Varying the ΔE_{CRR} by a factor of 2 had no qualitative effect on the conclusions of our simulations. The CRR ternary rate coefficient is taken as $K_{CRR} = 3.8 \times 10^{-9} T_e^{-4.5}$ cm^{6}s^{-1}.[38] Heat transfer from the electron gas to neutrals (He) and ions occurs via electron/He collisions, electron-ion coulombic collisions, and by rotational excitation of H_3^+ between the rotational levels (1,1) and (2,1). We use recently calculated thermal rates (see Ref. 76) for rotational energy transfer. Electron-electron collisions establish and maintain a maxwellian energy distribution of the electron gas.

The maxwellization of the electron gas by electron-electron coulombic collisions[83,84] is much faster than the cooling processes under our conditions. Hence, we can define an electron temperature and write a simple equation for the internal energy of the electron gas U:

$$\frac{dU}{dt} = Q_{CRR} - Q_{elastic} - Q_{e/i} - Q_{Rot}, \tag{A1}$$

where the Q_{CRR}, $Q_{elastic}$, $Q_{e/i}$, and Q_{Rot} terms represent the heating by CRR, cooling by elastic collisions with neutrals, cooling by coulombic collisions with ions, and cooling by rotational excitation of ions, respectively. This equation can be rewritten in terms of relaxation times defined in Table II:

$$\frac{dT_e}{dt} = \frac{2\Delta E_{CRR}/3k_B}{\tau_{CRR}} - \frac{T_e - T_G}{{}^\varepsilon\tau_{e/He}} - \frac{T_e - T_{Kin}}{{}^\varepsilon\tau_{e/i}} - \frac{T_e - T_{Rot}}{{}^\varepsilon\tau_{Rot}}. \tag{A2}$$

In determining the electron temperature, the time derivative term can be neglected, because the relaxation processes are fast enough to maintain the equilibrium temperature at each time during the afterglow. The electron temperature is then obtained by numerically solving Eq. (A2) with zero time derivative.

For the beginning we use the theory of CRR of atomic ions[38] to estimate a rate of CRR of H_3^+ ions, then the effective binary rate of CRR should be comparable to the rate of effective binary recombination at 77 K and $n_e > 10^{10}$ cm^{-3} (see plots in Figs. 11 and 13). We deliberately chose conditions where a large influence of CRR can be expected. We then numerically model afterglow recombination in the presence of electron heating by CRR and compare the results to our experimental data. The evolution of electron density on axis of

Downloaded 28 Jun 2012 to 195.113.25.123. Redistribution subject to AIP license or copyright; see http://jcp.aip.org/about/rights_and_permissions

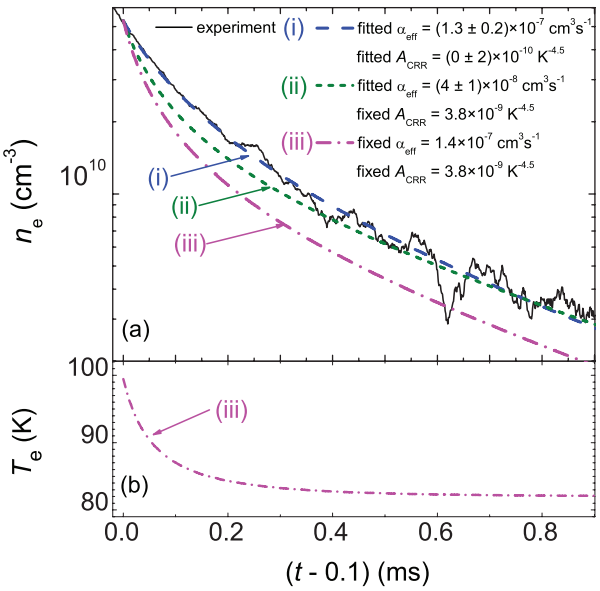

FIG. 14. Model fits of sample data measured in normal hydrogen at 77 K. Panel (a): The dashed line (i) shows the best fit to the data when α_{eff} and A_{CRR} are treated as free parameters. The short dashed line (ii) indicates the best fit when α_{eff} is treated as a free parameter, but A_{CRR} is taken as that given by the Stevefelt formula.[38] The dashed-dotted line (iii) shows model results assuming that both the Stevefelt value of A_{CRR} and the FALP values of α_{eff} (Ref. 34) are correct. Panel (b): The corresponding evolution of the electron temperature calculated for conditions corresponding to fit (iii).

the discharge tube is given by the differential equation (4b) augmented with the CRR term

$$\frac{dn_e}{dt} = -K_{CRR}(T_e)\, n_e^3 - \alpha_{eff} n_e^2 - \frac{n_e}{\tau_D}, \qquad \text{(A3)}$$

where T_e is given by Eq. (A2) and is dependent on n_e. In the numerical models, the value of K_{CRR} was taken as $K_{CRR} = A_{CRR} T_e^{-4.5}$ cm^{6}s^{-1} with either $A_{CRR} = 3.8 \times 10^{-9}$ K$^{4.5}$ or with A_{CRR} as a free fitting parameter.[38] The latter choice is permissible since no accurate measurement or theory of CRR for H_3^+ ions is available. Figure 14 compares numerical fits to sample data measured in normal hydrogen at 77 K. As before, the first 100 μs of the afterglow were excluded to eliminate possible effects of ion formation in the early afterglow.

It can be seen in Fig. 14 that the best fit to the data is obtained for a value of the CRR coefficient close to zero (line (i) in Fig. 14). The fit obtained under the constraint that K_{CRR} is given by the Stevefelt formula is noticeably worse, even when α_{eff} is reduced (line (ii)). An even worse agreement is obtained when α_{eff} is taken as the FALP value measured previously[34] (see panel (a) of Fig. 11) and the Stevefelt value is used for K_{CRR} (line (iii)). Since the previous FALP measurements were performed at lower electron densities, they should not be affected by CRR even if the Stevefelt value of K_{CRR} is appropriate for H_3^+.

The same fitting procedures were applied to several of our normal and enriched hydrogen datasets and led to the same conclusion that CRR has only a negligible effect. Hence, we did not correct the measured values of α_{eff} for CRR contributions. The apparent absence of CRR is surprising. It is known to occur for atomic ions and the high Rydberg states involved in CRR are essentially the same for molecular ions. On the other hand, it is also possible that the electron temperature in the experimental afterglow plasmas was somewhat higher than we estimate. This would greatly reduce the rate of CRR but make only a minor difference in the dissociative recombination coefficient of H_3^+.

[1] T. Oka, Philos. Trans. R. Soc. London, Ser. A **364**, 2847 (2006).
[2] E. Herbst and W. Klemperer, Astrophys. J. **185**, 505 (1973).
[3] N. Indriolo, G. A. Blake, M. Goto, T. Usuda, T. Oka, T. R. Geballe, B. D. Fields, and B. J. McCall, Astrophys. J. **724**, 1357 (2010).
[4] J. Glosik, Int. J. Mass Spectrom. **1369**, 15 (1994).
[5] K. N. Crabtree, N. Indriolo, H. Kreckel, B. A. Tom, and B. J. McCall, Astrophys. J. **729**, 15 (2011).
[6] S. F. dos Santos, V. Kokoouline, and C. H. Greene, J. Chem. Phys **127**, 124309 (2007).
[7] M. Larsson, Philos. Trans. R. Soc. London, Ser. A **358**, 2433 (2000).
[8] J. Glosik, R. Plasil, T. Kotrik, P. Dohnal, J. Varju, M. Hejduk, I. Korlov, S. Roucka, and V. Kokoouline, Mol. Phys. **108**, 2253 (2010).
[9] R. Plasil, J. Glosik, V. Poterya, P. Kudrna, J. Rusz, M. Tichy, and A. Pysanenko, Int. J. Mass Spectrom. **218**(2), 105 (2002).
[10] D. Smith and P. Spanel, Int. J. Mass Spectrom. **129**, 163 (1993).
[11] R. Johnsen, J. Phys.: Conf. Ser. **4**, 83 (2005).
[12] R. Johnsen and S. L. Guberman, Adv. At., Mol., Opt. Phys. **59**, 75 (2010).
[13] M. Larsson and A. Orel, *Dissociative Recombination of Molecular Ions* (Cambridge University Press, Cambridge, England, 2008).
[14] V. Kokoouline, C. H. Greene, and B. D. Esry, Nature (London) **412**, 891 (2001).
[15] V. Kokoouline and C. H. Greene, Phys. Rev. A **68**, 012703 (2003).
[16] B. J. McCall, A. J. Honeycutt, R. J. Saykally, T. R. Geballe, N. Djuric, G. H. Dunn, J. Semaniak, O. Novotny, A. Al-Khalili, A. Ehlerding, F. Hellberg, S. Kalhori, A. Neau, R. Thomas, F. Osterdahl, and M. Larsson, Nature (London) **422**, 500 (2003).
[17] H. Kreckel, M. Motsch, J. Mikosch, J. Glosik, R. Plasil, S. Altevogt, V. Andrianarijaona, H. Buhr, J. Hoffmann, L. Lammich, M. Lestinsky, I. Nevo, S. Novotny, D. A. Orlov, H. B. Pedersen, F. Sprenger, A. S. Terekhov, J. Toker, R. Wester, D. Gerlich, D. Schwalm, A. Wolf, and D. Zajfman, Phys. Rev. Lett. **95**, 263201 (2005).
[18] B. J. McCall, A. J. Huneycutt, R. J. Saykally, N. Djuric, G. H. Dunn, J. Semaniak, O. Novotny, A. Al-Khalili, A. Ehlerding, F. Hellberg, S. Kalhori, A. Neau, R. Thomas, A. Paal, F. Osterdahl, and M. Larsson, Phys. Rev. A **70**, 052716 (2004).
[19] M. Larsson, B. McCall, and A. Orel, Chem. Phys. Lett. **462**, 145 (2008).
[20] D. R. Bates, M. F. Guest, and R. A. Kendall, Planet. Space Sci. **41**(1), 9 (1993).
[21] H. Kreckel, O. Novotny, K. N. Crabtree, H. Buhr, A. Petrignani, B. A. Tom, R. D. Thomas, M. H. Berg, D. Bing, M. Grieser, C. Krantz, M. Lestinsky, M. B. Mendes, C. Nordhorn, R. Repnow, J. Stutzel, A. Wolf, and B. J. McCall, Phys. Rev. A **82**, 042715 (2010).
[22] A. Petrignani, S. Altevogt, M. H. Berg, D. Bing, M. Grieser, J. Hoffmann, B. Jordon-Thaden, C. Krantz, M. B. Mendes, O. Novotny, S. Novotny, D. A. Orlov, R. Repnow, T. Sorg, J. Stutzel, A. Wolf, H. Buhr, H. Kreckel, V. Kokoouline, and C. H. Greene, Phys. Rev. A **83**, 032711 (2011).
[23] J. Mikosch, H. Kreckel, R. Wester, J. Glosik, R. Plasil, D. Gerlich, D. Schwalm, and A. Wolf, J. Chem. Phys. **121**(22), 11030 (2004).
[24] A. Petrignani, D. Bing, O. Novotny, M. H. Berg, H. Buhr, M. Grieser, B. Jordon-Thaden, C. Krantz, M. B. Mendes, S. Menk, S. Novotny, A. D. A. Orlov, R. Repnow, J. Stutzel, X. Urbain, and A. Wolf, J. Phys. Chem. A **114**, 4864 (2010).
[25] U. Hechtfischer, Z. Amitay, P. Forck, M. Lange, J. Linkemann, M. Schmitt, U. Schramm, D. Schwalm, R. Wester, D. Zajfman, and A. Wolf, Phys. Rev. Lett. **80**, 2809 (1998).
[26] J. Varju, S. Roucka, T. Kotrik, R. Plasil, and J. Glosik, J. Phys.: Conf. Ser. **227**, 012026 (2010).
[27] J. Varju, M. Hejduk, P. Dohnal, M. Jilek, T. Kotrik, R. Plasil, D. Gerlich, and J. Glosik, Phys. Rev. Lett. **106**, 203201 (2011).
[28] D. Smith and P. Spanel, Methods Exp. Phys. **29**(A), 273 (1995).
[29] D. Bates and S. Khare, Proc. Phys. Soc. Lond. **85**, 231 (1965).
[30] D. R. Bates, A. E. Kingston, and W. P. McWhirter, Philos. Trans. R. Soc. London, Ser. A **267**, 297 (1962).

Downloaded 28 Jun 2012 to 195.113.25.123. Redistribution subject to AIP license or copyright; see http://jcp.aip.org/about/rights_and_permissions

[31]E. W. McDaniel, J. B. A. Mitchell, and M. E. Rudd, *Atomic Collisions, Heavy Partricle Projectiles* (Wiley Interscience, New York, 1993).
[32]T. Kotrik, P. Dohnal, S. Roucka, P. Jusko, R. Plasil, J. Glosik, and R. Johnsen, Phys. Rev. A **83**, 032720 (2011).
[33]J. Glosik, I. Korolov, R. Plasil, O. Novotny, T. Kotrik, P. Hlavenka, J. Varju, I. A. Mikhailov, V. Kokoouline, and C. H. Greene, J. Phys. B **41**, 191001 (2008).
[34]J. Glosik, R. Plasil, I. Korolov, T. Kotrik, O. Novotny, P. Hlavenka, P. Dohnal, J. Varju, V. Kokoouline, and C. Greene, Phys. Rev. A **79**, 052707 (2009).
[35]J. Glosik, I. Korolov, R. Plasil, T. Kotrik, P. Dohnal, O. Novotny, J. Varju, S. Roucka, C. Greene, and V. Kokoouline, Phys. Rev. A **80**, 042706 (2009).
[36]J. Glosik, R. Plasil, I. Korolov, O. Novotny, and T. Kotrik, J. Phys.: Conf. Ser. **192**, 012005 (2009).
[37]T. Kotrik, P. Dohnal, I. Korolov, R. Plasil, S. Roucka, J. Glosik, C. Greene, and V. Kokoouline, J. Chem. Phys. **133**, 034305 (2010).
[38]J. Stevefelt, J. Boulmer, and J. Delpech, Phys. Rev. A **12**, 1246 (1975).
[39]T. Pohl, D. Vrinceanu, and H. R. Sadeghpour, Phys. Rev. Lett. **100**, 223201 (2008).
[40]T. Kotrik, P. Dohnal, P. Rubovic, R. Plasil, S. Roucka, S. Opanasiuk, and J. Glosik, Eur. Phys. J. Appl. Phys. **56**, 24011 (2011).
[41]T. Amano, J. Chem. Phys. **92**, 6492 (1990).
[42]T. Amano, Astrophys. J. **329**, L121 (1988).
[43]M. Hejduk, P. Dohnal, J. Varju, P. Rubovic, R. Plasil, and J. Glosik, Plasma Sources Sci. Technol. **21**, 024002 (2012).
[44]J. Glosik, O. Novotny, A. Pysanenko, P. Zakouril, R. Plasil, P. Kudrna, and V. Poterya, Plasma Sci. Technol. **12**, S117 (2003).
[45]K. N. Crabtree, B. A. Tom, and B. J. McCall, J. Chem. Phys. **134**, 194310 (2011).
[46]K. N. Crabtree, C. Kauffman, B. Tom, E. Beçka, B. McGuire, and B. J. McCall, J. Chem. Phys. **134**, 194311 (2011).
[47]J. Tennyson, see http://www.tampa.phys.ucl.ac.uk/ftp/astrodata/h3+/ for a list of H_3^+ transitions (2011).
[48]P. F. Goldsmith, T. Velusamy, D. Li, and W. D. Langer, Astrophys. J. **715**, 1370 (2010).
[49]J. Glosik, R. Plasil, V. Poterya, P. Kudrna, M. Tichy, and A. Pysanenko, J. Phys. B **34**(15), L485 (2001).
[50]D. Romanini, A. A. Kachanov, N. Sadeghi, and F. Stoeckel, Chem. Phys. Lett. **264**(3-4), 316 (1997).
[51]P. Macko, G. Bano, P. Hlavenka, R. Plasil, V. Poterya, A. Pysanenko, O. Votava, R. Johnsen, and J. Glosik, Int. J. Mass Spectrom. **233**, 299 (2004).
[52]P. Hlavenka, R. Plasil, G. Bano, I. Korolov, D. Gerlich, J. Ramanlal, J. Tennyson, and J. Glosik, Int. J. Mass Spectrom. **255-256**, 170 (2006).
[53]J. Glosik, P. Hlavenka, R. Plasil, F. Windisch, D. Gerlich, A. Wolf, and H. Kreckel, Philos. Trans. R. Soc. London, Ser. A **364**(1848), 2931 (2006).
[54]P. Hlavenka, I. Korolov, R. Plasil, J. Varju, T. Kotrik, and J. Glosik, Czech J. Phys. **56**, B749 (2006).
[55]C. M. Lindsay and B. J. McCall, J. Mol. Spectrosc. **210**, 60 (2001).
[56]L. Neale, S. Miller, and J. Tennyson, Astrophys. J. **464**, 516 (1996).
[57]S. Tam and M. Fajardo, Rev. Sci. Instrum. **70**, 1926 (1999).
[58]B. A. Tom, S. Bashler, Y. Miyamoto, T. Momose, and B. J. McCall, Rev. Sci. Instrum. **80**, 016108 (2009).
[59]J. Lang, private communication (2011).
[60]R. Plasil, P. Hlavenka, P. Macko, G. Bano, A. Pysanenko, and J. Glosik, J. Phys.: Conf. Ser. **4**, 118 (2005).
[61]I. Korolov, T. Kotrik, R. Plasil, J. Varju, M. Hejduk, and J. Glosik, Contrib. Plasma Phys. **48**(5–7), 521 (2008).
[62]R. Plasil, I. Korolov, T. Kotrik, J. Varju, P. Dohnal, Z. Donko, G. Bano, and J. Glosik, J. Phys.: Conf. Ser. **192**, 012023 (2009).
[63]R. Plasil, I. Korolov, T. Kotrik, P. Dohnal, G. Bano, Z. Donko, and J. Glosik, Eur. Phys. J. D **54**, 391 (2009).
[64]J. Glosik, G. Bano, R. Plasil, A. Luca, and P. Zakouril, Int. J. Mass Spectrom. **189**, 103 (1999).
[65]Y. P. Raizer, *Gas Discharge Physics* (Springer–Verlag, Berlin, 1991) p. 14.
[66]J. Kim, L. Theard, and W. Huntres, Int. J. Mass Spectrom. **15**, 223 (1974).
[67]F. B. Yousif, G. Hinojosa, J. de Urquijo, C. Cisneros, and I. Alvarez, Int. J. Mass Spectrom. **171**(1–3), 127 (1997).
[68]E. Ferguson, J. Phys. Chem. **90**, 731 (1986).
[69]R. Plasil, J. Varju, M. Hejduk, P. Dohnal, T. Kotrik, and J. Glosik, J. Phys.: Conf. Ser. **300**(1), 012023 (2011).
[70]M. Quack, Mol. Phys. **34**, 477 (1977).
[71]M. Cordonnier, D. Uy, R. M. Dickson, K. E. Kerr, Y. Zhang, and T. Oka, J. Chem. Phys. **113**, 3181 (2000).
[72]T. Oka and E. Epp, Astrophys. J. **613**, 349 (2004).
[73]D. Gerlich, F. Windisch, P. Hlavenka, R. Plasil, and J. Glosik, Philos. Trans. R. Soc. London, Ser. A **364**, 3007 (2006).
[74]K. Park and J. C. Light, J. Chem. Phys. **126**, 044305 (2007).
[75]E. Hugo, O. Asvany, and S. Schlemmer, J. Chem. Phys. **130**, 164302 (2009).
[76]V. Kokoouline, A. Faure, J. Tennyson, and C. Greene, Mon. Not. R. Astron. Soc. **405**, 1195 (2010).
[77]R. Plasil, I. Korolov, T. Kotrik, and J. Glosik, Int. J. Mass Spectrom. **275**, 80 (2008).
[78]P. Dohnal, M. Hejduk, J. Varju, P. Rubovic, S. Roucka, T. Kotrik, R. Plasil, R. Johnsen, and J. Glosik, "Binary recombination of para and ortho-H_3^+ with electrons at low temperatures," Philos. Trans. R. Soc. London, Ser. A (in press) (Conference Proceeding 2012).
[79]J. Glosik, R. Plasil, A. Pysanenko, O. Novotny, P. Hlavenka, P. Macko, and G. Bano, J. Phys.: Conf. Ser. **4**, 104 (2005).
[80]M. R. Flannery, J. Chem. Phys. **95**(11), 8205 (1991).
[81]R. J. Saykally, E. A. Michael, J. Wang, and C. H. Greene, J. Chem. Phys. **133**, 234302 (2010).
[82]S. Byron, R. C. Stabler, and P. I. Bortz, Phys. Rev. Lett. **8**, 376 (1962).
[83]F. F. Chen, *Introduction to Plasma Physics* (Plenum, New York, 1974).
[84]D. Trunec, P. Spanel, and D. Smith, Chem. Phys. Lett. **372**, 728 (2003).
[85]A. V. Phelps, see http://jila.colorado.edu/~avp/collision_data/ for compilation of electron cross sections (2011)
[86]A. A. Dougal and L. Goldstein, Phys. Rev. **109**, 615 (1958).
[87]J. Ramanlal and J. Tennyson, Mon. Not. R. Astron. Soc. **354**, 161 (2004).

Downloaded 28 Jun 2012 to 195.113.25.123. Redistribution subject to AIP license or copyright; see http://jcp.aip.org/about/rights_and_permissions

INFLUENCE OF THE 22-POLE TRAP IMPERFECTIONS ON THE INTERACTION OF IONS WITH A NEUTRAL BEAM

Bibliographic record of the attached publication:

Roučka, Š, P. Jusko, I. Zymak, D. Mulin, R. Plašil, and J. Glosík (2011). "Influence of the 22-pole Trap Imperfections on the Interaction of Ions with a Neutral Beam." In: *WDS'11 Proceedings of Contributed Papers: Part II - Physics*. Prague, Czech Republic: Matfyzpress, pp. 158–164.

Influence of the 22-pole Trap Imperfections on the Interaction of Ions with a Neutral Beam

Š. Roučka, P. Jusko, I. Zymak, D. Mulin, R. Plašil, and J. Glosík
Charles University, Faculty of Mathematics and Physics, Prague, Czech Republic.

Abstract. The temperature dependence of the rate coefficient of the associative detachment reaction ($H^- + H \rightarrow H_2 + e^-$) was studied using the Atomic Beam—22-pole Trap Apparatus (AB-22PT). A discrepancy between the data measured at different combinations of ion and atom temperatures was observed. This contribution discusses various imperfections of the 22-pole trap as possible causes of this effect. Numerical models of these imperfections are compared to the experimental data. The measured discrepancy is best explained by a presence of few millivolt patch field on the surface of the 22-pole rods.

Introduction

This work is motivated by the recent measurement of the associative detachment reaction (AD) $H^- + H \rightarrow H_2 + e^-$ performed in our laboratory. The measurement was carried out in the Atomic Beam—22-pole Trap apparatus (AB-22PT), which is described by Borodi et al. [2009]; Plasil et al. [2011]; Gerlich et al. [2011] in detail. The results of this experiment are being prepared for publication by Jusko et al. [2011]. A basic description of the experiment is presented below and a schematic drawing of the experiment is shown in Figure 1. During the measurement a cloud of H^- ions is stored in the

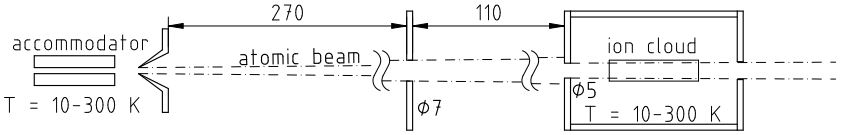

Figure 1. Schematic drawing of the AB-22PT experiment configuration. Dimensions are in millimeters.

cryogenic 22-pole radiofrequency trap, which has variable temperature $T_{22\mathrm{PT}}$ in the range 10 K $< T_{22\mathrm{PT}} <$ 300 K. The ions are thermalized by buffer gas collisions at a temperature close to the $T_{22\mathrm{PT}}$. The ions interact with a cold effusive beam of atomic hydrogen. The beam flows from the accommodator nozzle. The accommodator has also a variable temperature T_{ACC} in the range 10 K $< T_{\mathrm{ACC}} <$ 300 K. The temperature of atoms is close to the accommodator temperature [Borodi et al., 2009]. The interaction temperature T of the two ensembles with different temperatures is given by the arithmetic average

$$T = \frac{T_{\mathrm{ACC}} + T_{22\mathrm{PT}}}{2} \tag{1}$$

in case of equal particle masses.

Our experimental procedure for measuring the temperature dependence of the rate coefficient is described by Jusko et al. [2011] in detail. Since the produced density of H atoms has a complicated dependence on the accommodator temperature, we always perform a sequence of measurements at a fixed accommodator temperature and a variable 22-pole temperature. Sets of measurements performed at different accommodator temperatures are then stitched together by the least squares method. This method consists in binning the data with respect to temperature axis and finding the multiplicative factor for uncalibrated data which minimizes the squared differences between the calibrated and uncalibrated data in the overalapping region. The result of this procedure for datasets at $T_{\mathrm{ACC}} = 10$ K and $T_{\mathrm{ACC}} =$ 50 K are presented in Figure 2 (left panel). A discrepancy between the measurements at the same interaction temperature for different datasets can be seen at low temperatures. This effect can be explained by a $T_{22\mathrm{PT}}$ temperature depence of the overlap between the atomic beam and ion cloud. This hypothesis was supported by measuring the laser photodetachment rate. Multiple measurements of the photodetachment temperature dependence were performed with laser pointed into different areas of the trap. A 660 nm 200 mW diode laser was used to obtain the presented results. Qualitatively equal effects were obtained also using a 532 nm 5 mW solid state diode pumped frequency doubled laser.

Several measurements used a narrow laser beam (FWHM of intensity ≈ 1 mm) and other measurements used a wide beam (FWHM of intensity > 1 cm). Only the central portion of the broad beam can enter the trap through the 5 mm trap aperture. Therefore, the light intensity inside inside the aperture is nearly constant, which closely mimics the atomic beam profile. Under our experimental conditions no temperature dependence of the photodetachment rate should be observed. However, Figure 2 (right panel) shows a significant temperature dependence of the measured photodetachment rate. Depending on

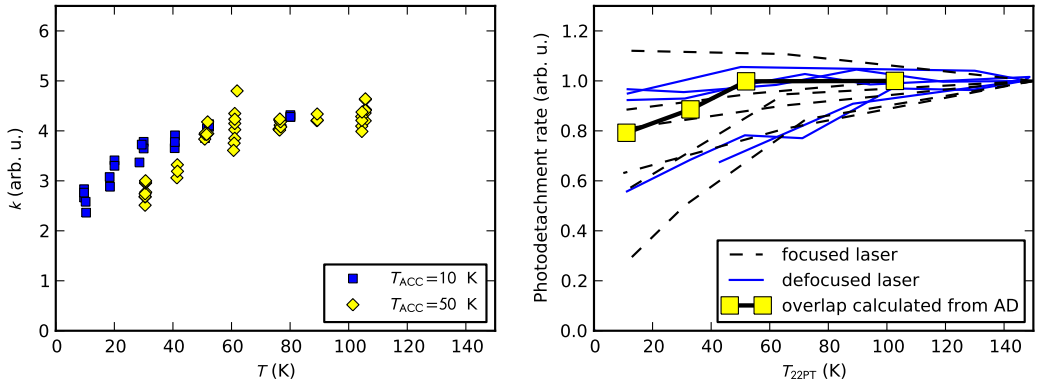

Figure 2. The uncalibrated rate coefficient measurements. The graph shows the discrepancy between the measurements performed at different accommodator temperatures (left panel). Dependence of the photodetachment rate on the 22-pole trap temperature is shown in the right panel. For explanation of the calculated overlap see section Results.

the precise laser pointing, the photodetachment is decreasing with temperature at different rate. Only one of the measurements shows an increase of the photodetachment rate with decreasing temperature. This clearly indicates, that ions are being redistributed by varying the $T_{22\mathrm{PT}}$ and are probably concentrating in an effective potential minimum with decreasing temperature. Since the majority of measurements shows a decrease of the photodetachment rate with decreasing temperature, the effective potential minimum is probably located out of the reach of the neutral or laser beam.

In the theoretical section below, some basic concepts regarding the interaction of the trapped ions with a neutral beam are introduced. In the section Results we will analyse and correct the measured data and provide possible explanations of this effect based on numerical simulations of the ion cloud spatial distribution under various conditions.

The density of the atomic beam was determined by the chemical probing with CO_2^+ [Borodi et al., 2009]. The CO_2^+ has a higher mass than H^- and a different RF amplitude was used for the calibration measurement. Therefore the ion cloud has a different shape and the measured effective H density has to be corrected by a factor which will be derived in the theoretical section of this article. The calibration measurement with CO_2^+ was carried out at $T_{22\mathrm{PT}} = 30$ K and $T_{\mathrm{ACC}} = 50$ K.

Theory

We only briefly introduce the relevant equations of the theory of motion in oscillatory fields under the adiabatic conditions. For details refer to Gerlich [1992]. It can be shown that under the adiabatic conditions [Gerlich, 1992] the oscillating electric field described by $\boldsymbol{E}(\boldsymbol{x},t) = \boldsymbol{E}_0(\boldsymbol{r})\cos(\Omega t + \delta) + \nabla\phi_{\mathrm{s}}(\boldsymbol{r})$ produces an effective potential V^* acting on a particle of mass m

$$V^* = \frac{q^2 E_0^2}{4m\Omega^2} + q\phi_s \,. \tag{2}$$

In case of an ideal linear 2-n pole without DC potential the effective potential can be calculated analytically to give

$$V^* = \frac{1}{8}\frac{(qV_0)^2}{\epsilon}\hat{r}^{2n-2}\,; \qquad \epsilon = \frac{1}{2n^2}m\Omega^2 r_0^2\,; \qquad \hat{r} = r/r_0\,, \tag{3}$$

where V_0 is the potential amplitude on the poles and r_0 is the inner diameter of the multipole. In particular, the inner radius of our 22-pole $r_0 = 1$ cm; RF frequency 18.0 MHz was used throughout our measurements. The turning radius of a particle with radial component of energy E_{m} trapped in the

multipole is then given by

$$r_m = \left(\frac{8E_m\epsilon}{(qV_0)^2}\right)^{\frac{1}{2n-2}} . \tag{4}$$

In the atomic beam–ion cloud arrangement used in our experiment, the rate of reaction $\dot{N}_\mathrm{i}$ can be obtained by integrating over the overlap of the atomic beam with the ion cloud

$$\dot{N}_\mathrm{i} = k(T)\int_{\boldsymbol{r}} n_\mathrm{H}(\boldsymbol{r})n_\mathrm{i}(\boldsymbol{r})\mathrm{d}\boldsymbol{r}\,, \tag{5}$$

where $k(T)$ is the reaction rate coefficient, n_H is the H atom density and n_i is the ion density. We can rewrite this expression in terms of macroscopic variables as

$$\dot{N}_\mathrm{i} = k(T)N_\mathrm{i}N_\mathrm{H}\,, \tag{6}$$

where N_i is the number of ions in the trap and N_H is the effective H atom density defined by

$$N_\mathrm{H} = \int_{\boldsymbol{r}} n_\mathrm{H}(\boldsymbol{r})\frac{n_\mathrm{i}(\boldsymbol{r})}{N_\mathrm{i}}\mathrm{d}\boldsymbol{r}\,. \tag{7}$$

In our experimental configuration, the ion cloud confined in the 22-polar field has a larger diameter than the atomic beam. Thanks to the adiabatic conditions, the ions could be considered approximately a canonical statistical ensemble in contact with a heat-bath (neutral gas). The spatial distribution of ions is the given by the Boltzmann distribution. Due to the flat potential minimum of the 22-pole trap, the cloud can be considered homogeneous over the intersection with the atomic beam. The effective H atom density is then proportional to the ion density on axis, which is inversely proportional to the cloud cross section area, which in turn is proportional to the square of the turning radius:

$$N_\mathrm{H} \sim n_\mathrm{i}(r=0) \sim \frac{1}{r_m^2} \sim \left(\frac{8T\epsilon}{(qV_0)^2}\right)^{\frac{-1}{n-1}} . \tag{8}$$

Since the proportionality is the same for all energies, we have replaced E_m with the temperature. By retaining only the relevant coefficients we obtain a relation for scaling of the effective H atom density in the 22-pole due to the change of the overlap

$$N_\mathrm{H} \sim \left(\frac{Tm}{V_0^2}\right)^{-\frac{1}{10}} . \tag{9}$$

This factor can be used to correct the effective H atom density determined by the CO_2^+ chemical probing. The RF amplitude used in our experiment was $V_0 = 25$ V for H^- and $V_0 = 50$ V for CO_2^+. The ratio of effective densities under these conditions with identical temperatures is $N_\mathrm{H}(H^-)/N_\mathrm{H}(CO_2^+) = 1.271$.

The theoretical scaling of the overlap for H^- and CO_2^+ is plotted in Figure 3 relative to the overlap of H^- at 150 K. Experimental data in the plot are explained below.

Results

Experimental: We will now discuss a method to extract the scaling of the beam-cloud overlap from the observed data. We directly observe the decay rate $X(T_\mathrm{ACC}, T_\mathrm{22PT}) = \dot{N}_\mathrm{i}/N_\mathrm{i} = k(T(T_\mathrm{ACC}, T_\mathrm{22PT}))\cdot N_\mathrm{H}(T_\mathrm{ACC}, T_\mathrm{22PT})$. The interaction temperature T is the average of the reactant temperatures given by equation (1). We assume, that the dependence of N_H on T_22PT is caused by some processes in the 22-pole trap and is not related to the H atom temperature. Therefore it can be separated into $N_\mathrm{H}(T_\mathrm{ACC}, T_\mathrm{22PT}) = N(T_\mathrm{ACC})P(T_\mathrm{22PT})$, where the overlap factor P is defined as unity at the highest temperature of our measurement. We can now write

$$X(T_\mathrm{ACC}, T_\mathrm{22PT}) = K(T_\mathrm{ACC} + T_\mathrm{22PT})N(T_\mathrm{ACC})P(T_\mathrm{22PT})\,, \tag{10}$$

where $K(T) = k(T/2)$ for simplicity. From the measured data we now select four measurements performed at two different interaction temperatures T using different combinations of T_22PT and T_ACC

$$X(T'_\mathrm{ACC}, T_\mathrm{22PT})\,; \quad X(T'_\mathrm{ACC}, T'_\mathrm{22PT})\,; \quad X(T_\mathrm{ACC}, T''_\mathrm{22PT})\,; \quad X(T_\mathrm{ACC}, T'''_\mathrm{22PT})\,. \tag{11}$$

The temperatures are related by equations

$$T_{\mathrm{ACC}} + T''_{22\mathrm{PT}} = T'_{\mathrm{ACC}} + T_{22\mathrm{PT}}\,; \quad T_{\mathrm{ACC}} + T'''_{22\mathrm{PT}} = T'_{\mathrm{ACC}} + T'_{22\mathrm{PT}}\,. \tag{12}$$

The N factor can be eliminated by dividing the measurements performed at the same T_{ACC}.

$$\frac{X(T'_{\mathrm{ACC}}, T_{22\mathrm{PT}})}{X(T'_{\mathrm{ACC}}, T'_{22\mathrm{PT}})} = \frac{K(T'_{\mathrm{ACC}} + T_{22\mathrm{PT}})}{K(T'_{\mathrm{ACC}} + T'_{22\mathrm{PT}})} \frac{P(T_{22\mathrm{PT}})}{P(T'_{22\mathrm{PT}})} \tag{13}$$

$$\frac{X(T_{\mathrm{ACC}}, T''_{22\mathrm{PT}})}{X(T_{\mathrm{ACC}}, T'''_{22\mathrm{PT}})} = \frac{K(T_{\mathrm{ACC}} + T''_{22\mathrm{PT}})}{K(T_{\mathrm{ACC}} + T'''_{22\mathrm{PT}})} \frac{P(T''_{22\mathrm{PT}})}{P(T'''_{22\mathrm{PT}})} \tag{14}$$

After calculating the ratio of equations (13) and (14) the unknown rate coefficient K can be eliminated with use of relations (12)

$$P(T'''_{22\mathrm{PT}}) = P(T''_{22\mathrm{PT}}) \frac{P(T'_{22\mathrm{PT}})}{P(T_{22\mathrm{PT}})} \frac{X(T'_{\mathrm{ACC}}, T_{22\mathrm{PT}})}{X(T'_{\mathrm{ACC}}, T'_{22\mathrm{PT}})} \frac{X(T_{\mathrm{ACC}}, T'''_{22\mathrm{PT}})}{X(T_{\mathrm{ACC}}, T''_{22\mathrm{PT}})}\,. \tag{15}$$

The above equation is a recursive relation for determining P. Since no discrepancy in the measured data is apparent at temperatures above 50 K, we assume that P is equal to unity above 50 K. This assumption provides us with a sufficient boundary condition for solving the equation (15). This technique was applied on the experimental data from Figure 2 (left panel). The results are presented in Figure 3. The obtained overlap factor was then used to correct the rate coefficient measurements for publication by Jusko et al. [2011].

These quantitative results clearly support the qualitative analysis performed in the introduction. At low temperatures, the ions should be concentrated in the potential minimimum on axis and the overlap should increase. However, the observations indicate, that the potential minimum is located outside of atomic H beam.

An additional measurement was performed at $T_{22\mathrm{PT}} = 70$ K by measuring the associative detachment rate as a function of RF amplitude in the trap. According to equation (2), by operating the trap at a low RF amplitude $V_0 = 7.5$ V we were able to achieve the same effective potential for H^- as for CO_2^+ at $V_0 = 50$ V. The correction factor was thus determined experimentally by calculating the ratio of observed H^- AD reaction rates at different RF amplitudes with a result $N_{\mathrm{H}}(H^-)/N_{\mathrm{H}}(CO_2^+) = 1.37 \pm 0.08$. The error estimate was determined purely from the goodness of fit. The observed value differs slightly from the theoretical one. However, the difference is well below 10 %. Due to the discrepancy of the H^- overlap scaling from theory (Figure 2) we expect a slightly different correction factor at 30 K where the chemical probing was performed. A conservative error estimate of the calibration procedure 20 % was used in our error analysis.

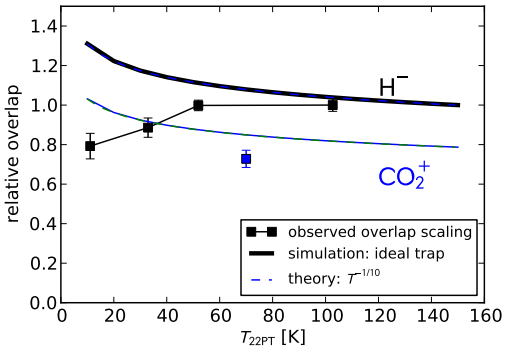

Figure 3. The theoretical beam-cloud overlap scaling in comparison with numerically and experimentally obtained results. The solid line corresponding to the numerical model is indistinguishable from the theoretical dashed line. The experimentally observed overlap scaling of H^- ion cloud differs significantly from the theory at low temperatures. The ratio of CO_2^+ and H^- overlaps is, however, close to the theoretical value.

Simulations: The observed effect of decrease in the overlap with decreasing temperature can be explained by various imperfections of the 22-pole trap. We have set up several simplified models of possible scenarios. A two dimensional model of an infinitely long 22-pole trap is used in all studied cases.

The effective potential is calculated from equation (2). The DC potential ϕ_s and the RF potential ϕ_0 are calculated separately by solving the Poisson equation with Dirichlet boundary condition on the rods and with a zero Dirichlet boundary condition on the distant domain boundary outside of trap. The Poisson equation was solved by means of the finite element method. The mesh was generated by gmsh [Geuzaine and Remacle, 2009]. The DOLFIN software from the FEniCS project [Logg and Wells, 2010] was used for solving the Poisson equation and all subsequent data processing. Once the effective potential was calculated, the thermal ion distribution given by the Boltzmann distribution was obtained from

$$n_i(\boldsymbol{r}) = \exp\left(-\frac{V^*(\boldsymbol{r})}{k_\mathrm{B}T}\right) \Big/ \int_\mathrm{trap} \exp\left(-\frac{V^*(\boldsymbol{r}')}{k_\mathrm{B}T}\right) \mathrm{d}\boldsymbol{r}' \ . \tag{16}$$

Finally, the overlap was obtained by integrating the fraction of ions in the beam, which has diameter approximately 5 mm. The whole procedure was repeated with parameters of CO_2^+ and H^- for several temperatures in order to obtain the temperature dependence of the overlap. In our plots, the overlap is normalized to the value corresponding to H^- trapped in the ideal trap at 150 K under our experimental conditions. The results calculated for the ideal trap are plotted in Figure 3. The simulated curves are indistinguishable from the theoretical curves, which validates the assumptions of the theoretical model and the correctness of our numerical model.

The first case studied by our model is the possibility of mechanical deformation of the 22-pole. We investigate a possible offset between the rod assemblies of opposite polarities. This effect was observed by Hlavenka et al. [2009] and investigated using numerical simulation by Otto et al. [2009]. Our model replicates the results of Otto et al. [2009]. By simulating high enough offset, it is possible to mimic the behavior observed in our experiment, since ions start hiding in the ten potential minima outside of the beam at low temperatures. See Figure 4 for a plot of the calculated H^- density distribution at 30 K and the overlap temperature dependence. However, a very high deformation of 0.24 mm is needed to explain the observed behavior. In our 22-pole, the rods are fixed on both sides of the trap and such a deformation seems to be an improbable explanation of the observed effects.

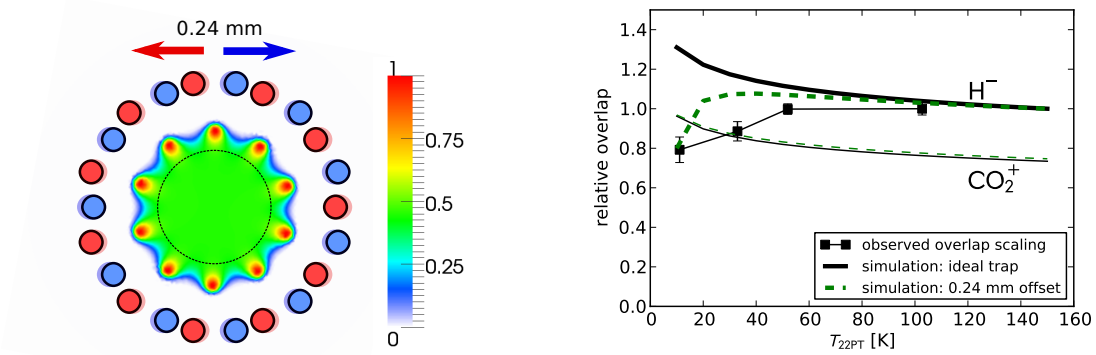

Figure 4. Influence of an offset between the two rod assemblies. The H^- density distribution at 30 K (left panel). The color palette is normalized to unity in the maximum of this plot and is valid for all subsequent plots. The cloud-beam overlap as a function of temperature (right panel).

The other investigated case is the possibility of complete grounding of one of the rods. A more probable scenario would be only a partial disconnecting from the RF combined with charging up of the rod. The effect of charging or patch fields is investigated separately in the next paragraph though. See Figure 5 for a plot of the calculated overlap temperature dependence and H^- density distribution at 30 K. Interestingly, the grounding of one of the rods has virtually no effect on the overlap. Therefore it cannot explain the observed behavior.

Finally, the influence of patch fields was investigated. The patch fields are caused by inhomogeneities of the polycrystalline metal and by surface coating with thin layers of impurities. They can occur on various scales with various intensities. For our study a case of a large patch with a small ±10 mV potential was chosen, because its effect resembles more closely the observed behavior. The magnitude and scale of the simulated patch is in agreement with the measurements of patch effects on metal surfaces [Darling et al., 1992; Rossi and Opat, 1992]. See Figure 6 for a plot of the calculated ion density distribution at 30 K and overlap temperature dependence. The effect of both positive and negative patch was investigated. As expected, the effect of attractive potential distortion is more pronounced, since the ions are accumulated in the deeper potential minimum outside of the beam at low temperatures.

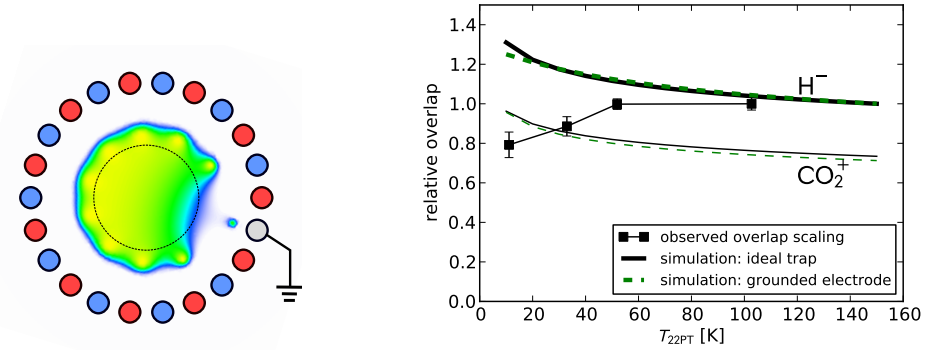

Figure 5. Influence of grounding of one electrode. The H^- density distribution at 30 K (left panel). The cloud-beam overlap as a function of temperature (right panel).

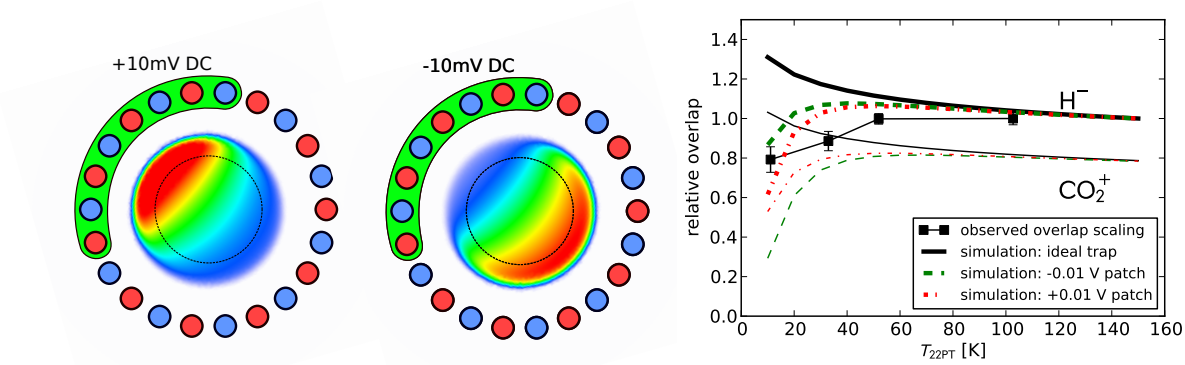

Figure 6. Influence of positive and negative patch fields. The H^- density distribution at 30 K (left panel). The cloud-beam overlap as a function of temperature (right panel).

Although a quantitative agreement with the measured data is not achieved, the magnitude of the effect is well reproduced by the simulation with realistic input parameters. As the patch effects cannot be expected to be translationally symmetric, a fully 3D model would be needed to account properly for the patch distribution and the end-electrode effects.

Conclusion

A discrepancy in the data measured using the 22-pole trap was observed. By analysis of the measured data a correction factor was obtained, which was then used to correct the final results. Several possible explanations of the observed effect were proposed. All of the explanations were based on possible imperfections of the 22-pole trap. From the computational simulations of these imperfections we conclude, that the most probable of our explanations is the presence of DC patch fields in the trap. The ratio of overlaps between CO_2^+ and H^-, which is important for our H density calibration procedure, does not differ from the theoretical value by more than 20 % in our models at 30 K. We therefore use 20 % as the error estimate for the H density calibration.

A possible solution to the problem of patch fields is cleaning of the trap described by Gerlich [1992]. Alternatively, the effect on H beam calibration can be eliminated by trapping the CO_2^+ in the same effective potential as a reference measurement with H^-.

Acknowledgments. This work is a part of the research plan MSM 0021620834 and grant OC10046 financed by the Ministry of Education of the Czech Republic and was partly supported by GACR (202/07/0495, 202/08/H057, 205/09/1183, 202/09/0642), by GAUK 25709, GAUK 406011, GAUK 388811 and by COST Action CM0805 (The Chemical Cosmos). We wish to thank prof. D. Gerlich for providing us with his know-how of ion trapping technique in valuable discussions. The AB-22PT instrument has been developed in Chemnitz in the group of prof. D. Gerlich with contributions from S. Schlemmer, G. Borodi, and A. Luca and the help from many other people. Since 2010 the instrument is operated in the Faculty of Mathematics and Physics of the Charles University in Prague. We thank the Chemnitz University of Technology and the DFG for lending us the 22-pole trap instrument.

References

Borodi, G., Luca, A., and Gerlich, D., Reactions of CO_2^+ with H, H_2 and deuterated analogues, *Int. J. Mass Spectrom.*, *280*, 218–225, 2009.

Darling, T. W., Rossi, F., Opat, G. I., and Moorhead, G. F., The fall of charged particles under gravity: A study of experimental problems, *Rev. Mod. Phys.*, *64*, 237–257, 1992.

Gerlich, D., Inhomogeneous RF fields: a versatile tool for the study of processes with slow ions, *Adv. Chem. Phys*, *82*, 1992.

Gerlich, D., Borodi, G., Luca, A., Mogo, C., and Smith, M. A., Reactions between Cold CHx+ and Slow H and H2, *Z. Phys. Chem.*, *225*, 475–492, 2011.

Geuzaine, C. and Remacle, J.-F., Gmsh: A 3-D finite element mesh generator with built-in pre- and post-processing facilities, *Int. J. Numer. Meth. Eng.*, *79*, 1309–1331, 2009.

Hlavenka, P., Otto, R., Trippel, S., Mikosch, J., Weidemuller, M., and Wester, R., Absolute photodetachment cross section measurements of the O^- and OH^- anion, *J. Chem. Phys.*, *130*, 061 105, 2009.

Jusko, P., Roučka, Š., Zymak, I., Plašil, R., Gerlich, D., and Glosik, J., Rate Coefficient of Associative Detachment Reaction $H^- + H \rightarrow H_2 + e^-$ at 10–135 K Measured Using Ion Trap, *J. Chem. Phys.*, in preparation, 2011.

Logg, A. and Wells, G. N., DOLFIN: Automated finite element computing, *ACM Trans. Math. Softw.*, *37*, 20:1–20:28, 2010.

Otto, R., Hlavenka, P., Trippel, S., Mikosch, J., Singer, K., Weidemuller, M., and Wester, R., How can a 22-pole ion trap exhibit ten local minima in the effective potential?, *J. Phys. B*, *42*, 154 007, 2009.

Plasil, R., Mehner, T., Dohnal, P., Kotrik, T., Glosik, J., and Gerlich, D., Reactions of cold trapped CH^+ ions with slow H atoms, *Astrophys. J.*, submitted, 2011.

Rossi, F. and Opat, G. I., Observations of the effects of adsorbates on patch potentials, *J. Phys. D.*, *25*, 1349, 1992.